MODELLING OF FLEXOELECTRIC GRAPHENE-BASED STRUCTURES: BEAM, PLATE, WIRE AND SHELL

Ph.D. Thesis

By

SHINGARE KISHOR BALASAHEB

(Roll No. 1701203008)

DISCIPLINE OF MECHANICAL ENGINEERING

INDIAN INSTITUTE OF TECHNOLOGY INDORE

FEBRUARY 2021

MODELLING OF FLEXOELECTRIC GRAPHENE-BASED STRUCTURES: BEAM, PLATE, WIRE AND SHELL

A THESIS

Submitted in partial fulfillment of the requirements for the award of the degree
of

DOCTOR OF PHILOSOPHY

by

SHINGARE KISHOR BALASAHEB

(Roll No. 1701203008)

DISCIPLINE OF MECHANICAL ENGINEERING

INDIAN INSTITUTE OF TECHNOLOGY INDORE

FEBRUARY 2021

INDIAN INSTITUTE OF TECHNOLOGY INDORE

CANDIDATE'S DECLARATION

I hereby certify that the work which is being presented in the thesis entitled **MODELLING OF FLEXOELECTRIC GRAPHENE-BASED STRUCTURES: BEAM, PLATE, WIRE AND SHELL** in the partial fulfillment of the requirements for the award of the degree of **DOCTOR OF PHILOSOPHY** and submitted in the **DEPARTMENT OF MECHANICAL ENGINEERING, Indian Institute of Technology Indore**, is an authentic record of my own work carried out during the time period from December 2017 to February 2021 under the supervision of **Dr. Shailesh I. Kundalwal**, **Associate Professor, Indian Institute of Technology Indore.**

The matter presented in this thesis has not been submitted by me for the award of any other degree of this or any other institute.

February 04, 2021
Signature of the student with date
(SHINGARE KISHOR BALASAHEB)

This is to certify that the above statement made by the candidate is correct to the best of my/our knowledge.

(DR. S. I. KUNDALWAL) **(04.02.2021)**

Signature of Thesis Supervisor with date
(Dr. SHAILESH I. KUNDALWAL)

Shingare Kishor Balasaheb has successfully given his/her Ph.D. Oral Examination held on **4-FEB-2021**.

Signature of Chairperson (OEB) Date: 4th FEB 2021	Signature of External Examiner Date: 5th FEB 2021	Signature(s) of Thesis Supervisor Date: 4th FEB 2021
Signature of PSPC Member #1 Date: 4th FEB 2021	S. Samal Signature of PSPC Member #2 Date: 4th FEB 2021	Signature of PSPC Member #3 Date: 4th FEB 2021
Signature of Convener, DPGC Date: 4th FEB 2021	Signature of Head of Discipline Date: 4th FEB 2021	

Acknowledgements

It is a great pleasure for me to acknowledge all the people who have helped and supported me to complete this Thesis. First and foremost, I express my deep and heartfelt gratitude to my supervisor **Dr. Shailesh Ishwarlal Kundalwal.** I have had the privilege of being associated with him throughout this entire period of doctoral studies. I have been fortunate to have a supervisor who cared so much about my work, and who responded to my questions and queries so promptly. I have received continuous academic support, inspiration and encouragement from him. This has not only enriched me academically but has also nourished my inner self and changed my perspective and attitude a lot. It is though this association with him that I have been able to acquire, develop and sharpen the skills and the scientific methodologies which are invaluable for good independent research. His immense knowledge, guidance, observations and comments helped me a lot to establish the overall direction of the research and to move forward with investigation in depth. For all this, I will remain indebted and grateful to him for my entire life.

I am extremely happy to express my gratitude towards my PSPC members **Dr. Yuvraj Madhukar,** Discipline of Mechanical Engineering, **Dr. Sumanta Samal,** Discipline of Metallurgy Engineering and Materials Science**, Dr. Santanu Manna,** Discipline of Mathematics, Indian Institute of Technology Indore for their valuable suggestions and comments to improve my work. I am grateful to **Head**, **DPGC Convener,** all the faculty members and staff of Discipline of Mechanical Engineering, **IIT Indore** for providing encouraging environment to carry out research effectively.

I would like to acknowledge **Prof. Neelesh Kumar Jain, Director, IIT Indore** for providing a conducive environment for research and opportunity to explore my research capabilities at IIT Indore. I am also thankful to **The Dean of Academic Affairs, The Dean of Research and Development and The Dean of Student Affairs, IIT Indore**. I acknowledge and thankful to **CSIR, Govt. of India** for providing fellowship to pursue my doctoral studies.

A very special thanks to **Dr. Sachin Chavan, Dr. Ajit Dhanawade, Dr. Manojkumar Dalvi, Mr. Ghuge** and **Mr. Digvijay Shelke** who always suggested and encouraged me to pursue my doctoral studies during my teaching.

I take this opportunity to thank each and every one of my friends. There have been so many of you – it is impossible to name all of you. I am indebted to my seniors, lab mates and colleague researchers especially **Mr. Rohit Kothari, Mr. Vijay Choyal, Mr. Madhur Gupta, Mr. Sidram Hirmukhe, Mr. Vaibhav Kathavate, Mr. Vaibhav Nemane** and **Mr. Achyut Kulkarni** for their cooperation and stay so as to make my PhD

journey joyful and with whom I have spent so much time discussing both technical and non-technical stuff.

It is impossible to imagine a life without family. I would like to acknowledge my father **Mr. Balasaheb Shingare** and mother **Mrs. Shobha Shingare** for their continuous inspiration during the entire period of my stay at IIT Indore and for appreciating my work with great patience and understanding. I salute you both for the selfless love, care, pain and sacrifice you did to shape my life. Although you hardly understood what I researched on, you were willing to support any decision I made. It gives me immense pleasure and satisfaction to express my respect and gratitude to my elder brother **Mr. Sharad Shingare** and his wife **Mrs. Sonali Shingare** for their constant inspiration and unconditional moral support. I would like to express my deepest love to my sweet nephew **Kartik** for bringing happiness in my life whose innocence refreshed me and my family during difficult times. Also, a special thanks to my uncles and all in-laws for their continuous inspiration. Last but not the least, I would like to thank my wife **Mrs. Shital Shingare** for her love, motivations, valuable prayers and support which provided me strength and for coming as good luck in my life during my PhD journey.

Finally, I am thankful to all who directly or indirectly contributed, helped and supported me.

-Kishor Balasaheb Shingare

Indian Institute of Technology Indore

Date: 04-02-2021

Dedicated To

My Beloved Family

Mother, Father, Wife, Brother, Sister In-law and Little Champ for their love, care and blessings

Abstract

Owing to its unique multifunctional and scale-dependent physical properties, a graphene is emerged as a promising reinforcement to enhance the overall response of its nanotailored composite materials. Most recently, the piezoelectricity phenomenon in graphene sheets was found through interplay between different non-centrosymmetric pores, curvature and flexoelectricity concept. This has added new functionality to the existing non-piezoelectric graphene. An overview of the literature revealed that the graphene-reinforced polymer matrix nanocomposite-based structures find numerous nanoelectromechanical systems (NEMS) and allow researchers to tailor their mechanical, thermal and electrical properties as per requirements. Such a piezoelectric graphene reinforced in the polymer matrix may be called as "*graphene-reinforced nanocomposite* (GRNC)". Surprisingly, the application of piezoelectric graphene for modelling of graphene-based structures is not explored yet and this has provided the motivation for this Thesis. Therefore, the purpose of present research is to model the GRNC-based beams, plates, wires and shells.

The prediction of effective elastic, piezoelectric as well as dielectric properties of GRNC are required priori. Therefore, the effective properties of GRNC were determined first as the open literature do not provide the same accounting the piezoelectric, flexoelectric and surface effects. In the first, the elastic properties of pristine and defective graphene sheets were determined via molecular dynamics simulations and the obtained results are found to be in good agreement with the existing experimental and numerical results. In the second, the micromechanical models based on the mechanics of materials (MOM), strength of materials (SOM) and finite element (FE) were developed to predict the effective elastic, piezoelectric and dielectric properties of GRNC. The developed models predict that the piezoelectric coefficients of GRNC account for the actuation capability of a graphene layer in the transverse direction due to the applied electric field in the plane. The predictions by analytical and numerical models are found

in good agreement. Finally, the obtained effective properties of GRNC were used to study the electromechanical behaviour of GRNC-based beams, plates, wires and shells.

An analytical model based on the linear piezoelectricity and Euler-Bernoulli theory was developed to investigate the electromechanical response of GRNC cantilever beam under both electrical and mechanical loads accounting the flexoelectric effect. In another attempt, the electromechanical behavior of GRNC beams with flexoelectric and surface effects were investigated using size-dependent Euler-Bernoulli theory and Galerkin's weighted residual method. Analytical and FE models were developed to study the static response of flexoelectric GRNC beams under point load with various boundary conditions: cantilever, simply-supported and clamped-clamped. The cantilever nanobeam shows a softer elastic behavior compared to that of simply-supported and clamped-clamped nanobeams for positive surface stress and the reverse is true for negative surface stress. On the contrary, simply-supported and clamped-clamped nanobeams show stiffer elastic behavior due to positive surface stress effect and vice versa. The results predicted by both analytical and FE models are found to be in better agreement. Outcomes reveal that the flexoelectric and surface effects on the static response of GRNC beams are significant and should be taken into account. The electromechanical behavior of GRNC plates with flexoelectric effect was studied by deriving an analytical model based on Kirchhoff's plate theory and Navier's solution. The static and dynamic responses of simply-supported flexoelectric GRNC plates under different loadings such as uniformly distributed, non-uniformly distributed, inline and point loads were investigated. Our results reveal that the flexoelectric effect on the static and dynamic responses of GRNC plate is substantial and cannot be neglected.

Analytical and FE models were developed to study the electromechanical responses such as electric potential and deflection of cylindrical GRNC cantilevered nanowire with flexoelectric effect. Results show that the piezoelectric potential in the GRNC nanowire depends on the transverse force but it is not a function of the force acting along its axial direction. The electric potential in the tensile and compressive sections of nanowire is antisymmetric along its cross-section, making it as a "parallel plate capacitor" for nanopiezotronics applications. The predictions of potential distributions across the GRNC nanowire show better agreement with FE predictions.

Finally, the analytical and FE models were developed for the elastic cylindrical shell laminated with flexoelectric GRNC layer based on Kirchhoff–Love theory considering both piezoelectric and flexoelectric effects to investigate the electric potential distributions in it. Developed models envisage the results for the distribution of electric potentials in GRNC shell and results predicted by analytical model with piezoelectric effect are found to be in better agreement with FE predictions. It is found that the electromechanical behavior of laminated shell is significantly improved due to the incorporation of flexoelectric effect.

To summarize, this Thesis reports the enhancement in electromechanical response of GRNC structures due to the incorporation of flexoelectric effect. The electromechanical response of GRNC structures such as beam, plate, wire and shell can be engineered to achieve the desired electromechanical characteristics using different boundary and loading conditions as well as different parameters such as aspect ratio, thickness, diameter, length and volume fraction of graphene. Our study highlights the possibility of developing light-weight and high-performance piezoelectric graphene-based NEMS such as sensors, actuators, nanogenerators and distributors as the existing piezoelectric material such as Lead Zirconate Titanate (PZT) is heavy, brittle and toxic (Ibn-Mohammed et al., 2017).

Keywords: *Graphene; Piezoelectricity; Flexoelectricity; Surface effect; Micromechanics; Mechanics of materials; Strength of materials; Finite element method; Nanocomposite structures; NEMS.*

TABLE OF CONTENTS

LIST OF FIGURES

LIST OF TABLES

List of Abbreviations and Symbols

Abbreviations and Symbols

1D	One dimensional
2D	Two dimensional
3D	Three dimensional
1-2-3 and x-y-z	Problem coordinate and principal material coordinate systems
A	Cross-section of the beam (m^2)
A_e	Effective electrode area of piezo- or flexo-electric patch (m^2)
A_x and A_Φ	Lame parameters in the axial and circumferential directions, respectively
A_{mn} , B_{mn} and C_{mn}	Amplitude of shape functions (m)
a	Length of GRNC plate (m)
b	Width of GRNC beam or plate (m)
C	Beam cross-sectional perimeter (m)
$[C^r]$	Elastic coefficient matrix of the *r*–th phase (GPa or N/m^2)
C_{ijkl}	Fourth order elastic coefficient tensor (GPa)
C_{ij}^{eff}, e_{ij}^{eff} and $\in_{ij}^{eff}$	Effective elastic (GPa), piezoelectric (C/m^2) and dielectric (F/m) coefficients of GRNC, respectively.
d	Nodal displacement vector
D_3^g and D_3^m	Electric displacements of the graphene and polyimide polymer matrix, respectively (C/m^2)
D_i	Electric displacement vector (C/m^2)
D_γ^s	Surface electric displacement (C/m)
E	Young's modulus (GPa)
E_i	Electric field vector (V/m)
E_γ^s	Surface electric field (V)
$(EI)_{cantilever}$	Effective bending rigidity of GRNC cantilever beam (N/m)

$(EI)^{eff}$	Effective bending rigidity (N/m)
e_{33}, e_{31} and e_{15}	Axial, transverse and shear Piezoelectric coefficients, respectively (C/m^2)
e_{31}^s	Surface piezoelectric coefficient (C/m)
e_{ijk} and d_{ijk}	Third order piezoelectric stress and strain tensors, respectively (C/m^2 and C/N)
F	Nodal force vector
f_{ijkl} and μ_{ijkl}	Fourth order flexocoupling and flexoelectric tensors, respectively (V and C/m)
f_x	Transverse force (N)
h	Height of GRNC beam (m)
h_f	Thickness of GRNC layer/patch (m)
I_y	Moment of inertia of the beam (m^4)
I^*	Perimeter moment of inertia (m^3)
I	Moment of inertia of nanowire (m^4)
K	Global stiffness matrix
L	Length of GRNC nanowire or shell (m)
l_e	Length of GRNC beam (m)
[M]	Stress concentration tensor
$\widetilde{M}$	Virtual work done (Nm or J)
M	Bending moment (Nm)
M_s	Surface bending moment (N)
[N]	Strain concentration tensor
N_1, N_2, N_3 and N_4	Shape functions in FE analysis
{n}	Unit vector
P_i	Piezoelectric polarization (C/m^2)
P	Point load (N)
F	Shear force (N)
q_0	Uniformly distributed load (MPa)
SS	Simply-supported

$[S^r]$	Elastic compliance matrix of the *r*–th phase (m^2/N)
T_z^s	Lateral loadings (N)
U	Electric Gibbs free energy density function (J)
U_s	Surface internal energy density function (J)
U_{oc}	Total internal energy stored under open circuit conditions (J)
U_{sc}	Total internal energy stored under short circuit conditions (J)
$U_{imn}(x, \Phi)$	Mode shape function
u^s	Surface displacement
u, v and w	Displacement vector in the respective x, y and z direction (m)
u(x) and w(x)	Horizontal and vertical deformations of the beam, respectively (m)
(w) and (φ)	Translational and rotational degree of freedom of beam, respectively
Ω	Volume of the RVE of GRNC (m^3)
v_g	Volume fraction of the graphene in GRNC
v_m	Volume fraction of the matrix in composite
$w_{cantilever}$	Deflection of cantilever GRNC beam (m)
w (x, y)	Deflection of simply-supported GRNC plate (m)
$\{\varepsilon\}$	Strain vector
$\{\bar{\varepsilon}_{ij}\}$	Volume average strain vector
$\{\varepsilon^*\}$	Eigenstrain vector
$\{\varepsilon^0\}$	Uniform strain vector
$\{\varepsilon^r\}$	Strain vector of the *r*–th phase
$\{\varepsilon^m\}$	Strain vector of the matrix phase
ε_1^r, ε_2^r, ε_3^r	Normal strains along the principal material coordinate axes 1, 2 and 3, respectively, in the *r*–th phase
ε_{12}^r, ε_{13}^r, ε_{23}^r	Shearing strains in the *r*–th phase
$\{\varepsilon^{nc}\}$	Strain vector of the GRNC
$\varepsilon_{\alpha\beta}^s$	Surface strain (1/m)

$\eta_{ij,k}$	Higher order strain gradient tensor (1/m)
$\{\sigma\}$	Stress vector (GPa)
$\{\bar{\sigma}_{ij}\}$	Volume average stress vector (GPa)
$\{\sigma^0\}$	Uniform stress vector (GPa)
$\{\sigma^r\}$	Stress vector of the *r*–th phase (GPa)
$\{\sigma^g\}$	Stress vector of the graphene (GPa)
σ_1^r, σ_2^r, σ_3^r	Normal stresses along the principal material coordinate axes 1, 2 and 3, respectively, in the *r*–th phase (GPa)
σ_{12}^r, σ_{13}^r, σ_{23}^r	Shearing stresses in the *r*–th phase (GPa)
$\{\sigma^{nc}\}$	Stress vector of the GRNC (GPa)
$\sigma_{\alpha\beta}^s$	Surface moment stress (N/m)
τ_{ijk}	Higher order stress gradient tensor (N/m)
β_{kl}	Second order tensor of reciprocal dielectric susceptibility (m/F)
ϵ_0	Permittivity of air or vacuum (F/m)
ξ^{eff}	Effective EMC coefficient
$\eta_{mn}(t)$	Modal participation factor
η_0, η_1 and η_a	Krenchel orientation, critical length efficiency and agglomeration factor
ω_{mn}	Resonant frequency (Hz)
$\emptyset$	Electric potential vector (V)
$\emptyset^s$	Surface electric potential vectors (V)
$\emptyset_{ten,com}^{max}$	Maximum electric potential of GRNC nanowire at tension and compression (V)
$\emptyset_{total}^{Piezo}$	Piezoelectric potential in GRNC shell (V)
$(\emptyset_{mn}^{flexo})_{Total}$	Total modal electric potential due to flexoelectricity in GRNC shell (V)

Subscripts and Superscripts

r	r–th phase of constituent of GRNC

nc	GRNC composite
eff	Effective coefficient
g and m	For graphene and polyimide matrix
b	For bulk material
s	For surface material
u and l	Top and bottom surfaces of beam, respectively

Greek Letters

ρ	Density (Kg/m^3)
ρ_s	Surface charge density (C/m^2)
ρ_v	Volume charge density (C/m^3)
$\emptyset$	Electric potential (V)
Φ	Circumferential direction
ω	Natural and resonant frequency (Hz)
θ	Angle (degree or radian)
ϑ	Poisson’s ratio
ε	Strain
σ	Cauchy stress (N/m^2)
τ	Higher order stress or surface stress (N/m)
δ_{ij}	Kronecker delta
π	Approximately 3.1416
ξ	EMC coefficient
α	Transverse direction in shell
γ and Γ	Constants used in mathematical formulation
λ	Constant defined in text
κ	Radius of curvature (m^{-1})
Σ	Summations

ACRONYMS

AIREBO	Adaptive intermolecular reactive empirical bond order
CNT	Carbon nanotube
CVD	Chemical vapour deposition
DOF	Degrees of freedom
EMC	Electromechanical coupling
FE	Finite element
FETs	Field effect transistors
GRNC	Graphene reinforced nanocomposite
GO	Graphene or graphite oxide
GNPs and GNS	Graphene nanoplatelets and graphene nanosheets, respectively
LAMMPS	Large-scale molecular massively parallel simulator
MD	Molecular dynamics
MWCNT	Multi-walled carbon nanotube
MOM	Mechanics of materials
NEMS	Nanoelectromechanical systems
ROM	Rules-of-mixture
RVE	Representative volume element
SHM	Structural health monitoring
SOM	Strength of materials
SWCNT	Single-walled carbon nanotube
UDL	Uniformly distributed load
VDL	Varying distributed load

Chapter 1

Introduction and Literature Review

In this Chapter, a brief introduction to the graphene as well as review of literature on graphene-reinforced nanocomposite (GRNC) and its structures such as beam, plate and shell are presented. Also, the concepts of flexoelectricity and piezoelectricity are presented. Based on the review of literature, the scope of work for this Thesis is identified and the objectives of the dissertation are presented. Organization of the Chapters is delineated at the end of this Chapter.

1.1 Graphene

The ground-breaking discovery of two-dimensional (2-D) atomic-thick graphene layer was carried out by Novoselov and Geim in 2004 by peeling off highly oriented pyrolytic graphite (HOPG) to obtain a graphene sheet with the help of “Scotch Tape” method. In 2010, for such an innovative discovery, they awarded with the Nobel Prize in Physics. Owing to its unique multifunctional and scale-dependent physical properties, the global interest in this “novel 2D material” is still growing, which can be observed from the increasing publications per year in scientific research, academia and industry. Figure 1.1 illustrates the schematic representations of graphene layer. It can be observed that a single layer of sp^2-hybridized carbon atoms closely packed in a honeycomb lattice structure. A graphene layer is made of carbon atoms which are arranged in hexagonal packing arrays. The strong covalent bond of ~0.142 nm long exists between two carbon atoms of graphene. For carbon-based materials, the graphene can be a building block. Graphene can be used as a versatile material because it can be (i) covered up into zero-dimensional (0-D) fullerene, (ii) rolled into one-dimensional (1-D) carbon nanotube (CNT), and (iii) stacked into three-dimensional (3-D) graphite.

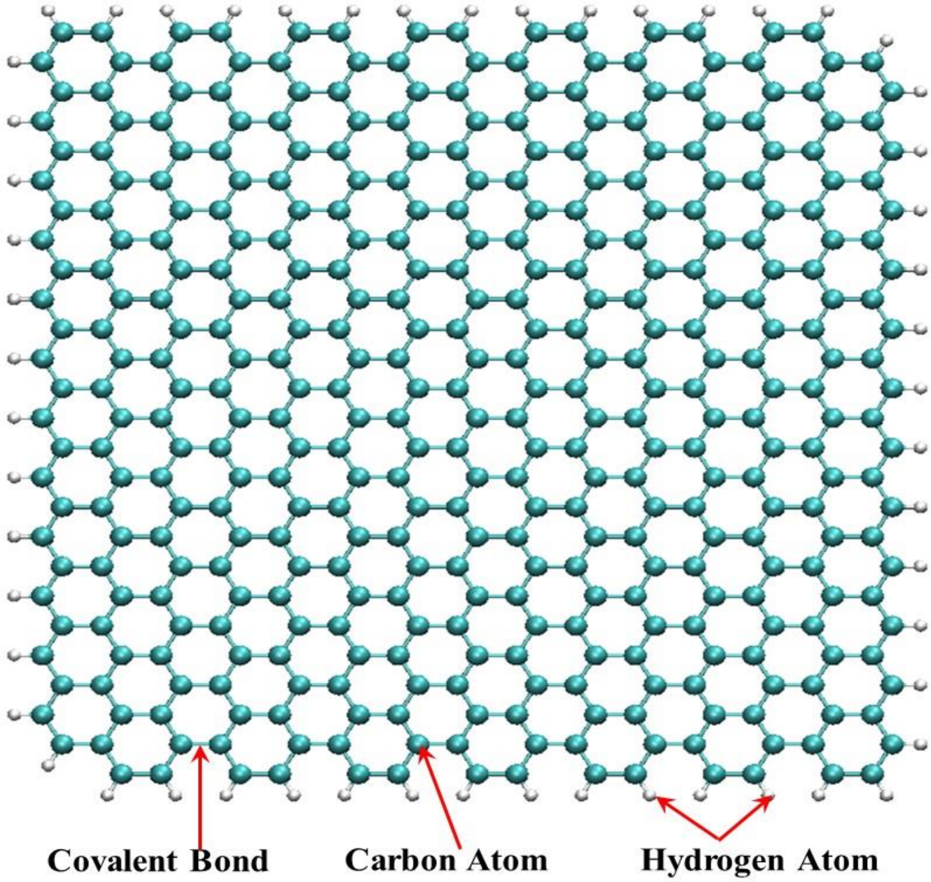

Figure 1.1: Atomic structure of a functionalized graphene sheet.

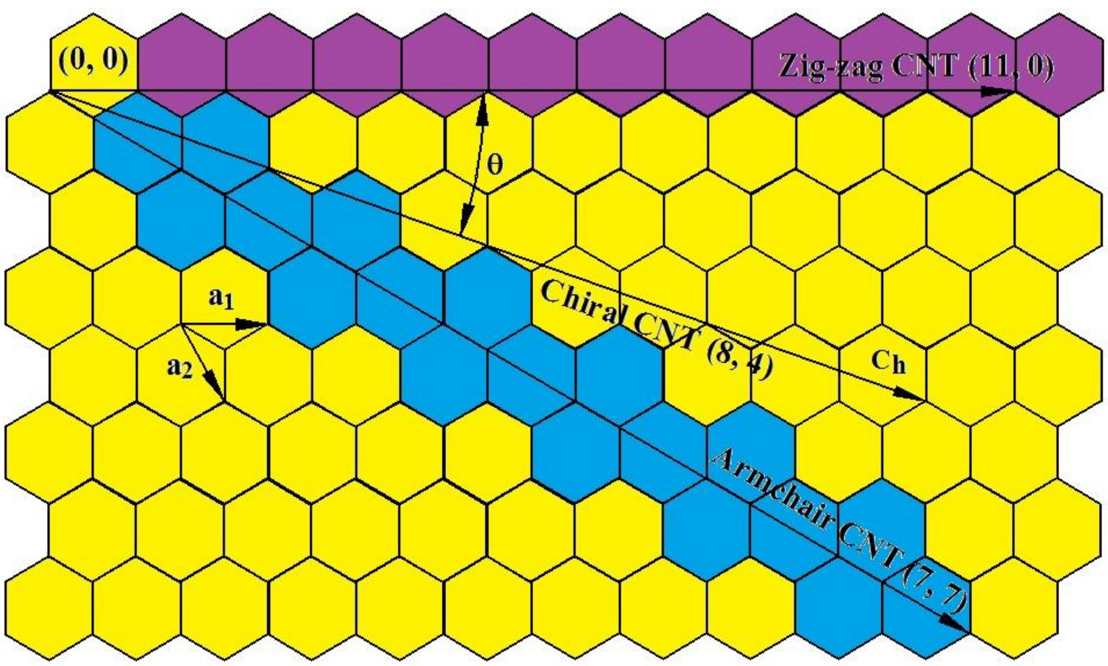

Figure 1.2: Schematic diagram of a hexagonal graphene sheet to identify the types of CNTs.

By rolling a graphene sheet, CNT can be formed as a hollow seamless cylinder. A widely used approach to identify the types of CNTs such as armchair, zigzag, and chiral depend on the rolling direction of a graphene sheet, as shown in Fig. 1.2. In general, carbon nanostructures are recognized as advanced nanomaterials with outstanding thermomechanical and electrical properties.

1.1.1 Properties of Graphene

A graphene has captivated massive response from researchers due to its exceptional properties such as Young's modulus (~1.1 TPa), electrical conductivity (~6000 S/cm), thermal conductivity (~5000 W/m/K), ultimate tensile strength (130 GPa), high electrochemical sensitivity and scale-dependent electronic properties (Zhang et al., 2005; Balandin et al., 2008; Du et al., 2008; Lee et al., 2008; Gupta and Batra, 2010; Gangwar et al., 2012; Verma et al., 2014; Cui et al., 2016; Alian et al., 2017; Kundalwal et al., 2017; Su et al., 2018; Wang et al., 2020). Moreover, it possesses large surface area (2630 m^2/g) and electron mobility (~250,000 cm^2/Vs) at room temperature and these unique properties make it striking material for use in multifarious applications. Graphene is a zero-bandgap semiconductor with tunable electrical properties, and hence it is more suitable candidate for micro- and nano-electromechanical systems (MEMS/NEMS) applications. Therefore, graphene is extensively considered as one of the most remarkable materials of 21^{st} century which possesses distinct properties from its parent/bulk graphite form. The extraordinary geometrical and material properties as well as characteristics of a graphene are listed in Table 1.1.

Apart from the above-mentioned unique properties, few recent attempts were made to show piezoelectric activity in the non-piezoelectric graphene layer that increased its multifunctionality. Most recently, the piezoelectric effect in non-piezoelectric graphene layers is found by Kundalwal et al. (2017) using a flexoelectric phenomenon via quantum mechanics calculations. This study showed that the presence of strain gradient in non-piezoelectric graphene sheet does not only affect the ionic positions, but also the asymmetric redistribution of the electron density, which induces strong polarization in the graphene sheet. The resulting axial and normal piezoelectric coefficients of graphene sheet were determined using two loading conditions: (i) a graphene sheet containing non-centrosymmetric pore subjected to an axial load and (ii) a pristine graphene sheet subjected to a bending moment. Their study showed the electromechanical couplings in the graphene sheet can be altered by varying the size and shape of non-centrosymmetric pores and radius of curvature (Fig. 1.3).

Table 1.1: Geometrical and material properties as well as characteristics of a graphene.

Graphene	**Properties**	**Reference**
Dimension	2-D	Novoselov et al. (2004)
Bond Length	~0.142 nm	Kundalwal et al. (2017)
Bond Type	Covalent	Daniel and Vitaly (2016)
Thickness	~0.34 nm	Gong et al. (2010)
Structure	Hexagonal Honeycomb Lattice structure	Young et al. (2012)
Hybridization	sp^2	Young et al. (2012)
Young's Modulus	~1.1 TPa	Lee et al. (2008)
Ultimate Tensile Strength	~130 GPa	Lee et al. (2008)
Electrical Conductivity	~6000 S/cm	Du et al. (2008)
Thermal Conductivity	~5000 W/m/K	Balandin et al. (2008)
Electron Mobility	~250,000 cm^2/Vs	Du et al. (2008)
Specific Surface Area	2630 m^2/g	Gong et al. (2010)
Bandgap	Zero	Daniel and Vitaly (2016)
Transparency	~97%	Daniel and Vitaly (2016)
Piezoelectricity	Non-piezoelectric	Kundalwal et al. (2017)
When Wrapped	Fullerene (0-D)	Zhao et al (2020)
When Rolled	CNTs (1-D)	Zhao et al (2020)
When Stacked	Graphite (3-D)	Zhao et al (2020)
Fabrication Methods	Mechanical, liquid, and Electrochemical Exfoliation, CVD (Origin- "Scotch Tape Method")	Young et al. (2012)
Derivatives	GO, GNPs, GNs	Young et al. (2012)

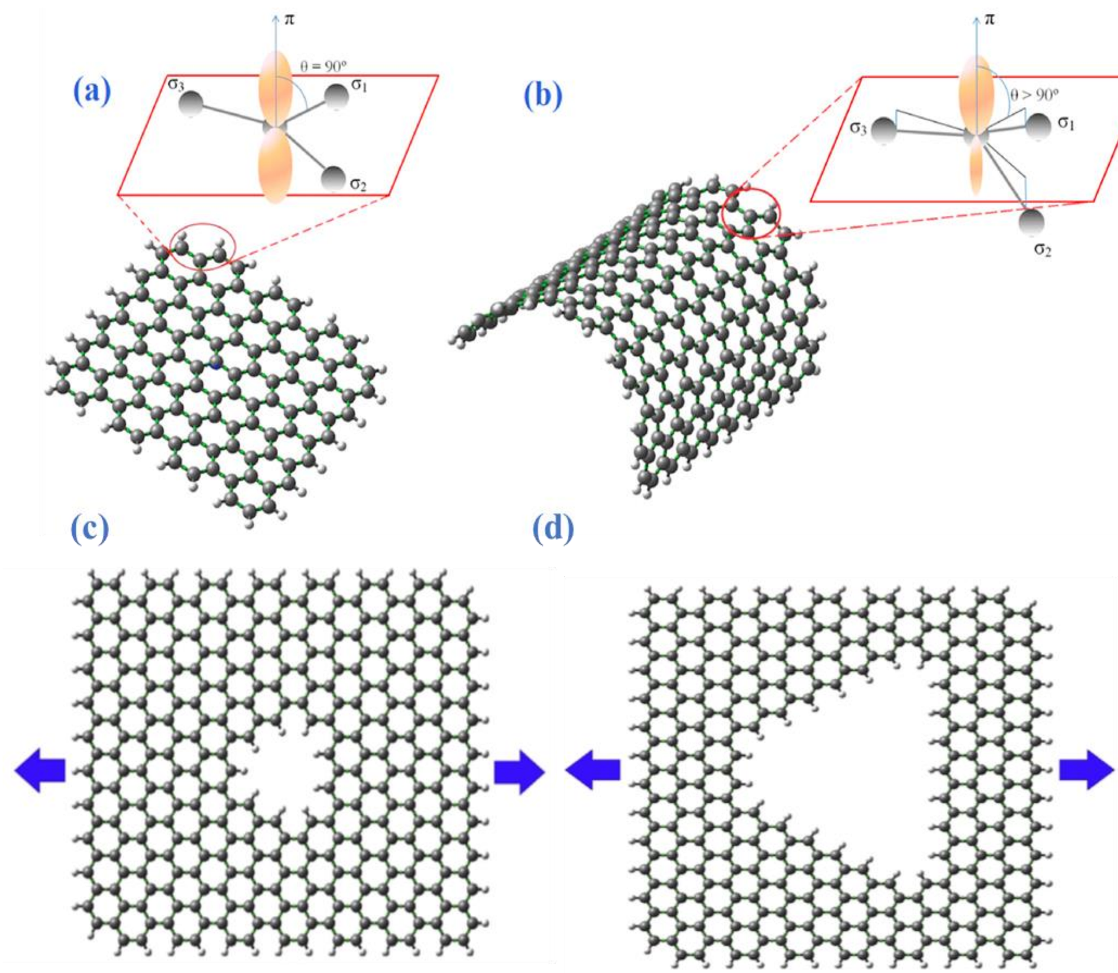

Figure 1.3: Graphene sheets in which p-orbitals are (a) symmetric and (b) asymmetric; Passivated armchair graphene sheet with trapezoidal pore subjected to an axial stress: (c) 4% vacancy and (d) 19.5% vacancy. (Courtesy by Kundalwal et al., 2017)

Graphene is being widely used in the NEMS applications. For instance, using the nonlocal theory for elastic plate, the vibration analysis of single atomic-layered graphene is investigated by Pradhan and Murmu (2009). Conley et al. (2011) proposed a practical realization of the strain-engineering scheme to control electron properties of graphene cantilevers subjected to significant variation of strain. Graphene beams were extensively studied in the last decade (Li et al. 2012 and references therein). Free-standing carbon nanomaterial hybrid sheets, consisting of CNTs, exfoliated graphite nanoplatelets and nanographene platelets, were prepared by Hwang et al. (2013) using various material combinations and compositions. Under tensile strains, these carbon nanomaterial sheets showed piezoresistive behavior, characterized by a change in electrical resistance with applied strain.

Huang et al. (2006) and Pei et al. (2010) determined the atomic volume from the relaxed graphene sheet with the thickness of 3.4 Å. They computed the stress in the graphene sheet by averaging the obtained stress of each carbon atom in it. Various researchers obtained the properties of pristine and defected graphene using molecular dynamic simulations as well as experimental tests (Lee et al. 2008; Jing et al. 2012; Dewapriya et al. 2015). Jing et al. (2012) used COMPAAS force field to model the defective graphene sheets containing vacancies which were functionalized by hydrogen atoms on the dangling bonds. They reported that the percentage of reduction in Young's modulus is ~1.6% in case of graphene containing 6 carbon atom vacancies and the percentage of reduction is ~1.53% for functionalized graphene with 6 missing carbon atoms. This is attributed to the hydrogenation and saturation of the dangling bonds at the edges and porosity in graphene sheet. Similarly, Zelisko et al. (2014) examined the influence of shape and size of pores on the 2-D graphene nitride sheets to generate piezoelectricity in them using first-principle calculations.

To simplify computational efforts, several researchers modeled the graphene sheet as a continuum plate in order to obtain its bulk properties (Park et al. 2010; Roberts et al. 2010; Politano and Chiarello 2013, and references therein; Hosseini-Hashemia et al. 2018). Most of the existing studies on the straining of graphene are based on the analytical as well as numerical solutions using the concept of continuum elasticity and hence, the graphene can be used as a continuum medium (Gupta and Batra 2010; Gradinar et al. 2013; Verma et al. 2014; Bahamon et al. 2015). They suggested that the displacement of each carbon atom in homogeneously deformed graphene layer is given by the deformation of the continuum medium, on which the atom is embedded. Kvashnin et al. (2015) reported that a graphene sheet does not show any polarization until the instantaneous quantum fluctuation is responsible for the van der Waals interactions.

Chandratre et al. (2012) confirmed mathematically that the piezoelectric response can be artificially exhibited in non-piezoelectric material like graphene in the form of nanoribbon incorporated with the defected holes. Rodrigues et al. (2015) studied the electromechanical properties of a single-layer graphene transferred onto SiO_2 calibration grating substrates via piezoresponse force microscopy and confocal Raman spectroscopy. The calculated vertical piezocoefficient of graphene was found about 1.4 nmV^{-1}, that is, much higher than that of conventional piezoelectric materials such as lead zirconate titanate (PZT) and comparable to that of relaxor single crystals. The observed piezoresponse and achieved strain in graphene are associated with the chemical interaction of graphene's carbon atoms with the oxygen from underlying SiO_2.The results provide a basis for future applications of graphene layers for sensing, actuating and energy harvesting.

From the above literature, the researchers probably thought that graphene may be useful as nanoscale fillers for developing novel nanocomposites, and this conjecture motivated them to predict the properties of graphene and its composites. On the other hand, piezoelectric polymers are lightweight and environmentally friendly, but typically show weaker piezoelectric response. The conventional piezoelectric materials and piezoceramics are brittle, bulky and toxic (Bernholc et al. 2004; Berger et al., 2005). As compared to the existing piezoelectric materials, there is always a search for lightweight, high performance and environmentally benign new piezoelectric materials like graphene. Therefore, since the discovery of graphene, researchers are carrying out extensive research to determine the properties of graphene-reinforced composite for designing and developing its structures, as reviewed in the following Sections. Therefore, the existence of flexoelectricity in non-piezoelectric graphene layer could be used to develop graphene-based composite structures for next-generation NEMS applications. Hence, we discuss the graphene-reinforced composite and its various structural health monitoring (SHM) applications in Section 1.2.

1.2 Graphene-Based Composites

The review of literature presented in Section 1.1 confirms that graphene possesses exceptionally high electro-thermo-mechanical and scale-dependent physical properties. The increase in demand of light-weight and high-strength materials in transport and aerospace industries invites the researchers to use advanced technology for the development of new multifunctional materials and their structures with superior properties that are not met easily by conventional materials. Polymer nanocomposites are excellent structural materials that have desired and tailorable properties which can be used in a variety of applications. Recently, polymer matrix composite fascinated the attention of researchers because of its high mechanical properties and specific stiffness. Over the past two decades, to fulfill increasing demands of high stiffness and strength of materials, several researchers experimentally incorporated the graphene layers in conventional polymer matrices.

1.2.1 Properties of Graphene-Based Composites

Extensive research is dedicated to the introduction of graphene as modifier to the conventional bulk composites in order to improve their multifunctional properties. Several researchers utilized deriavtives of graphene in a very effective way in the form of graphene nanosheets (GNs), graphene nanoplatelets (GNPs), graphite oxide and graphene oxide (GO) or reduced graphene oxide (rGO) into the matrix. These derivatives of graphene, due to their cost-effective chemical reduction and oxidation techniques, show promising ways towards the bulk fabrication and use of graphene with excellent electro-thermo-mechanical and gas barrier properties for the commercial as well as NEMS (Zhu et al., 2014; Cui et al., 2016). The graphene-based polymer nanocomposite materials have fascinated much attention (Zhu et al., 2014; Shen et al., 2017). Also, they can be used as chemical sensors because of their extraordinary sensitivity. The graphene-reinforced composites are being fabricated using different methods such as flake powder metallurgy and semi-solid powder processing (Wang et al., 2012; Ji et al., 2016; Tian et al., 2016; Chen et al., 2018). They summarized and reviewed the numerous methods of synthesis of graphene-based nanocomposites and showed the significant enhancement in their mechanical properties with a mere use of 0.3 wt.% of graphene over that of pure matrix.

Recently, the metal/ceramic matrix composite fascinated the attention of researchers because of its high mechanical properties and specific stiffness. Therefore, the graphene was incorporated into the aluminum-based matrix in the literature. As a matter of fact, the piezo- and flexo-electric metal matrix composite must act as a capacitor for energy harvesting applications including the concept of dielectric medium. One of the challenges in using the aluminum as a matrix phase with graphene as a reinforcement in the two-phase composite is its conductive property, due to this, the electron charges generated from the flexo- and piezo-electricity may get compensated. Therefore, we must use the insulating matrix materials with a specific dielectric constant.

Hence, an aluminum oxide/alumina (Al_2O_3) can be used as matrix material because of its electrically insulating and dielectric properties. The aluminum forms a very thin layer of insulating alumina by anodization that acts as the dielectric of capacitor. Alumina is one of the most used ceramic material which can be served as a substrate for integrated circuits. Several investigators used alumina as a matrix material in the composite for various applications (Sun et al., 2005; Masson, 2009; Wang et al., 2011; Liu et al., 2012; Popat and Desai, 2013; Wozniak et al., 2015); therefore, in our study, alumina was also considered as a matrix material for GRNC.

Bhavanasi et al. (2016) reported the energy harvesting performance with the proficient transfer of electromechanical energy for the film made of bilayer GO and PVDF-TrFE. They observed that GO film improved the voltage output and power density of about 2 and 2.5 times, respectively, when compared to the PVDF-TrFE film without GO. Kandpal et al. (2017) experimentally investigated the enhancement of piezo-potential response such as output voltage of nanogenerator with the accumulation of GNPs into the polymer nanocomposite which can be used as an energy harvester. Dasari et al. (2018) experimentally examined the GO-reinforced aluminum composite using the liquid phase mixing and powder metallurgy techniques. Few studies elucidated the methods of production, applications, inventions and limitations of composites made of graphene and its derivatives (Mohan et al., 2018; Sreenivasulu et al., 2018). They focused on several components of fortifying, scattering strategies and blended composites utilizing graphene. Specifically, graphene-based polymer nanocomposite possesses good semiconducting properties (Yildirim and Ozturk, 2018), which makes it suitable to produce a strain sensor having a high gauge factor.

The quest for utilizing exceptional electro-thermo-mechanical properties of graphene led to the opening of an emerging area of research on the development of graphene-based structures such as beam, plate and shell because these structures are the important building blocks of MEMS/NEMS applications. The present dissertation is focused on these structures.

1.2.2 Graphene-Based Beams and Piezoelectric Nanowire

The composite structures are being widely used in the various MEMS/NEMS applications and composite beam is one of the most important structural elements. For instance, Rafiee et al. (2009) studied the buckling behavior of graphene-reinforced epoxy nanocomposite (GNC) beam and they found that the addition of 0.1 wt.% of graphene fillers into the epoxy results in ~52% enhancement of buckling property of GNC beam. Momeni et al. (2010) developed the multi-physics analytical model to determine the electric potential of zinc-oxide (ZnO) nanocomposite beams. They used the perturbation theory for decoupling constitutive equations. Feng et al. (2017) examined the nonlinear bending behavior of polymer nanocomposite beams reinforced with multi-layered GNPs that are non-uniformly dispersed in the thickness direction of the beam. They found that the bending performance of polymer matrix nanocomposite beam significantly improved by adding a small amount of GNPs. Many researchers studied the functionally graded (FG)-GNC laminated beams supported by elastic foundations to investigate their nonlinear bending and buckling, thermal postbuckling as well as dynamic instability under the consideration of thermal environment (Chen et al., 2017; Shen et al., 2017; Wu et al., 2017). They also found that the nonlinear behavior of composite beams enhanced significantly due to the addition of a small quantity of graphene and its derivatives. With the application of Ritz method and algebraic polynomials, thermal postbuckling analysis was performed to study the nonlinear thermal stability of GNC laminated beams under uniform temperature rise (Kiani and Mirzaei, 2018). Based on the first-order shear deformation theory, Zhang et al. (2018) analyzed the bending, buckling, and vibration behaviors of FG multi-layered GO-reinforced composite beams. They also obtained effective mechanical properties of GO-reinforced composite using the modified Halpin-Tsai approach. Recently, Wang et al. (2019) developed a two-dimensional elasticity model considering uniform dispersion of graphene in each layer of a laminated graphene composite beam to study its free vibration and bending behaviors.

Similar to piezoelectric nanobeam structures, the piezoelectric nanowire is considered as a first prototype of nanogenerator (Wang and Song, 2006), which fascinated the intense interest among the researchers for its potential applications. The most commonly used nanodevices based on piezoelectric cylindrical nanowires include piezoelectric field-effect transistors (FETs), piezoelectric resonators and nanopiezotronics. Particular nanostructures such as nanobeams and nanoplates have certain restricted applications due to their geometrical configurations, and the cylindrical nanowire is another key structural health monitoring (SHM) element to overcome the restrictions posed by nanobeams and nanoplates. The electric potential in the tensile and compressive sections of nanowire is antisymmetric along its cross-section, making it as a "parallel plate capacitor" for nanopiezotronics applications such as nanogenerator and piezoelectric FETs due to the potential drop across the nanowire which assists as the gate voltage (Wang and Song, 2006; Wang, 2007). For instance, Gao and Wang (2007) investigated the distribution of piezoelectric potential in cylindrical ZnO nanowire using the perturbation theory. They compared their analytical results with numerical FE simulations. Shao et al. (2010) proposed the simple continuum model for evaluating the distribution of electric potential generated in the cantilever nanorod bent by the uniform force applied at its tip. Momeni et al. (2010) developed the multi-physics analytical model to determine the electric potential of ZnO nanocomposite. From these studies it is found that the piezoelectric effect in nanostructures play a significant role on their working mechanisms, especially nanowire-based nanogenerators. The working mechanism of nanowire largely depends on its deformation which generates electric polarization across its surface.

1.2.3 Graphene-Based Plates

Piezoelectric nanoplates are another important type of structural elements used for NEMS. Several researchers used graphene in composite structures such as nanoplates and nanofilms, and studied their static and dynamic characteristics. For example, using the nonlocal theory for elastic plate, the vibration analysis of single atomic-layered graphene was investigated by Pradhan and Murmu (2009). Thin composite plates are another important type of structural elements that have potential applications in NEMS due to their linear behavior and high sensitivity. For instance, Panigrahi (2009) and Nimje and Panigrahi (2014) carried out the damage analysis and FE numerical simulation for stress and failure of functionally graded adhesively bonded laminated graphite-epoxy composite plates. The experimental study by Parashar and Mertiny (2012) reported that the buckling capacity of the plate increases when the graphene-reinforced composite is enriched with only low percentage of graphene. They reported 26% enhancement in the buckling capacity of graphene-based composite plate under the unidirectional compression with only 6% volume fraction of graphene. Using the FE method and multiscale approach, Chandra et al. (2012) highlighted the enhancement of natural frequencies and mode shapes of graphene/polymer composite plates (Fig. 1.4). They found that as the plate aspect ratio increases, the natural frequency of graphene/epoxy composite plates decreases.

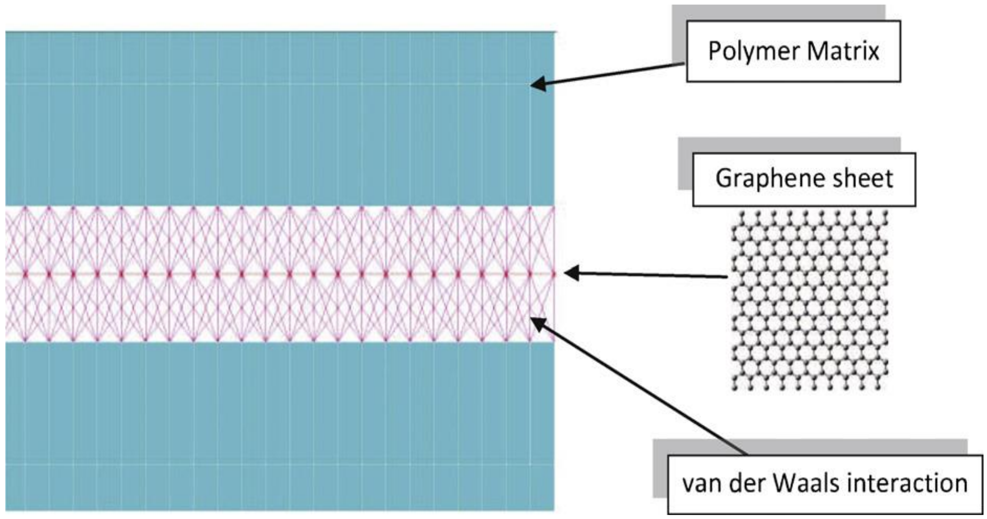

Figure 1.4: Multiscale model of GRP Composite. (Courtesy: Chandra et al. 2012)

The influence of surface effects on the nanoscale plate was investigated by Liu and Rajapakse (2013) and Sapsathiarn and Rajapakse (2017) to study its static and dynamic behavior. They also derived a solution for the nanoscale rectangular plates using the FE approach. Li and Narita (2014) proposed an active control method to reduce the wind-induced vibration of laminated composite plates using a velocity feedback control strategy. Saber et al. (2014) developed hybrid PZT based piezoelectric composite plates for sensory applications by incorporating the thin film of multi-walled carbon nanotubes (MWCNTs) and GNPs. The nanocomposite films showed significant improvement in the effective piezoelectric and stiffness properties of resulting nanocomposite by ~50% and 200%, respectively. They also reported that the use of GNPs in the composite is better than MWCNTs when the dynamic response and poling behavior are considered. Sadeghzadeh (2016) studied the multilayer graphene-reinforced plate using the multiscale approach. He reported that the spaced multilayer graphene sheets are more efficient than the stacked multilayer graphene sheets having interlayer distance 0.34 nm, that is, no metallic nanoparticles or fullerenes exist between two adjacent graphene layers. Song et al. (2017) studied the free and forced vibrations of multilayer GNP-reinforced composite plates subjected to the axial compression and transverse loadings. They revealed that the small amount of GNPs significantly increases the critical buckling load of composite plate and reduces its vibration.

Feng et al. (2017) found that the bending performance of polymer matrix nanocomposite significantly improved by adding small amount of GNPs. The micromechanical model and multiscale approach were developed by Shen et al. (2017) for analyzing the post-buckling behavior of FG graphene-based laminated composite plates under the uniaxial compression in thermal environments. Zhao et al. (2017) investigated the bending and vibration behavior of FG GNP-reinforced trapezoidal plates using the FE method. They also predicted the effective material properties such as Young's modulus, mass density and Poisson's ratio of GNP-nanocomposite using the modified Halpin-Tsai model and rules-of-mixture. Karimi et al. (2017) investigated the effect of different parameters such as nonlocal and surface layers on the in-phase and out-of-phase natural frequencies of double-layer piezoelectric nanoplate subjected to the thermo-electro-mechanical loadings. Garcia-Macias et al. (2018) found that the performance of GNP reinforcements in the composite plate is superior as compared to CNTs in terms of stiffening effect and load-bearing capacity.

1.2.4 Graphene-Based Shells

Composite beams and plates have certain restricted applications due to their geometrical configurations and design of zero curvature, and the cylindrical shell and nanowire are another key structural elements to overcome the restrictions posed by beams and plates. For instance, the influence of surface energy effect introduced by Sahmani et al. (2016) on the nonlinear- and post-buckling behavior of nanoscale piezoelectric shells under a longitudinal compression with electromechanical loadings. Wang and co-authors (2018a, 2018b) investigated the eigenvalue buckling and torsional analysis of FG graphene platelets (GPLs)-reinforced composite shells using the FE method. They also conducted the parametric analysis to study the effect of distributions, geometry and weight fraction of GPLs as well as presence of cut-out, number of layers and shell dimensions on the buckling behavior. Liu et al. (2018) examined the free vibration and buckling characteristics of non-uniformly distributed GPL-reinforced composite shell. They presented numerical results considering different dispersion patterns of GPLs. Recently, Habibi et al. (2019) studied the wave propagation behavior of size-dependent

GPL-reinforced composite shell which was coupled with the piezoelectric layer and they also explored the influence of piezoelectric layer thickness, GPL weight fraction and wave number on the phase velocity. Most recently, Karimiasl et al. (2020) examined the nonlinear vibration behavior of a multiscale doubly curved sandwich nanocomposite shell rested on the elastic foundation, exposed to the hygrothermal environment. By using the Halpin-Tsai model, they studied a three-phase composite with fiber-polymer-GPL and fiber-polymer-CNT. Liu et al. (2020) proposed the layout design of piezoelectric actuators for active control vibration of thin-walled smart structures. Findings from the literature indicate that the use of graphene and its derivatives, as reinforcements, significantly enhances the overall properties and response of resulting composites and its structures.

1.2.5 Challenges in Fabrication of Graphene-Based Composites

The review of literature presented in preceding Sections on graphene-reinforced composite and its structures confirms that one can use graphene as nanofiller and modifiers in conventional polymer matrices and composite structures. Note that there are still some challenges regarding the manufacturing of layered nanocomposites with a higher weight fractions of graphene with a specific thickness on the order of nanometer (nm). In the literature, nanofabrication techniques such as layer-by-layer (LbL) assembly and dispersion method, which mainly deal with the interaction between cation and anions of adjacent graphene layers, are commonly used to fabricate graphene-based thin films (Gamboa et al., 2010). Some researchers fabricated graphene-based nanocomposite samples with 1% to 90% volume fractions of graphene and its derivatives such as graphite oxide and graphene oxide using above mentioned nanofabrication methods (Gong et al., 2012; Young et al., 2012; Yang et al., 2013; Papageorgiou et al., 2017). Using these techniques, the fabrication of thin graphene-based nanocomposite films can be fabricated and the film thickness on the order of nm can be tailored by varying the number of graphene layers (Yang et al., 2013; Prolongo et al., 2014; Tzeng et al., 2015; Prolongo et al., 2018). Some challenges are associated with these techniques such as in every step of LbL technique, the layered graphene structure is required to be rinsed with deionized water followed by the drying for a specific time that may lead to error and non-uniform deposition. Mature fabrication techniques are evolving as the applications of 2-D graphene sheets become more defined, and thin structures made of their layers are being fabricated at relatively low-cost. Some experimental studies reported the axial and transverse properties of graphene-based nanocomposites (Zhao et al. 2010; Khan et al. 2012; Ji et al. 2016; García-Macías et al. 2018). They showed that the axial effective properties of graphene-based composite vary linearly with graphene volume fraction. They also showed that the axial properties follow the rules-of-mixture and iso-strain conditions perfectly.

The review of literature presented herein indicate that the graphene-based composites and their structures are vastly studied in the last decade. Nevertheless, to date, to the best of the current researchers' knowledge, no single study exists on studying the electromechanical behavior of graphene-based composite as well as its nanostructures considering the size-dependent flexoelectric, piezoelectric and surface effects, which can offer many opportunities for developing next-generation NEMS. Flexoelectric and piezoelectric concepts are discussed in next Section.

1.3 Size-dependent Properties

1.3.1 Flexoelectricity and Piezoelectricity

Over the last two decades, the flexoelectricity phenomenon has received much attention from both fundamental and application point of view with the aim of developing NEMS. Flexoelectricity is the response of electric polarization to an applied strain gradient and is developed as a consequence of crystal symmetry in all materials. Recent advances in nanoscale technologies have renewed the interest in flexoelectricity due to the obvious existence of large strain gradients at the nanoscale level that leads to strong electromechanical coupling. The symmetry breaking at surfaces and interfaces in nonpolar materials allows new forms of electromechanical coupling such as surface piezoelectricity and flexoelectricity, which cannot be induced in the bulk materials. For the first time, the flexoelectricity phenomenon was observed in the crystal plates by Mashkevich and Tolpygo (1957), while theoretical predictions for the flexoelectric coefficients were reported by Kogan (1964). He provided the approximate predictions by using the relation of electronic charge (e) in electron volt and lattice parameter (a), and the determined values of flexoelectric coefficients are reported in the range of $10^{-12} - 10^{-6}\mathrm{C/m}$.

Piezoelectricity was first discovered by French physicists, Jacques and Pierre Curie in 1880. Afterward, Gabriel Lippmann deduced mathematical relation for the inverse piezoelectric effect from the fundamental principles of thermodynamics in 1881, which was not predicted by Curie brothers. Piezoelectricity–electrical polarization induced by a uniform strain (or vice-versa)–is the most widely known and exploited forms of electromechanical coupling that exists in non-centrosymmetric crystals. In non-centrosymmetric crystals, the absence of center of inversion results in the presence of polarization. Specifically, in contrast to the piezoelectricity, the flexoelectricity phenomenon presents in nanomaterial having inversion symmetry, and even the centrosymmetric crystal can also be polarized by breaking its inversion symmetry and applying non-uniform strain gradient. Unlike, piezoelectricity phenomenon which can be found only in 20 non-centrosymmetric point groups, the flexoelectricity exists in all dielectric and insulating materials with 32 crystallographic point groups and the electromechanical coupling can be generated in non-piezoelectric materials (Maranganti et al., 2006; Sharma et al., 2007). For a better understanding of flexoelectricity, first the concept of piezoelectricity and its mathematical relation is described as follows:

$$P_i \sim d_{ijk}\varepsilon_{jk} \tag{1}$$

In the above relation, P_i denotes the polarization vector, ε_{jk} is the strain tensor and d_{ijk} is the piezoelectric tensor. Similar to the piezoelectricity, flexoelectricity also shows two discrete strain and electric field gradient-dependent electromechanical couplings such as direct as well as inverse flexoelectric effects. Flexoelectricity ia a size-dependent phenomenon. Thus, the flexoelectric effect is a preferred electromechanical coupling in MEMS/NEMS applications. The constitutive relation (1) for the total polarization vector accounting the flexoelectric effect may be re-written as:

$$P_i \sim d_{ijk}\varepsilon_{jk} + f_{ijkl}\frac{d\varepsilon_{jk}}{dx_l} \tag{2}$$

where f_{ijkl} is the flexoelectric tensor and $\frac{d\varepsilon_{jk}}{dx_l}$ is the higher order strain gradient tensor.

According to the variational principle for dielectrics, Maranganti et al. (2006) established a comprehensive framework considering the flexoelectric effect and provided solutions for the governing equations of an isotropic centrosymmetric material using

Green's function. Using combined atomistic and theoretical methods, Majdoub et al. (2008) studied the “effective” size-dependent electrocmechanical response of piezoelectric and non-piezoelectric nanoscale cantilever beams subjected to inhomogeneous strain. A few analytical studies also conducted to incorporate the effect of flexoelectricity which identified in some of the structural elements. Gharbi et al. (2011) observed an important role of flexoelectricity in the hardening of ferroelectrics at nano-indentation. Morozovska et al. (2011) reported that flexoelectricity plays an important role in the electromechanical response of moderate conductors. Based on the theory developed by Hadjesfandiari (2013), Li et al. (2014) studied the three-layer microbeam comprised of a flexoelectric dielectric layer using the size-dependent model. Wang and Wang (2016) developed a theoretical model for the micro/nanoscale beam considering the flexoelectric effect. Rupa and Ray (2017) obtained the exact solutions for the static response of simply-supported flexoelectric nanobeam. The beam was subjected to the applied mechanical load on its top surface while it was activated with the prescribed voltage at its top and bottom surfaces. Using density functional theory calculations, Kundalwal et al. (2017) reported the existence of polarization in non-piezoelectric graphene layer using flexoelectricity concept. Their study showed the electromechanical couplings in the graphene layer can be tailored by changing the size and shape of non-centrosymmetric pores and radius of curvature. It can be clearly observed that the flexoelectricity plays an important role on the performance of static and dynamic behavior of various structures.

1.3.2 Surface Effect

In recent years, apart from the flexoelectric effect, the surface effects have attracted great interest from fundamental as well as practical point of view. According to the linear theory of surface elasticity and its extended theories, a continuum model is presented by Gurtin and Murdoch (1975). Gurtin and Murdoch theory is based on the assumption of the deformable surface having zero or negligible thickness which is adhered to bulk material considering the perfect bond amongst the surface and bulk material. The surface effect can also be known as a size-dependent phenomenon. The surface effects are mainly responsible to generate the size-dependent electromechanical response from the bulk material because of its reduced geometrical dimensions to the nanoscale. As size of material decreases, its surface area and volume decrease as the square and cube of the length dimension, respectively. Therefore, a much more dramatic enhancement in the surface energy is expected as a result of decreasing the material size that can be obtained by tailoring the shapes of bulk/parent material. For instance, the surface energy effect on the static and dynamic response of elastic and piezoelectric nanomaterials were examined by various researchers (Miller and Shenoy, 2000; Huang and Yu, 2006; He and Lilley, 2008; Ru, 2009; Chen, 2011; Yan and Jiang, 2011), and they found that the surface effect influences the performance of energy harvester as its size gets reduced to the nanoscale. Therefore, surface effects can contribute extensively to the electromechanical response when the size of the structure scaled down. Specifically, the pioneering work on the surface effect on nanostructure investigated by Shen and Hu (2010) using the theory of dielectrics accounting the influence of the piezoelectric and flexoelectric effects with the consideration of surface parameters, which offers a mathematical framework to explore and compute the electromechanical response in nano-dielectrics. Liu and Rajapakse (2010, 2011, 2013) developed the continuum and finite element models to demonstrate the influence of surface effects accounting the parameters like residual surface stresses and lame constants on the static/dynamic behavior of nanobeams and nanoplates without considering the piezoelectric and flexoelectric effects. According to the state-space formulation, Chen (2011) studied the influence of surface effect on a thin piezoelectric body and demonstrated the relationship between the surface piezoelectric constant and the thickness of surface layer. Using size-dependent Euler-Bernoulli theory, Yan and Jiang (2011) determined the static response of piezoelectric cantilever nanobeam accounting the residual surface effects and neglecting the flexoelectric effect.

1.4 Scope and Objectives of the Dissertation

The review of literature reveals that the exceptionally attractive properties of graphene can be exploited to develop graphene-reinforced polymer matrix composite and its structures. The literature reviewed in Section 1.2 authenticates an overview of the research signifying that the graphene reinforcements in the polymer matrix provides feasible means to tailor the elastic, piezoelectric and dielectric properties of the resulting nanocomposites. Such a graphene-reinforced in the polymer matrix may be called as graphene-reinforced nanocomposite (GRNC).

The prediction of the effective properties of a novel GRNC is an important issue. In order to establish this novel GRNC as the multifunctional composite for structural applications, the effective elastic, piezoelectric and dielectric properties of this composite must be known a priori. No studies, however, have reported the effective properties of GRNC. Moreover, the electromechanical behavior of GRNC-based structures is not studied yet considering the flexoelectric effect. Such lack in studies provide an ample scope for further research on developing accurate models for studying the effective properties and electromechanical response of GRNC-based structures such as beams, plates, wires and shells. Hence, the present research is directed to determine the effective electromechanical properties such as elastic, piezoelectric and dielectric properties of GRNC, and to develop analytical and numerical models for investigating the electromechanical behaviour of GRNC beams, plates, wires and shells. Towards that direction, it is intended to accomplish the tasks of following objectives:

- Determine the elastic properties of defective graphene sheets using MD simulations.
- Develop analytical micromechanics models for predicting the effective elastic, piezoelectric and dielectric properties of GRNC. Develop numerical micromechanics models to validate the analytical predictions of effective properties of GRNC.
- Develop an analytical model using the Euler beam theory to investigate the static response of GRNC nanobeam subjected to mechanical and electrical loadings considering the flexoelectric effect.
- Develop an analytical model using the Euler-Bernoulli beam theory to investigate the static response of GRNC nanobeam subjected to electromechanical loading considering the flexoelectric/surface effect.
- Develop FE model based on the Galerkin's weighted residual method to validate the analytical predictions of electromechanical response of GRNC nanobeams.
- Investigate the effect of piezoelectricity and flexoelectricity on the static and dynamic behavior of GRNC nanoplates subjected to electromechanical loading using Kirchhoff's plate theory.

- Develop analytical and 3D FE models to investigate the effect of piezoelectricity and flexoelectricity on GRNC cylindrical nanowire subjected to electromechanical loading.
- Develop an analytical model for the elastic shell laminated with GRNC layer based on Kirchhoff–Love theory considering both piezoelectric and flexoelectric effects to investigate the electric potential distributions in it. Develop 3D FE models to validate the analytical results.

1.5 Organization of the Thesis

The remaining part of the Thesis is organized as follows:

- Chapter 2 deals with the development of analytical and numerical models for predicting the effective elastic, piezoelectric and dielectric properties of GRNC in conjunction with the molecular dynamics simulations for estimating the elastic properties of defective graphene sheets.
- Chapter 3 deals with the study of electromechanical behavior of GRNC nanobeams, accounting the piezoelectric and flexoelectric effects, by deriving the analytical and FE models.
- Chapter 4 deals with the study of electromechanical behavior of GRNC beams, accounting the flexoelectric and surface effects, by using size-dependent Euler-Bernoulli theory, linear piezoelectricity and Galerkin's weighted residual method.
- Chapter 5 deals with the study of electromechanical behavior of GRNC plates with flexoelectric effect by using Kirchhoff's plate theory, Navier's solution and extended linear piezoelectricity theory.
- Chapter 6 deals with the study of electromechanical behavior of GRNC nanowire with flexoelectric effect by deriving the analytical model based on the concept of strain gradient and FE model.
- Chapter 7 deals with the study of electromechanical behavior of elastic shell laminated with GRNC layer, accounting the piezoelectric and flexoelectric effects, by using Kirchhoff–Love theory and FE models.
- Chapter 8 summarizes the major conclusions drawn from the research work presented in the Thesis and the further scope of research. The references are alphabetically listed at the end of Thesis.

Chapter 2

Modeling of Graphene and GRNC

This Chapter presents some important preliminary concepts, emphasizing the Hill's average strain concentration tensors and their relationship to composite stiffness. Next, the atomistic modeling of defective graphene layers using molecular dynamics simulations is shown. Subsequently, the hierarchical steps involved in the analytical and finite element (FE) modeling of a novel graphene-reinforced nanocomposite (GRNC) are described. The micromechanical models based on the mechanics of materials (MOM), strength of materials (SOM) and FE models are developed to determine the effective elastic, piezoelectric and dielectric coefficients of GRNC. The obtained predictions of effective properties of GRNC are compared and validated.

2.1 Preliminaries

The Hooke's law for an elastic material can be written as follows

$$\{\sigma^r\} = [C^r]\{\varepsilon^r\}, \tag{2.1a}$$

where $\{\sigma^r\}$ and $\{\varepsilon^r\}$ denote the stress and strain vectors, respectively, and $[C^r]$ is the elastic stiffness matrix of the r^{th} phase of composite. The inverse relation of Eq. (2.1a) is given as:

$$\{\varepsilon^r\} = [S^r]\{\sigma^r\}, \tag{2.1b}$$

in which $[S^r]$ denote the compliance of the r^{th} phase of composite.

2.1.1 Average Stress and Strain

When a composite material is loaded, the point wise stress field $\{\sigma(x)\}$ and the respective strain field $\{\varepsilon(x)\}$ become non-uniform on the microscale. The solution of these non-uniform fields is a challenging problem. Though many useful results can be found in terms of the average stress and strain (Hill, 1963,1964) by assuming a large enough representative volume element (RVE) comprising several fibers, but small compared to any length scale over which the average loading or deformation of the composite varies.

The volume average stress $\{\overline{\sigma}\}$ and strain $\{\overline{\varepsilon}\}$ are defined as the averages of the point wise stress $\{\sigma(x)\}$ and strain $\{\varepsilon(x)\}$ over the volume Ω as follows:

$$\{\overline{\sigma}\} = \frac{1}{\Omega}\int_{\Omega}\{\sigma(x)\}\ d\Omega, \quad \text{and} \quad \{\overline{\varepsilon}\} = \frac{1}{\Omega}\int_{\Omega}\{\varepsilon(x)\}\ d\Omega. \tag{2.2}$$

It is also appropriate to define the volume average stresses and strains for the fiber and matrix phases. To find these, first we divide the volume Ω into the volume occupied by the fibers (Ω^f) and matrix (Ω^m), for the two-phase composite, as follows:

$$v_f + v_m = 1, \tag{2.3}$$

in which v_f and v_m are the volume fractions of fiber and matrix phases in the composite, respectively. The average fiber and matrix stresses are the averages over the respective volumes and can be written as:

$$\{\overline{\sigma}^f\} = \frac{1}{\Omega^f}\int_{\Omega_f}\{\sigma(x)\}\ d\Omega, \quad \text{and} \quad \{\overline{\sigma}^m\} = \frac{1}{\Omega^m}\int_{\Omega_m}\{\sigma(x)\}\ d\Omega\,. \tag{2.4}$$

Similarly, the average strains for the fiber and matrix can be obtained.

The relationships amongst the fiber and matrix averages, and the overall averages can be derived from the earlier definitions and these are as follows:

$$\{\overline{\sigma}\} = v_f\{\overline{\sigma}^f\} + v_m\{\overline{\sigma}^m\}, \tag{2.5a}$$

$$\{\overline{\varepsilon}\} = v_f\{\overline{\varepsilon}^f\} + v_m\{\overline{\varepsilon}^m\}. \tag{2.5b}$$

An important related outcome is the average strain theorem. Let the average volume (Ω) subjected to the surface displacements $\{u^0(x)\}$ consistent with the uniform strain $\{\varepsilon^0\}$. Then, the average strain within the region is

$$\{\overline{\varepsilon}\} = \{\varepsilon^0\}. \tag{2.6}$$

Hill (1963) proved this theorem by replacing the definition of the strain tensor $\{\varepsilon\}$ in terms of the displacement vector $\{u\}$ into the definition of average strain $\{\overline{\varepsilon}\}$, and applying Gauss's theorem, the result is:

$$\{\bar{\varepsilon}_{ij}\} = \frac{1}{\Omega}\int_S \left(\{u_i^0\}\{n_j\} + \{n_i\}\{u_j^0\}\right) dS. \tag{2.7}$$

where S denotes the surface of Ω and {n} is a unit vector normal to dS. The average strain within the volume Ω is totally determined by the displacements on the surface of volume, so the displacements consistent with the uniform strain must produce the identical value of the average strain. A corollary of such an assumption is that one can obtain a perturbation strain by taking difference between the local strain and the average strain as follows:

$$\{\varepsilon^{per}(x)\} = \{\varepsilon(x)\} - \{\bar{\varepsilon}\}, \tag{2.8a}$$

then the volume average of $\{\varepsilon^{per}\}(x)$ must equal to zero

$$\{\bar{\varepsilon}^{per}\} = \frac{1}{\Omega}\int_\Omega \{\varepsilon^{per}(x)\}\ d\Omega = 0. \tag{2.8b}$$

The corresponding theorem for the average stress also holds. Hence, if the surface tractions consistent with uniform stress $\{\sigma^0\}$ applied on surface (S) then the average stress can be expressed as:

$$\{\bar{\sigma}\} = \{\sigma^0\}. \tag{2.8c}$$

2.1.2 Average Properties and Strain Concentration

The aim of the micromechanics models is to determine the averaged effective properties of composite, although these require proper definitions. At this juncture, we use the direct method by Hashin (1983) in which the RVE is exposed to the constant surface displacements with the uniform strain $\{\varepsilon^0\}$. The average composite stiffness is the matrix [C] that measures such uniform strain to the average stress. From Eq. (2.6), we can obtain:

$$\{\bar{\sigma}\} = [C]\{\bar{\varepsilon}\}. \tag{2.9a}$$

The average compliance matrix [S] is defined in the same way by applying tractions consistent with the uniform stress $\{\sigma^0\}$ on the surface of the average volume. Then, using Eq. (2.8c), the result is:

$$\{\bar{\varepsilon}\} = [S]\{\bar{\sigma}\}. \tag{2.9b}$$

Hill (1963) presented an important concept related to the strain [M] and stress [N] fourth-order concentration tensors. Basically, these are the ratios of average fiber stress (or strain) and the respective average strain (or stress) in the composite and can be expressed as:

$$\{\bar{\varepsilon}^f\} = [M]\{\bar{\varepsilon}\} \quad \text{and} \tag{2.10a}$$

$$\{\bar{\sigma}^f\} = [N]\{\bar{\sigma}\}, \tag{2.10b}$$

where $[M]$ and $[N]$ are the fourth order tensors and, in general, they must be found from a solution of the microscopic strain and stress fields, respectively. Different micromechanics models provide different ways to approximate $[M]$ and $[N]$. Note that both $[M]$ and $[N]$ have the minor symmetries of the stiffness or compliance matrix, but lack the major symmetry. That is,

$$M_{ijkl} = M_{jikl} = M_{ijlk}, \tag{2.11a}$$

but in general,

$$M_{ijkl} \neq M_{klij}. \tag{2.11b}$$

For later use it will be convenient to have an alternate strain concentration tensor $[\widehat{M}]$ that relates the average fiber strain to the average matrix strain, as follows:

$$\{\bar{\varepsilon}^f\} = [\widehat{M}]\{\varepsilon^m\}. \tag{2.11c}$$

This is related to $[M]$ by

$$[M] = [\widehat{M}]\left[(1 - v_f)[I] + v_f[\widehat{M}]\right]^{-1}, \tag{2.11d}$$

in which $[I]$ represents the fourth order unit tensor. Using equations now in hand, one can express the average composite stiffness in terms of the strain concentration tensor $[M]$, and the fiber and matrix elastic properties (Hill, 1963).

In general, these stress and strain concentration tensors must be found from a solution of the microscopic stress or strain fields. Equating Eqs. (2.1), (2.5a), (2.5b), (2.9a) and (2.10a), we can obtain:

$$[C] = [C^m] + v_f\left([C^f] - [C^m]\right)[M]. \tag{2.12a}$$

The equation for the compliance is

$$[S] = [S^m] + v_f\left([S^f] - [S^m]\right)[N]. \tag{2.12b}$$

Note that Eqs. (2.12a and 2.12b) are not independent, $[S] = [C]^{-1}$. Hence, the strain concentration tensor $[M]$ and the stress concentration tensor $[N]$ are not independent either. The choice of which one to use in any instance is a matter of convenience.

To find the use of stress and strain concentration tensors, we noticed that the Voigt average corresponds to the assumption that both the fiber and matrix experience equal uniform strain i.e., iso-strain conditions. Then $\{\bar{\varepsilon}\} = \{\bar{\varepsilon}^{f}\}$ and $[M] = [I]$, and from Eq. (2.12a), the stiffness of the composite can be written as:

$$[C^{Voigt}] = v_f[C^f] + v_m[C^m]. \tag{2.12c}$$

Recall that the Voigt average corresponds to the upper bound on the stiffness of composite. The Reuss average considers that both the fiber and matrix experience equal uniform stress i.e., iso-stress conditions. This implies that $[N] = [I]$, and from Eq. (2.12b), the compliance of the composite can be written as:

$$[S^{Reuss}] = v_f[S^f] + v_m[S^m]. \tag{2.12d}$$

2.2 Elastic Properties of Graphene Sheets

The introduction and literature review Chapter reveals that a thorough understanding of mechanics of graphene is needed to exploit its full potential. The piezoelectric properties of graphene sheets containing non-centrosymmetric pores are already reported in the literature, but their elastic properties are not available. Before proceeding for the prediction of effective properties of GRNC, the elastic properties of graphene sheets containing non-centrosymmetric pores need to be determined priori. The capability of continuum models to capture atomistic data at nanoscale-level of graphene is questionable. This encourages the use of molecular dynamics (MD) simulations to determine the elastic properties of graphene sheets.

MD is the most commonly used modeling technique for the simulation of nanostructured materials because it allows accurate predictions of interactions between atoms and molecules at the atomic scale level. In the 1950s, the method was firstly introduced by theoretical physicists. MD simulation is mainly used into two steps. The first step includes the determination of the interacting forces between a system of atoms through molecular mechanics potential fields, and the second step consists of tracing movements of atoms using Newton's equations of motion. Molecules are described by a “ball and spring” model in force field methods, with atoms having different sizes and “softness” and bonds having different lengths and “stiffness”. Force field methods are also referred to as *molecular mechanics* (MM) methods. The *classical mechanics* (CM) deals with motion of bodies (including the special case in which bodies remain at rest) in accordance with Newtonian mechanics (Jensen, 2017). The term *classical mechanics* was coined to loosely label the set of equations that describe reality at scales where quantum and relativistic effects are negligible. The obvious advantage of MD over classical models is that it provides a route to dynamical properties of the system: transport coefficients, time-dependent responses to perturbations, rheological properties and vibrational infrared (IR) spectra, thermo-mechanical properties, and many more exceptional characteristics. Therefore, MD simulations were carried out herein to determine the elastic properties of pristine and defective graphene sheets.

The MD simulations were carried out to determine the elastic properties of (i) pristine graphene sheet and (ii) defective graphene sheets containing 4.5% and 20% vacancies in form of non-centrosymmetric pores. Schematics of such graphene layers are shown in Fig. 2.1. All MD simulations were conducted with large-scale atomic/molecular massively parallel simulator (LAMMPS) (Plimpton 1995), and the molecular interactions in graphene were described in terms of Adaptive Intermolecular Reactive Empirical Bond Order (AIREBO) force fields (Stuart et al., 2000). During the uniaxial deformation of the graphene, the stresses were determined on the atomistic scale using virial stress tensor defined by Eq. (2.14) (Allen and Tildesley, 1987); as follows:

$$\overline{\sigma} = \frac{1}{\Omega}\sum_{i=1}^{N}\left(\frac{m_i}{2}{v_i}^2 + F_i r_i\right), \qquad (2.13)$$

in which Ω is the volume of atoms; v_i, m_i, r_i, and F_i denote the velocity, mass, position and force of the ith atom, respectively. Then, the stress-strain curves during the tensile loading were obtained, and Young's modulus (E) and Poisson's ratio (μ) of pristine and defective graphene sheets were determined. The determination of values of E and μ was accomplished by using the simple strain energy density elastic constant relations. The equivalent continuum graphene sheet was assumed to be a flat plate considering its wall thickness of 3.4 A˚ (Kundalwal and Meguid 2017). A direct transformation to continuum properties was then made by assuming that the potential energy density of discrete atomic interactions of neighbouring atoms is equal to the strain energy density of the continuous substance occupying a graphene volume. The atomic volume was determined from the relaxed graphene sheet with the thickness (t) of 3.4 Å (Huang et al., 2006; Pei et al., 2010).

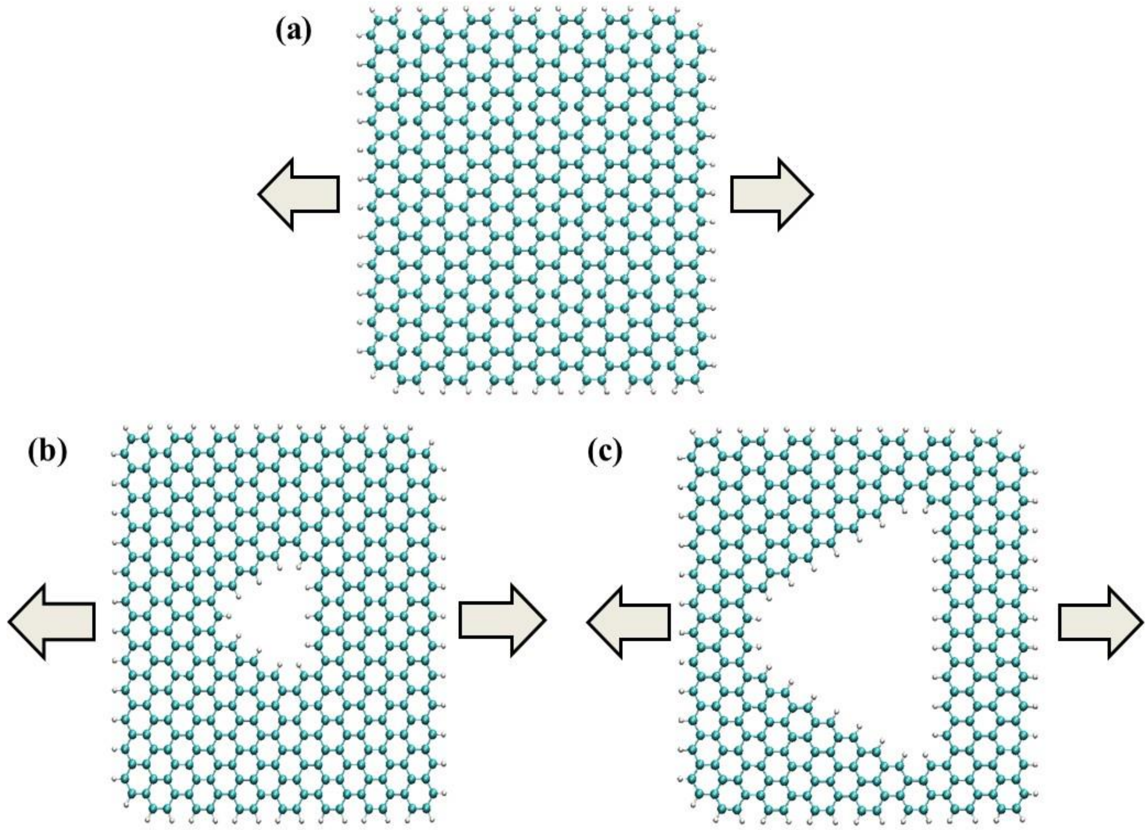

Figure 2.1: Armchair graphene sheets subjected to axial stress: (a) Pristine; and with trapezoidal pores: (b) 4.5% and (c) 20% vacancies.

2.3 Effective Properties of GRNC

It was identified in the previous Chapter that the development of GRNC by reinforcing the 2D graphene sheets into the polymer matrix may be the most plausible way to harness structural benefits from their exceptionally high electro-thermo-mechanical properties. Subsequently, it was objectified to determine the effective elastic, piezoelectric as well as dielectric properties of GRNC so that this composite can be assessed as a superior material for structural and NEMS applications. As a first endeavor, analytical and finite element (FE) models were derived in this Chapter for predicting the effective properties of a novel GRNC. The effective properties of GRNC were determined by varying the volume fraction of graphene. Several studies used the different homogenization techniques and micromechanical models like shear-lag, Halpin-Tsai, couple-stress, self-consistent, Mori–Tanaka, Hashin–Shtrikman, composite cylinder/sphere assemblage (CCA and CSA), rules-of-mixture (ROM) and multi-level model for studying the mechanical behavior of composites (Bouyge et al., 2001, 2002; Yang and Meguid, 2013; Chen et al., 2014; Chatzigeorgiou et al., 2019) and the predictions were validated with the experimental estimates (Gong et al., 2012; Young et al., 2012; Papageorgiou et al., 2017). Therefore, we used mROM model to determine the effective elastic properties of GRNC considering the geometrical factors of embedded graphene such as orientation, length and agglomeration. These factors are important as it is very difficult to obtain uniform dispersion and alignment of nanofillers in the matrix during the fabrication of nanocomposites. Krenchel orientation factor (η_0), critical length efficiency factor (η_1) and agglomeration factor (η_a) were taken into consideration as follows (Papageorgiou et al., 2020):

$$\mathrm{E_c = \eta_0 \eta_1 E_f\, \eta_a v_f + E_m v_m}, \tag{2.14}$$

where $\mathrm{E_m}$ and $\mathrm{E_m}$ denote the elastic modulus of graphene and matrix. The values of η_0, η_1 and η_a factors become unity in case of aligned and non-agglomerated graphene layers perfectly bonded with the surrounding matrix (Papageorgiou et al., 2020).

2.3.1 Mechanics of Materials (MOM) Approach

This sub-section presents the derivation of analytical micromechanics model using the MOM approach for determining the effective elastic, piezoelectric and dielectric properties of GRNC comprised of graphene layers and polymer matrix. Assuming a graphene sheet as a piezoelectric continuum and the polyimide/alumina as the matrix, the elastic, piezoelectric as well as dielectric properties of GRNC were determined. Several researchers developed analytical and numerical models of graphene considering it as a continuum medium using the theory continuum elasticity (Gupta and Batra, 2010; Gradinar et al., 2013; Verma et al., 2014; Bahamon et al., 2015; Cui et al., 2016). This suggests that the displacement of each carbon atom in homogeneously deformed graphene layer is given by the deformation of the continuum medium on which the atom is embedded.

A novel GRNC is reinforced with the multilayers of piezoelectric graphene sheets and polyimide/alumina matrix. Such GRNC can be considered as composed of rectangular RVEs comprising graphene and polyimide/alumina matrix, as shown in Fig. 2.2, and we limited the development of our micromechanical model to a single RVE. We assumed that (i) reinforcements are continuous, parallel and aligned, (ii) no slippage occurs between a graphene reinforcement and the surrounding matrix, (iii) matrix is free from voids, and (vi) the resulting nanocomposite is linearly elastic and homogeneous (Gao and Li, 2005; Song and Youn, 2006; Jiang et al., 2009; Kundalwal and Ray, 2011, 2013). It is considered that the upper and lower surfaces of reinforcements and GRNC lamina are electroded and the electric field is applied along its thickness. It is also assumed that electrodes do not contribute or influence on the stiffness of homogenized GRNC. The conducting electrodes maintain constant electrostatic potentials on both the upper and lower surfaces of GRNC lamina. Hence, the electric polarization exists in the piezoelectric medium when it is kept in a parallel plate capacitor with an electric potential applied across the lamina even if these parallel plates are not in contact with the lamina. Such GRNC lamina demonstrates the inverse piezoelectric effect and may be considered as a capacitor having two parallel plates in which the graphene reinforcements and matrix act as the dielectric medium.

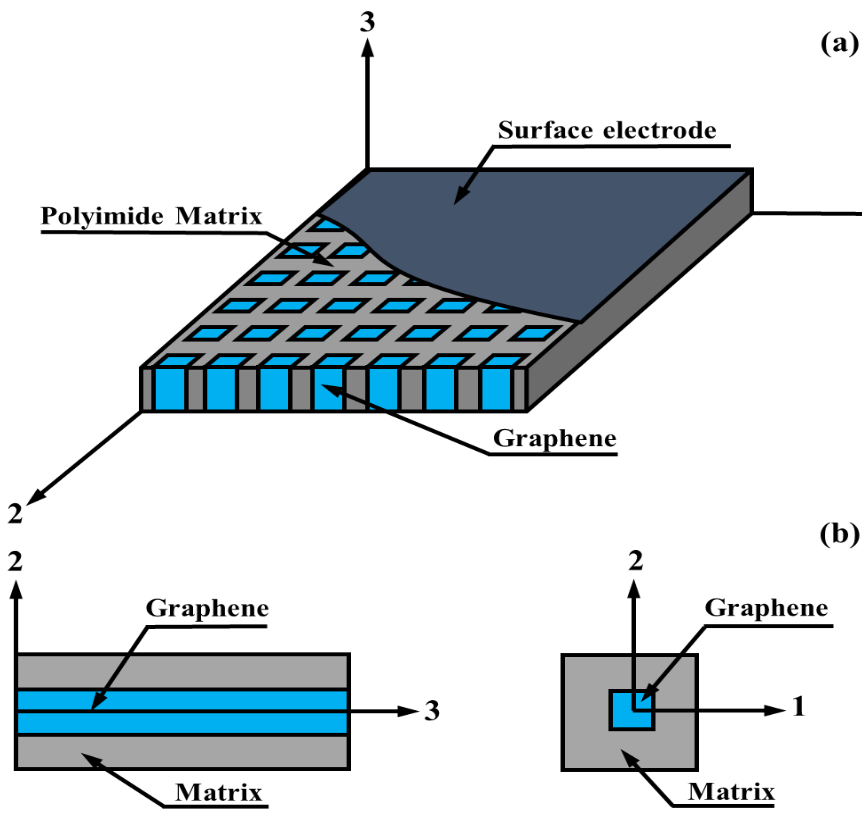

Figure 2.2: (a) Schematic representation of a GRNC lamina and (b) cross-sections of an RVE of GRNC.

The effective properties of GRNC were obtained by modifying the existing MOM model (Kundalwal and Ray, 2011). Figure 2.2(b) demonstrates an RVE of GRNC lamina in which the graphene layers are incorporated along its thickness direction. Smith and Auld (1991) used the strength of materials (SOM) approach to predict the effective elastic and piezoelectric properties of 1–3 piezoelectric composite in which PZT fibers of square cross-section were surrounded by the epoxy matrix. Note that the effective elastic and piezoelectric properties predicted by Smith and Auld (1991) are most feasible for controlling the thickness mode oscillations of thin composite plates. Our micromechanical analysis is confined to the RVE of GRNC (see Fig. 2.2) for determining the effective properties of bulk GRNC.

Note that the thickness of GRNC lamina is assumed to be very small and normal stresses can be induced in it due to the applied electric field (E_3) along the 3–axis of GRNC. The constitutive equations for the constituents of GRNC can be written as follows:

$$\{\sigma^g\} = [C^g]\{\varepsilon^g\} - \{e^g\}E_3, \text{and} \quad \{\sigma^m\} = [C^m]\{\varepsilon^m\}, \tag{2.15a}$$

$$\{\sigma^r\} = \begin{Bmatrix} \sigma_1^r \\ \sigma_2^r \\ \sigma_3^r \\ \sigma_{23}^r \\ \sigma_{13}^r \\ \sigma_{12}^r \end{Bmatrix}, \quad \{\varepsilon^r\} = \begin{Bmatrix} \varepsilon_1^r \\ \varepsilon_2^r \\ \varepsilon_3^r \\ \varepsilon_{23}^r \\ \varepsilon_{13}^r \\ \varepsilon_{12}^r \end{Bmatrix}, \tag{2.15b}$$

$$[C^r] = \begin{bmatrix} C_{11}^r & C_{12}^r & C_{13}^r & 0 & 0 & 0 \\ C_{12}^r & C_{22}^r & C_{23}^r & 0 & 0 & 0 \\ C_{13}^r & C_{23}^r & C_{33}^r & 0 & 0 & 0 \\ 0 & 0 & 0 & C_{44}^r & 0 & 0 \\ 0 & 0 & 0 & 0 & C_{55}^r & 0 \\ 0 & 0 & 0 & 0 & 0 & C_{66}^r \end{bmatrix}, \quad \{e^g\} = \begin{Bmatrix} e_{31}^g \\ e_{32}^g \\ e_{33}^g \\ 0 \\ 0 \\ 0 \end{Bmatrix}, r = \text{g and m}$$

In above equations, the respective g and m superscripts represent the graphene and polyimide/alumina matrix. The superscript r is used to indicate the corresponding constituent phase; σ_1^r, σ_2^r, and σ_3^r are the normal stresses in the directions 1, 2, and 3, respectively; ε_1^r, ε_2^r, and ε_3^r are the respective normal strains; σ_{12}^r, σ_{13}^r, and σ_{23}^r are the shear stresses; ε_{12}^r, ε_{13}^r, and ε_{23}^r are the shear strains; C_{ij}^r ($i, j = 1, 2$ and 6) are the elastic coefficients of rth phase; and e_{31}^g, e_{32}^g, and e_{33}^g are the piezoelectric coefficients of a graphene.

We assumed that the GRNC lamina is homogeneous in which graphene and matrix are linearly elastic (Gao and Li, 2005; Song and Youn, 2006; Jiang *et al.*, 2009; Kundalwal and Ray, 2011, 2013). The ROM and iso-field (iso-stress and iso-strain) conditions can be used to model the condition of perfect bonding between a reinforcement and the surrounding matrix (Smith and Auld, 1991; Benveniste and Dvorak, 1992; Ray, 2006;

Esteva and Spanos, 2009; Kundalwal and Ray, 2011). The iso-strain condition permits us to consider the normal strains in homogenized composite and its constituents are the same along the reinforcement direction while the iso-stress condition indicates that the transverse stresses in the respective constituents are same along the transverse direction of the reinforcement. The ROM permits us to define the normal stress and transverse as well as shear strains of the phases with respect to their volume fractions.

Using iso-strain and -stress conditions (Smith and Auld, 1991; Benveniste and Dvorak, 1992; Ray, 2006), the perfect bonding amongst a graphene layer and the matrix can be modeled by satisfying the following:

$$\begin{Bmatrix} \sigma_1^g \\ \sigma_2^g \\ \varepsilon_3^g \\ \sigma_{23}^g \\ \sigma_{13}^g \\ \sigma_{12}^g \end{Bmatrix} = \begin{Bmatrix} \sigma_1^m \\ \sigma_2^m \\ \varepsilon_3^m \\ \sigma_{23}^m \\ \sigma_{13}^m \\ \sigma_{12}^m \end{Bmatrix} = \begin{Bmatrix} \sigma_1^{NC} \\ \sigma_2^{NC} \\ \varepsilon_3^{NC} \\ \sigma_{23}^{NC} \\ \sigma_{13}^{NC} \\ \sigma_{12}^{NC} \end{Bmatrix}, \tag{2.16}$$

Therefore, the ROM was used to determine the effective elastic properties of GRNC assuming graphene reinforcement as continuum layers embedded into the matrix. Hence, using the ROM, we can write:

$$v_g \begin{Bmatrix} \varepsilon_1^g \\ \varepsilon_2^g \\ \sigma_3^g \\ \varepsilon_{23}^g \\ \varepsilon_{13}^g \\ \varepsilon_{12}^g \end{Bmatrix} + v_m \begin{Bmatrix} \varepsilon_1^m \\ \varepsilon_2^m \\ \sigma_3^m \\ \varepsilon_{23}^m \\ \varepsilon_{13}^m \\ \varepsilon_{12}^m \end{Bmatrix} = \begin{Bmatrix} \varepsilon_1^{NC} \\ \varepsilon_2^{NC} \\ \sigma_3^{NC} \\ \varepsilon_{23}^{NC} \\ \varepsilon_{13}^{NC} \\ \varepsilon_{12}^{NC} \end{Bmatrix}, \tag{2.17}$$

in which the superscript NC denotes the quantities of RVE of GRNC, and v_g and v_m are the volume fractions of a graphene layer and matrix, respectively. Using Eqs. (2.15–2.17), the stress and strain vectors of homogenized GRNC can be written in terms of the respective stress and strain vectors of constituent phases as follows:

$$\{\sigma^{NC}\} = [C_1]\{\varepsilon^g\} + [C_2]\{\varepsilon^m\} - \{e_1\}E_3,$$
$$[C_3]\{\varepsilon^g\} - [C_4]\{\varepsilon^m\} = \{e_2\}E_3 \quad \text{and} \tag{2.18}$$
$$\{\varepsilon^{NC}\} = [V_1]\{\varepsilon^g\} + [V_2]\{\varepsilon^m\}.$$

The matrices appeared in Eqs. (2.18) are given as follows:

$$[C_1]=\begin{bmatrix} C_{11}^{g} & C_{12}^{g} & C_{13}^{g} & 0 & 0 & 0 \\ C_{12}^{g} & C_{22}^{g} & C_{23}^{g} & 0 & 0 & 0 \\ v_g C_{13}^{g} & v_g C_{23}^{g} & v_g C_{33}^{g} & 0 & 0 & 0 \\ 0 & 0 & 0 & C_{44}^{p} & 0 & 0 \\ 0 & 0 & 0 & 0 & C_{55}^{p} & 0 \\ 0 & 0 & 0 & 0 & 0 & C_{66}^{p} \end{bmatrix},$$

$$[C_2]=\begin{bmatrix} 0 & 0 & 0 & 0 & 0 & 0 \\ 0 & 0 & 0 & 0 & 0 & 0 \\ v_m C_{13}^{m} & v_m C_{23}^{m} & v_m C_{33}^{m} & 0 & 0 & 0 \\ 0 & 0 & 0 & 0 & 0 & 0 \\ 0 & 0 & 0 & 0 & 0 & 0 \\ 0 & 0 & 0 & 0 & 0 & 0 \end{bmatrix}, \{e_1\}=\begin{Bmatrix} e_{31}^{g} \\ e_{32}^{g} \\ v_g e_{33}^{g} \\ 0 \\ 0 \\ 0 \end{Bmatrix}, \{e_2\}=\begin{Bmatrix} -e_{31}^{g} \\ -e_{32}^{g} \\ 0 \\ 0 \\ 0 \\ 0 \end{Bmatrix},$$

$$[C_3]=\begin{bmatrix} C_{11}^{g} & C_{12}^{g} & C_{13}^{g} & 0 & 0 & 0 \\ C_{12}^{g} & C_{22}^{g} & C_{23}^{g} & 0 & 0 & 0 \\ 0 & 0 & 1 & 0 & 0 & 0 \\ 0 & 0 & 0 & C_{44}^{g} & 0 & 0 \\ 0 & 0 & 0 & 0 & C_{55}^{g} & 0 \\ 0 & 0 & 0 & 0 & 0 & C_{66}^{g} \end{bmatrix}, [C_4]=\begin{bmatrix} C_{11}^{m} & C_{12}^{m} & C_{13}^{m} & 0 & 0 & 0 \\ C_{12}^{m} & C_{22}^{m} & C_{23}^{m} & 0 & 0 & 0 \\ 0 & 0 & 1 & 0 & 0 & 0 \\ 0 & 0 & 0 & C_{44}^{m} & 0 & 0 \\ 0 & 0 & 0 & 0 & C_{55}^{m} & 0 \\ 0 & 0 & 0 & 0 & 0 & C_{66}^{m} \end{bmatrix},$$

$$[V_1]=\begin{bmatrix} v_g & 0 & 0 & 0 & 0 & 0 \\ 0 & v_g & 0 & 0 & 0 & 0 \\ 0 & 0 & 1 & 0 & 0 & 0 \\ 0 & 0 & 0 & v_g & 0 & 0 \\ 0 & 0 & 0 & 0 & v_g & 0 \\ 0 & 0 & 0 & 0 & 0 & v_g \end{bmatrix}, \text{and } [V_2]=\begin{bmatrix} v_m & 0 & 0 & 0 & 0 & 0 \\ 0 & v_m & 0 & 0 & 0 & 0 \\ 0 & 0 & 0 & 0 & 0 & 0 \\ 0 & 0 & 0 & v_m & 0 & 0 \\ 0 & 0 & 0 & 0 & v_m & 0 \\ 0 & 0 & 0 & 0 & 0 & v_m \end{bmatrix}.$$

Making the use of Eq. (2.16) into Eq. (2.18), a constitutive relation for the GRNC can be written as:

$$\{\sigma^{NC}\}=[C^{NC}]\{\varepsilon^{NC}\}-\{e^{NC}\}E_3, \tag{2.19}$$

in which $[C^{NC}]$ and $\{e^{NC}\}$ are the matrices for the effective elastic and piezoelectric properties of GRNC, respectively, and can be obtained as follows:

$$[C^{NC}]=[C_1][V_3]^{-1}+[C_2][V_4]^{-1},$$

$$[V_3]=[V_1]+[V_2][C_4]^{-1}[C_3],$$

$$[V_4]=[V_2]+[V_1][C_3]^{-1}[C_4] \text{ and}$$

$$\{e^{NC}\} = \{e_1\} + [C_1][V_3]^{-1}[V_2][C_4]^{-1}\{e_2\} - [C_2][V_4]^{-1}[V_1][C_3]^{-1}\{e_2\}. \tag{2.20}$$

From Eq. (2.20), the effective piezoelectric coefficients of GRNC can be identified as $e_{31} = e^{NC}(1)$, $e_{32} = e^{NC}(2)$, and $e_{33} = e^{NC}(3)$.

Here, the effective piezoelectric constant e_{31} of the GRNC defines the normal stress induced in transverse 1–direction due to the application of a unit electric field in longitudinal 3–direction (Smith and Auld, 1991; Kumar and Chakraborty, 2009). Similarly, the effective piezoelectric constants e_{32} and e_{33} define the normal stresses induced in the respective 2– and 3–directions. While the piezoelectric constant e_{15} quantifies the induced shear stress about 2–direction per unit electric field applied in the 1–direction. It may be noted that the MOM model cannot provide the solution to determine the effective piezoelectric constant (e_{15}). Therefore, the closed form expressions of effective piezoelectric constants of GRNC from Ref. (Kumar and Chakraborty, 2009) are given below:

$$e_{15} = e_{15}^{g}\left(1 - \frac{v_m C_{55}^{g}}{v_g C_{55}^{m} + v_m C_{55}^{g}}\right), \tag{2.21a}$$

$$e_{24} = e_{24}^{g}\left(1 - \frac{v_m C_{44}^{g}}{v_g C_{44}^{m} + v_m C_{44}^{g}}\right). \tag{2.21b}$$

Note that the GRNC is the transversely isotropic material with the 3–axis as the axis of symmetry; therefore, $e_{31} = e_{33}$ and $e_{24} = e_{15}$. Hence, only the three independent piezoelectric constants (e_{31}, e_{33} and e_{15}) are required to study the piezoelectric behavior of GRNC.

Consequently, the effective dielectric constant ($\in_{33}^{NC}$) of GRNC is derived by using the following relation (Ray and Pradhan, 2006):

$$\in_{33}^{NC} = v_g \in_{33}^{g} + v_m \in_{33}^{m} + e_{31}^{g} v_g v_m / (v_m C_{11}^{g} + v_g C_{11}^{m}). \tag{2.22}$$

2.3.2 Strength of Materials (SOM) Model

In this sub-section, the SOM model was modified and developed using the MOM and Hill's average concentration factor for point-wise analysis of GRNC for determining its effective properties. Figure 2.3 demonstrates a constructional representation of an RVE picked from the continuum of GRNC in which the graphene reinforcement is in the 1–3 plane. The problem coordinates and principal material coordinate systems are represented by 1-2-3 and x-y-z, respectively, and Fig. 2.3(b) demonstrates the RVE of GRNC. We have not performed any transformation, therefore, the principal material coordinates of Fig. 2.3(b) are exactly matching with the problem coordinate system of Fig. 2.3(a).

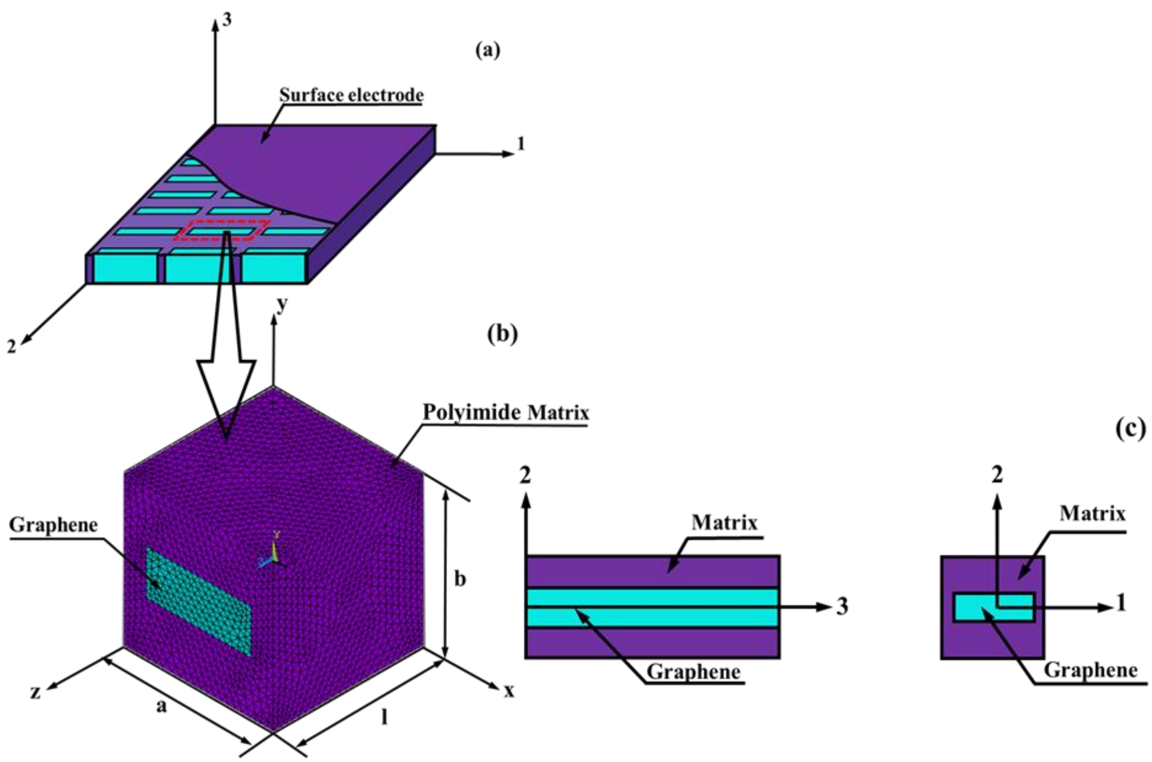

Figure 2.3: (a) Schematic of a GRNC lamina, (b) FE mesh of RVE of GRNC, and (c) longitudinal and transverse cross-sections of RVE of GRNC.

Considering the graphene as a continuum plate, the SOM model developed by Kundalwal and Ray (2011) was modified by incorporating Hill's average concentration factor for point-wise analysis of the local structure of GRNC to determine its effective elastic, piezoelectric and dielectric properties. The constitutive relations for the different phases of a GRNC with respect to the principal coordinate system (1–2–3) of material can be written as follows:

$$\{\sigma^r\} = [C^r]\{\varepsilon^r\}, \qquad r = g,\ m,\ \text{and NC} \tag{2.23}$$

Note that the thickness of GRNC lamina is assumed to be very small, and hence the constant electric field E_3 acts across its thickness. Thus, the constitutive equations for the electric displacement components of the graphene can be obtained as:

$$D_3^g = \{e^g\}'\{\varepsilon^g\} + \{\in_{33}^g\}E_3^g, \tag{2.24}$$

$$D_3^m = \{\in_{33}^m\}E_3^m\,. \tag{2.25}$$

D_3^g and D_3^m are the electric displacements of the corresponding phases; and E_3^g and E_3^m are the electric fields of the corresponding phases.

Note that the GRNC is considered as a transversely isotropic material with 3–axis as the symmetry axis, and accordingly, the above relations are written. Making use of Eqs. (2.15–2.16 and 2.22–2.23) and the stress as well as strain vectors of constituent phases, the stress and strain vectors of GRNC can be expressed as:

$$\{\sigma^{NC}\} = [C_1]\{\varepsilon^g\} + [C_2]\{\varepsilon^m\} - \{e_1\}E_3, \tag{2.26}$$

in which

$$\{\sigma^{NC}\} = \begin{Bmatrix} \sigma_1^{NC} \\ \sigma_2^{NC} \\ \sigma_3^{NC} \\ \sigma_{23}^{NC} \\ \sigma_{13}^{NC} \\ \sigma_{12}^{NC} \end{Bmatrix}, [C_1] = \begin{bmatrix} C_{11}^g & C_{12}^g & C_{13}^g & 0 & 0 & 0 \\ C_{12}^g & C_{22}^g & C_{23}^g & 0 & 0 & 0 \\ v_g C_{13}^g & v_g C_{23}^g & v_g C_{33}^g & 0 & 0 & 0 \\ 0 & 0 & 0 & C_{44}^g & 0 & 0 \\ 0 & 0 & 0 & 0 & C_{55}^g & 0 \\ 0 & 0 & 0 & 0 & 0 & C_{66}^g \end{bmatrix},$$

$$[C_2] = v_m \begin{bmatrix} 0 & 0 & 0 & 0 & 0 & 0 \\ 0 & 0 & 0 & 0 & 0 & 0 \\ C_{13}^m & C_{23}^m & C_{33}^m & 0 & 0 & 0 \\ 0 & 0 & 0 & 0 & 0 & 0 \\ 0 & 0 & 0 & 0 & 0 & 0 \\ 0 & 0 & 0 & 0 & 0 & 0 \end{bmatrix} \text{and } \{e_1\} = \begin{Bmatrix} e_{31}^g \\ e_{32}^g \\ v_g e_{33}^g \\ 0 \\ 0 \\ 0 \end{Bmatrix}. \tag{2.27}$$

Our aim is to establish the relationship between the average electric field in the homogenized GRNC and that in the individual phases. As stated earlier, the reinforcements are considered as coated with electrodes and thus the reinforcement–matrix interface act as a very thin metal conductor. Despite of fact, the electric field within the metallic conductor is zero and thus, the metallic conductor placed between two dielectrics separates the charges generated in it. As discussed, while developing MOM model, it can be possible to develop the constant electric field in both the graphene and matrix phases for proper distribution of spatially constant electric field/voltage on the electrodes at the graphene-matrix interface. Therefore, using the ROM and considering the equal electric fields in the constituent phases ($E_3^g = E_3^m$), we can obtain the relation for D_3 (electric displacement in the homogenized GRNC lamina along its thickness); as follows (Ray, 2006):

$$D_3 = v_g D_3^g + v_m D_3^m. \tag{2.28}$$

Using the concept of pointwise average stress and strain discussed in preliminary Section 2.1, the relations for the piezoelectric composite were derived. In order to derive the constitutive relations for the GRNC lamina which characterizes the inverse piezoelectric effect, average strain vector of GRNC $\{\varepsilon\}$ and the average electric field E_3 in the 3–direction need to be correlated with the average stress vector $\{\sigma\}$ generated in the GRNC. This can be obtained in terms of the average strains in GRNC and the electric fields in the constituents by determining the local strain fields in the constituent phases of GRNC, that is, graphene and matrix. Based on Hill's average concentration approach (Hill, 1964), the average strain fields in the constituent phases can be derived as (Ray, 2006):

$$\{\varepsilon^g\} = [X^g]\{\varepsilon^{NC}\} + \{Y^g\}E_3 \text{ and } \{\varepsilon^m\} = [X^m]\{\varepsilon^{NC}\} + \{Y^m\}E_3. \tag{2.29}$$

$[X^r]$ and $\{Y^g\}$ represent the averages concentration factors ($[6 \times 6]$ and $[6 \times 1]$). Thus, a total 42 concentration factors of each phase (graphene reinforcement and matrix) are to be determined for determining the effective properties of GRNC. The detailed procedure for determining 84 constants is discussed below.

According to the iso-strain conditions (Eq. 2.25b), applied electric field (E_3) and composite strain $\{\varepsilon_3\}$, the factor X_{33}^r becomes unity and some of them vanish as below:

$$X_{33}^r = 1, X_{3i}^r = 0 \text{ , i} = 1, 2, 4, .., 6 \text{ and}$$

$$Y_{33}^r = 0 \text{ , r} = \text{g and m}. \tag{2.30}$$

According to the ROM (Eq. 2.25a), electric field (E_3) and composite strain $\{\varepsilon_3\}$, the following relations can be obtained:

$$v_g X_{ij}^g + v_m X_{ij}^m = \delta_{ij}, \text{ i} = 1, 2, 4, 5, 6 \text{ and j} = 1, 2, 3, \ldots, 6, \tag{2.31a}$$

$$v_g Y_{i1}^g + v_m Y_{i1}^m = 0 \text{ , i} = 1, 2, 4, 5 \text{ and } 6. \tag{2.31b}$$

In Eq. (2.31a), δ_{ij} is the Kronecker delta:

$$\delta_{ij} = \begin{cases} 0, & \text{if i} \neq \text{j} \\ 1, & \text{if i} = \text{j} \end{cases}$$

Finally, using the iso-stress condition given by Eq. (2.25b), we can obtain the following relations:

$$\sum_{i=1}^{3}(C_{ki}^{g}X_{ij}^{g} - C_{ki}^{m}X_{ij}^{m}) = 0, \qquad j = 1,2,3 \ldots 6;\ k = 1 \text{ and } 2 \tag{2.32a}$$

$$\sum_{i=1}^{3}(C_{ki}^{g}Y_{i1}^{g} - C_{ki}^{m}Y_{i1}^{m}) = e_{3k}^{g}, \qquad k = 1 \text{ and } 2 \tag{2.32b}$$

$$C_{ii}^{g}X_{ik}^{g} - C_{ii}^{m}X_{ik}^{m} = 0\,, i = 4, 5, 6, \qquad k = 1, 2, 3, \ldots, 6 \tag{2.32c}$$

$$C_{ii}^{g}Y_{i1}^{g} - C_{ii}^{m}Y_{i1}^{m} = 0\,, \qquad i = 4, 5, 6. \tag{2.32d}$$

It may be noted from Eqs. (2.31) and (2.32) that there are 48 concentration factors which can be obtained from simple solutions of 48 homogeneous equations. For example, using Eqs. (2.31a) and (2.32a), one can obtain the following expressions:

$$(C_{11}^{g} + \frac{v_g}{v_m}C_{11}^{m})X_{14}^{g} + (C_{12}^{g} + \frac{v_g}{v_m}C_{12}^{m})X_{24}^{g} = 0, \tag{2.33a}$$

$$(C_{12}^{g} + \frac{v_g}{v_m}C_{12}^{m})X_{14}^{g} + (C_{22}^{g} + \frac{v_g}{v_m}C_{22}^{m})X_{24}^{g} = 0. \tag{2.33b}$$

Note that the determinant of the matrix obtained from the coefficients appeared in Eqs. (2.33a) and (2.33b) is nonsingular. Thus, it can be concluded that only straight-forward solutions of these factors are plausible, i.e.,

$$X_{14}^{g} = X_{24}^{g} = 0. \tag{2.34}$$

Similarly, other concentration factors will become zero and the concentration matrix with all nonzero elements can be obtained as:

$$[X^{r}] = \begin{bmatrix} X_{11}^{g} & X_{12}^{g} & X_{13}^{g} & 0 & 0 & 0 \\ X_{21}^{g} & X_{22}^{g} & X_{23}^{g} & 0 & 0 & 0 \\ 0 & 0 & 1 & 0 & 0 & 0 \\ 0 & 0 & 0 & X_{44}^{g} & 0 & 0 \\ 0 & 0 & 0 & 0 & X_{55}^{g} & 0 \\ 0 & 0 & 0 & 0 & 0 & X_{66}^{g} \end{bmatrix}, \ \{Y^{r}\} = \begin{Bmatrix} Y_{11}^{g} \\ Y_{21}^{g} \\ 0 \\ 0 \\ 0 \\ 0 \end{Bmatrix}, r = g \text{ and } m. \tag{2.35}$$

Subsequently, non-zero concentration factors of graphene and matrix phases appeared in Eq. (2.35) can be exclusively computed for a specific graphene volume fraction by making use of remaining 11 non-homogeneous relations [Eqs. (2.31) and (2.32)]. Finally, non-zero concentration factors related to the graphene phase {A} can be obtained as follows:

$$\{A\} = [Q]^{-1}\{B\}. \tag{2.36}$$

where

$$\{A\} = \left[\, X_{23}^{g} \quad X_{13}^{g} \quad X_{22}^{g} \quad X_{12}^{g} \quad X_{21}^{g} \quad X_{11}^{g} \quad Y_{11}^{g} \quad Y_{21}^{g} \,\right]',$$

$$\{B\} = \left[\, -v_m\left(C_{23}^{g} - C_{23}^{m}\right) \quad -v_m\left(C_{13}^{g} - C_{13}^{m}\right) \quad C_{22}^{m} \quad C_{12}^{m} \quad C_{12}^{m} \quad C_{11}^{m} \quad v_m e_{31}^{g} \quad v_m e_{32}^{g} \,\right]',$$

$$[Q] = \begin{bmatrix} q_{11} & q_{12} & 0 & 0 & 0 & 0 & 0 & 0 \\ q_{12} & q_{22} & 0 & 0 & 0 & 0 & 0 & 0 \\ 0 & 0 & q_{11} & q_{12} & 0 & 0 & 0 & 0 \\ 0 & 0 & q_{12} & q_{22} & 0 & 0 & 0 & 0 \\ 0 & 0 & 0 & 0 & q_{11} & q_{12} & 0 & 0 \\ 0 & 0 & 0 & 0 & q_{12} & q_{22} & 0 & 0 \\ 0 & 0 & 0 & 0 & 0 & 0 & q_{11} & q_{12} \\ 0 & 0 & 0 & 0 & 0 & 0 & q_{12} & q_{22} \end{bmatrix},$$

$$q_{11} = v_m C_{22}^{g} + v_g C_{22}^{m},\ \ q_{12} = v_m C_{12}^{g} + v_g C_{12}^{m}\ \text{ and } q_{22} = v_m C_{11}^{g} + v_g C_{11}^{m}. \tag{2.37}$$

Using the following relation, we can determine the remaining three factors of graphene layer/s:

$$X_{ii}^{g} = \frac{C_{ii}^{m}}{\left(v_g C_{ii}^{m} + v_m C_{ii}^{g}\right)}\ ,\ \ i\ =\ 4, 5 \text{ and } 6. \tag{2.38}$$

Eventually, by substituting Eqs. (2.29) and (2.35) in Eqs. (2.26) and (2.28), the constitutive expression for the GRNC lamina is obtained as:

$$\{\sigma^{NC}\} = [C^{NC}]\{\varepsilon^{NC}\} - \{e^{NC}\}E_3, \tag{2.39a}$$

$$D_3 = \{e^{NC}\}'\{\varepsilon^{NC}\} + \epsilon_{33}\, E_3, \tag{2.39b}$$

where the effective elastic and piezoelectric tensors of the GRNC are represented by $[C^{NC}]$ and $\{e^{NC}\}$, respectively, and they can be written as:

$$[C^{NC}] = [C_1][X^g] + [C_2][X^m] \text{ and } \{e^{NC}\} = \{e_1\} - [C_1]\{Y^g\} - [C_2]\{Y^m\}, \tag{2.40}$$

in which

$$\{e^{NC}\} = \{e^{NC}_{31} \quad e^{NC}_{32} \quad e^{NC}_{33} \quad 0 \quad 0 \quad 0\}',$$

where

$$e^{NC}_{31} = e^{g}_{31} - \left(C^{g}_{11}Y^{g}_{11} + C^{g}_{12}Y^{g}_{21}\right),\ e^{nc}_{32} = e^{g}_{32} - (C^{g}_{12}Y^{g}_{11} + C^{g}_{22}Y^{g}_{21}),$$

$$e^{NC}_{33} = \left(v_g e^{g}_{33}\right) - v_g\left(C^{g}_{13}Y^{g}_{11} + C^{g}_{23}Y^{g}_{21}\right) - v_m(C^{m}_{13}Y^{m}_{11} + C^{m}_{23}Y^{m}_{21}). \tag{2.41}$$

Similar to the MOM model, the effective dielectric coefficient ($\in^{NC}_{33}$) of the GRNC can be obtained using Eq. (2.21).

2.3.3 FE Modeling of GRNC

The analytical micromechanics models developed in the preceding Sections are based on the assumptions of ROM and iso-field conditions as well as consideration of no slippage between the graphene reinforcement and matrix which imply continuity of displacements and tractions between them. However, it may be imperative to justify the validity of such assumptions considered for developing the analytical models. Numerical or experimental investigations may be carried out to verify these assumptions because both the analyses do not require any such approximations.

Therefore, in the current Section, FE models were developed to validate the assumptions used in analytical models by employing the commercial software ANSYS 15.0. The FE simulations were carried out to determine the fully coupled electromechanical problem and thus the elastic, piezoelectric and dielectric properties of GRNC can be obtained by creating three dimensional RVE using 20 node coupled field element “solid 226” having displacement (U_x, U_y, U_z) as well as electric potential (volt.) degrees of freedom (DOF). Figures 2.4 and 2.5 show the RVE and FE mesh of GRNC, respectively, which were homogenized and analyzed under various boundary conditions. FE model of the RVE of homogenous transversely isotropic GRNC with its axis of transverse isotropy aligned along the 3–axis was developed for determining the independent elastic, piezoelectric and dielectric coefficients: C^{eff}_{11}, C^{eff}_{12}, C^{eff}_{13}, C^{eff}_{33}, C^{eff}_{44}, e^{eff}_{31}, e^{eff}_{33}, e^{eff}_{15}, and $\in^{eff}_{33}$. These effective coefficients of the GRNC can be determined by applying the appropriate boundary conditions to the RVE. Therefore, the determination of particular effective coefficient of GRNC from the FE model needs to prescribe the appropriate loading and boundary conditions on the faces of RVE.

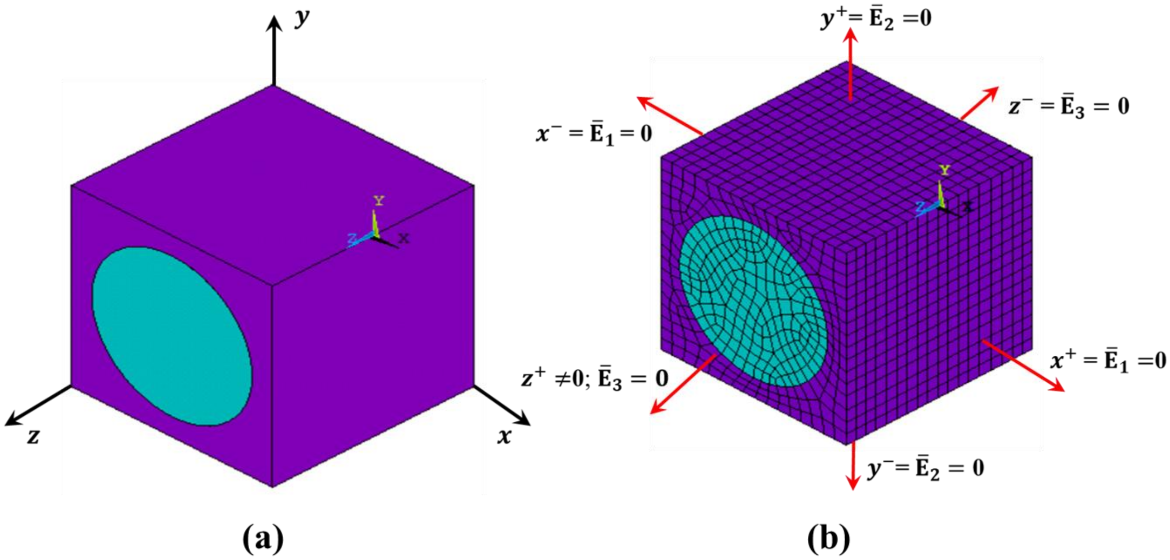

Figure 2.4: (a) GRNC RVE consisting graphene and matrix and (b) boundary conditions applied on RVE for C_{33}^{eff}.

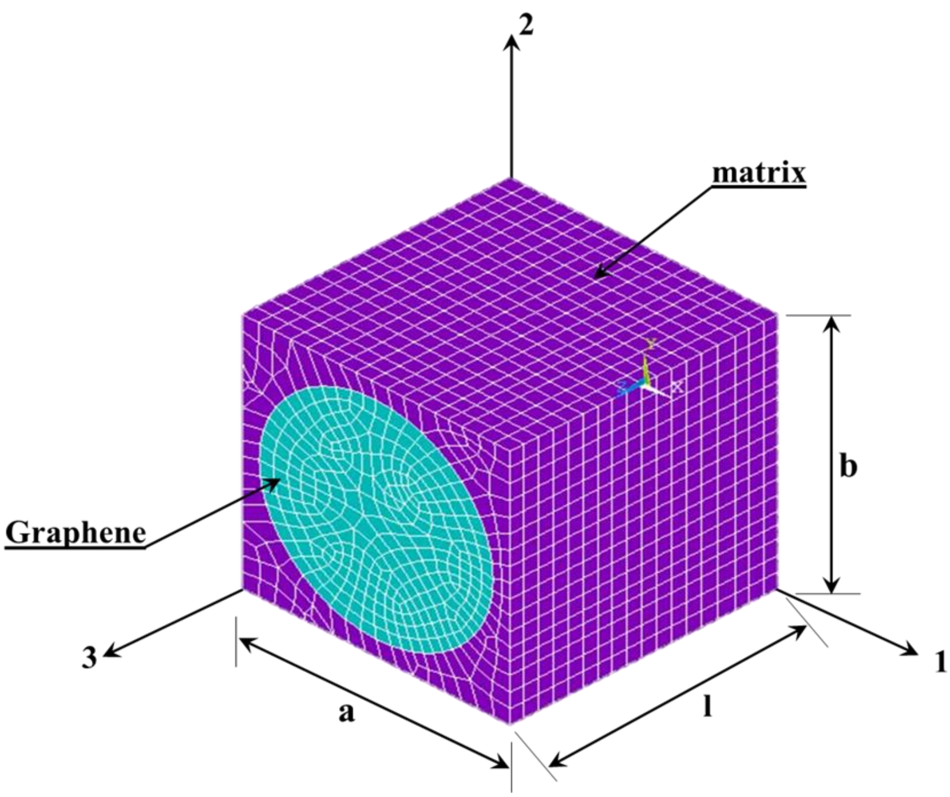

Figure 2.5: FE mesh of RVE of GRNC.

The combined electromechanical relations of GRNC are given by Eq. (2.43) in which C_{ij}^{eff}, e_{ij}^{eff} and ϵ_{ij}^{eff} are the effective elastic, piezoelectric and permittivity constants of GRNC, respectively.

$$\begin{Bmatrix} \bar{\sigma}_{11} \\ \bar{\sigma}_{22} \\ \bar{\sigma}_{33} \\ \bar{\sigma}_{23} \\ \bar{\sigma}_{13} \\ \bar{\sigma}_{12} \\ \bar{D}_1 \\ \bar{D}_2 \\ \bar{D}_3 \end{Bmatrix} = \begin{bmatrix} C_{11}^{eff} & C_{12}^{eff} & C_{13}^{eff} & 0 & 0 & 0 & 0 & 0 & -e_{31}^{eff} \\ C_{12}^{eff} & C_{22}^{eff} & C_{13}^{eff} & 0 & 0 & 0 & 0 & 0 & -e_{31}^{eff} \\ C_{13}^{eff} & C_{13}^{eff} & C_{33}^{eff} & 0 & 0 & 0 & 0 & 0 & -e_{33}^{eff} \\ 0 & 0 & 0 & C_{44}^{eff} & 0 & 0 & 0 & -e_{15}^{eff} & 0 \\ 0 & 0 & 0 & 0 & C_{55}^{eff} & 0 & -e_{15}^{eff} & 0 & 0 \\ 0 & 0 & 0 & 0 & 0 & C_{66}^{eff} & 0 & 0 & 0 \\ 0 & 0 & 0 & 0 & e_{15}^{eff} & 0 & \epsilon_{11}^{eff} & 0 & 0 \\ 0 & 0 & 0 & e_{15}^{eff} & 0 & 0 & 0 & \epsilon_{22}^{eff} & 0 \\ e_{31}^{eff} & e_{31}^{eff} & e_{33}^{eff} & 0 & 0 & 0 & 0 & 0 & \epsilon_{33}^{eff} \end{bmatrix} \begin{Bmatrix} \bar{\varepsilon}_{11} \\ \bar{\varepsilon}_{22} \\ \bar{\varepsilon}_{33} \\ \bar{\varepsilon}_{23} \\ \bar{\varepsilon}_{13} \\ \bar{\varepsilon}_{12} \\ \bar{E}_1 \\ \bar{E}_2 \\ \bar{E}_3 \end{Bmatrix}. \qquad (2.43)$$

Under the conditions of the imposed electromechanical loads on the RVE of GRNC, the average stress $\{\bar{\sigma}_{ij}\}$, strain $\{\bar{\varepsilon}_{ij}\}$, electrical displacement $\{\bar{D}_i\}$ and electric field $\{\bar{E}_i\}$ are defined as below:

$$\{\bar{\sigma}_{ij}\} = \frac{1}{\Omega}\int_{\Omega}\{\sigma_{ij}\}dV, \qquad \{\bar{\varepsilon}_{ij}\} = \frac{1}{\Omega}\int_{\Omega}\{\varepsilon_{ij}\}dV,$$
$$\{\bar{D}_i\} = \frac{1}{\Omega}\int_{\Omega}\{D_i\}dV\,, \qquad \{\bar{E}_i\} = \frac{1}{\Omega}\int_{\Omega}\{E_i\}dV. \qquad (2.44)$$

where Ω represents the volume of RVE of GRNC and the quantity with an overbar represents the volume averaged quantity. It is evident from Eq. (2.43) that if at any point in the GRNC only one normal strain is present while the other strain components are zero then three normal stresses exist. The ratio between any one of these three normal stresses and the normal strain yields a particular effective coefficient. Thus, three such effective coefficients at a point can be determined with one numerical experiment. Hence, the determination of particular effective elastic, piezoelectric and dielectric coefficients from the FE model need to prescribe the appropriate boundary conditions on the faces of RVE, as described in subsequent sub-sections.

2.3.3.1 Determination of C_{13}^{eff} and C_{33}^{eff}

In order to compute the effective elastic coefficients C_{13}^{eff} and C_{33}^{eff} of GRNC, the RVE shown in Fig. 2.6 can be deformed in such a way that the normal strain ε_{33} is only present in it while all other strain components are zero. In order to achieve such state of strains, displacements at the five boundary surfaces ($x = 0$ and a; $y = 0$ and b; $z = 0$) need to be prescribed to zero. It should be noted that x, y and z denote the coordinates corresponding to 1, 2 and 3-axes, respectively. A uniform normal displacement ($w = z^+ \neq 0$) along the 3-direction needs to be applied on the surface ($z = l$) of the RVE such that it is subjected to $\bar{\varepsilon}_{33}$ only. For the sake of clarity, an applied boundary constrain is shown in Fig. 2.4 (b). Likewise, the electric fields (voltage DOF) at all faces are required to constrain to zero ($\bar{E}_1 = \bar{E}_2 = \bar{E}_3 = 0$). Using Eqs. (2.44), the average stresses and strains ($\bar{\sigma}_{11}$, $\bar{\sigma}_{33}$, and $\bar{\varepsilon}_{33}$) can be obtained. Then, the values of effective elastic coefficients $C_{33}^{eff}(= \bar{\sigma}_{33}/\bar{\varepsilon}_{33})$ and $C_{13}^{eff}(= \bar{\sigma}_{11}/\bar{\varepsilon}_{33})$ can be determined using Eq. (2.43) for different volume fractions of graphene. Figure 2.6 shows the stress and strain distributions in the RVE obtained along the graphene direction.

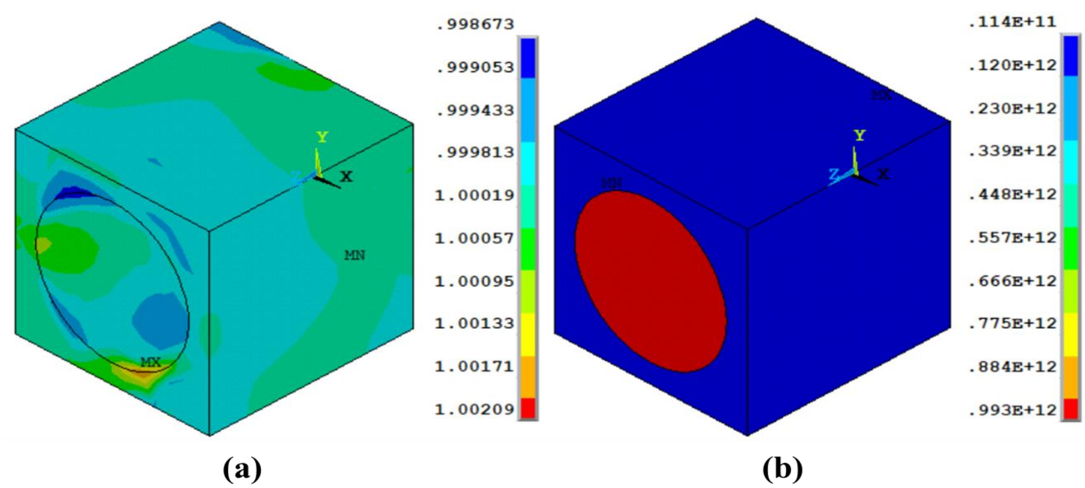

Figure 2.6: FE simulations showing distributions of (a) strain ε_{33} and (b) stress σ_{33} in the RVE of GRNC.

2.3.3.2 Determination of C_{11}^{eff} and C_{12}^{eff}

In order to determine the effective elastic coefficients C_{11}^{eff} and C_{12}^{eff} of GRNC, the RVE is subjected to the states of strain such that only normal strain $\bar{\varepsilon}_{11}$ is present while all other strain components are zero ($\bar{\varepsilon}_{22} = \bar{\varepsilon}_{33} = \bar{\varepsilon}_{23} = \bar{\varepsilon}_{13} = \bar{\varepsilon}_{12} = 0$). Such states of strain can be attained by constraining the surfaces of RVE in the following manner:

$$u = 0 \text{ at } x = 0;\ v = 0 \text{ at } y = 0 \text{ and } b;\ w = 0 \text{ at } z = 0 \text{ and } l.$$

In the same way, the electric field at all surfaces of RVE are required to constrain to zero ($\bar{E}_1 = \bar{E}_2 = \bar{E}_3 = 0$). Due to the essential boundary conditions, the uniform normal displacement ($u = x^{+} \neq 0$) is required to apply on the surface $x = a$ of the RVE such that it is under the application of $\bar{\varepsilon}_{11}$ only. Using Eqs. (2.43) and (2.44), the average stresses and strain ($\bar{\sigma}_{11}$, $\bar{\sigma}_{22}$, and $\bar{\varepsilon}_{11}$) can be obtained to determine the values of C_{11}^{eff} ($= \bar{\sigma}_{11} / \bar{\varepsilon}_{11}$) and C_{12}^{eff} ($= \bar{\sigma}_{22} / \bar{\varepsilon}_{11}$). The distributions of stresses and strains are shown in Fig. 2.7 when the deformation is applied to the RVE in the transverse direction to the length of graphene.

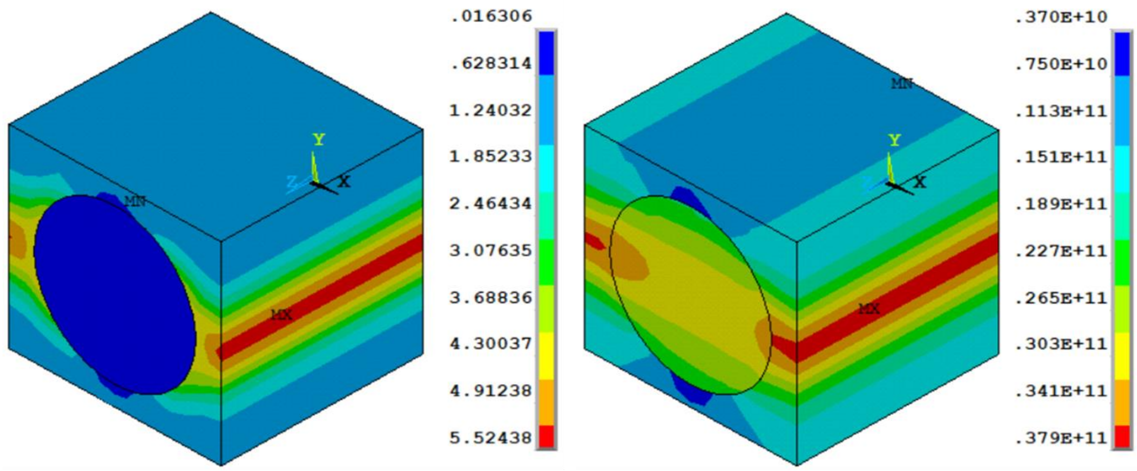

(a) **(b)**

Figure 2.7: FE simulations showing distributions of (a) strain ε_{11} and (b) stress σ_{11} in the RVE of GRNC.

2.3.3.3 Determination of C_{44}^{eff}, e_{15}^{eff} and C_{66}^{eff}

To determine the effective elastic coefficient C_{44}^{eff} of GRNC, an out-of-plane shear in the $y - z$ plane of the RVE is required to subject the pure shear deformation in such a way that the shear strain $\bar{\varepsilon}_{23}$ is non-zero while the remaining strain components are zero. Such states of strain can be achieved by prescribing the surface given by $z = 0$ of the RVE and imposing the uniform distributed tangential force on the surface given by $z = l$. In the same way, the electric potential at all surfaces of the RVE are required to constrain to zero ($\bar{E}_1 = \bar{E}_2 = \bar{E}_3 = 0$).

Subsequently, the average shear stress and strain ($\bar{\sigma}_{23}$ and $\bar{\varepsilon}_{23}$) induced in the RVE can be determined using Eq. (2.44). Finally, the effective elastic coefficient C_{44}^{eff} can be determined using the relation: $\bar{\sigma}_{23} / \bar{\varepsilon}_{23}$. Note that the effective elastic coefficient C_{66}^{eff} is not independent elastic coefficient and it can be computed directly from the relation $\left(C_{11}^{eff} - C_{12}^{eff}\right)/2$.

In order to determine the effective piezoelectric coefficient e_{15}^{eff}, the boundary conditions similar to obtain C_{44}^{eff} can be used such that the RVE is imposed to shear strain $\bar{\varepsilon}_{23}$ only ($\bar{\varepsilon}_{11} = \bar{\varepsilon}_{22} = \bar{\varepsilon}_{33} = \bar{\varepsilon}_{13} = \bar{\varepsilon}_{12} = 0$) and electric potential needs to be constrained to zero on the two surfaces of RVE ($\bar{E}_1 = \bar{E}_2 = 0$). Using Eq. (2.43), the values of e_{15}^{eff} can be determined using the ratio $e_{15}^{eff} = \bar{D}_2 / \bar{\varepsilon}_{23}$ for different volume fractions of graphene. Figure 2.8 depicts the distributions of in-plane shear stresses and strains in the RVE of GRNC.

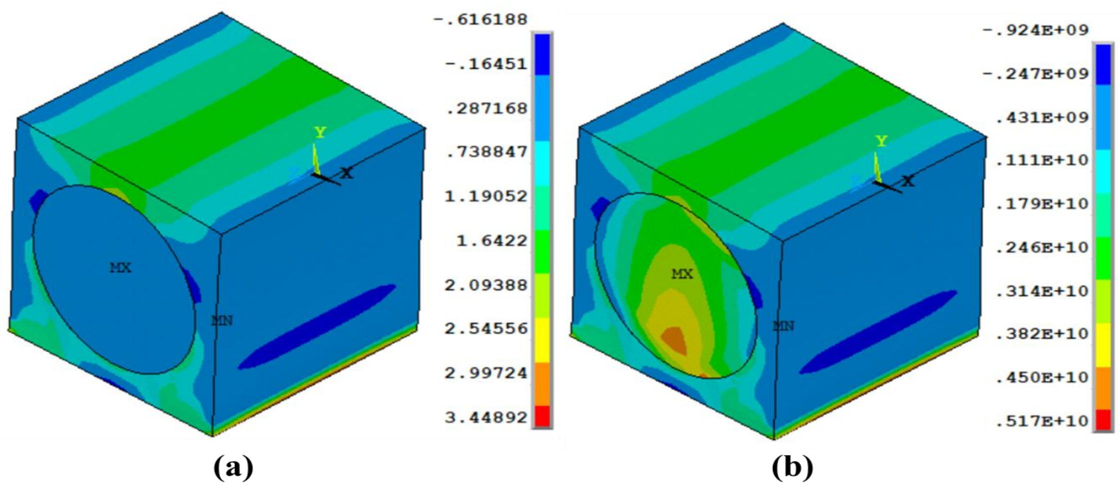

Figure 2.8: FE simulations showing distributions of (a) shear strain (γ_{12}) and (b) shear stress (τ_{12}) in the RVE of GRNC.

2.3.3.4 Determination of e_{33}^{eff}, e_{13}^{eff} and $\in_{33}^{eff}$

The effective piezoelectric coefficients e_{13}^{eff} and e_{33}^{eff} are proportional to the in-plane and out-of-plane actuations of piezoelectric material, respectively. In order to determine the values of e_{13}^{eff}, e_{33}^{eff} and $\in_{33}^{eff}$, the opposite boundary conditions as used in case of C_{33}^{eff} and C_{13}^{eff} (Fig. 2.4b) were used so that their normal displacements are zero ($\bar{\varepsilon}_{11} = \bar{\varepsilon}_{22} = \bar{\varepsilon}_{33} = 0$).

The uniform electric potential needs to apply to the RVE in 3−direction and its remaining surfaces are required to constrain to zero electric potentials ($\bar{E}_1 = \bar{E}_2 = 0$). Figure 2.9 illustrates the distributions of electric displacement and electric potential in the RVE. Subsequently, the average values of $\bar{\sigma}_{11}$, $\bar{\sigma}_{33}$, $\bar{D}_3$ and $\bar{E}_3$ can be computed using Eq. (2.44). Then, using Eq. (2.43), the effective values of e_{33}^{eff}, e_{13}^{eff}, and $\in_{33}^{eff}$ can be determined using the respective ratios $-\bar{\sigma}_{33} / \bar{E}_3$, $-\bar{\sigma}_{11} / \bar{E}_3$ and $-\bar{D}_3 / \bar{E}_3$.

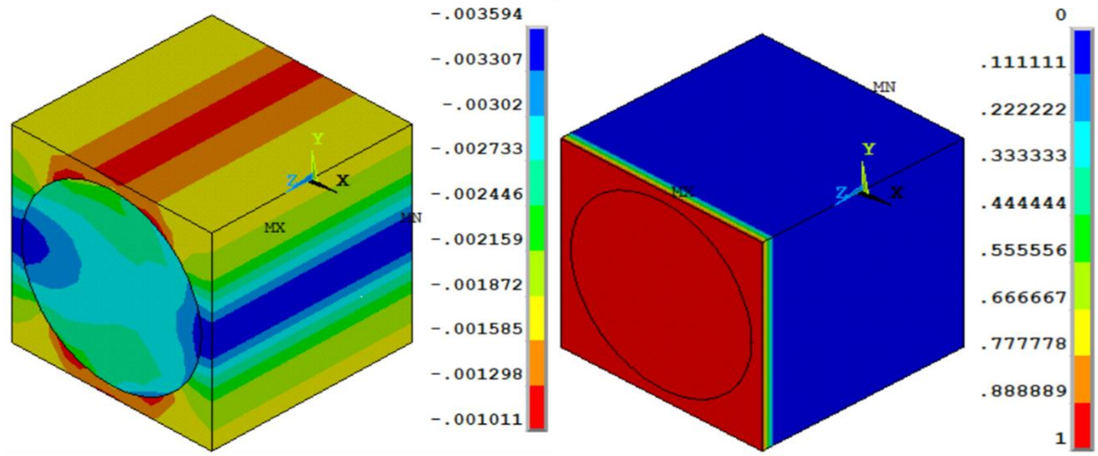

(a) **(b)**

Figure 2.9: FE simulations showing the distributions of (a) stresses (σ_{11}) and (b) electric potential ($\bar{E}_3$) in the RVE of GRNC.

2.4 Results and Discussions

In this Section, the predictions of effective elastic, piezoelectric and dielectric properties of GRNC are presented using the different models developed in the preceding Sections.

2.4.1 Elastic Properties of Graphene Sheet

In this sub-section, the elastic properties of (i) pristine graphene sheet and (ii) defective graphene sheets containing 4.5% and 20% vacancies in form of non-centrosymmetric pores using MDS were determined, as summarized in Table 2.1.

Table 2.1: The elastic properties of pristine and defected graphene sheets.

Material	E (GPa)	μ
Pristine Graphene	985	0.265
Graphene with 4.5 % vacancy	969	0.265
Graphene with 20% vacancy	890	0.265

The predictions of pristine graphene agree well with the existing results obtained by using different modeling techniques and potentials as well as experimental estimates (Lee et al., 2008; Jing et al., 2012; Dewapriya et al., 2015). In case of defective graphene, the current results were validated with those reported by Jing et al. (2012). They used COMPAAS force field to model the defective graphene sheets containing vacancies which were functionalized by hydrogen atoms on the dangling bonds. The percentage of reduction in Young's modulus ~1.6% in case of graphene containing 6 carbon atom vacancies (i.e., 4.5% vacancies) was found to be close with that reported by Jing et al. (2012). They reported the percentage of reduction ~1.53% for functionalized graphene with 6 missing carbon atoms. In case of 20% vacancies, the elastic properties of graphene are not much significantly affected. This is attributed to the hydrogenation and saturation of the dangling bonds at the edges and porosity in the graphene sheet (Jing et al., 2012).

2.4.2 Comparisons of Results of MOM and FE Models

In this sub-section, the numerical outcomes of the effective properties of GRNC determined by MOM and FE models are discussed. The properties of the pristine and defective graphene sheets as well as polyimide are summarized in Table 2.2. We considered both pristine and defected graphene (with 4.5% and 20% vacancies) sheets. The graphene sheet under consideration consists of 224 carbon atoms and accordingly, the normal piezoelectric coefficient (e_{33}) was determined as 0.221 C/m^2 when the value of $\rho =$ 15.2 Å. The piezoelectric properties of pristine and defective graphene sheets were taken from Ref. Kundalwal et al. (2017).

Table 2.2: Material properties of constituents of GRNC.

Material	**E (GPa)**	**μ**	$\mathbf{e_{31}}$ **(C/m^2)**	$\mathbf{e_{33}}$ **(C/m^2)**	$\mathbf{\epsilon_{33}}$ **(F/m)**
Pristine Graphene	985	0.265	-0.221	0.221	1.106 x 10^{-10} (Muñoz-Hernández et al. 2017)
Graphene with 4.5 % vacancy	969	0.265	-0.027	0.027	1.106 x 10^{-10}
Graphene with 20% vacancy	890	0.265	-0.12	0.12	1.106 x 10^{-10}
Polyimide	4.2 (Odegard et al. 2005)	0.4 (Odegard et al. 2005)	-	-	3.009 x 10^{-11} (Li et al. 2015)

For the sake of brevity, the results for effective properties of GRNC are presented considering the pristine graphene while the results for the defected graphene sheets in GRNC are not shown here. Some predictions of the effective properties of GRNC considering the volume fraction of both pristine and defected graphene as 0.5 are summarized in Table 2.3.

Table 2.3: Effective properties of GRNC ($v_g = 0.5$).

Material	C_{11} (GPa)	C_{12} (GPa)	C_{66} (GPa)	e_{31} (C/m^2)	e_{33} (C/m^2)	ϵ_{33} (F/m)
Pristine Graphene	17.853	11.876	2.988	-0.0019	0.167	7.026×10^{-11}
Graphene with 4.5 % vacancy	17.851	11.874	2.988	-0.0002	0.0204	7.034×10^{-11}
Graphene with 20% vacancy	17.838	11.863	2.987	-0.0011	0.0910	7.029×10^{-11}

The thickness of single layer of graphene sheet was considered as 0.34 nm (i.e., distance between two adjacent layers of multi-layered graphene). The chemical vapour deposition (CVD) process is one of the most common methods for the preparation of high-quality thin 2D films on the order of micrometer (Xu et al., 2014). Practically, the reinforcement volume fraction in the composite can vary typically from 0.2 to 0.7. Our selection of use of graphene volume fraction was based on the fact that several researchers fabricated nanocomposite samples with 5% to 90% volume fraction of graphene and its derivatives such as graphite oxide and graphene oxide (GO) using unique nanofabrication techniques: dispersion method, layer-by-layer assembly and solution blending route (Gamboa et al., 2010; Gong et al., 2012; Young et al., 2012; Yang et al., 2013; Papageorgiou et al., 2017). The assemblies of multi-layers of GO and polyethylenimine were presented by tailoring the thickness of number of GO layers. In case of bilayer of GO and polyethylenimine, the thickness of assembly near about ~5 nm was achieved. In some other studies, the thickness of assembly was achieved in the range of 8-10 nm using 4 to 30 graphene platelets (Yang et al., 2013; Prolongo et al., 2014; Tzeng et al., 2015; Prolongo et al., 2018). Using these techniques, the fabrication of a GRNC can be achieved on the order of nm. Hence, the range from 0.2 to 0.7 was considered to analyze the effect of graphene volume fraction (v_g) on the elastic, piezoelectric and dielectric properties of GRNC. Unless otherwise mentioned, the pristine graphene was considered, as shown in Figs. 2.9–2.14. In FE simulations, the governing equations were solved by using a linear perturbation for piezoelectric analysis and the sparse direct solver was used for structural analysis. First, the FE mesh convergence was carried out to study the effect of element size on the effective properties of GRNC for obtaining the reliable results.

Figure 2.10 demonstrates the variation of effective elastic constant C_{11}^{NC} of GRNC against the value of v_g. It may be observed that the values of C_{11}^{NC} are overestimated by the MOM model compared to the FE results, especially for the higher values of v_g. It is well known fact that the transverse elastic properties of composite are mostly the function of matrix material properties; therefore, the predictions of both the models are in good agreement for the lower values of v_g or higher values of v_m. The discrepancy increases between the predictions by both the models in Fig. 2.10 with the value of v_g. It is attributed to the fact that the transverse properties of composite are matrix dependent and hence the discrepancy between predictions by both the models increases as the graphene volume fraction increases. This clearly indicate that the MOM model cannot accurately model iso-stress conditions applied to the RVE of GRNC whereas the Poisson's effect in GRNC is accurately captured by FE simulations. The determined values of C_{22}^{NC} are found to be identical to those of C_{11}^{NC} and are not shown here. This is attributed to the fact that the constructional feature of GRNC demonstrates the transversely isotropic behavior with the axis of symmetry along the 3–direction.

Figure 2.11 shows the variation of effective elastic constant C_{23}^{NC} of GRNC against the v_g. The predicted values of C_{23}^{NC} by the MOM approach are slightly lower than that of FE predictions and this indicates that the Poisson's effect in GRNC is accurately captured by the former. Due to the exerted load along the axis of symmetry, the extension-extension coupling occurs between the different normal stress (σ_{33}) and normal strain (ε_{22}), and FE simulations captured such coupling accurately. The predictions of values of C_{13}^{NC} are found to be same as those of C_{23}^{NC} and are not shown here for the sake of brevity. It may be observed from Figs. 2.10 and 2.11 that the predictions by both the models differ as the value of v_g increases. Such discrepancy exists because the transverse properties of composite are matrix dependent and hence the discrepancy between the predictions by models increases as the value of v_m decreases. This clearly indicates that the MOM model cannot accurately model the iso-stress conditions (Eq. 2.16) applied to the RVE of GRNC.

Figure 2.12 depicts the variation of effective axial elastic constant C_{33}^{NC} of GRNC with the values of v_g. It is observed that the values of C_{33}^{NC} vary almost linearly with the values of v_g and both the models predict indistinguishable results. This comparison also ensures the validity of ROM as well as the assumptions adopted to develop MOM model, especially the iso-strain condition. The existing experimental studies also reported the same for the axial properties of graphene-based nanocomposite (Zhao et al., 2010; Khan et al., 2012; Ji et al., 2016; García-Macías et al., 2018). Note that the effective longitudinal or axial elastic constant is usually determined by using the iso-strain condition, which models actual experiments almost exactly, along the axis of symmetry and therefore, the predictions of values of C_{33}^{NC} are identical to that of Voigt-upper bound predictions. It can be observed from Figs. 2.9 and 2.11 that the magnitude of values of C_{33}^{NC} is significantly higher than that of the values of C_{11}^{NC} for a given value of v_g. This indicates that the axial stiffness of GRNC lamina is enhanced by aligning the graphene layer in the same direction. The effective elastic constant C_{66}^{NC} is a function of elastic constants C_{11}^{NC} and C_{12}^{NC} and hence, the predictions C_{66}^{NC} are not shown here.

Figures 2.13–2.15 demonstrate the variations of effective piezoelectric coefficients e_{31}^{NC} and e_{33}^{NC} as well as the axial dielectric constant $\in_{33}^{NC}$ of GRNC against the value of v_g. It can be observed from Fig. 2.13 that the value of e_{31}^{NC} increases with the increase in the graphene volume fraction. Since the GRNC is transversely isotropic material with the axis of symmetry being aligned along the 3–direction, the values of e_{32}^{NC} of GRNC are found to be identical those of e_{31}^{NC}. It can be seen from Figs. 2.14 and 2.15 that both the models predict almost identical and linear estimates for the values of e_{33}^{NC} and $\in_{33}^{NC}$ for a vast range of v_g, respectively. Comparison of results obtained by the MOM and FE models reveals that the former model yields conservative predictions for most of the elastic and piezoelectric properties of GRNC.

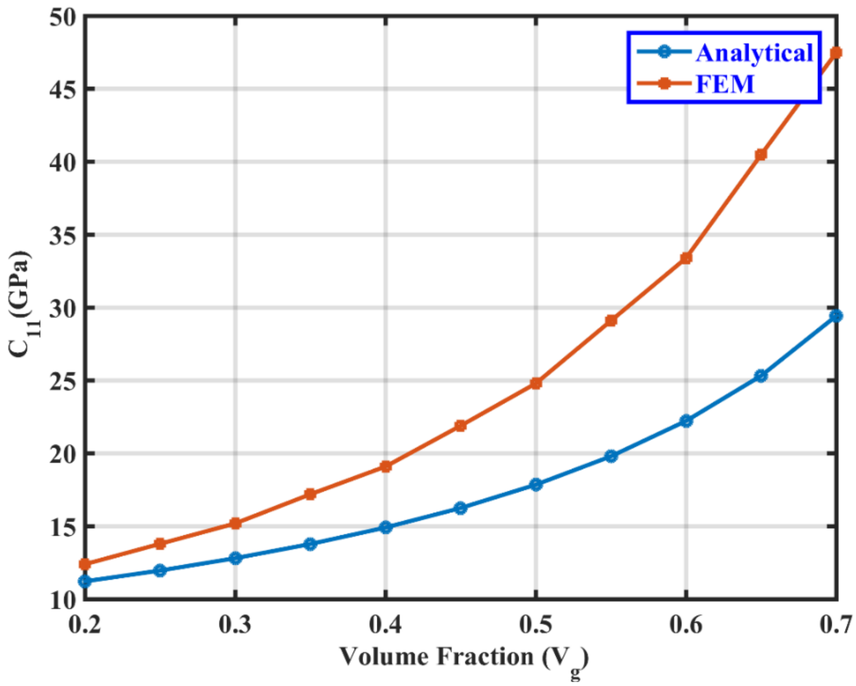

Figure 2.10: Variation of effective elastic constant (C_{11}^{NC}) of GRNC with the graphene volume fraction (v_g).

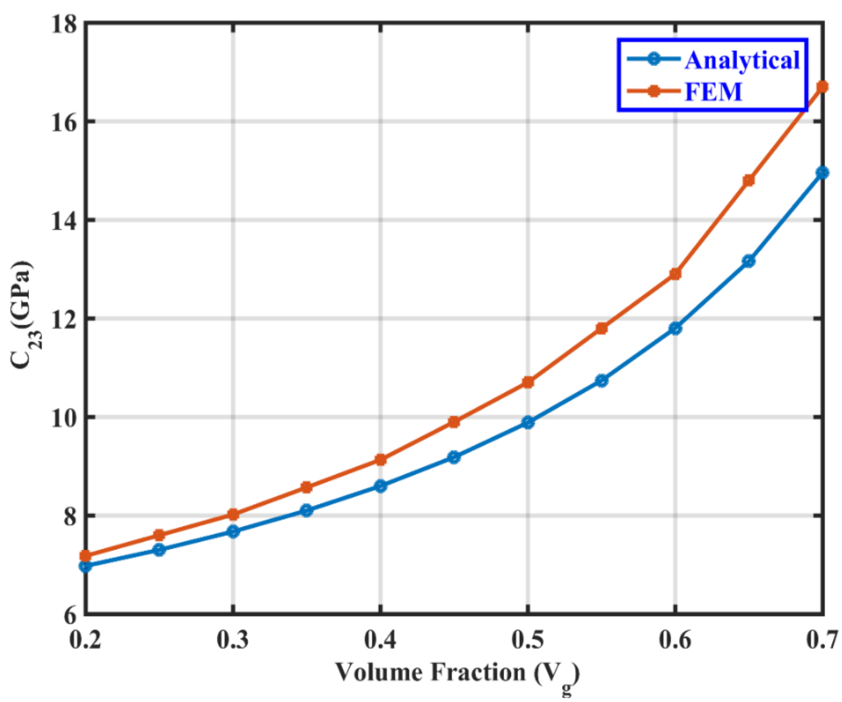

Figure 2.11: Variation of effective elastic constant (C_{23}^{NC}) of GRNC with the graphene volume fraction (v_g).

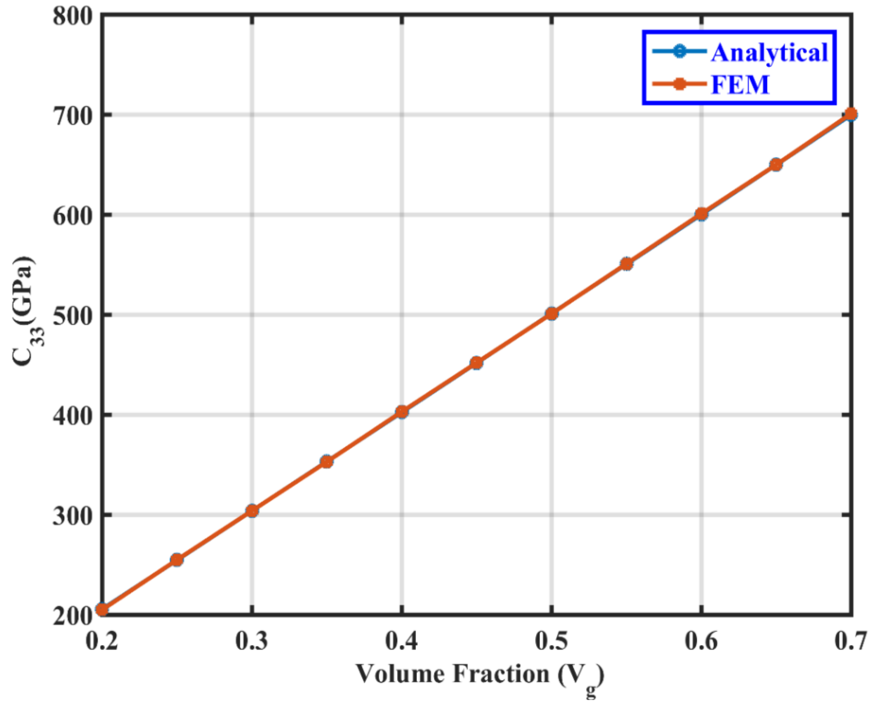

Figure 2.12: Variation of effective elastic constant (C_{33}^{NC}) of GRNC with the graphene volume fraction (v_g).

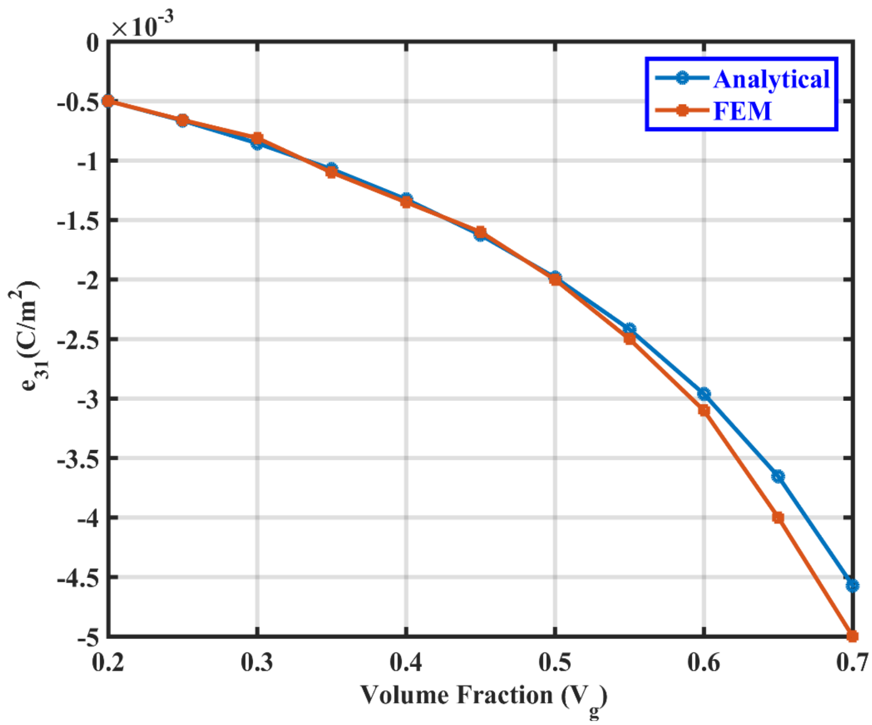

Figure 2.13: Variation of effective piezoelectric constant (e_{31}^{NC}) of GRNC with the graphene volume fraction (v_g).

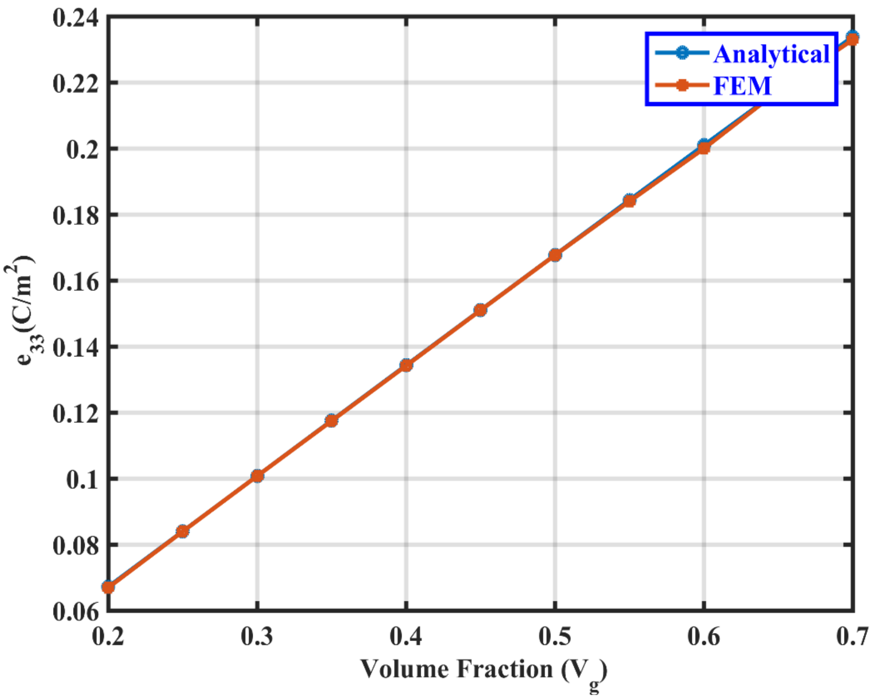

Figure 2.14: Variation of effective piezoelectric constant (e_{33}^{NC}) of GRNC with the graphene volume fraction (v_g).

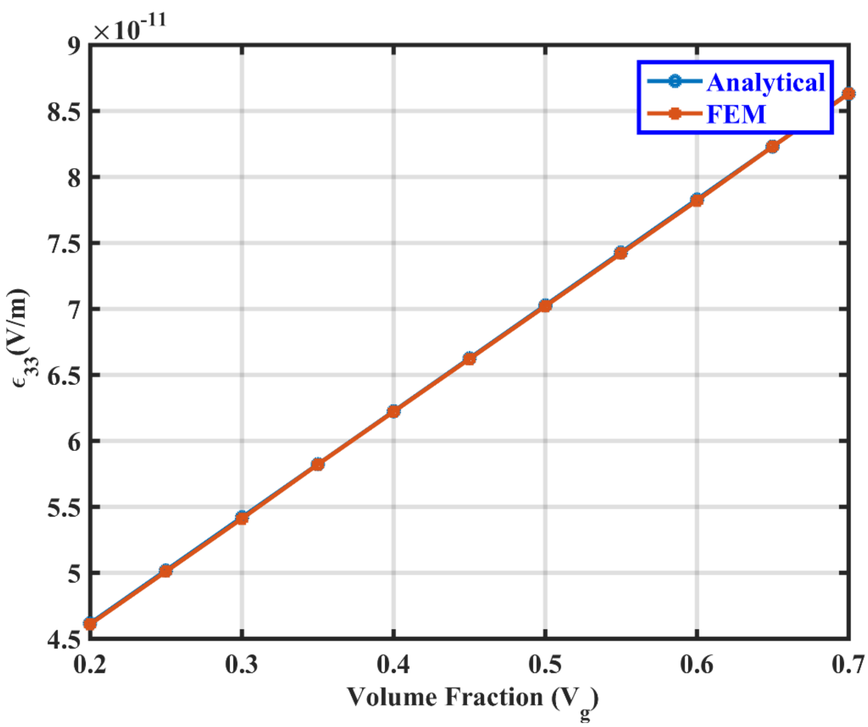

Figure 2.15: Variation of effective dielectric constant ($\in_{33}^{NC}$) of GRNC with the graphene volume fraction (v_g).

2.4.3 Comparisons of Results of SOM and FE Models

In this sub-section, the predictions of effective elastic, piezoelectric and dielectric properties of GRNC obtained by SOM and FE models are presented and discussed. The material properties of the pristine graphene and polyimide are summarized in Table 2.2. Theoretically, the volume fraction of a square graphene sheet in the RVE with square cross-section can vary from 0 to 1, but we have considered the graphene volume fraction (v_g) range from 0.2 to 0.9. The effective properties of GRNC determined using both the models are presented in Figs. 2.15–2.21. In case of FE simulations, the discretization of GRNC RVE was done in such a way that the value of v_g in each simulation is represented by a specific number of FE elements. In FE analysis, the linear perturbation procedure and sparse direct solver were used for the piezoelectric and structural analysis, respectively, to solve the governing equations. The FE mesh convergence was carried out to obtain reliable results and the same are summarized in Table 2.4. This table clearly shows that after a certain number of elements the prediction of C_{11}^{NC} does not change and we carried out such convergence study for determining all other elastic constants considering the whole range of v_g from 0.2 to 0.9 with step size of 0.05.

Table 2.4: Convergence of elastic stiffness coefficients.

Element type	**Mesh level**	**Number of Elements**	**Number of Nodes**	$\mathbf{C_{11}}$ **(GPa)**
Solid 226	Coarse	8518	12975	33.58
Solid 226	Medium	33110	47785	33.51
Solid 226	Fine	55385	79412	33.47
Solid 226	Finer	90877	128948	33.42
Solid 226	Finest	112092	143886	33.42

Figure 2.16 shows the comparison of values of C_{11}^{NC}(or C_{22}^{NC}) against v_g. Note that the GRNC is transversely isotropic material with the axis of symmetry being along the 3–

axis and thus, the numerical estimates of C_{11}^{NC} and C_{22}^{NC} of GRNC are identical. It can be observed from Fig. 2.16 that the values of C_{11}^{NC} obtained by SOM model are in good coherence with the FE predictions at the lower values of v_g and the former model slightly underestimates the predictions at higher values of v_g. The deviation between the set of results occurs because the transverse elastic properties of GRNC are mainly matrix dependent properties and thus, the good agreement is found between the predictions by both the models at lower values of v_g.

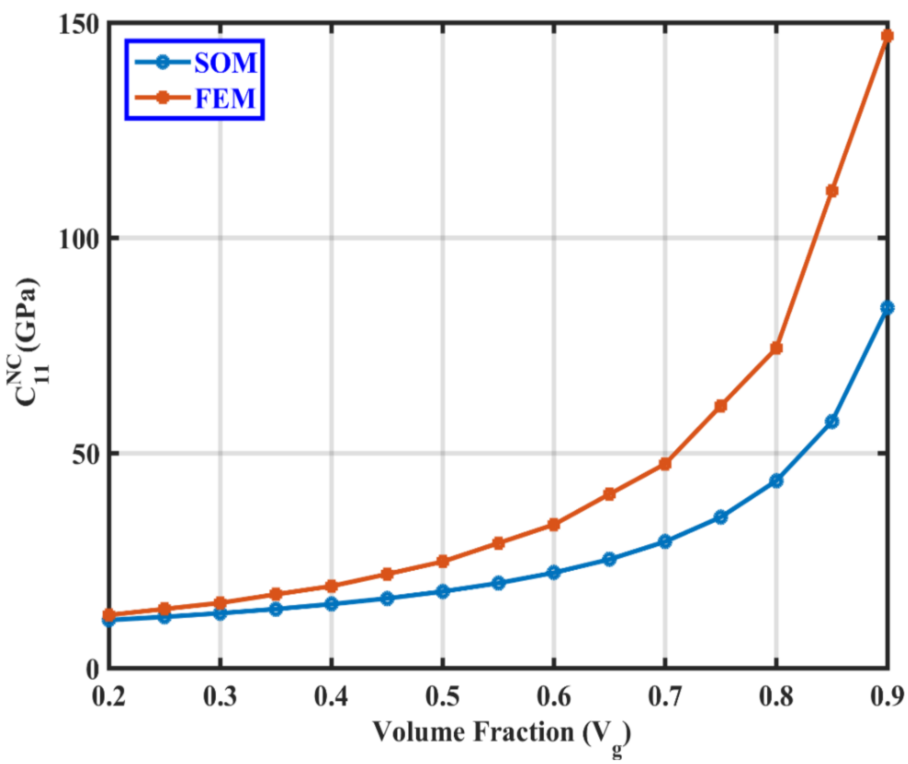

Figure 2.16: Comparison of values of C_{11}^{NC} (or C_{22}^{NC}) vs V_g.

Figure 2.17 demonstrates the comparison of values of C_{33}^{NC} against v_g. It can be noticed that the values of C_{33}^{NC} vary almost linearly over the entire range of v_g. The results predicted by both the models are indistinguishable. This also confirms the validity of ROM as well as the assumptions adopted for developing the SOM model. For instance, it is worth to mention that the effective elastic constant (C_{33}^{NC}) was computed using the iso-strain condition (Eq. 2.25b) and such approximation exactly fits with the Voigt-upper bound and experimental linear estimates.

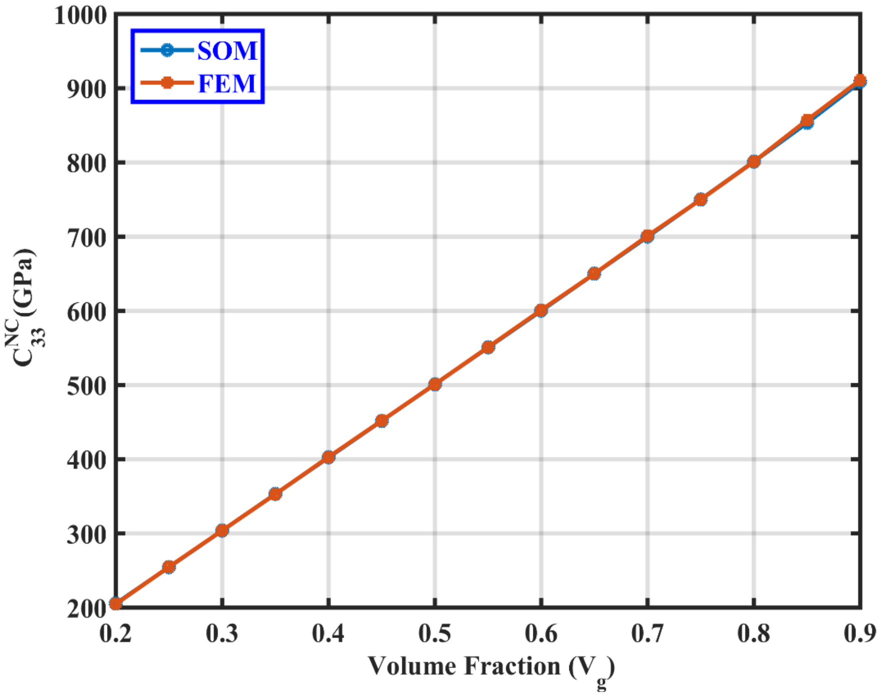

Figure 2.17: Comparison of values of C_{33}^{NC} vs V_g.

Likewise, the good agreement is found between the predictions of values of C_{13}^{NC} (or C_{23}^{NC}) by both the models, as shown in Fig. 2.18. The determined values of C_{23}^{NC} by the SOM approach are slightly lower than those predicted by the FE model and this indicate that the Poisson's effect in GRNC is correctly modelled by the latter. The elastic constants C_{13}^{NC} and C_{23}^{NC} represent the extension-extension coupling (i.e., Poisson's effect) which occurs between the different normal stress (σ_{33}) and normal strains (ε_{11} and ε_{22}), due to an application of load in the 3-direction and hence, the numerical estimates of C_{13}^{NC} and C_{23}^{NC} of GRNC are exactly same. Figure 2.19 shows the comparison of values of C_{44}^{NC} against v_g. The values of C_{44}^{NC} are purely based on the out-of-plane shear imposed to the RVE of GRNC. It can be noticed that the SOM model underestimates the values of C_{44}^{NC} compared to the FE model, particularly for higher values of v_g. It may be due to the fact that the square packing array of RVEs that possesses low transverse isotropy and in-plane behavior. The existing studies also reported the same trends of results (Pettermann and Suresh, 2000; Odegard, 2004). Their results reveal that the analytical estimations of only the axial shear modulus corresponding to the elastic behavior of composite can be altered compared to the experimental estimates.

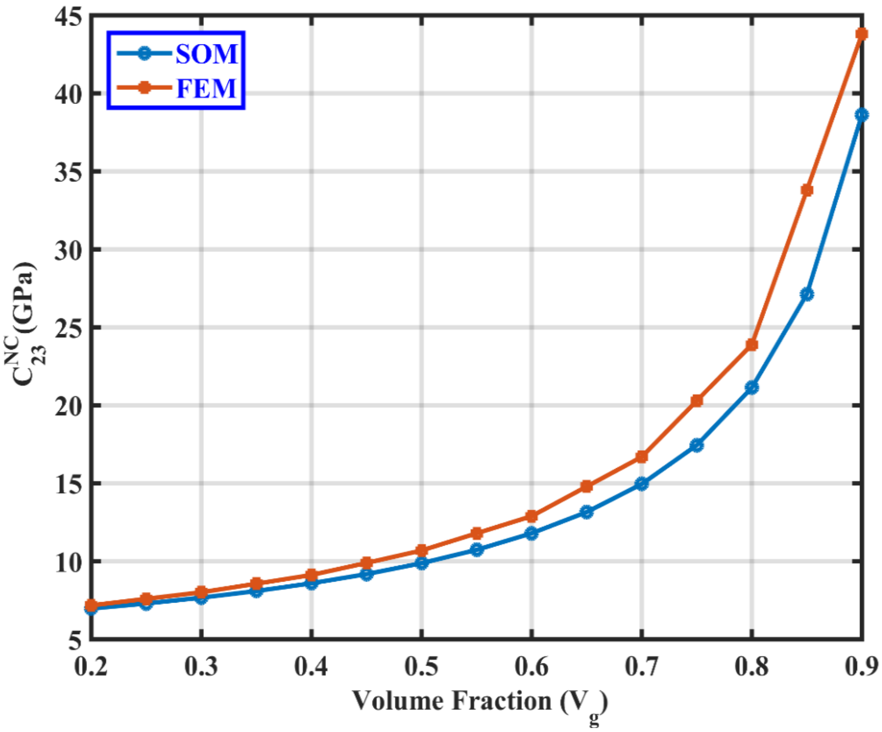

Figure 2.18: Comparison of values of C_{13}^{NC} (or C_{23}^{NC}) vs V_g.

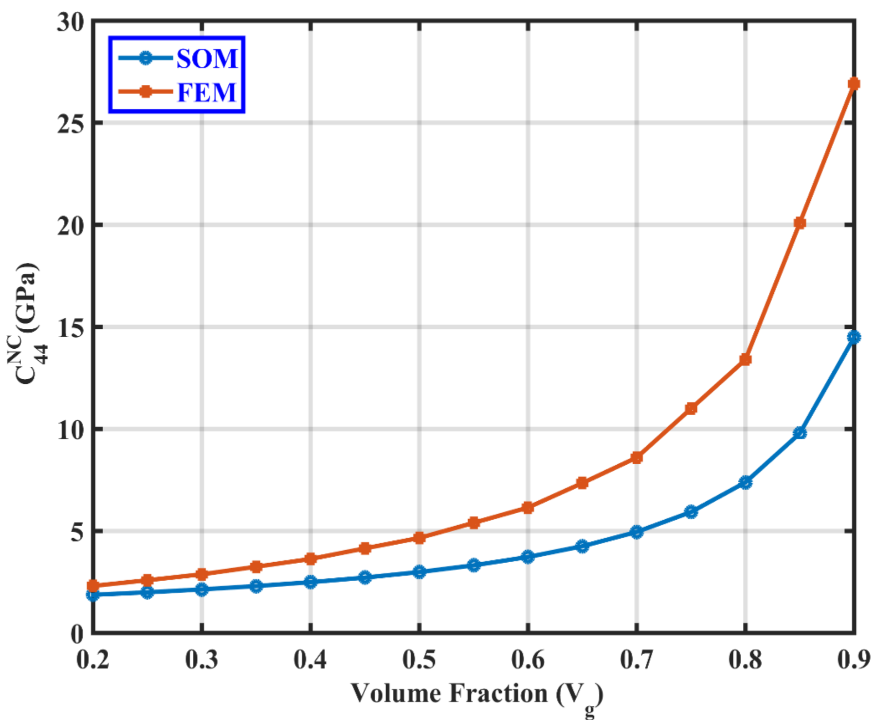

Figure 2.19: Comparison of values of C_{44}^{NC} vs V_g.

Figures 2.20–2.22 show the comparison of the effective piezoelectric and dielectric constants (e_{31}^{NC}, e_{33}^{NC} and $\in_{33}^{NC}$) of GRNC against the values of v_g. It is important to mention that the piezoelectric constants e_{31}^{NC} and e_{33}^{NC} indicate the normal stresses induced in the transverse and axial directions of reinforcement, respectively, due to the electric field applied along the 3–axis. It can be noticed from Fig. 2.20 that the values of e_{31}^{NC} increase with the values of v_g and the predictions by both the models agree well confirming the validity of assumptions adopted for developing SOM model. Note that the values of e_{32}^{NC} of the GRNC are found to be similar to that of e_{31}^{NC} as the axis of symmetry of GRNC coincides with the 3–direction. Likewise, the predictions of values of $\in_{33}^{NC}$ of GRNC by both the models are in excellent agreement, as shown in Fig. 2.22. Note that the estimations of values of e_{33}^{NC} and $\in_{33}^{NC}$ of GRNC, which vary linearly with the values of v_g, are corresponding to the Voigt-upper bound estimates. It is clearly seen from Fig. 2.21 that the predicted values of e_{33}^{NC} of GRNC are less than the values of e_{33}^{g} of graphene when its volume fraction surpasses a particular limit. This phenomenon is attributed to the effect of transverse stresses exerted by the matrix phase on the GRNC and the actual average electric field in graphene becomes equal to the applied electric field.

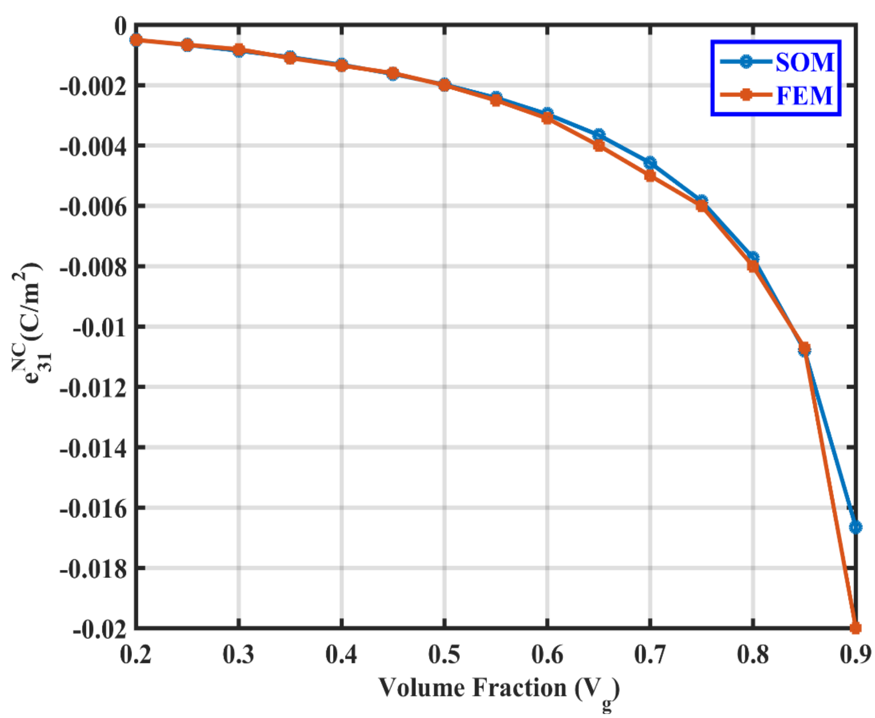

Figure 2.20: Comparison of values of e_{31}^{NC} vs V_g.

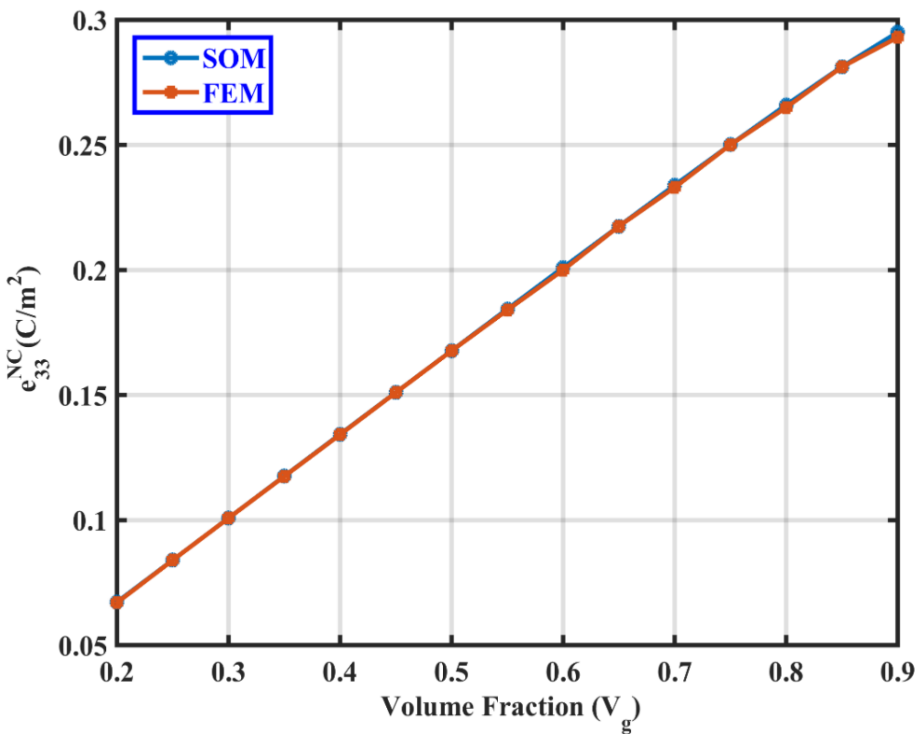

Figure 2.21: Comparison of values of e_{33}^{NC} vs V_g.

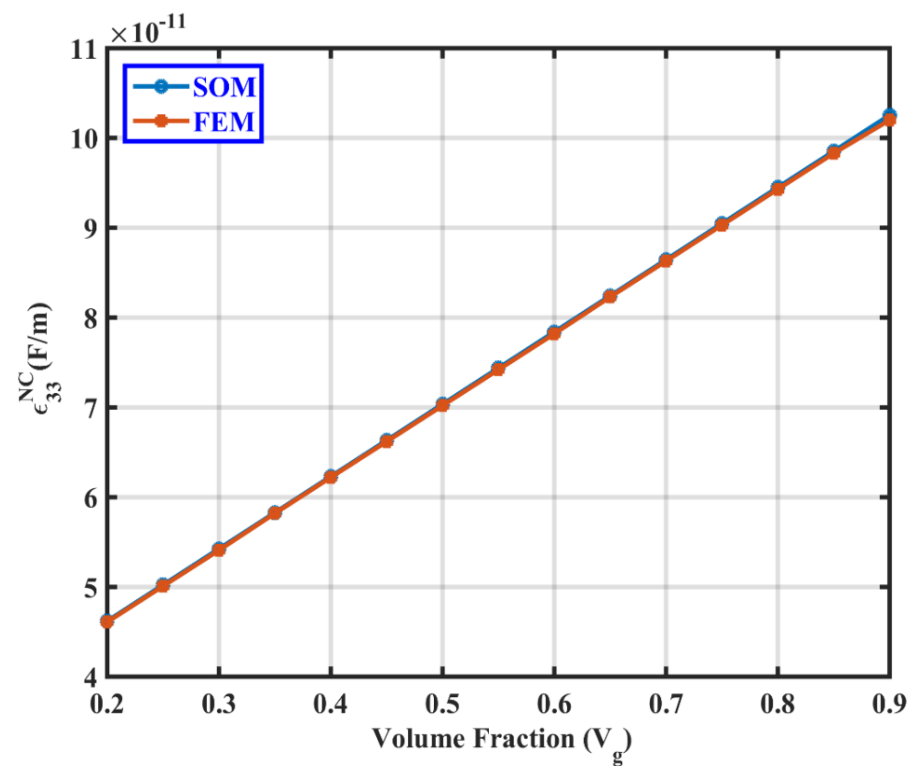

Figure 2.22: Comparison of values of $\in_{33}^{NC}$ vs V_g.

2.4.4 Comparisons of Results of MOM and FE Models for Alumina Matrix

In this sub-section, the numerical outcomes of the effective properties of GRNC determined by the MOM and FE models are discussed. The properties of the graphene and alumina are summarized in Table 2.2 and 2.5.

Table 2.5: Properties of alumina matrix.

Material	E (GPa)	μ	$\in_{33}$ (F/m)
Alumina	70 (Wang et al. 2011)	0.33 (Wang et al. 2011)	1.504×10^{-11} (Sundar et al. 2016)

We determined the effective properties of GRNC by considering the range of v_g from 0.2 to 0.7. Figure 2.23 illustrates the variation of the effective axial elastic coefficient (C_{33}^{NC}) of GRNC with the v_g. It may be observed that the value of C_{33}^{NC} increases almost linearly with v_g. Almost 100 % agreement between the two sets of values of C_{33}^{NC} determined by the MOM and FE models ensures the validity of assumptions and ROM for deriving the MOM model. Note that the coefficient C_{33}^{NC} was determined considering the iso-strain condition along the graphene direction and hence, such estimation belongs to the Voigt-upper bound. Figure 2.24 demonstrates the variation of coefficient C_{13}^{NC} with v_g. The MOM model overestimates the value of C_{13}^{NC} as compared to the FE estimates. This is attributed to the fact that the Poisson’s effect was modeled appropriately in the FE simulations. Figures 2.25 and 2.26 demonstrate the variation of coefficients C_{11}^{NC} and C_{12}^{NC} with the v_g. It may be observed from Figs. 2.25 and 2.26 that the MOM model overestimates the respective values of C_{11}^{NC} and C_{12}^{NC} over that of FE predictions, especially at larger value of v_g. This is due to the fact that the transverse elastic properties of composites are usually the function of properties of matrix and the predictions of both models are well agreed at lower v_g. As expected, the predictions by both models differ significantly as value of v_g increases. Figure 2.27 demonstrates the variation of coefficient C_{44}^{NC} with v_g. Once again, the MOM model overestimates the values of C_{44}^{NC} over that of FE predictions, especially at larger v_g.

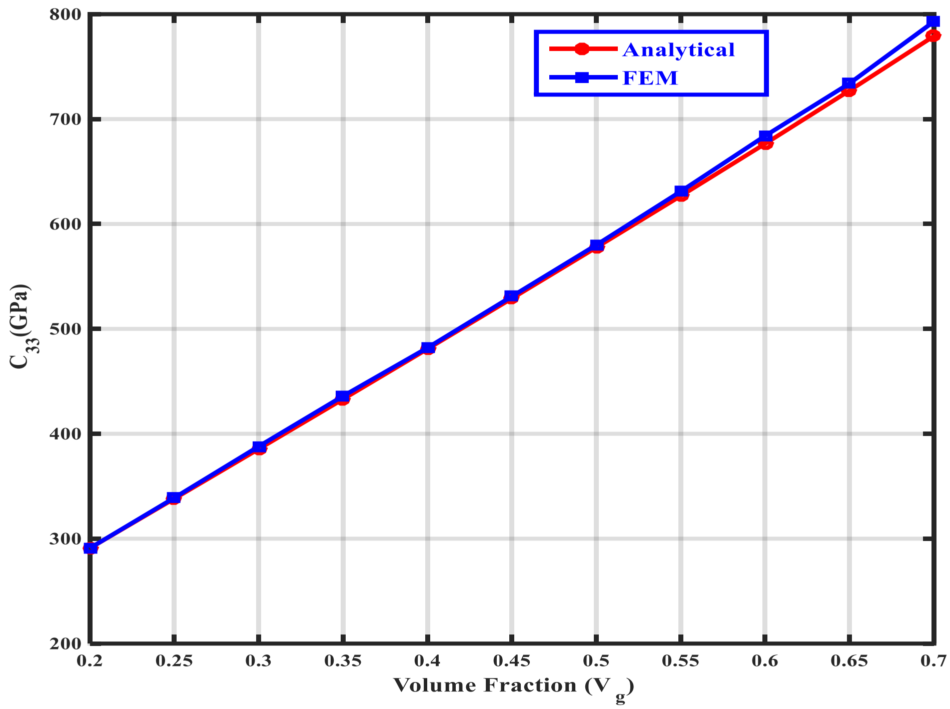

Figure 2.23: Variation of the effective elastic coefficient (C_{33}^{NC}) of GRNC with the graphene volume fraction (v_g).

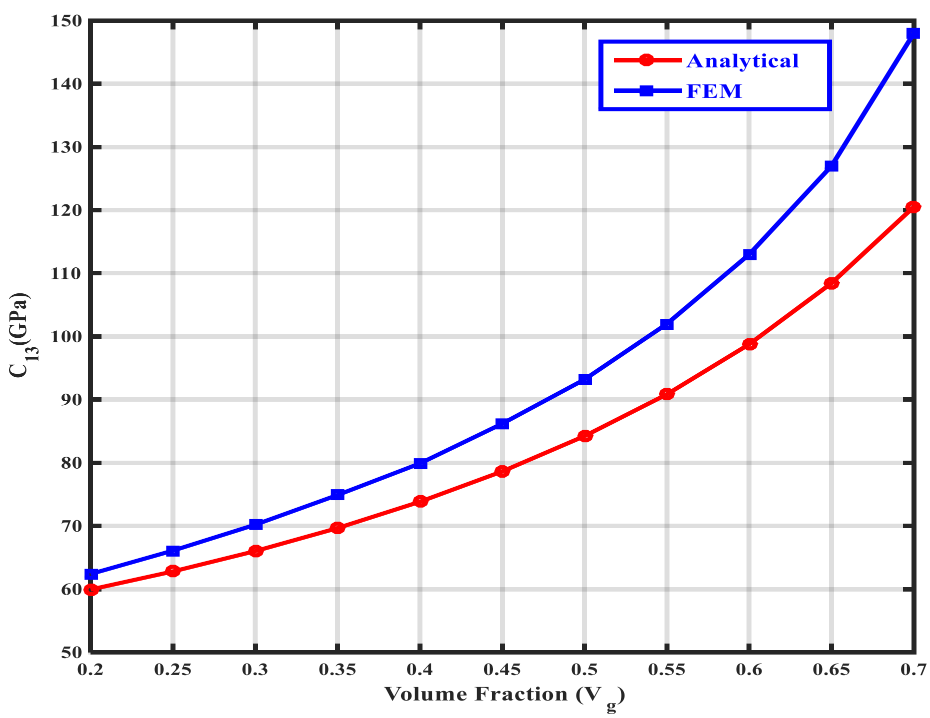

Figure 2.24: Variation of the effective elastic coefficient (C_{13}^{NC}) of GRNC with the graphene volume fraction (v_g).

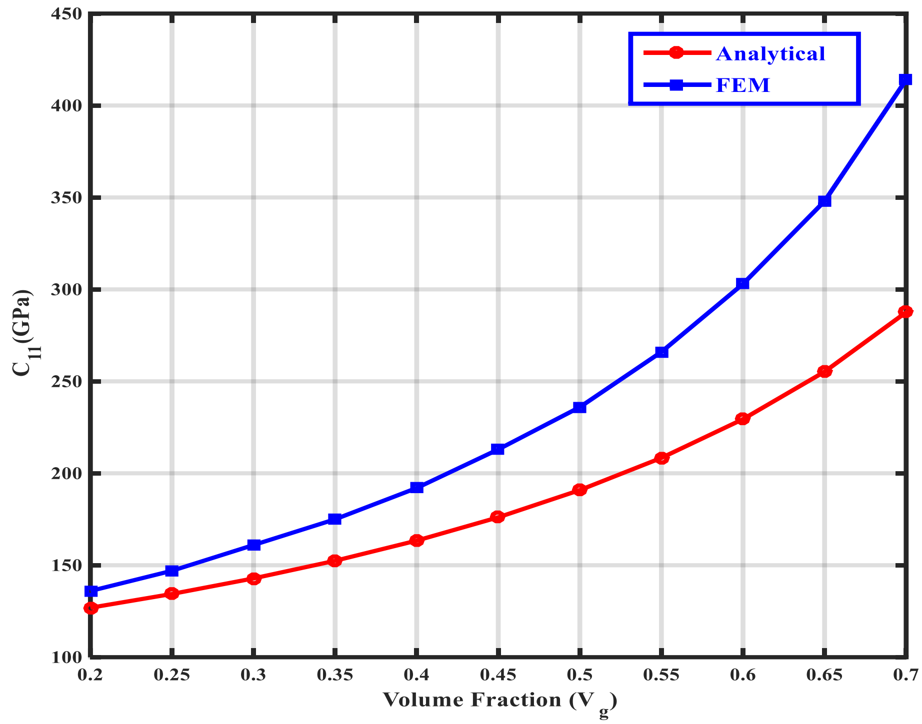

Figure 2.25: Variation of the effective elastic coefficient (C_{11}^{NC}) of GRNC with the graphene volume fraction (v_g).

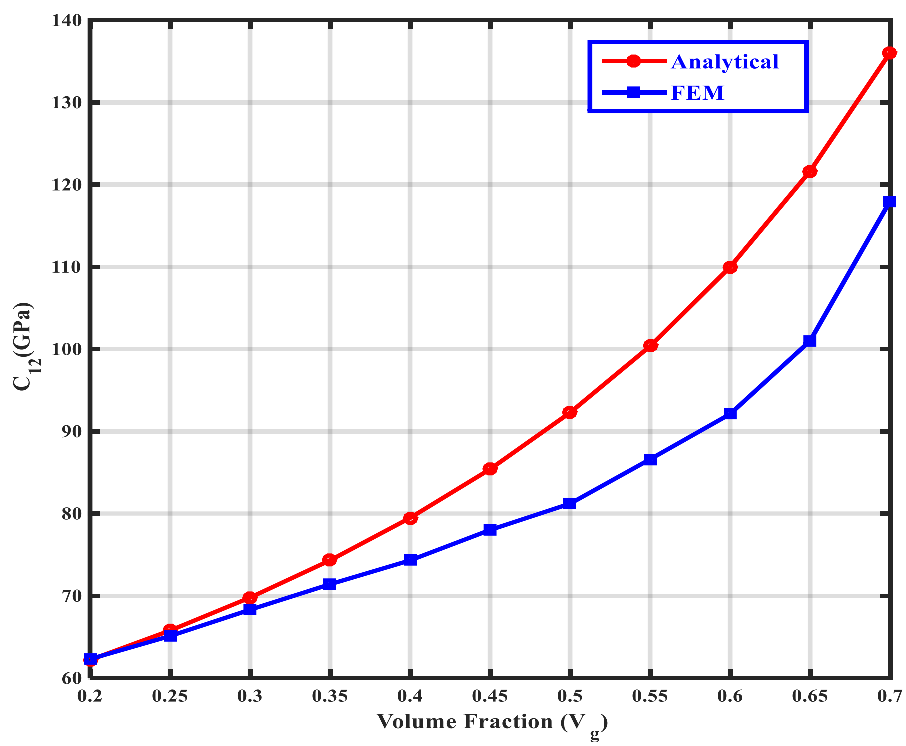

Figure 2.26: Variation of the effective elastic coefficient (C_{12}^{NC}) of GRNC with the graphene volume fraction (v_g).

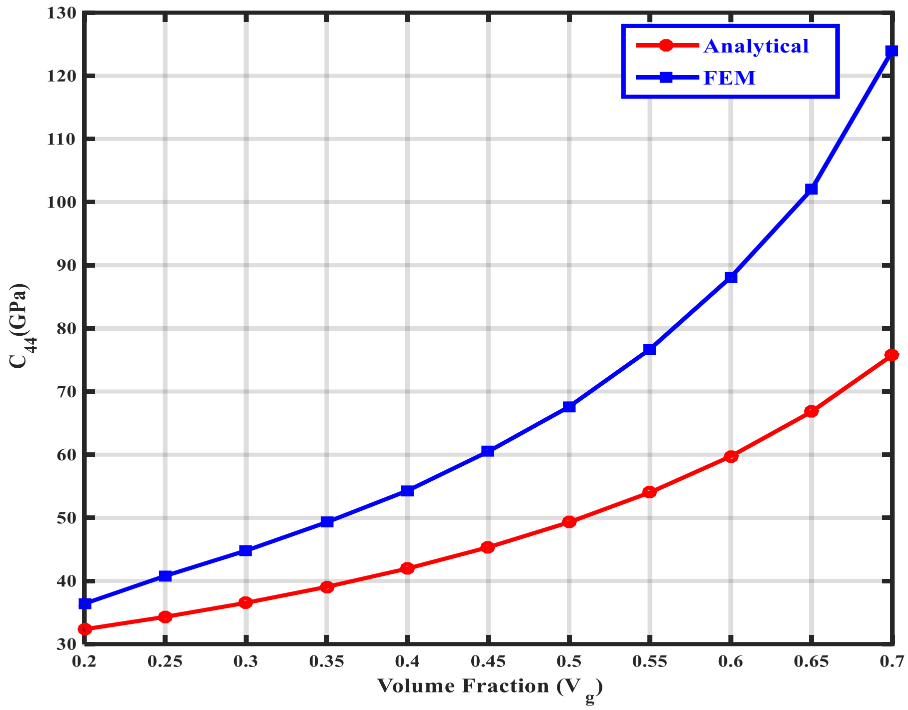

Figure 2.27: Variation of the effective elastic coefficient (C_{44}^{NC}) of GRNC with the graphene volume fraction (v_g).

Figures 2.28 and 2.29 demonstrate the variation of axial effective dielectric ($\in_{33}^{\mathrm{NC}}$) and piezoelectric coefficient (e_{33}^{NC}) with the v_g. Both figures reveal that the values of $\in_{33}^{\mathrm{NC}}$ and e_{33}^{NC} increased linearly as the value of v_g increases. Moreover, it may be observed from this comparison that the results are in excellent agreement validating the analytical micromechanics model used herein. This is attributed to the imposition of electric potential in the reinforcement direction. Figure 2.30 illustrates the variation of effective piezoelectric coefficient (e_{31}^{NC}) of GRNC with the v_g. It may be observed from this figure that the magnitude of e_{31}^{NC} increases with the v_g. Figure 2.30 clearly shows a good correlation between the analytical and FE predictions at a wide range of v_g. Figure 2.31 demonstrates the variation of coefficient e_{15}^{NC} with the graphene volume fraction. This figure shows that that the magnitude of e_{15}^{NC} increases with the value of v_g as found in case of e_{31}^{NC}. It may also be observed from Fig. 2.31 that the predictions of both models are well agreed at lower v_g. Compared to other piezoelectric coefficients, the predictions of e_{15}^{NC} are found to more sensitive to the larger volume fractions of graphene and this is attributed to the consideration of boundary conditions and in-plane behavior of GRNC; the same was attributed to the variation of values of C_{44}^{NC} as shown in Fig. 2.27.

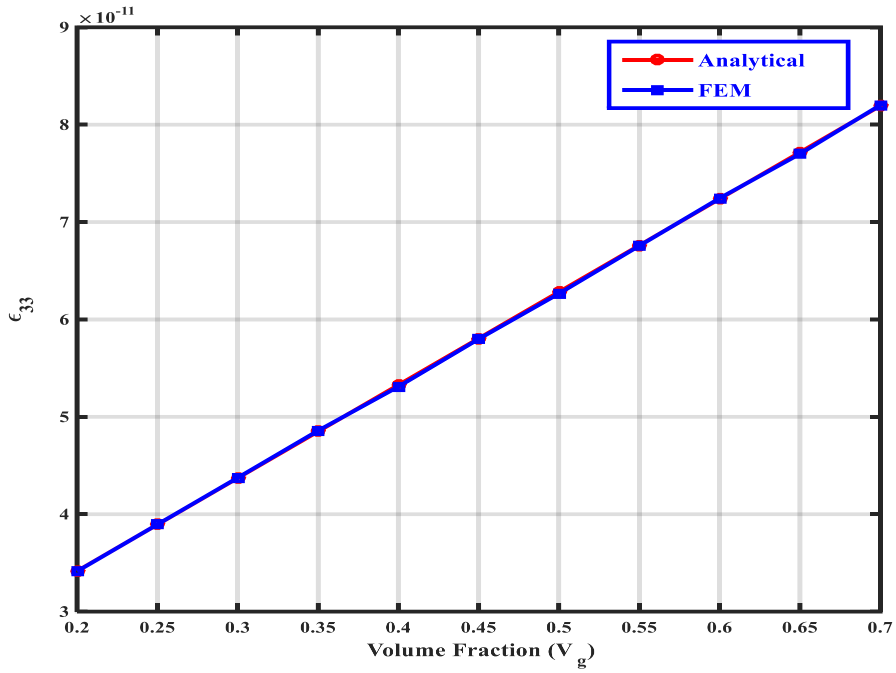

Figure 2.28: Variation of the effective dielectric coefficient ($\in_{33}^{NC}$) of GRNC with the graphene volume fraction (v_g).

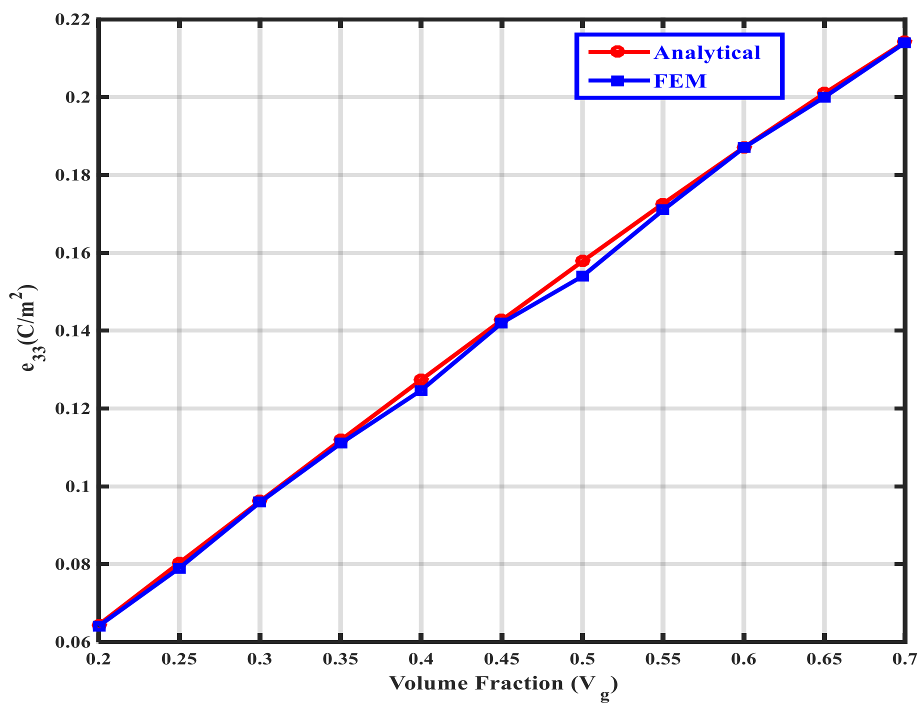

Figure 2.29: Variation of the effective piezoelectric coefficient (e_{33}^{NC}) of GRNC with the graphene volume fraction (v_g).

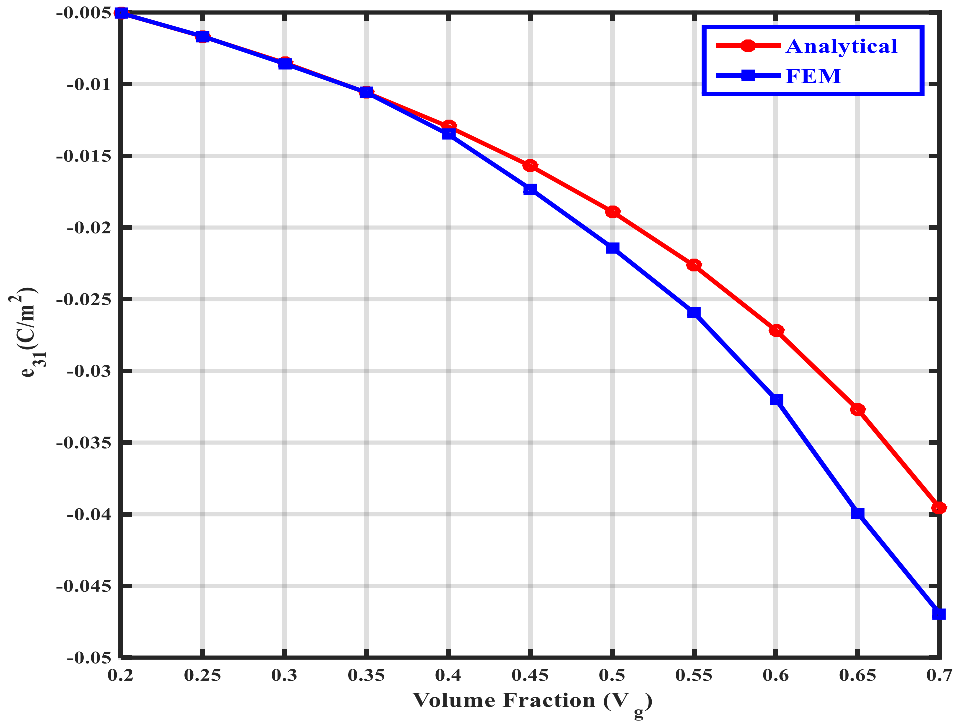

Figure 2.30: Variation of the effective piezoelectric coefficient (e_{31}^{NC}) of GRNC with the graphene volume fraction (v_g).

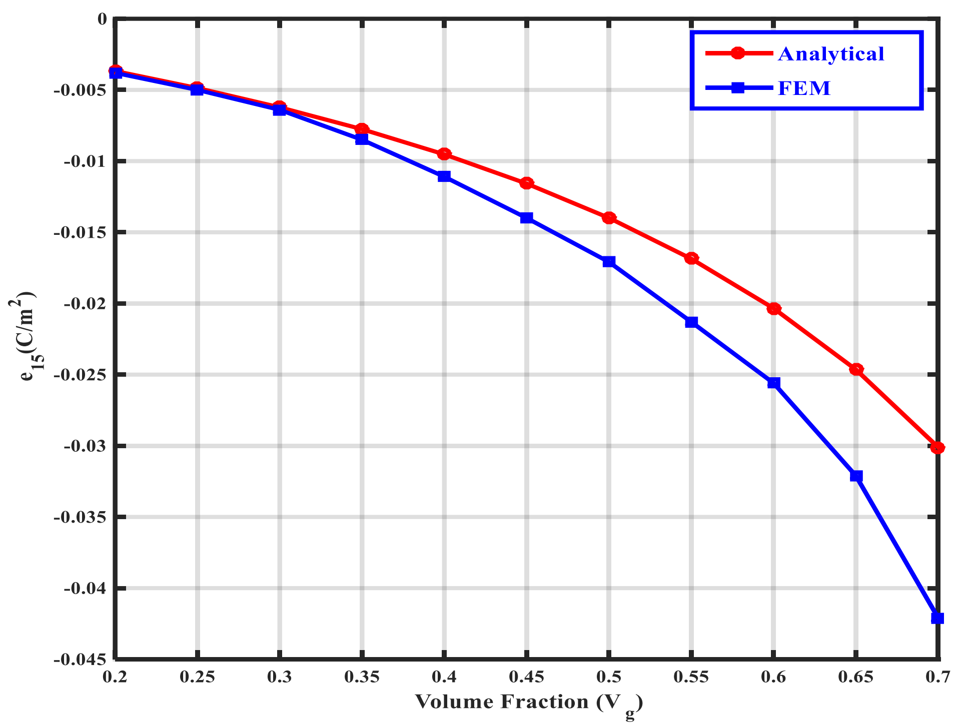

Figure 2.31: Variation of the effective piezoelectric coefficient (e_{15}^{NC}) of GRNC with the graphene volume fraction (v_g).

The comparisons shown in Figs. 2.10–2.31 conclude that the excellent agreement exists between the predictions by analytical and numerical micromechanics models for small volume fractions of graphene. The analytical micromechanics models require much less computational time than the FE model, and one may use the analytical micromechanical model for intuitive predictions of the effective elastic, piezoelectric and dielectric properties of any novel nanocomposites.

2.5 Conclusions

The elastic properties of pristine and defective graphene sheets were determined via molecular dynamics (MD) simulations and the obtained results are found in good agreement with the existing experimental and numerical results. The micromechanical and FE analysis of a novel graphene-reinforced nanocomposite (GRNC) composed of multilayers of piezoelectric graphene and polyimide/alumina matrix was carried out. The graphene reinforcements were incorporated and aligned in 1–3 plane into matrix. Two analytical models based on the micromechanics paradigm such as the mechanics of materials (MOM) and strength of materials (SOM) models as well as finite elements (FE) models were developed to predict the effective properties of GRNC. The MOM and SOM models were derived using the iso-field conditions and ROM. It is assumed that the graphene and polymer matrix are perfectly bonded, and the FE models were derived for validating the assumptions adopted in the analytical models. The developed analytical and numerical models envisage that the effective piezoelectric constants of GRNC account for the actuating capability in its transverse direction due to the applied electric field in the plane. The predictions of effective properties of GRNC by analytical and FE models are found to be in good agreement for the small volume fractions of graphene. If the loading is applied along the graphene reinforcement of GRNC then the effective constants C_{33}^{eff}, C_{13}^{eff}, e_{33}^{eff}, e_{31}^{eff} and $\in_{33}^{eff}$ show higher and reliable results by both the models. If the loading is applied in a transverse direction to the graphene reinforcement, results obtained results for C_{11}^{eff}, C_{12}^{eff}, C_{44}^{eff} and C_{66}^{eff} show the discrepancies between the predictions by both the models because these constants are influenced by in-plane behavior of composite and are matrix dependent.

The effective properties of GRNC obtained in this Chapter will be used for investigating the electromechanical response of GRNC structures in subsequent Chapters. The electromechanical behavior of GRNC nanobeam, considering the flexoelectric effect, is studied in the next Chapter.

Chapter 3

Electromechanical Behavior of Flexoelectric GRNC Beams

In this Chapter, the electromechanical behavior of GRNC beams with flexoelectric effect is investigated by deriving an analytical model based on Euler-Bernoulli theory. The effect of graphene volume fractions and flexoelectricity are taken into consideration for studying the electromechanical behavior of GRNC cantilever nanobeams.

3.1 Introduction

In recent years, beam and plate structural elements have fascinated a lot of interest in NEMS applications, and the former has great advantages over the latter due to its high sensitivity and linear behavior. In this Chapter, an analytical model based on the linear piezoelectricity and Euler-Bernoulli theory was also developed to investigate the electromechanical response of GRNC cantilever beam under both the electrical and mechanical loads accounting the flexoelectric effect. The electromechanical behavior of GRNC cantilever beam was studied to achieve the desired response via a number of ways such as by varying the volume fraction of graphene and application of electrical load.

3.2 Electromechanical response of GRNC Beams

In this Section, a mathematical model is derived to investigate the electromechanical response of GRNC nanobeams considering the flexoelectric effect. In recent advances, the tremendous research on nanocomposite structures has been carried out in the last decade with the aim of developing NEMS. Among all structural elements, piezoelectric cantilever beams have found many applications such as sensors, transducers and actuators in NEMS due to its linear behavior and high sensitivity. Therefore, here an attempt is made to show the electromechanical response of a cantilever beam made of

GRNC in which strain gradient was incorporated using its effective properties obtained in previous chapter. The generalized equation for the internal energy density function can be written as follows (Shen and Hu 2010):

$$U = \frac{1}{2}\beta_{kl}P_kP_l + \frac{1}{2}C_{ijkl}\varepsilon_{ij}\varepsilon_{kl} + d_{ijk}\varepsilon_{ij}P_k + f_{ijkl}u_{i,jk}P_l\,, \tag{3.1}$$

where P_i, u_i and ε_{ij} are the components of polarization, displacement and strain vectors, respectively; C_{ijkl} , d_{ijk} and β_{kl} are the fourth order elastic coefficient, third order piezoelectric coefficient and second order reciprocal dielectric susceptibility tensors, respectively; and f_{ijkl} is the fourth order flexoelectric coefficient tensor. The strain tensor is defined as:

$$\varepsilon_{ij} = \frac{1}{2}\left(\frac{\partial u_i}{\partial x_j} + \frac{\partial u_j}{\partial x_i}\right). \tag{3.2}$$

Then, the constitutive equations can be expressed as:

$$\sigma_{ij} = \frac{\partial U}{\partial \varepsilon_{ij}} = C_{ijkl}\varepsilon_{kl} + d_{ijk}P_k, \tag{3.3a}$$

$$\tau_{ijm} = \frac{\partial U}{\partial u_{i,jm}} = f_{ijmk}P_k, \tag{3.3b}$$

$$E_i = \frac{\partial U}{\partial P_i} = \beta_{ij}P_j + d_{jki}\varepsilon_{jk} + f_{jkli}u_{j,kl}, \tag{3.3c}$$

where σ_{ij}, E_i and τ_{ijm} are the Cauchy stress tensor, electric field and moment stress or the higher order stress, respectively. In higher order stress, τ_{ijm} is induced by the flexoelectric effect while it is not present in the classical theory of piezoelectricity. The various tensorial terms in Eq. (3.3) are given by

$$\begin{Bmatrix} \sigma_x \\ \sigma_y \\ \sigma_z \\ \sigma_{yz} \\ \sigma_{xz} \\ \sigma_{xy} \end{Bmatrix} = \begin{bmatrix} C_{11} & C_{12} & C_{13} & 0 & 0 & 0 \\ C_{12} & C_{22} & C_{23} & 0 & 0 & 0 \\ C_{13} & C_{23} & C_{33} & 0 & 0 & 0 \\ 0 & 0 & 0 & C_{44} & 0 & 0 \\ 0 & 0 & 0 & 0 & C_{55} & 0 \\ 0 & 0 & 0 & 0 & 0 & C_{66} \end{bmatrix} \begin{Bmatrix} \varepsilon_x \\ \varepsilon_y \\ \varepsilon_z \\ 2\varepsilon_{yz} \\ 2\varepsilon_{xz} \\ 2\varepsilon_{xy} \end{Bmatrix} + \begin{bmatrix} d_{11} & d_{21} & d_{31} \\ d_{12} & d_{22} & d_{32} \\ d_{13} & d_{23} & d_{33} \\ d_{14} & d_{24} & d_{34} \\ d_{15} & d_{25} & d_{35} \\ d_{16} & d_{26} & d_{36} \end{bmatrix} \begin{Bmatrix} P_x \\ P_y \\ P_z \end{Bmatrix}, \tag{3.3d}$$

$$\begin{Bmatrix} E_x \\ E_y \\ E_z \end{Bmatrix} = -\begin{bmatrix} d_{11} & d_{12} & d_{13} & d_{14} & d_{15} & d_{16} \\ d_{21} & d_{22} & d_{23} & d_{24} & d_{25} & d_{26} \\ d_{31} & d_{32} & d_{33} & d_{34} & d_{35} & d_{36} \end{bmatrix} \begin{Bmatrix} \varepsilon_x \\ \varepsilon_y \\ \varepsilon_z \\ 2\varepsilon_{yz} \\ 2\varepsilon_{xz} \\ 2\varepsilon_{xy} \end{Bmatrix} + \begin{bmatrix} \beta_{11} & 0 & 0 \\ 0 & \beta_{22} & 0 \\ 0 & 0 & \beta_{33} \end{bmatrix} \begin{Bmatrix} P_x \\ P_y \\ P_z \end{Bmatrix}. \tag{3.3e}$$

A schematic of GRNC cantilever beam is shown in Fig. 3.1 which has width b, length L and height h, referred to the Cartesian coordinate system x–z. A GRNC cantilever beam considered to be made of graphene and alumina matrix. The arrangement of graphene and alumina matrix layers can be varied to obtain a different volume fraction of graphene (40%, 60% and 80%) for the piezoelectric analysis. Here, the thickness of each single graphene layer was taken as 0.34 nm (Alian et al. 2015a,b, 2017; Kundalwal and Meguid 2017) and the number of graphene layers varied according to their volume fraction in the GRNC by keeping the interlayer distance as 0.34 nm.

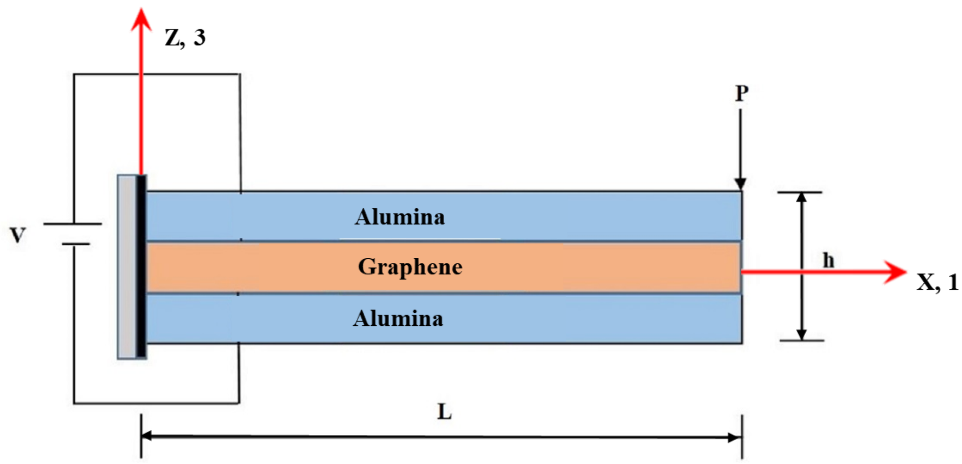

Figure 3.1: Schematic of GRNC cantilever beam.

A constant concentrated load is applied at the free end $(x = L)$ of a cantilever beam and a constant voltage V is applied at its upper and lower surfaces i.e., at $z = +\frac{h}{2}$ and $z = -\frac{h}{2}$, respectively. If the $w(x)$ is the transverse displacement of the beam then using Euler-Bernoulli hypotheses, the axial displacement at any point in it is given as (Yan and Jiang 2013):

$$u(x, z) = u_0(x) - z\frac{dw(x)}{dx}, \tag{3.4a}$$

where $u_0(x)$ is the axial displacement along the longitudinal axis of beam which may be introduced by mechanical and electric loads due to the electromechanical coupling or flexoelectric effect. Using Eq. (3.2), the non-zero strain can be written as:

$$\varepsilon_x = \frac{du_0}{dx} - z\frac{d^2w}{dx^2}. \tag{3.4b}$$

Here, the thickness of a cantilever beam is considered as very small as compared to its length ($h \ll L$). Hence, one can assume that the transverse displacement of a cantilever beam is greater as compared to its longitudinal displacement. Therefore, strain gradient $\varepsilon_{x,x} = \frac{d^2u_0}{dx^2} - z\frac{d^3w}{dx^3}$ can be omitted because it is negligible as compared to $\varepsilon_{x,z} = -\frac{d^2w}{dx^2}$. Note that the strain-gradient polarization from the cantilever beam can be obtained only by applying the transverse loading on it. Therefore, for further formulation, we considered the flexoelectric effect induced by this strain gradient $-\frac{d^2w}{dx^2}$.

The electric field (E_z), considering it to be only present in the z-direction, can be determined using Eqs. (3.3c) and (3.4a) as follows:

$$E_z = \beta_{33}P_z + d_{31}\varepsilon_x + f_{13}\varepsilon_{x,z}. \tag{3.5}$$

The extra term ($f_{13}\varepsilon_{x,z}$) in the above equation is different from the theory of linear piezoelectricity which contributes to the flexoelectric effect. For a complete formulation of the problem, in the absence of body charges, the Gauss' law is expressed as (Yan and Jiang, 2015):

$$-\epsilon_0\frac{\partial^2\emptyset}{\partial z^2} + \frac{\partial P_z}{\partial z} = 0, \tag{3.6a}$$

where $\epsilon_0 = 8.85 \times 10^{-12}$ C/Vm or F/m is the permittivity of free space or vacuum and $\emptyset$ is an external applied electric potential.

If beam is subjected to the external electric field along (z–direction) thickness, then the relation between electric potential ($\emptyset$) and electric field (E_z) is given by

$$E_z = -\emptyset_{,z} = -\frac{\partial\emptyset}{\partial z}. \tag{3.6b}$$

With consideration of the electric boundary condition $\emptyset\left(\frac{h}{2}\right) = V$ (volt) and $\emptyset\left(-\frac{h}{2}\right) = 0$, the polarization ($P_z$) and electric field ($E_z$) from Eqs. (3.5) and (3.6a) can be written in terms of u_0 and w, respectively, as follows:

$$P_z = \frac{\epsilon_0\, d_{31}}{\epsilon_0\, \beta_{33} + 1} z\frac{d^2w}{dx^2} - \frac{d_{31}}{\beta_{33}}\frac{du_0}{dx} + \frac{f_{13}}{\beta_{33}}\frac{d^2w}{dx^2} - \frac{V}{\beta_{33}h}, \tag{3.7a}$$

$$E_z = -\left(\frac{d_{31}}{\epsilon_0\, \beta_{33} + 1} z\frac{d^2w}{dx^2} + \frac{V}{h}\right), \tag{3.7b}$$

As the width and thickness of a cantilever beam are very small as compared to its length ($b = h \ll L$); therefore, it was considered as plane-stress problem ($\sigma_z = \sigma_{xz} = \sigma_{yz} = 0$) and due to very small width, σ_y can also be eliminated. Therefore, we considered only axial stress (σ_x) for the further analysis.

By substituting Eq. (3.7a) into Eq. (3.3a), the axial stress (σ_x) can be determined as:

$$\sigma_x = \left(C_{11} - \frac{d_{31}^2}{\beta_{33}}\right)\frac{du_0}{dx} - \left(C_{11} - \frac{\epsilon_0\, d_{31}^2}{\epsilon_0\, \beta_{33} + 1}\right) z\frac{d^2w}{dx^2} + \frac{d_{31}f_{13}}{\beta_{33}}\frac{d^2w}{dx^2} - \frac{d_{31}V}{\beta_{33}h}. \tag{3.8}$$

Using Eq. (3.8), the axial force (F_x) can be determined as follows:

$$F_x = \int_{-\frac{h}{2}}^{\frac{h}{2}} \sigma_x\, dz = bh\left[\left(C_{11} - \frac{d_{31}^2}{\beta_{33}}\right)\frac{du_0}{dx} + \frac{d_{31}f_{13}}{\beta_{33}}\frac{d^2w}{dx^2} - \frac{d_{31}V}{\beta_{33}h}\right]. \tag{3.9}$$

It is observed from Eqs. (3.8) and (3.9) that the axial force (F_x) is developed in the beam due to the strain, and electromechanical coupling exists between the strain gradient and applied electric loading. But in case of the cantilever beam which is not subjected to any mechanical load in axial direction, this force is obvious zero due to traction free condition. Therefore, Eq. (3.9) can be rewritten as:

$$bh\left[\left(C_{11} - \frac{d_{31}^2}{\beta_{33}}\right)\frac{du_0}{dx} + \frac{d_{31}f_{13}}{\beta_{33}}\frac{d^2w}{dx^2} - \frac{d_{31}V}{\beta_{33}h}\right] = 0, \tag{3.10a}$$

$$-\left(C_{11} - \frac{d_{31}^2}{\beta_{33}}\right)\frac{du_0}{dx} = \frac{d_{31}f_{13}}{\beta_{33}}\frac{d^2w}{dx^2} - \frac{d_{31}V}{\beta_{33}h}\,. \tag{3.10b}$$

Because of the absence of external body forces and mechanical loads in the axial direction, the relaxation strain in the cantilever beam is present which plays an important role in its softer and stiffer behavior. The relaxation strain can be defined as:

$$\frac{du_0}{dx} = \frac{\left(\frac{d_{31}f_{13}}{\beta_{33}}\frac{d^2w}{dx^2} - \frac{d_{31}V}{\beta_{33}h}\right)}{-\left(C_{11} - \frac{d_{31}^2}{\beta_{33}}\right)}. \tag{3.11}$$

The governing equation of piezoelectric nanobeams including the effect of flexoelectricity is obtained using the energy method. Using Eqs. (3.3a–3.3c), the internal energy density function (Eq. 1) can be reduced to:

$$U = \frac{1}{2}\left(\sigma_x \varepsilon_x + \tau_{xxz}\varepsilon_{x,z} + E_z P_z\right). \tag{3.12a}$$

From Eqs. (3.3b) and (3.7a), we can write expression for τ_{xxz} as follows:

$$\tau_{xxz} = \left[\left(\frac{\epsilon_0\ d_{31} f_{13}}{\epsilon_0\ \beta_{33}+1} z + \frac{f_{13}^2}{\beta_{33}}\right)\frac{d^2 w}{dx^2} - \frac{d_{31} f_{13}}{\beta_{33}}\frac{du_0}{dx} - \frac{V f_{13}}{\beta_{33} h}\right]. \tag{3.12b}$$

Next, the variational principle can be formulated over the entire volume (Ω) of GRNC piezoelectric beam and can be written as (Mindlin 1968):

$$-\delta \int_{\Omega} H d\Omega + \delta W = 0, \tag{3.13a}$$

where the relationship between the internal energy and electric enthalpy density functions can be defined as (Shen and Hu 2010):

$$H = U - \frac{1}{2} \epsilon_0\ \emptyset_{,z}\emptyset_{,z} + \emptyset_{,z} P_z. \tag{3.13b}$$

For cantilever beam, W is the work done by resultant axial force.

Subsequently, the governing equations of GRNC piezoelectric cantilever beam can be obtained as follows:

$$\left(C_{11} - \frac{d_{31}^2}{\beta_{33}}\right) bh \frac{d^2 u_0}{dx^2} + \left(\frac{d_{31} f_{13} bh}{\beta_{33}}\right)\frac{d^3 w}{dx^3} = 0\,, \tag{3.14a}$$

$$\left(\left(C_{11} - \frac{\epsilon_0\ d_{31}^2}{\epsilon_0\ \beta_{33}+1}\right)\frac{bh^3}{12} - \frac{f_{13}^2 bh}{\beta_{33}}\right)\frac{d^4 w}{dx^4} + \left(\frac{d_{31} f_{13} bh}{\beta_{33}}\right)\frac{d^3 u_0}{dx^3} = 0. \tag{3.14b}$$

For the cantilever beam, the transverse displacement (w) and slope $\left(\frac{dw}{dx}\right)$ can be obtained using the following boundary conditions:

$$w = \frac{dw}{dx} = 0 \text{ at } x = 0. \tag{3.15}$$

The moment and force at x = L become:

$$\left(\left(C_{11} - \frac{\epsilon_0\ d_{31}^2}{\epsilon_0\ \beta_{33}+1}\right)\frac{bh^3}{12} - \frac{f_{13}^2 bh}{\beta_{33}}\right)\frac{d^2 w}{dx^2} + \left(\frac{d_{31} f_{13} bh}{\beta_{33}}\right)\frac{du_0}{dx} + \frac{f_{13} Vb}{\beta_{33}} = 0, \tag{3.16a}$$

$$-\left(\left(C_{11} - \frac{\epsilon_0\ d_{31}^2}{\epsilon_0\ \beta_{33}+1}\right)\frac{bh^3}{12} - \frac{f_{13}^2 bh}{\beta_{33}}\right)\frac{d^3 w}{dx^3} - \left(\frac{d_{31} f_{13} bh}{\beta_{33}}\right)\frac{d^2 u_0}{dx^2} + F = 0. \tag{3.16b}$$

where the first terms in above equations are the effective bending rigidity considering the flexoelectric effect. Substituting the boundary conditions $(0 \leq x \leq L)$ in governing Eqs. (3.16a) and (3.16b) of GRNC cantilever beam, the transverse deflection can be obtained as follows:

$$w_{cantilever} = \frac{Px^2}{6(EI)_{cantilever}}(x - 3L) - \frac{C_{11} f_{13} V b x^2}{2(\beta_{33} C_{11} - d_{31}^2)(EI)_{cantilever}}, \quad (3.17a)$$

where

$$(EI)_{cantilever} = \left(C_{11} - \frac{\epsilon_0\, d_{31}^2}{\epsilon_0\, \beta_{33} + 1}\right)\frac{bh^3}{12} - \frac{f_{13}^2 bh}{\beta_{33}} - \frac{d_{31}^2 f_{13}^2 bh}{\beta_{33}(\beta_{33} C_{11} - d_{31}^2)},$$

$$(EI)_{cantilever} \cong \left(C_{11} - \frac{\epsilon_0\, d_{31}^2}{\epsilon_0\, \beta_{33} + 1}\right)\frac{bh^3}{12} - \frac{f_{13}^2 bh}{\beta_{33}}.$$

In absence of flexoelectricity effect $(f_{13} = 0)$, Eq. (3.17a) gets reduced to

$$w_{cantilever} = \frac{Px^2}{6(EI)_{cantilever}}(x - 3L). \quad (3.17b)$$

3.3 Results and Discussions

The properties predicted by the analytical (MOM) approaches were considered for investigating the effect of flexoelectricity on the electromechanical response of GRNC cantilever beam.

3.3.1 Electromechanical Behavior of GRNC Beams

In this sub-section, the electromechanical behavior of GRNC cantilever nanobeams, accounting the flexoelectric effect, subjected to the electrical and mechanical loadings is studied. A concentrated force P = 1nN was applied at the end of GRNC beam having width, $b = h$, length, $l = 20h$ and $f_{13} = 5V$. To investigate the effect of flexoelectricity on the electromechanical response of GRNC beam, three discrete values of graphene volume fractions (v_g) are considered as 0.4, 0.6 and 0.8, and the electrical potentials are considered as –1V, –5V, and –10V. Figures 3.2–3.4 illustrate the effect of flexoelectricity on the GRNC beam for different graphene volume fractions and electric potentials. In our simulations, negative electric potential was applied over the surface of GRNC beam. These results reveal that the effective bending rigidity of GRNC beams with consideration of the flexoelectricity $(f_{13} \neq 0)$ is higher than that of neglecting flexoelectric effect (f_{13} = 0). Conversely, as positive electric potential (+V) was applied to the beam, the softer elastic behavior exhibited by it when the effect of flexoelectricity (f_{13}) was taken into account; then, induced inhomogeneous boundary conditions to the bending behavior of GRNC beam were found exactly opposite to its effective bending rigidity. Inhomogeneous boundary condition is nothing but the addition of positive and negative relaxation moments according to the applied negative and positive electric potentials, respectively. Thus, it can be concluded that the stiffer and softer elastic behavior of GRNC cantilever beam can be altered by varying electric potential ($\pm$V) and it may find wide applications in NEMS. It may be observed from Figs. 3.2–3.4 that the responses of GRNC beams improve as the values of volume fraction of graphene and applied electrical potential are increased. This is attributed to the fact that the flexoelectric effect enhances as the applied electrical potential increases. From the above discussion, it may be observed that the deflections of GRNC beams remarkably influenced by the electromechanical loadings and strain gradients effects.

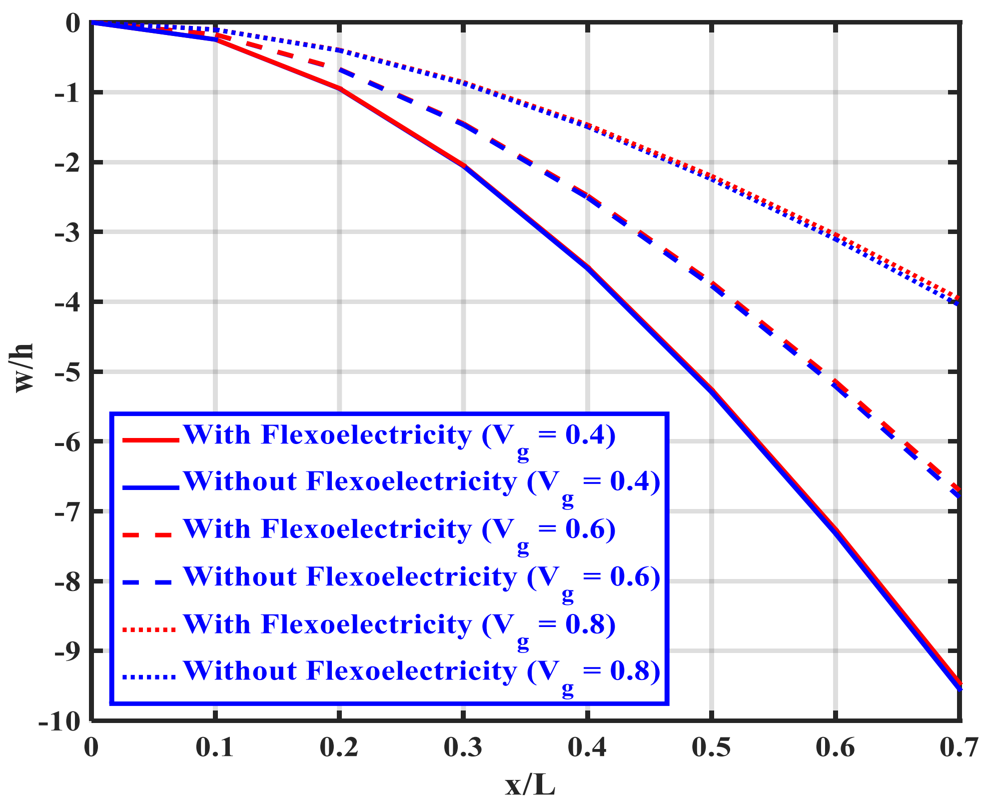

Figure 3.2: Deflection of GRNC cantilever beam along its length with different graphene volume fractions at V = –1V.

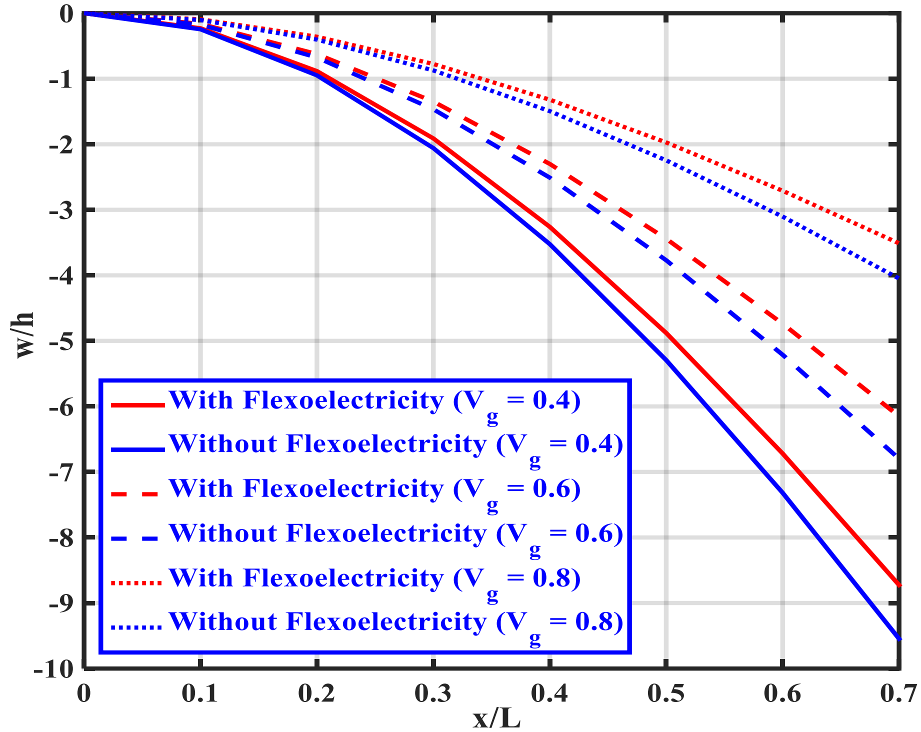

Figure 3.3: Deflection of GRNC cantilever beam along its length with different graphene volume fractions at V = –5V.

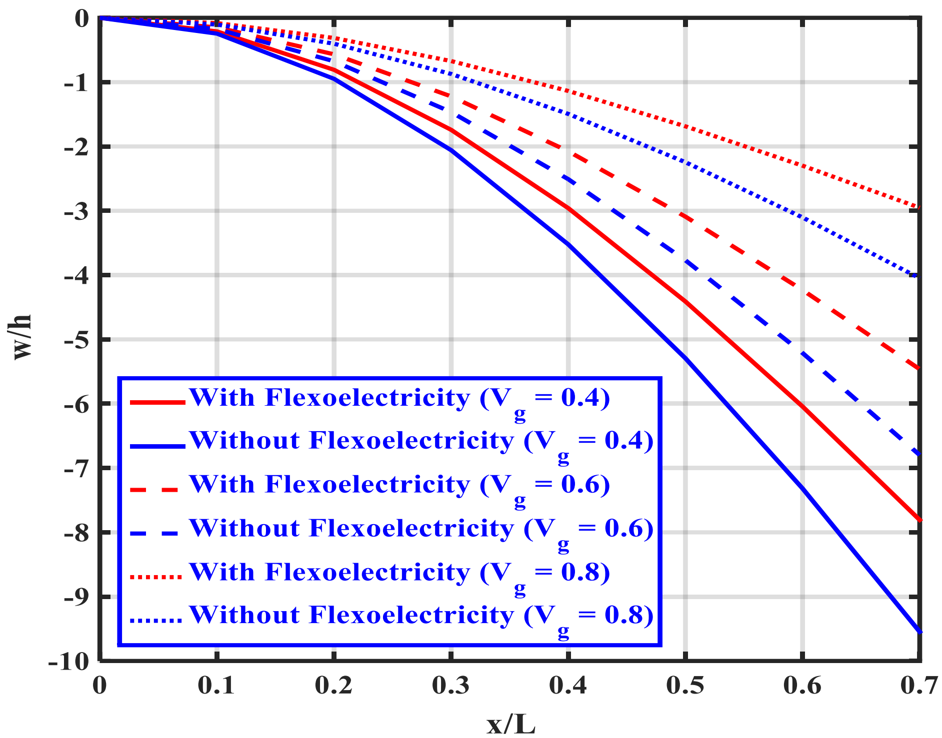

Figure 3.4: Deflection of GRNC cantilever beam along its length with different graphene volume fractions at V = –10V.

3.4 Conclusions

First, the MOM and FE models were developed to predict the effective properties of alumina-based GRNC. Second, the determined effective properties were used to a case study of a cantilever nanobeam made of GRNC for investigating its electromechanical response. For this purpose, an analytical beam model was derived using the extended linear piezoelectricity and Euler-Bernoulli theory incorporating the flexoelectricity effect. Specific attention was given to investigate the effect of graphene volume fraction and electrical loads. Our results demonstrate that the flexoelectricity significantly influences the electromechanical response of GRNC beams with a mere use of 40 % volume fraction of graphene. It is revealed that the electromechanical response of GRNC beam is improved with the increase in the graphene volume fraction and it can be tuned via applying different electric potentials. The current results are significant, which revealed that the flexoelectric phenomenon in graphene induced due to the strain gradient can be exploited to form next generation NEMS for various applications such as sensors, actuators, switches and smart electronics.

At this juncture, it is important to mention that the surface effect was not considered for studying the electromechanical behavior of GRNC nanobeams in this Chapter. Therefore, the electromechanical behavior of GRNC nanobeams, considering both the flexoelectric and surface effects, is studied in the next Chapter by developing analytical and FE models.

Chapter 4

Electromechanical Behavior of GRNC Beams Accounting Flexoelectric and Surface Effects

In this Chapter, the electromechanical behavior of GRNC beams with flexoelectric and surface effects are investigated using size-dependent Euler-Bernoulli theory, linear piezoelectricity and Galerkin's weighted residual method. Analytical and FE models are developed to study the static response of GRNC nanobeams with various boundary conditions: cantilever, simply-supported and clamped-clamped. The effective properties of GRNC obtained in Chapter 2 are utilized.

4.1 Introduction

The review of literature presented in Chapter 1 reveals that the size-dependent flexoelectricity phenomenon attracted a lot of research interest in NEMS applications. In recent years, apart from flexoelectricity, it is broadly acknowledged that the surface conditioned contributions exist at a nanoscale level in various solid nanomaterials. Therefore, surface effects can contribute extensively to the electromechanical response when the size of the structure scaled down. Piezoelectric nanobeam is basic building block of the NEMS applications and it is essential to study its electromechanical response subjected to the different loading and boundary conditions. The electromechanical behavior of a novel GRNC nanobeam considering flexoelectric effect was investigated in the previous Chapter. However, the electromechanical behavior of GRNC nanobeams considering both the flexoelectric and surface effects is yet to be studied. In this Chapter, apart from the flexoelectric effect, the surface effects such as the surface stress as well as surface modulus and piezoelectricity were considered for studying the electromechanical behavior of GRNC nanobeams. Specifically, this Chapter is concerned with the development of an analytical model based on Euler-Bernoulli beam theory for the GRNC nanobeam to study its electromechanical response considering different boundary conditions: cantilever, simply-supported and clamped-clamped. FE models are also developed based on Galerkin's weighted residual method for validating the analytical results. The effects of flexoelectricity and surface parameters on the electromechanical coupling (EMC) coefficient of nanobeams are also investigated.

4.2 Beam Formulation

In this Section, a mathematical model is derived to investigate the electromechanical response of GRNC nanobeams. The electric Gibbs free internal energy density function can be divided into two categories: (i) for bulk material and (ii) considering the surface effect. Assuming infinitesimal deformation, the electric Gibbs free internal energy density function for bulk material (U) can be expressed as follows (Abdollahi et al., 2014):

$$U = -\frac{1}{2}\in_{ij} E_i E_j + \frac{1}{2}C_{ijkl}\varepsilon_{ij}\varepsilon_{kl} - e_{ijk}E_i\varepsilon_{jk} - \mu_{ijkl}E_i\eta_{jkl}$$
$$+r_{ijklm}\varepsilon_{ij}\eta_{klm} + \frac{1}{2}g_{ijklmn}\eta_{ijk}\eta_{lmn}\,, \tag{4.1}$$

where $\in_{ij}$ is the second order dielectric permittivity tensor, C_{ijkl} is the fourth order elastic tensor, e_{ijk} is the third order piezoelectric tensor and μ_{ijkl} is the fourth order flexoelectric tensor. r_{ijklm} indicates the strain and strain gradient coupling tensor and g_{ijklmn} is related to the pure nonlocal elastic strain gradient terms. For simplicity, the terms r_{ijklm} and g_{ijklmn} with higher order gradients are neglected.

The strain (ε_{ij}), strain gradient ($\eta_{ij,k}$) and electric field (E_i) components can be expressed as:

$$\varepsilon_{ij}=\frac{1}{2}\left(\frac{\partial u_i}{\partial x_j}+\frac{\partial u_j}{\partial x_i}\right). \tag{4.2a}$$

To simplify Eq. (4.2a), one can write

$$\varepsilon_{ij} = \frac{1}{2}\left(u_{j,i} + u_{i,j}\right), \tag{4.2b}$$

$$\eta_{ij,k} = \varepsilon_{ij,k} = \frac{1}{2}\left(u_{j,ik} + u_{i,jk}\right), \text{and} \tag{4.2c}$$

$$E_i = -\emptyset_{,i}\ , \tag{4.2d}$$

in which u_i and $\emptyset$ are the components of displacement vector and electric potential, respectively. Thus, the constitutive relations for the material subjected to the small deformation can be written as:

$$\sigma_{ij} = \frac{\partial U}{\partial \varepsilon_{ij}} = C_{ijkl}\,\varepsilon_{kl} - e_{kij}\,E_k, \tag{4.3a}$$

$$\tau_{jkl} = \frac{\partial U}{\partial \eta_{jkl}} = -\,\mu_{ijkl}E_i\ , \text{ and} \tag{4.3b}$$

$$D_i = -\frac{\partial U}{\partial E_i} = \epsilon_{ij}\,E_j + e_{ijk}\varepsilon_{jk} + \mu_{ijkl}\eta_{jkl}\ . \tag{4.3c}$$

By using Eqs. (4.3a – 4.3c) into Eq. (4.1), we can rewrite the expression for bulk material as follows:

$$\delta U = \frac{1}{2}\sigma_{ij}\delta\varepsilon_{ij} + \frac{1}{2}\tau_{ijk}\delta\eta_{ij,k} - \frac{1}{2}D_i\delta E_i\ , \tag{4.3d}$$

in which σ_{ij} is the stress tensor, ε_{ij} is the strain tensor, τ_{ijk} is the higher order stress gradient tensor, $\eta_{ij,k}$ is the higher order strain gradient tensor and D_i is the electric displacement vector. At the surface for the piezoelectric body with surface effects, the internal energy density function becomes:

$$\delta U_s = \frac{1}{2}\sigma^{o}_{\alpha\beta}\delta\varepsilon^{s}_{\alpha\beta} + \frac{1}{2}\sigma^{s}_{\alpha\beta}\delta\varepsilon^{s}_{\alpha\beta} - \frac{1}{2}D^{s}_{\gamma}\delta E^{s}_{\gamma}\ , \tag{4.4}$$

where $\sigma^{o}_{\alpha\beta}$ indicates the second order surface stress tensor, $\sigma^{s}_{\alpha\beta}$ denotes the surface moment stress, D^{s}_{γ} indicates the surface electric displacement, E^{s}_{γ} and $\varepsilon^{s}_{\alpha\beta}$ denote the electric field and surface strain, respectively, and they can be obtained as:

$$\varepsilon^{s}_{\alpha\beta} = \frac{1}{2}\left(u^{s}_{\alpha,\beta} + u^{s}_{\beta,\alpha}\right), \text{and} \tag{4.5}$$

$$E^{s}_{\gamma} = -\emptyset^{s}, \gamma, \tag{4.6}$$

in which u^{s} and $\emptyset^{s}$ indicate the surface displacement and surface electric potential vectors, respectively.

The constitutive relationships for the surface (with superscript 's') are almost the same as that of constitutive relations for bulk material but some residual terms are also present.

From Eq. (4.4), the linear constitutive equations can be determined considering the surface effects as:

$$\sigma^{s}_{\alpha\beta} = \frac{\partial U_s}{\partial \varepsilon^{s}_{\alpha\beta}} = \tau_{\alpha\beta} + C^{s}_{\alpha\beta\gamma k}\varepsilon^{s}_{\gamma k} - e^{s}_{k\alpha\beta}E^{s}_{k}\text{, and} \tag{4.7}$$

$$D^{s}_{\gamma} = -\frac{\partial U_s}{\partial E^{s}_{\gamma}} = \epsilon^{s}_{\gamma k}\, E^{s}_{k} + e^{s}_{\gamma k\beta}\varepsilon^{s}_{\alpha\beta}. \tag{4.8}$$

The axial load in the beam (see Fig. 4.1) does not exist and the displacement fields using Euler–Bernoulli beam theory can be written as:

$$u(x) = \varepsilon_x = -z\,\frac{dw(x)}{dx} = -zw'(x). \tag{4.9}$$

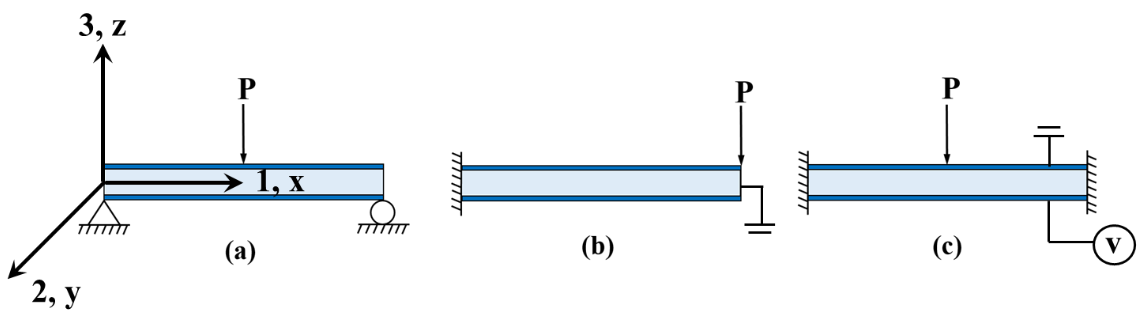

Figure 4.1: Nanobeams under point load with different boundary conditions: (a) simply-supported, (b) cantilever with open circuit and (c) clamped-clamped with short circuit.

The horizontal and vertical deformations of the beam are denoted by $u(x)$ and $w(x)$, respectively. Using Eqs. (4.2) and (4.9), the nonzero strain and strain-gradients are obtained as:

$$\varepsilon_{xx} = -z\,\frac{d^2w}{dx^2} = -zw''; \; \eta_{xxx} = -z\,\frac{d^3w}{dx^3} = -zw'''; \; \eta_{zxx} = -\frac{d^2w}{dx^2} = -w''. \tag{4.10}$$

Note that the principal material and problem coordinate systems are aligned with each other and the sub-indices x, y and z in Eq. (4.10) indicate the local deformation of a beam in the respective 1, 2 and 3 directions. Making use of Eqs. (4.3a – 4.3c) and (4.10) into Eq. (4.3d), the bulk internal energy density function can be re-expressed as:

$$\delta U = \int_{\Omega} (\sigma_{xx}\delta\varepsilon_{xx} + \tau_{zxx}\delta\eta_{zxx} + \tau_{xxx}\delta\eta_{xxx})d\Omega$$

$$= -\int_0^L M\delta w''dx - \int_0^L M_h\delta w'''dx - \int_0^L P\delta w''dx, \qquad (4.11a)$$

in which

$$M = \int_A \sigma_{xx} z dA \; ; \; F = \int_A \tau_{zxx} dA \; ; \text{ and } M_h = \int_A \tau_{xxx} z dA, \qquad (4.11b)$$

where $\int_A dA$ indicates the integration over the whole area 'A' in case of bulk material. Similarly, making the use of Eqs. (4.5 – 4.10) into Eq. (4.4), surface internal energy density function is given by

$$\delta U_s = \int_a \frac{d\sigma_{xx}^s}{dx} z\delta w' \, da - \int_{z=\frac{h}{2}} (\sigma_{xx}^s k)^u \delta w \, da + \int_{z=\frac{-h}{2}} (\sigma_{xx}^s k)^l \delta w da$$

$$= \int_0^L \frac{dM_s}{dx} \delta w' dx - \int_0^L T_z^s \delta w dx, \qquad (4.12a)$$

where $\int_a da$ indicates the integration over the small infinitesimal surface area 'a'.

By using Eq. (4.7), the axial surface stress σ_{xx}^s can be expressed as:

$$\sigma_{xx}^s = \tau_0 + C_{11}^s \varepsilon_x^s - e_{31}^s E_z^s \, . \qquad (4.12b)$$

By using Eq. (4.9) for surface effect, σ_{xx}^s can be rewritten as:

$$\sigma_{xx}^s = \tau_0 + C_{11}^s \left(-z\frac{d^2w}{dx^2}\right) - e_{31}^s E_z^s, \qquad (4.12c)$$

in which τ_0 is the constant residual surface stress.

The surface bending moment (M_s) and lateral loadings (T_z^s) can be expressed as:

$$M_s = \int_c \sigma_{xx}^s z \, dC \, ; \; T_z^s = \int_{z=\frac{h}{2}} (\sigma_{xx}^s k)^u \, da - \int_{z=\frac{-h}{2}} (\sigma_{xx}^s k)^l \, da, \qquad (4.12d)$$

where C is the beam cross-sectional perimeter, h denotes height and superscripts 'u' and 'l' represent the top and bottom surfaces of the beam, respectively; and $k = \frac{d^2w}{dx^2}$ is the curvature and it can be determined by using the Euler-Bernoulli theory.

If the beam is subjected to uniform transverse load $q(x)$, end force Q, and end moment $\widetilde{M}$, the virtual work done induced due to the external forces is obtained as:

$$\delta W \;=\; \int_0^L q(x)\delta w dx + Q\delta w + \widetilde{M}\delta w' \;. \tag{4.13}$$

By using Eqs. (4.11– 4.13), the principle of virtual displacement is obtained as:

$$\delta W - (\delta U + \;\delta U_s) = \int_0^L q(x)\delta w dx + \; Q\delta w \;+\; \widetilde{M}\delta w' -$$

$$\left(\int_0^L M\delta w''\,dx + \int_0^L M_h\delta w'''dx + \int_0^L P\delta w''\,dx + \int_0^L \frac{dM_s}{dx}\delta w' dx - \int_0^L T_z^s\delta w dx\right), \tag{4.14}$$

By applying integration by-parts, Eq. (4.14) is re-expressed as:

$$\delta W - (\delta U + \;\delta U_s)$$
$$= M_h\delta w''\,\Big|_0^L + Q\delta w + \widetilde{M}\delta w' - \left(\frac{dM}{dx} + \frac{dF}{dx} - \frac{d^2M_h}{dx^2} + \frac{dM_s}{dx}\right)\delta w\,\Big|_0^L +$$

$$\int_0^L\left(\frac{d^2M}{dx^2} + \frac{d^2F}{dx^2} - \frac{d^3M_h}{dx^3} + \frac{d^2M_s}{dx^2} + q(x) + T_z^s\right)\delta w dx + \left(M + F - \frac{dM_h}{dx}\right)\delta w'\,\Big|_0^L. \tag{4.15}$$

Due to the arbitrariness of δw, the governing equation can be developed from Eq. (4.15) as follows:

$$\frac{d^2M}{dx^2} + \;\frac{d^2F}{dx^2} - \;\frac{d^3M_h}{dx^3} + \;\frac{d^2M_s}{dx^2} + q(x) + T_z^s \,=\, 0. \tag{4.16}$$

Using the boundary conditions given below at the ends of a beam (x = 0 and L):

$$M_h \quad \text{or} \quad \frac{d^2w(x)}{dx^2},$$
$$\left(M + F - \frac{dM_h}{dx}\right) \qquad \text{or} \;\frac{dw(x)}{dx},$$
$$\frac{d}{dx}\left(M + F - \;\frac{dM_h}{dx} + \;M_s\right) \quad \text{or} \quad w(x). \tag{4.17a}$$

For example, if cantilever beam subjected to end point load (P) then corresponding boundary conditions are written as follows (x = 0 and L):

At x = 0,

$$w(0) = w'(0) = 0$$
$$M_h = 0$$

At x = L,

$$M_h = 0$$

$$M(L) = M + F - \frac{dM_h}{dx} = 0,$$

$$Q(L) = \frac{dM}{dx} + \frac{dF}{dx} - \frac{d^2M_h}{dx^2} + \frac{dM_s}{dx} = -P\,. \tag{4.17b}$$

where M is the classical bending moment, F is the higher order axial couple, M_h is the higher order bending moment and M_s is the bending moment in case of stress effect.

In the open circuit condition (Fig. 4.1b), electric displacement on the surface should be zero ($D_z \to 0$). Therefore, using the constitutive Eqs. (4.3b and 4.8), the electric field can be derived as:

$$E_z = -\frac{e_{31}}{\epsilon_{33}}\varepsilon_{xx} - \frac{\mu_{31}}{\epsilon_{33}}\eta_{zxx}. \tag{4.18}$$

By using Eqs. (4.3), (4.10) and (4.18) into Eq. (4.11b), the following relation can be obtained:

$$M = -\left(C_{11} + \frac{e_{31}^2}{\epsilon_{33}}\right)I_y w''\,, \tag{4.19}$$

$$F = -\left(\frac{\mu_{31}^2}{\epsilon_{33}}\right)w''A\,, \tag{4.20}$$

in which A and I_y indicate the area of cross-section and moment of inertia of the beam, respectively.

Similarly, Eq. (4.12b) may be rewritten as:

$$M_s = -\left(C_{11}^s + e_{31}^s\frac{e_{31}}{\epsilon_{33}}\right)I^* w'', \tag{4.21a}$$

where I^* is the perimeter moment of inertia.

For a beam having rectangular cross-section with height h and width b, the relation for I^* is given by Liu and Rajapakse (2010):

$$I^* = \frac{h^3}{6} + \frac{bh^2}{2}\,. \tag{4.21b}$$

On the upper and lower surfaces of the beam, the curvatures have the equivalent magnitudes but reverse directions. Hence, by ignoring nonlinear effect caused due to term ($e_{31}^{s}E_{z}^{s}$) in Eq. (4.12c), the lateral loading (T_{z}^{s}) can be again reformulated as:

$$T_{z}^{s} = \int_{z=\frac{H}{2}} (\sigma_{xx}^{s}k)^{u}da - \int_{z=\frac{-H}{2}} (\sigma_{xx}^{s}k)^{l}da = S^{*}\tau_{0}\frac{d^{2}w}{dx^{2}}, \tag{4.22}$$

in which $S^{*} = 2b$.

Making the use of Eq. (4.16), the governing equation considering the flexoelectric and surface effects can be obtained as:

$$(EI)^{eff}\frac{d^{4}w}{dx^{4}} = S^{*}\tau_{0}\frac{d^{2}w}{dx^{2}} - q(x), \tag{4.23}$$

in which

$$(EI)^{eff} = \left(C_{11} + \frac{e_{31}^{2}}{\epsilon_{33}}\right)I + \left(\frac{\mu_{31}^{2}}{\epsilon_{33}}\right)A + \left(C_{11}^{s} + \frac{e_{31}^{s}e_{31}}{\epsilon_{33}}\right)I^{*}. \tag{4.24}$$

4.2.1 Static Loading on Beams

For obtaining the results in terms of nondimensional quantities, $\bar{x} = x/L$ and $\bar{w} = w/L$, Eq. (4.23) can be re-written as follows:

$$\frac{d^{4}\bar{w}}{d\bar{x}^{4}} - \Gamma\frac{d^{2}\bar{w}}{d\bar{x}^{2}} + \frac{q\,L^{3}}{(EI)^{eff}} = 0\,, \tag{4.25}$$

where $\Gamma = \frac{S^{*}\tau_{0}L^{2}}{(EI)^{eff}}$.

For obtaining the general solution, Eq. (4.25) is further simplified for a uniformly distributed load (q_{0}) as follows:

$$\bar{w} = C_{1}e^{\bar{x}\sqrt{\Gamma}} + C_{2}e^{-\bar{x}\sqrt{\Gamma}} + C_{3} + C_{4}\bar{x} + \frac{q_{0}L^{3}}{2\Gamma(EI)^{eff}}\bar{x}^{2}, \tag{4.26}$$

where C_1 to C_4 are the arbitrary constants to be determined by using the boundary conditions. In case of a cantilever beam subjected to an end-point load P (Fig. 4.1b), the necessary boundary conditions $\bar{w}(0) = \bar{w}'(0) = M(1) = 0, Q(1) = -P$ and $q_{0} = 0$ are used in Eq. (4.26). Subsequently, the constants C_1 to C_4 can be determined as follows:

$$C_1 = \frac{PL^2}{(EI)^{eff}\Gamma^{\frac{3}{2}}\left(e^{2\sqrt{\Gamma}}+1\right)};\ C_2 = -\frac{PL^2\ e^{2\sqrt{\Gamma}}}{(EI)^{eff}\Gamma^{\frac{3}{2}}\left(e^{2\sqrt{\Gamma}}+1\right)};$$

$$C_3 = \frac{PL^2\ \left(e^{2\sqrt{\Gamma}}-1\right)}{(EI)^{eff}\Gamma^{\frac{3}{2}}\left(e^{2\sqrt{\Gamma}}+1\right)};\ \text{and } C_4 = -\frac{PL^2}{(EI)^{eff}\Gamma}\,. \tag{4.27}$$

In case of a simply-supported beam subjected to midpoint load P (Fig. 4.1a), the unknown constants are determined using the following boundary conditions $\overline{w}(0) = \overline{w}'(1/2) = M(0) = 0, Q(1/2) = -P/2$ and $q_0 = 0$ in Eq. (4.26) as follows:

$$C_1 = \frac{PL^2}{2(EI)^{eff}\Gamma^{\frac{3}{2}}\left(e^{\sqrt{\Gamma}/2}+e^{-\sqrt{\Gamma}/2}\right)};\ C_2 = -\frac{PL^2}{2(EI)^{eff}\Gamma^{\frac{3}{2}}\left(e^{\sqrt{\Gamma}/2}+e^{-\sqrt{\Gamma}/2}\right)};$$

$$C_3 = 0;\ \text{and } C_4 = -\frac{PL^2}{2(EI)^{eff}\Gamma}\,. \tag{4.28}$$

In case of a clamped-clamped beam subjected to midpoint load P (Fig. 4.1c), the necessary boundary conditions are $\overline{w}(0) = \overline{w}'(0) = \overline{w}'(1/2) = 0, Q(1/2) = -P/2$ and $q_0 = 0$, and we can obtain the constants using Eq. (4.26) as follows:

$$C_1 = \frac{PL^2\ e^{-\sqrt{\Gamma}/2}}{2(EI)^{eff}\Gamma^{\frac{3}{2}}\left(e^{-\sqrt{\Gamma}/2}+1\right)};\ C_2 = -\frac{PL^2}{2(EI)^{eff}\Gamma^{\frac{3}{2}}\left(e^{-\sqrt{\Gamma}/2}+1\right)};$$

$$C_3 = \frac{PL^2\ \left(1-e^{-\sqrt{\Gamma}/2}\right)}{2(EI)^{eff}\Gamma^{\frac{3}{2}}\left(e^{-\sqrt{\Gamma}/2}+1\right)};\quad \text{and } C_4 = -\frac{PL^2}{2(EI)^{eff}\Gamma}. \tag{4.29}$$

4.2.2 Determination of Effective EMC Coefficient

The actuation and sensing performance of the beam primarily depends on the effective electromechanical coupling (EMC) coefficient. Particularly, the EMC coefficient is used in various applications such as enhancement of active control authority, vibration control, piezoelectric energy harvesting and detection of crack (Davis and Lesieutre, 1995; Kim et al., 2005; Beeby et al., 2006; Anton and Sodano, 2007). If we consider piezoelectric structures subjected to mechanical loading then the deformation throughout them may not be homogeneous. Thus, both open- and short-circuit energies (total internal energy) must be calculated using the integration over the volume of the piezoelectric structures. The homogeneous properties through the piezoelectric structure is only valid under the assumption of electric field ($E_z \to 0$) and electric displacement ($D_z \to 0$) can be set to zero through the whole piezoelectric structure. This condition is achieved due to open- and short-circuit configurations. Hence, by considering the homogeneous deformation throughout the piezoelectric structure, EMC can be defined as (Trindade and Benjeddou, 2009):

$$\mathrm{EMC} = \left(\frac{\text{electrical energy stored in the volume of a piezoelectric structure}}{\text{total mechanical strain energy supplied to the body}}\right)^{1/2}. \quad (4.30)$$

The total internal energy U can be written as:

$$U = \frac{1}{2}\int_{\Omega} (\sigma_{xx}\varepsilon_{xx} + \tau_{zxx}\eta_{zxx} + \tau_{xxx}\eta_{xxx})\, d\Omega + \frac{1}{2}\int_{a} (\sigma_{xx}^{s}\varepsilon_{xx})\, da. \quad (4.31)$$

where ‘Ω’ and ‘a’ denote the entire volume and surface area of the beam, respectively.

In the open circuit condition (Fig. 4.1b), electric displacement on the surface should be zero ($D_z \to 0$). With the help of constitutive relations for both surface and bulk effects, the total internal energy stored in the structure (U_{oc}) can be obtained as (Yan and Jiang, 2011):

$$U_{oc} = \frac{1}{2}\left(C_{11} + \frac{e_{31}^2}{\epsilon_{33}}\right)\int_A z^2\, dA \int_0^L \left(\frac{d^2w(x)}{dx^2}\right)^2 dx + \frac{1}{2}\left(\frac{\mu_{31}^2}{\epsilon_{33}}\right)\int_A dA \int_0^L \left(\frac{d^2w(x)}{dx^2}\right)^2 dx$$
$$+ \frac{1}{2}\left(C_{11}^s + e_{31}^s\frac{e_{31}}{\epsilon_{33}}\right)\int_s z^2\, ds \int_0^L \left(\frac{d^2w(x)}{dx^2}\right)^2 dx\ , \quad (4.32a)$$

$$U_{oc} = \frac{1}{2}\left[\left(C_{11} + \frac{e_{31}^2}{\epsilon_{33}}\right)\left(\frac{bh^3}{12}\right) + \left(C_{11}^s + e_{31}^s\frac{e_{31}}{\epsilon_{33}}\right)\left(\frac{h^3}{6} + \frac{bh^2}{2}\right) + \left(\frac{\mu_{31}^2}{\epsilon_{33}}\right)bh\right]$$
$$\int_0^L \left(\frac{d^2w(x)}{dx^2}\right)^2 dx\,. \quad (4.32b)$$

In short circuit condition (Fig. 4.1c), an electric field is zero ($E_z \to 0$). Similar to the open circuit condition, the total internal energy can be determined as:

$$U_{sc} = \frac{1}{2}\left[(C_{11})\left(\frac{bh^3}{12}\right) + (C_{11}^s)\left(\frac{h^3}{6} + \frac{bh^2}{2}\right)\right]\int_0^L \left(\frac{d^2w(x)}{dx^2}\right)^2 dx\,. \qquad (4.33)$$

The EMC coefficient can be determined using the same nonuniform strain ε_{xx} condition as follows (Trindade and Benjeddou, 2009):

$$(\xi^{eff})^2 = \frac{U_{oc} - U_{sc}}{U_{oc}} = \{e_{311}^2 bh^2 + e_{31}^s e_{31}(2h^2 + 6bh) + 12\mu_{31}^2 b\}$$
$$\{(C_{11} \in_{33} + e_{31}^2)bh^2 + (C_{11}^s \in_{33} + e_{31}^s e_{31})(2h^2 + 6bh) + 12\mu_{31}^2 b\}^{-1}\,. \qquad (4.34)$$

From Eq. (4.34) it can be revealed that the EMC coefficient is size-dependent when the flexoelectric and surface effects are taken into account. If the flexoelectricity is ignored $(\mu_{31} \to 0)$, the above expression for EMC coefficient, considering bulk and surface effects is reduced to:

$$\xi_2^{eff} = \sqrt{\frac{e_{31}^2 bh + e_{31}^s e_{31}(2h + 6b)}{(C_{11} \in_{33} + e_{31}^2)bh + (C_{11}^s \in_{33} + e_{31}^s e_{31})(2h + 6b)}}\,. \qquad (4.35)$$

If both the flexoelectric and surface effects are eliminated $(\mu_{31}, e_{31}^s, C_{11}^s \to 0)$, the above equation is deduced to the EMC coefficient of bulk piezoelectric materials (ξ_0^{eff}) as follows:

$$\xi_0^{eff} = \sqrt{\frac{e_{31}^2}{(C_{11} \in_{33} + e_{31}^2)}}\,. \qquad (4.36)$$

4.2.3 FE Formulation of Beam

In this, FE model of the GRNC beam subjected to the distributed load is developed, accounting both the flexoelectric and surface effects. Considering no axial force acting along the length of a beam and neglecting inertial terms, Eq. (4.23) can be rewritten as:

$$(EI)^{eff}\frac{d^4w}{dx^4} - (\tau_0 s^*)\frac{d^2w}{dx^2} + q(x) = 0. \qquad (4.37)$$

Using Galerkin's weighted residual method for the formulation of FE procedure, Eq. (4.37) can be reformulated as:

$$\Psi = \int_0^{l_e} \left\{ (EI)^{eff} \frac{d^4w}{dx^4} - (\tau_0 s^*) \frac{d^2w}{dx^2} + q(x) \right\} \bar{v} dx = 0. \qquad (4.38)$$

$\bar{v}$ is the weight function and l_e is the length of a beam. By applying the integration by parts, the Eq. (4.38) can be written in a weak form as follows:

$$\Psi = \int_0^{l_e} \left\{ (EI)^{eff} \frac{d^2w}{dx^2} \frac{d^2\bar{v}}{dx^2} + (\tau_0 s^*) \frac{dw}{dx} \frac{d\bar{v}}{dx} + q\bar{v} \right\} dx + \left(M \frac{d\bar{v}}{dx} - Q\bar{v} \right) \Bigg|_0^{l_e} = 0, \qquad (4.39)$$

in which the bending moment (M) and shear force (Q) can be written as:

$$M = -(EI)^{eff} \left(\frac{d^2w}{dx^2} \right) ; \; Q = -(EI)^{eff} \left(\frac{d^3w}{dx^3} \right) + (\tau_0 s^*) \frac{dw}{dx}.$$

Substituting the values of M and Q in Eq. (4.39), we can rewrite:

$$\Psi = \int_0^{l_e} \left\{ (EI)^{eff} \frac{d^2w}{dx^2} \frac{d^2\bar{v}}{dx^2} + (\tau_0 s^*) \frac{dw}{dx} \frac{d\bar{v}}{dx} + q\bar{v} \right\} dx$$

$$- \left\{ (EI)^{eff} \frac{d^2w}{dx^2} \frac{\partial\bar{v}}{\partial x} - (EI)^{eff} \left(\frac{d^3w}{dx^3} \right) \bar{v} + (\tau_0 s^*) \frac{dw}{dx} \bar{v} \right\} \Bigg|_0^{l_e} = 0 . \qquad (4.40)$$

Figure 4.2 demonstrates the two noded beam element considering the surface layer with two degrees of freedom (i.e., translational (w) and rotational (φ)) at every single node.

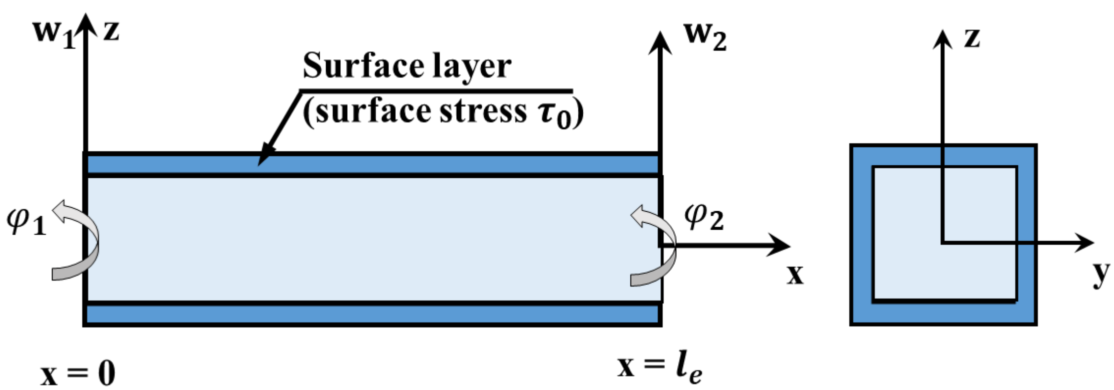

Figure 4.2: Beam element with two nodes.

Consequently, the nodal displacement vector is written as follows:

$$w^e = [w_1 \quad \varphi_1 \quad w_2 \quad \varphi_2]'\,. \tag{4.41}$$

The vertical displacement of a beam can be interpolated by using the shape function $N_i(x)$ as follows:

$$w = \sum N_i w^e{}_i\ , \qquad i = 1, 2, 3, 4. \tag{4.42}$$

N_1, N_2, N_3 and N_4 are termed as the shape functions or cubic interpolation functions for a beam element. For the beam element, $N_1 = 1$ and 0 when calculated at nodes 1 and 2, respectively. A term N_2 is related to φ_1 and we have $\frac{dN_2}{dx} = 1$ when calculated at node 1. Similarly, shape functions N_3 and N_4 have equivalent results for node 2. Using above analogy, all the shape functions can be written as:

$$N_1(x) = 1 - \frac{3x^2}{{l_e}^2} + \frac{2x^3}{{l_e}^3}\ ; N_2(x) = x - \frac{2x^2}{l_e} + \frac{x^3}{{l_e}^2},$$

$$N_3(x) = \frac{3x^2}{{l_e}^2} - \frac{2x^3}{{l_e}^3}\ ; N_4(x) = -\frac{x^2}{l_e} + \frac{x^3}{{l_e}^2}\,. \tag{4.43}$$

By substituting Eq. (4.42) into Eq. (4.40), we can write

$$\int_0^{l_e} \{(EI)^{eff} N''^T N'' + \tau_0 s^* N'^T N'\} v^e dx = -\int_0^{l_e} q(x) N dx. \tag{4.44}$$

The elemental stiffness matrix can be written as:

$$K_e = \int_0^{l_e} \left\{\{(EI)^{eff} N''^T N'' + \tau_0 s^* N'^T N'\} dx\right\}, \tag{4.45a}$$

$$K_e = \int_0^{l_e} \left\{(EI)^{eff} \left(\frac{d^2N}{dx^2}\right)^T \frac{d^2N}{dx^2} + (\tau_0 s^*)\left(\frac{dN}{dx}\right)^T \frac{dN}{dx}\right\} dx\,, \tag{4.45b}$$

$$K_e = \frac{(EI)^{eff}}{{l_e}^3}\begin{bmatrix} 12 & 6l_e & -12 & 6l_e \\ 6l_e & 4{l_e}^2 & -6l_e & 2{l_e}^2 \\ -12 & -6l_e & 12 & -6l_e \\ 6l_e & 12 & -6l_e & 4{l_e}^2 \end{bmatrix} + \frac{(\tau_0 s^*)}{30 l_e}\begin{bmatrix} 36 & 3l_e & -36 & 3l_e \\ 3l_e & 4{l_e}^2 & -3l_e & -{l_e}^2 \\ -36 & -3l_e & 36 & -3l_e \\ 3l_e & -{l_e}^2 & -3l_e & 4{l_e}^2 \end{bmatrix}. \tag{4.46}$$

Observation of Eq. (4.46) reveals that it is divided into two parts. The first part is similar to the modified stiffness matrix and the second part is related to the stiffness matrix considering the surface effects. The value of effective bending stiffness $(EI)^{eff}$ is influenced by the negative or positive value of the surface stress. Hence, the elemental nodal force vector can be written as:

$$f_e = -\int_0^{l_e} q(x)N^T\,dx\,. \tag{4.47}$$

The generalized nodal force vector includes the effect of uniformly distributed load (q_0) as well as the concentrated end-point load (P). In case of cantilever beam, if the element is subjected to the end-point load or uniformly distributed load, then the corresponding force vector can be written as:

$$f_e = -P[1 \quad l_e \quad -1 \quad 0]'\,, \tag{4.48a}$$

$$f_e = -\frac{q_0}{12}[6l_e \quad {l_e}^2 \quad 6l_e \quad -{l_e}^2]'\,. \tag{4.48b}$$

Similarly, we can determine the generalized nodal force vector for simply-supported and clamped-clamped beams. Using the assemblage of element stiffness and nodal force matrix, the equilibrium equation with global element stiffness and global force vectors are given by

$$Kd = f\,. \tag{4.49}$$

in which K, d and f denote the global stiffness matrix, displacement and global force vector, respectively.

4.3 Results and Discussions

4.3.1 Electromechanical Behavior of GRNC Beams

In this sub-section, the electromechanical behavior of GRNC nanobeams, accounting the flexoelectric and surface effects, subjected to the point load with different boundary conditions are studied. Different boundary conditions of beam such as cantilever, simply-supported and clamped-clamped are considered. The effective properties of GRNC considering 60% graphene volume fraction are considered and the same are summarized in Table 4.1.

Table 4.1: Properties of GRNC (v_g = 0.6).

C_{11}(GPa)	C_{12}(GPa)	C_{66}(GPa)	e_{31}(C/m^2)	e_{33}(C/m^2)	ϵ_{33}(F/m)
33.42	8.44	12.49	-0.0031	0.20	7.82 x 10^{-11}

The surface elastic modulus (C_{11s}) and coefficient of surface piezoelectricity (e_{31s}) were determined by assuming the thickness of surface layer as 1 nm (Ru, 2009; Chen, 2011; Zhang et al., 2012; Hu et al., 2014; Zhang et al., 2014; He, 2015). Surface material properties (C_{11s} and e_{31s}) are equal to those of the bulk properties of GRNC multiplied by thickness of surface layer. It is experimentally observed that for certain elastomers, crystals, ceramics and polymers, the flexoelectric coefficient (e/a) is in the range of $10^{-10} - 10^{-6}\mathrm{C/m}$; in which 'e' is the electron charge and 'a' is the lattice parameter (Kogan, 1964; Ma and Cross, 2003; Nguyen et al., 2013). Using experimental approaches, this was confirmed by Zubko et al. (2013) and to be more definite it is experimentally validated for polymers that the flexoelectric coefficient (μ_{31}) ranges from $10^{-8} - 10^{-9}\mathrm{C/m}$ (Chu and Salem, 2012; Jiang et al., 2013; Zhang et al., 2015). For further calculations herein, we have taken the value of $\mu_{31} \approx 10^{-9}\ \mathrm{C/m}$. The respective width (b) and length (l) of GRNC nanobeam are considered as $0.5\mathrm{h}$ and $20\mathrm{h}$.

Figures 4.3–4.5 illustrate that the flexoelectric and surface stress effects play a vital role in the elastic behavior of nanobeams. These figures also show the results for GRNC nanobeams neglecting flexoelectric and surface effects (i.e., conventional piezoelectric beam). It should be noted that one half of the beam deflection is shown in case of simply-supported and clamped-clamped beams by taking the advantage of symmetry. It is importantly noted that the separate as well as combined flexoelectric and surface effects significantly improves the elastic behavior of beams over that of conventional piezoelectric beams. For instance, it is revealed from Fig. 4.3 that the magnitude of normalized deflections of cantilever beams are decreased by ~19% and ~86% compared to that of conventional beam when only the flexoelectric effect and combined flexoelectric-surface effects are considered, respectively. Note that the elastic behavior of beam totally depends on the sign of surface stress, that is, either positive or negative ($\tau_0 > 0$ or $\tau_0 < 0$). For example, the cantilever nanobeam shows a softer elastic behavior compared to that of conventional nanobeam when $\tau_0 > 0$ and the reverse is true when $\tau_0 < 0$. On the contrary to the cantilever nanobeams, simply-supported and clamped-clamped nanobeams show stiffer elastic behavior when $\tau_0 > 0$ and vice versa. Our finding is coherent with the earlier results for static bending of nanowires considering the surface effect (He and Lilley, 2008). The demonstration of softer elastic behavior of the beam is attributed to the fact that the magnitude of applied point load becomes equal to the negative uniform transverse load in the same direction due to the surface stress effect in case of cantilever nanobeam; else, the beams show stiffer elastic behavior due to the positive uniform transverse load in case of simply-supported and clamped-clamped nanobeams. When the load is applied downwards then the cantilever nanobeam bent with concave curvature towards the negative z-axis. Hence, the additional transverse load is imposed due to the surface stress effect which counters the applied mechanical load. Therefore, the additional uniform transverse load improves the elastic behaviors of the simply-supported and clamped-clamped beams under applied downward loads. Note that the clamped-clamped nanobeam shows stiffer behavior compared to simply-supported beam because the former exhibits both downward and upward curvatures. For instance, the magnitude of normalized deflections of simply-supported beams (Fig. 4.4) are decreased by ~19% and ~68% compared to that of conventional beams when only the flexoelectric effect and combined flexoelectric-surface effects are considered, respectively; whereas as the corresponding reductions are ~19% and ~52% in case of clamped-clamped beams (Fig. 4.5). This is attributed to the stiffening of the simply-supported and clamped-clamped beams by a positive surface stress effect ($\tau_0 > 0$).

Our results clearly indicate that the sign of surface stress plays a vital role in the softening and stiffening behavior of nanobeams while flexoelectricity always stiffens the elastic behavior of nanobeams irrespective of boundary conditions. It is attributed to the fact that the effective bending rigidity of cantilever beam with flexoelectricity is higher than the conventional nanobeams. Surface stress softens the elastic behavior of cantilever beam while the flexoelectricity contributes to overcome this softness. From Figs. 4.3–4.5 it may be observed that the predictions by both analytical and FE models are in excellent agreement which provides strong evidence for the adequacy of the former method.

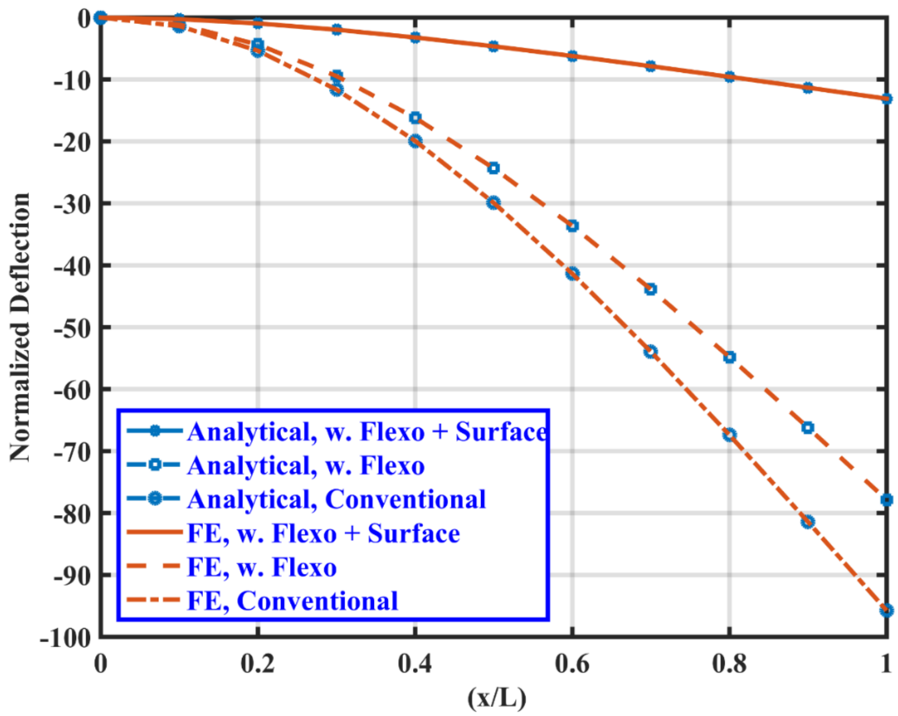

Figure 4.3: Variation of the normalized deflection of cantilever beam along its length under an end-point load P.

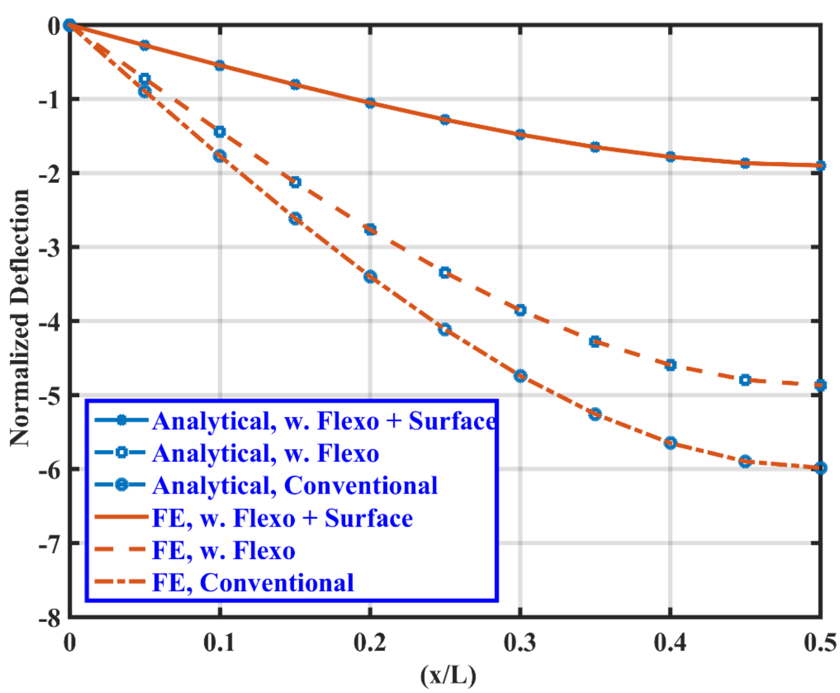

Figure 4.4: Variation of the normalized deflection of simply-supported beam along its length under a mid-point load P.

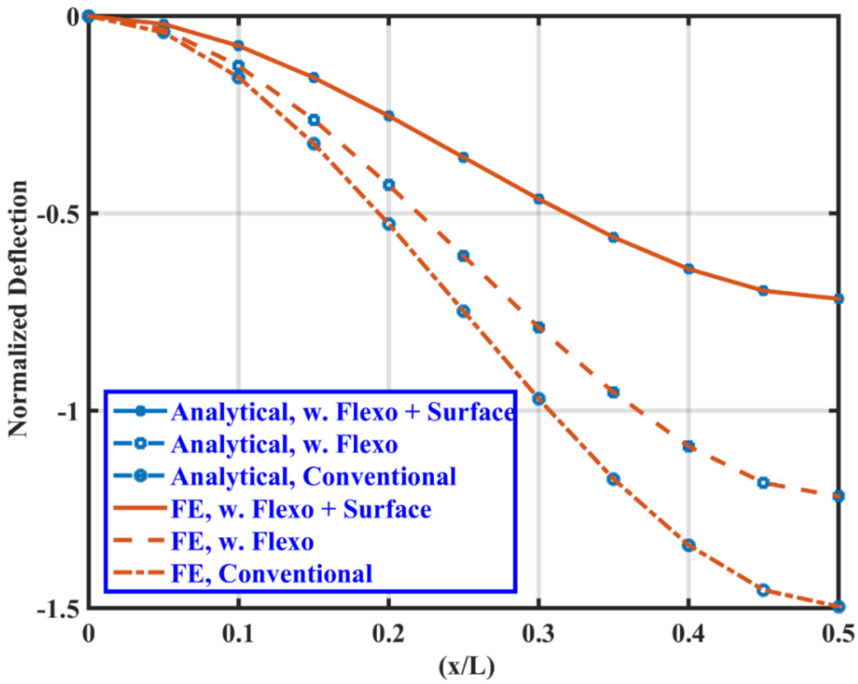

Figure 4.5: Variation of the normalized deflection of clamped-clamped beam along its length under a mid-point load P.

4.3.2 Electromechanical Coupling (EMC) Coefficient

Figure 4.6 demonstrates the flexoelectric and surface effects on the effective EMC coefficient (ξ^{eff}) against the thickness of GRNC nanobeam. Here, the EMC coefficient of nanobeams with the flexoelectric/surface effects (ξ^{eff}) is normalized by EMC coefficient of conventional beam (ξ_0^{eff}). From Fig. 4.6 it can be observed that the EMC coefficient significantly enhances as the beam thickness reduces and hence, it is also known as the size-dependent coefficient. The significant apparent piezoelectric effect is observed at the reduced thickness of beam due to the consideration of flexoelectric effect. It may be observed that the (i) EMC coefficient of nanobeams having a thickness less than 20 nm significantly increases compared to that of nanobeams with surface effects and (ii) EMC coefficient of nanobeams with only flexoelectric effect is enhanced by ~9% compared to that of nanobeams with combined flexoelectric-surface effects. It can also be noticed that the EMC coefficient is independent of the boundary conditions of beams and only depends on the size of nanostructure. Due to the flexoelectric effect, the enormous rise in the EMC coefficient at nanoscale level is likely to be beneficial for the enhancement of performance of NEMS applications.

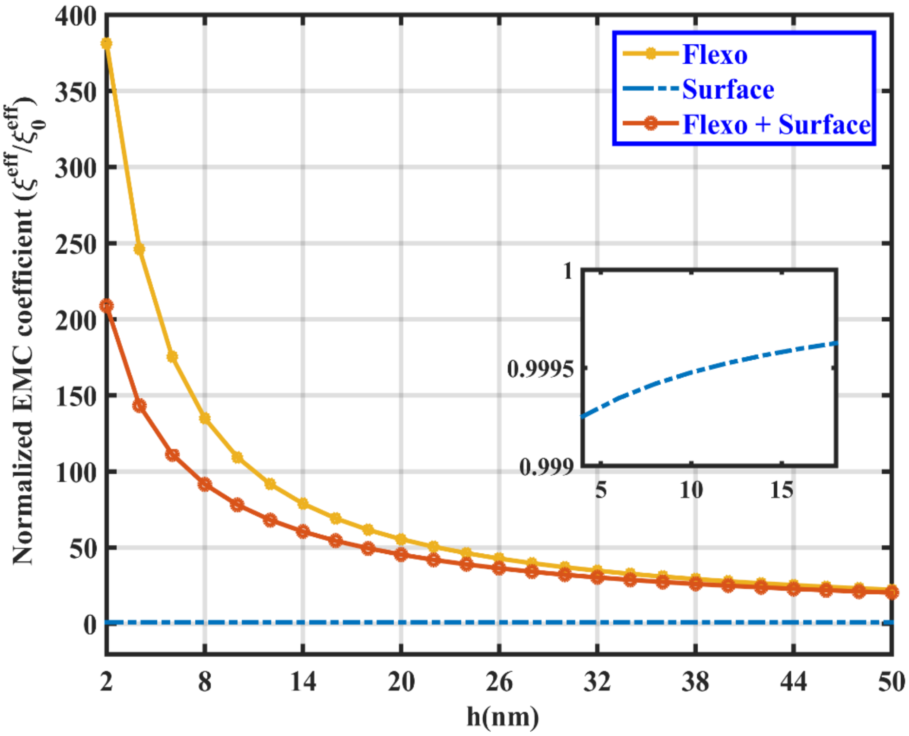

Figure 4.6: Variation of the normalized electromechanical coefficient $\left(\xi^{eff}/\xi_0^{eff}\right)$ against the thickness of nanobeam.

4.4 Conclusions

This Chapter dealt with the study of electromechanical behavior of GRNC nanobeams with various boundary conditions accounting the flexoelectric and surface effects. The closed-form solutions were obtained for investigating the electromechanical response of GRNC nanobeams based on the size-dependent Euler-Bernoulli and linear piezoelectricity theory accounting the flexoelectric and surface effects. Furthermore, the FE models were developed based on Galerkin's weighted residual method for validating the analytical results. The static deflections of GRNC cantilever, simply-supported and clamped-clamped nanobeams are reduced when (i) only the flexoelectric effect and (ii) the combined flexoelectric-surface effects are considered compared to that of corresponding conventional beams. The numerical outcomes reveal that the enhancement of EMC coefficient strongly depends on the size-dependent flexoelectric effect as the beam thickness reduces. Due to the incorporation of flexoelectric effect, it is found that the EMC coefficient of nanobeams having thickness less than 20 nm increases substantially, and such effect should be accounted for studying the static behavior of thin nanostructures. It is also concluded that the EMC coefficient is independent of the boundary conditions of beams and only depends on the size of nanostructure. Results reveal that the flexoelectric and surface effects on the static response of GRNC nanobeams are significant and should be taken into account.

The electromechanical behavior of GRNC nanoplate is studied in the next Chapter. The static and dynamic behavior of simply-supported GRNC nanoplate subjected to different loading conditions such as uniformly distributed, hydrostatic or varying distributed, point and in-line loadings accounting the flexoelectric effect are studied.

Chapter 5

Electromechanical Behavior of Flexoelectric GRNC Plates

In this Chapter, the electromechanical behavior of GRNC plates with flexoelectric effect is studied by deriving an analytical model based on Kirchhoff's plate theory, Navier's solution and extended linear piezoelectricity theory. The effective properties of GRNC obtained in Chapter 2 are utilized. The static and dynamic responses of simply-supported flexoelectric GRNC nanoplates under different loadings such as uniformly distributed, varying distributed, inline and point loads are investigated.

5.1 Introduction

The review of literature presented on graphene-based composite plates clearly indicate that graphene is the most attracting 2D material, vastly studied in the last decade. The analysis of the static and dynamic response of a flexible GRNC nanoplate considering the flexoelectric effect is yet to be studied, which can offer many opportunities for developing next generation NEMS. Therefore, an analytical model based on the Kirchhoff's plate theory, Navier's solution and extended linear piezoelectricity theory was developed to investigate the electromechanical response of simply supported GRNC plate under different loadings such as uniformly distributed (UD), point, in-line and varying distributed (VD) loads, accounting the flexoelectric effect. The electromechanical response of GRNC plates was investigated to attain the desired deflection characteristics and resonant frequencies for a range of NEMS using different flexoelectric coefficients as well as geometrical parameters such as aspect ratio, thickness of nanoplate and volume fraction of graphene.

5.2 Electromechanical Response of GRNC Plates

5.2.1 Governing Equations for GRNC Plates

In this sub-section, the governing equations for GRNC nanoplate subjected to the uniformly distributed mechanical load (q_0) are derived to investigate its static bending and dynamic behavior considering the flexoelectric effect. Figure 5.1 shows the schematic of simply-supported (SS) GRNC nanoplate having thickness h, length a and width b. A Cartesian coordinate system is used to describe the nanoplate with thickness along the z–axis and the mid plane of the undeformed nanoplate coincides with the x−y plane.

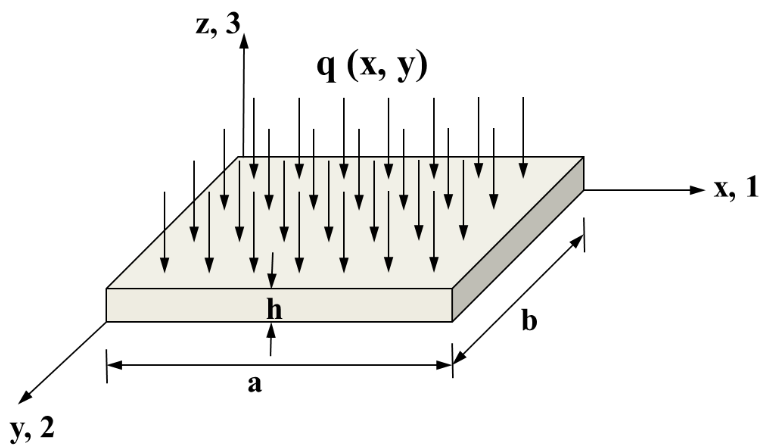

Figure 5.1: Schematic of GRNC nanoplate subjected to the uniformly distributed load.

- **Assumptions of Kirchhoff's plate theory:**
    - Straight lines normal to the mid-surface (i.e., transverse normals) before deformation remain straight after deformation.
    - The transverse normals are inextensible (i.e., do not experience elongation).
    - The thickness of the plate does not change during a deformation.
    - The transverse normals rotate such that they remain normal to the middle surface after deformation.

The first three assumptions signify that transverse displacement is independent of transverse (or thickness) coordinate and transverse normal strain is zero. The last assumption indicates zero transverse shear strain.

As per Kirchhoff's plate theory, the in-plane displacement of the plate in terms of transverse displacement $w(x, y, t)$ can be expressed as (Zhao et al., 2012):

$$u(x, y, z, t) = -z\frac{\partial w(x, y, t)}{\partial x}, \tag{5.1}$$

$$v(x, y, z, t) = -z\frac{\partial w(x, y, t)}{\partial y}, \tag{5.2}$$

$$w(x, y, z, t) = w(x, y, t), \tag{5.3}$$

in which (u, v, w) are the in-plane displacement components along the (x, y, z) coordinate directions, respectively; t is the time; and w is the transverse displacement of a point on the mid-plane (i.e., $z = 0$). The displacement field (Eqs. 5.1–5.3) indicates that straight lines normal to the x–y plane before deformation remain straight and normal to the mid-surface after deformation.

Consequently, the nonzero strains can be written as follows:

$$\varepsilon_{xx} = -z\frac{\partial^2 w}{\partial x^2}, \qquad \varepsilon_{yy} = -z\frac{\partial^2 w}{\partial y^2}, \qquad \varepsilon_{xy} = -z\frac{\partial^2 w}{\partial x\,\partial y}. \tag{5.4}$$

Assuming the electric field E_z exists only in the $z -$direction of the nanoplate, the in-plane dimensions and electric field components in the $x - y$ plane can be eliminated when they are compared with that in the thickness direction (Ying and Zhifei, 2005; Ray and Pradhan, 2006). By using the generalized equation for the electric Gibbs free energy density function (U) presented in previous Chapter 4, the constitutive relations can be reformulated as:

$$\sigma_{xx} = C_{11}\varepsilon_{xx} + C_{12}\varepsilon_{yy} - e_{31}E_z, \tag{5.5a}$$

$$\sigma_{yy} = C_{12}\varepsilon_{xx} + C_{11}\varepsilon_{yy} - e_{31}E_z, \tag{5.5b}$$

$$\tau_{xy} = 2C_{66}\varepsilon_{xy}, \tag{5.5c}$$

$$\tau_{xxz} = -\mu_{14}E_z, \tag{5.5d}$$

$$\tau_{yyz} = -\mu_{14}E_z, \tag{5.5e}$$

$$D_z = e_{31}\left(\varepsilon_{xx} + \varepsilon_{yy}\right) + \epsilon_{33} E_z + \mu_{14}\left(\eta_{xxz} + \eta_{yyz}\right), \tag{5.5f}$$

where $\mu_{14} = \mu_{3113} = \mu_{3223}$ (Shu *et al.*, 2011). For the sake of simplicity, the strain gradients other than $\eta_{xxz} = -\frac{\partial^2 w}{\partial x^2}$ and $\eta_{yyz} = -\frac{\partial^2 w}{\partial y^2}$ are assumed to be zero, since the associated flexoelectric coefficients or strain gradients are much smaller as compared to that along the thickness direction of GRNC nanoplate. Due to the absence of external electric field, the electric displacement equals electric polarization. Hence, it can be clearly seen that the 3rd term in Eq. (5.5f) indicates the polarization induced in the nanoplate due to the strain gradients.

Using the equation of Gauss' law of electrostatics ($\nabla . \mathrm{D} = \rho_s$), in the absence of free electric charge (ρ_s), the electric displacement for the thin nanoplate can be written as:

$$\frac{\partial \mathrm{D_z}}{\partial \mathrm{z}} = 0. \tag{5.6}$$

In case of open-circuit condition, on the surface of nanoplate the electric displacement is zero. Therefore, from Eq. (5.6), the internal electric field can be derived as follows:

$$\mathrm{E_z} = \frac{e_{31}}{\epsilon_{33}}\left(\frac{\partial^2 w}{\partial x^2} + \frac{\partial^2 w}{\partial y^2}\right) z + \frac{\mu_{14}}{\epsilon_{33}}\left(\frac{\partial^2 w}{\partial x^2} + \frac{\partial^2 w}{\partial y^2}\right). \tag{5.7}$$

From Eq. (5.7), it can be observed that the first term $\frac{e_{31}}{\epsilon_{33}}$ related to the piezoelectricity signifies the electric field induced due to the application of strains, and the second term $\frac{\mu_{14}}{\epsilon_{33}}$ related to the flexoelectricity signifies the electric field induced due to the application of strain gradients. Considering the flexoelectricity, the piezoelectricity associated internal electric field no longer remains anti-symmetric respective to the midplane of the nanoplate in the direction of its thickness. Then, taking the summation of the curvatures at an arbitrary point in the nanoplate as a whole, Eq. (5.7) can be rewritten as $\mathrm{E_z} = \frac{e_{31}z+\mu_{14}}{\epsilon_{33}}\mathrm{G}$ with $\mathrm{G} = \frac{\partial^2 w}{\partial x^2} + \frac{\partial^2 w}{\partial y^2}$. Note that the response of the electric field $\mathrm{E_z}$ to G depends on the z-coordinate. In addition, term $e_{31}z + \mu_{14}$ depend on the thickness of nanoplate and its flexoelectric coefficient. If the piezoelectric effect is not taken into account then the solution is attributed to the flexoelectric effect (i.e., μ_{14}).

The governing equations for the SS nanoplate problem can be derived using dynamic version of Hamilton's variational principle, such as (Reddy, 2003):

$$\delta \int_0^t (\mathrm{U} + \mathrm{W} - \mathrm{K})\mathrm{dt} = 0, \tag{5.8}$$

where U is the electric Gibbs free energy density. For the simplification of formulation, we considered open-circuit condition ($\mathrm{D_z} = 0$) and the terms r_{ijklm} and g_{ijklmn} with higher order gradients are neglected in Eq. (4.1) and hence, the relation of U can be reduced as:

$$\mathrm{U} = \frac{1}{2}\sigma_{ij}\varepsilon_{ij} + \frac{1}{2}\tau_{ijk}\eta_{ijk}. \tag{5.9}$$

If the vibration along the $x - y$ plane is ignored, then the kinetic energy (K) is given by

$$K = \frac{1}{2}\int_{\Omega} \rho \left(\frac{\partial w}{\partial t}\right)^2 d\Omega, \tag{5.10}$$

where Ω is the entire volume occupied by the GRNC nanoplate and ρ is the mass density. The work done (W) due to the application of external load can be determined as follows:

$$W = \int_0^a \int_0^b q_0 w dy dx. \tag{5.11}$$

An energy formulation for continuum electro-elasticity is based on the principle of minimum free energy, which is mainly suitable for complex materials with significant gradient effects and analysis of stability (Liu et al., 2013). Therefore, the governing equation can be written as:

$$\frac{\partial^2 M_{xx}}{\partial x^2} + \frac{\partial^2 M_{xy}}{\partial x\,\partial y} + \frac{\partial^2 M_{yx}}{\partial x\,\partial y} + \frac{\partial^2 M_{yy}}{\partial y^2} + \frac{\partial^2 N_{xxz}}{\partial x^2} + \frac{\partial^2 N_{yyz}}{\partial y^2} - \rho h \frac{\partial^2 w}{\partial t^2} + q_0 = 0. \tag{5.12}$$

Boundary conditions for SS rectangular GRNC nanoplate on all four edges are prescribed and can be deduced as (Reddy, 2003):

at $x = 0$ and $x = a$:

$$w = 0, M_{xx} = 0. \tag{5.13}$$

at $y = 0$ and $y = b$:

$$w = 0, M_{yy} = 0. \tag{5.14}$$

where M_{xx}, M_{xy}, M_{yx} and M_{yy} are the bending moments, and N_{xxz} and N_{yyz} are the axial forces along the thickness, and these can be obtained as follows:

$$M_{xx} = \int_{-h/2}^{h/2} \sigma_{xx} z dz,\ M_{yy} = \int_{-h/2}^{h/2} \sigma_{yy} z dz, M_{xy} = M_{yx} = \int_{-h/2}^{h/2} \tau_{xy} z dz\ , \tag{5.15}$$

$$N_{xxz} = \int_{-h/2}^{h/2} \tau_{xxz} dz, \qquad N_{yyz} = \int_{-h/2}^{h/2} \tau_{yyz} dz. \tag{5.16}$$

Substituting Eqs. (5.3a) and (5.7) into the constitutive relations (5.5a–5.5e), the explicit expressions for the stresses and higher-order stresses related to the transverse deflection (w) can be written as:

$$\sigma_{xx} = -\left(C_{11} + \frac{e_{31}^2}{\epsilon_{33}}\right)\frac{\partial^2 w}{\partial x^2}z - \left(C_{12} + \frac{e_{31}^2}{\epsilon_{33}}\right)\frac{\partial^2 w}{\partial y^2}z - \frac{e_{31}\mu_{14}}{\epsilon_{33}}\left(\frac{\partial^2 w}{\partial x^2} + \frac{\partial^2 w}{\partial y^2}\right), \tag{5.17}$$

$$\sigma_{yy} = -\left(C_{12} + \frac{e_{31}^2}{\epsilon_{33}}\right)\frac{\partial^2 w}{\partial x^2}z - \left(C_{11} + \frac{e_{31}^2}{\epsilon_{33}}\right)\frac{\partial^2 w}{\partial y^2}z - \frac{e_{31}\mu_{14}}{\epsilon_{33}}\left(\frac{\partial^2 w}{\partial x^2} + \frac{\partial^2 w}{\partial y^2}\right), \tag{5.18}$$

$$\tau_{xy} = -2C_{66}\frac{\partial^2 w}{\partial x\,\partial y}z, \tag{5.19}$$

$$\tau_{xxz} = \tau_{yyz} = -\frac{e_{31}\mu_{31}}{\epsilon_{33}}\left(\frac{\partial^2 w}{\partial x^2} + \frac{\partial^2 w}{\partial y^2}\right)z - \frac{\mu_{14}^2}{\epsilon_{33}}\left(\frac{\partial^2 w}{\partial x^2} + \frac{\partial^2 w}{\partial y^2}\right). \tag{5.20}$$

Making the use of Eqs. (5.17–5.20) into Eqs. (5.15–5.16), the bending moments can be obtained in terms of w as follows:

$$M_{xx} = -\left(C_{11} + \frac{e_{31}^2}{\epsilon_{33}}\right)\frac{h^3}{12}\frac{\partial^2 w}{\partial x^2} - \left(C_{12} + \frac{e_{31}^2}{\epsilon_{33}}\right)\frac{h^3}{12}\frac{\partial^2 w}{\partial y^2}, \tag{5.21}$$

$$M_{yy} = -\left(C_{12} + \frac{e_{31}^2}{\epsilon_{33}}\right)\frac{h^3}{12}\frac{\partial^2 w}{\partial x^2} - \left(C_{11} + \frac{e_{31}^2}{\epsilon_{33}}\right)\frac{h^3}{12}\frac{\partial^2 w}{\partial y^2}, \tag{5.22}$$

$$M_{xy} = M_{yx} = -2C_{66}\frac{h^3}{12}\frac{\partial^2 w}{\partial x\,\partial y}, \tag{5.23}$$

$$N_{xxz} = N_{yyz} = -\frac{\mu_{14}^2}{\epsilon_{33}}\left(\frac{\partial^2 w}{\partial x^2} + \frac{\partial^2 w}{\partial y^2}\right)h. \tag{5.24}$$

After careful observations of Eqs. (5.17–5.24), it can be observed that the flexoelectricity significantly influences the distribution of stress and higher-order stresses. Accordingly, the higher-order stress vanishes when the flexoelectric effect is not considered and the conventional bending moments are not influenced by the strain gradient. Moreover, the introduction of flexoelectric effect yields the summations of higher-order stresses.

Using Eqs. (5.21–5.24) into Eq. (5.12), the governing equation can be written in terms of w as follows:

$$D_{11}\left(\frac{\partial^4 w}{\partial x^4} + \frac{\partial^4 w}{\partial y^4}\right) + 2(D_{12} + 2D_{66})\frac{\partial^4 w}{\partial x^2\,\partial y^2} + \rho h\frac{\partial^2 w}{\partial t^2} = q_0, \tag{5.25}$$

with

$$\begin{cases} D_{11} = \left(C_{11} + \dfrac{e_{31}^2}{\epsilon_{33}}\right)\dfrac{h^3}{12} + \dfrac{\mu_{14}^2}{\epsilon_{33}} h \\ D_{12} = \left(C_{12} + \dfrac{e_{31}^2}{\epsilon_{33}}\right)\dfrac{h^3}{12} + \dfrac{\mu_{14}^2}{\epsilon_{33}} h \ . \\ D_{66} = C_{66}\dfrac{h^3}{12} \end{cases} \tag{5.26}$$

From above formulation, it is observed that flexoelectric effect has significant influence on the bending stiffness of nanoplate.

5.2.2 Exact Solution for Static Response of GRNC Plates

For static bending response of the GRNC nanoplates, the governing Eq. (5.25) can be re-written as follows (Reddy, 2003):

$$D_{11}\left(\frac{\partial^4 w}{\partial x^4} + \frac{\partial^4 w}{\partial y^4}\right) + 2(D_{12} + 2D_{66})\frac{\partial^4 w}{\partial x^2\, \partial y^2} = q_0 \ . \tag{5.27}$$

It may be noted that in the absence of flexoelectricity, the governing equation (5.27) follows the conventional classical Kirchhoff plate theory considering linear piezoelectricity. According to the conventional plate theory, for solving the governing Eq. (5.27) of the SS GRNC nanoplate, the following Fourier series can be used to determine $w\,(x, y)$.

$$w(x, y) = \sum_{m=1}^{\infty}\sum_{n=1}^{\infty} A_{mn} \sin\alpha x \sin\beta y \ , \tag{5.28}$$

where $\alpha = \frac{m\pi}{a}, \beta = \frac{n\pi}{b}$ and A_{mn} are the coefficients to be calculated for each m and n half wave numbers that should be satisfied everywhere in the domain of a nanoplate. It has previously corroborated that Eq. (5.28) satisfies the boundary conditions given in Eqs. (5.13–514). Using the expression of Fourier series, the uniformly distributed load $q_0\,(x, y)$ can be obtained as follows:

$$q(x, y) = \sum_{m=1}^{\infty}\sum_{n=1}^{\infty} Q_{mn} \sin\alpha x \sin\beta y \ , \tag{5.29}$$

with

$$w(x, y) = \frac{Q_{mn}}{d_{mn}} .$$

where Q_{mn} are the load coefficients for various types of loading as written as follows:

For (i) Uniform distributed load:

$$Q_{mn} = \frac{16q_0}{mn\pi^2}\,, \qquad m, n = 1, 3, 5, .. \tag{5.30a}$$

(ii) Linearly varying load:

$$Q_{mn} = \frac{8q_0 \cos m\pi}{mn\pi^2}\,, \qquad m, n = 1, 3, 5, .. \tag{5.30b}$$

(iii) Point load:

$$Q_{mn} = \frac{4P}{ab} \sin\frac{m\pi x_0}{a} \sin\frac{n\pi y_0}{b}\,, m, n = 1, 2, 3, .. \tag{5.30c}$$

(iv) Line load:

$$Q_{mn} = \frac{8q_0}{\pi a n} \sin\frac{m\pi x_0}{a}. \quad m = 1, 3, 5, ..; n = 1, 2, 3 \ldots \tag{5.30d}$$

$$d_{mn} = \left(\frac{\pi}{b}\right)^4 \left\{D_{11}\left(\frac{m}{a}\right)^4 + D_{12}\left(\frac{n}{b}\right)^4 + 2(D_{12} + 2D_{66})\left(\frac{mn}{ab}\right)^2\right\}. \tag{5.30e}$$

Substituting Eqs. (5.28–5.29) into Eq. (5.27), we can derive the solution for the SS nanoplate to obtain its transverse deflection.

$$w(x, y) =$$

$$= \frac{16q_0}{\pi^6} \sum_{m=1,3,5\ldots}^{\infty} \sum_{n=1,3,5\ldots}^{\infty} \frac{\sin\alpha x \sin\beta y}{mn\left\{D_{11}\left(\frac{m}{a}\right)^4 + D_{12}\left(\frac{n}{b}\right)^4 + 2(D_{12} + 2D_{66})\left(\frac{mn}{ab}\right)^2\right\}}. \tag{5.31}$$

5.2.3 Exact Solution for Dynamic Response of GRNC Plates

Using Eq. (5.25), the governing equation for the GRNC nanoplate can be written as:

$$D_{11}\left(\frac{\partial^4 w}{\partial x^4} + \frac{\partial^4 w}{\partial y^4}\right) + 2(D_{12} + 2D_{66})\frac{\partial^4 w}{\partial x^2\,\partial y^2} + \rho h\frac{\partial^2 w}{\partial t^2} = 0\,. \tag{5.32}$$

Similar to the conventional plate model, the harmonic solution for $w(x, y, t)$ is derived as:

$$w(x, y, t) = \sum_{m=1}^{\infty}\sum_{n=1}^{\infty} B_{mn} \sin\frac{m\pi x}{a} \sin\frac{n\pi y}{b}\, e^{i\omega_{mn} t}, \tag{5.33}$$

where B_{mn} is a constant indicating the mode shape amplitude; m and n are the half wave numbers; ω_{mn} is the resonant frequency; and $i = \sqrt{-1}$.

Making use of Eq. (5.33) into Eq. (5.32) yields the nanoplate resonant frequency; as follows:

$$D_{11}\left[\left(\frac{m\pi}{a}\right)^4 + \left(\frac{n\pi}{b}\right)^4\right] + 2(D_{12} + 2D_{66})\left(\frac{m\pi}{a}\right)^2\left(\frac{n\pi}{b}\right)^2 - \rho h\omega_{mn}^2 = 0. \quad (5.34)$$

Henceforth, the resonant frequency for nanoplate can be obtained for different order numbers m and n as:

$$\omega_{mn} = \left(\frac{\pi}{\rho h}\right)^2 \sqrt{D_{11}\left[\left(\frac{m}{a}\right)^4 + \left(\frac{n}{b}\right)^4\right] + 2(D_{12} + 2D_{66})\left(\frac{m}{a}\right)^2\left(\frac{n}{b}\right)^2}\ . \quad (5.35)$$

In this study, we only consider the mode (1,1) resonant frequency ω_{11} (i.e., fundamental frequency) with variation of aspect ratio and thickness of plate in subsequent section.

5.3 Results and Discussions

The effective properties of GRNC determined by means of MOM and FE models developed in the Chapter 2 were used for GRNC plates. To investigate the effect of flexoelectricity on the electromechanical response of GRNC plates, the effective properties of GRNC considering the volume fraction of graphene as 0.5 were taken from Table 2.3. For the sake of brevity, the results for GRNC plate are presented considering pristine graphene only. The mass density of GRNC (ρ_{nc}) is calculated using the simple rules-of-mixture: $\rho_{nc} = (\rho_g v_g) + (\rho_m v_m)$. We have taken values of ρ_g and ρ_m as 2200 kg/m^3 and 1330 kg/m^3, respectively (Odegard et al., 2005; Yolshina et al., 2016), and the calculated ρ_{nc} is 1765 kg/m^3. The magnitude of the applied uniformly distributed load on the GRNC plate is taken as $q_0 = 0.05$MPa. Recent experimental studies reported that the flexoelectric coefficients of certain ceramics and polymers are much larger than the previous estimates using different methods for values of flexoelectric coefficient. However, in experimental measurements of certain crystals, elastomers, polymers and ceramics, the predicted flexoelectric coefficient (e/a) was found to be in the range of 10^{-10}–10^{-6} C/m; where '$e = 1.602 \times 10^{-19}$C' is the electron charge and 'a' is the lattice constant in Å (Kogan, 1963; Ma and Cross, 2003). For instance, the experimentally predicted values of flexoelectric coefficients of polymers are found to be in the range from 10^{-8} to 10^{-9} C/m

(Chu and Salem, 2012; Jiang et al., 2013). Hence, unless otherwise mentioned, we considered the flexoelectric coefficient 10^{-9} C/m for current calculations.

5.3.1 Static Response of GRNC Plates

In this Section, the investigations are carried out to study the effect of flexoelectricity on the static response of GRNC nanoplates. The variation of normalized bending stiffness (D_{11}/D_{11}^{0}) of GRNC nanoplate with respect to its thickness (h) is plotted in Fig. 5.2, where D_{11} and D_{11}^{0} are the bending stiffnesses of GRNC nanoplate with and without flexoelectric effect, respectively. Note that the value of D_{11} depends only on the thickness of nanoplate and is independent of its in-plane dimensions, as seen from Eq. (5.26). Figure 5.2 reveals that the bending stiffness of GRNC nanoplate with flexoelectric effect is ~10 times higher than that of the conventional nanoplate (i.e., without flexoelectric effect) when the value of h is 1 nm. This difference is noticeable and cannot be ignored for studying the electromechanical response of thin nanostructures.

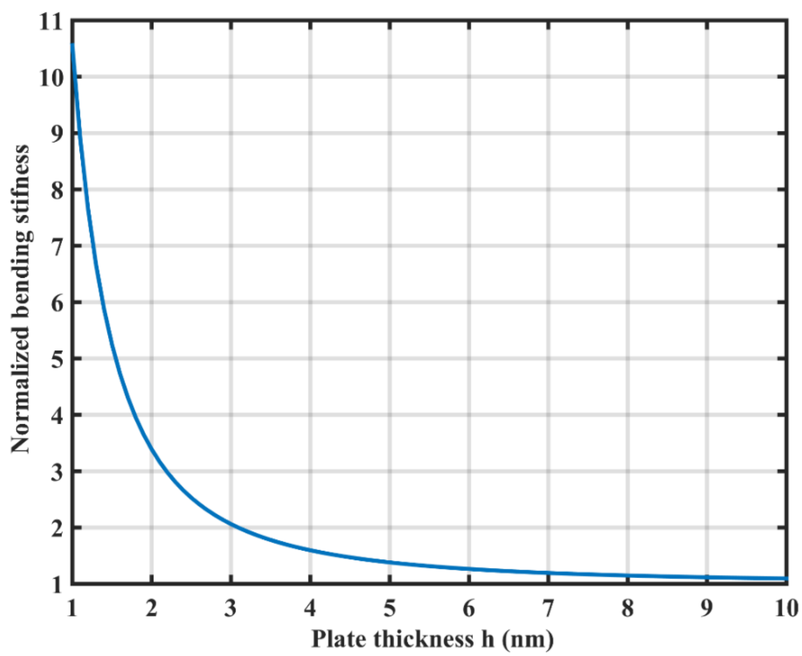

Figure 5.2: Effect of variation of plate thickness on the normalized bending stiffness.

As the thickness of nanoplate increases, the effect of flexoelectricity starts diminishing and this findings agree well with the results obtained by Zhou et al. (2016). From this, it can be concluded that the stiffness of nanoplate depends on the size or shape of nanostructure (constant or varying cross section). As expected, the normalized bending stiffness approaches unity when the flexoelectric effect vanishes. It may also be observed from Fig. 5.2 that the effect of flexoelectricity on the normalized bending stiffness of GRNC nanoplate is size dependent as it can be clearly seen from Eq. (5.26).

The effect of flexoelectricity on the static bending of GRNC nanoplate is examined here. Figures 5.3 and 5.4 demonstrate the variation of transverse deflections of SS GRNC nanoplates with and without flexoelectric effect for value of $m = 1$ and $n = 1$. The dimensions of the square GRNC nanoplate are taken as: $h = 4$ nm and $a = b = 50h$. Our selection of in-plane dimensions of nanoplate is based on the fact that the theory of Kirchhoff's plate provides better results when the aspect ratio of a plate is in the range of 5–80 (Yang et al., 2015). It can be observed from Figs. 5.3 and 5.4 that the maximum deflection of GRNC nanoplate occurs at its center i.e., at $x = a/2$ and $y = b/2$ for both the cases (with and without flexoelectric effect). The maximum deflection of GRNC nanoplate increases if its in-plane dimensions are increased $(a = b = 60h)$. It may also be observed that the deflection of GRNC nanoplate with flexoelectric effect is lower than that of the conventional plate for both the cases of in-plane dimensions.

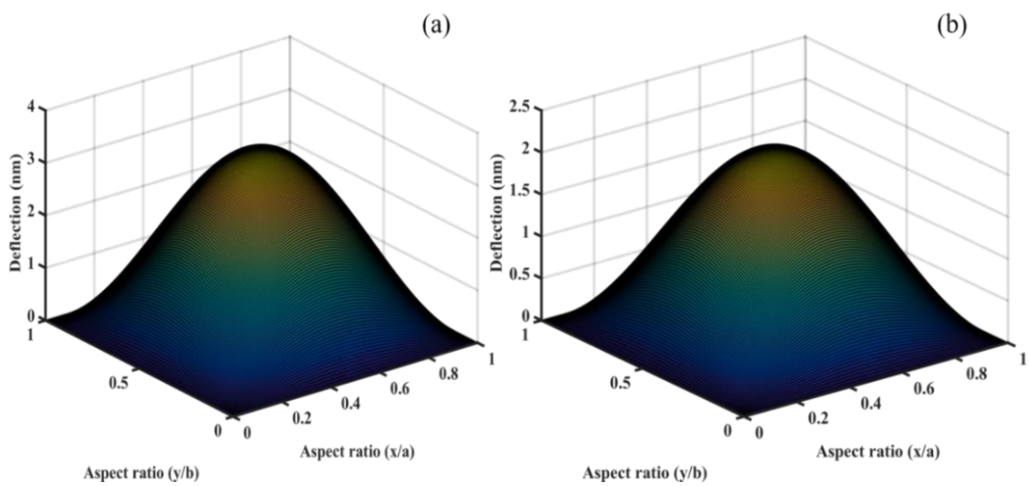

Figure 5.3: Deflection of GRNC nanoplate: (a) without flexoelectricity and (b) with flexoelectricity under UDL.

In addition, Figs. 5.3 (a) and (b) represent the 3-D representation of deflection of GRNC nanoplate with and without flexoelectric effect. The stiffness of GRNC nanoplate significantly improves due to the incorporation of flexoelectric effect over that of conventional nanoplate. These results clearly demonstrate the importance of flexoelectricity in the static bending of GRNC nanoplates which cannot be neglected at nanoscale level.

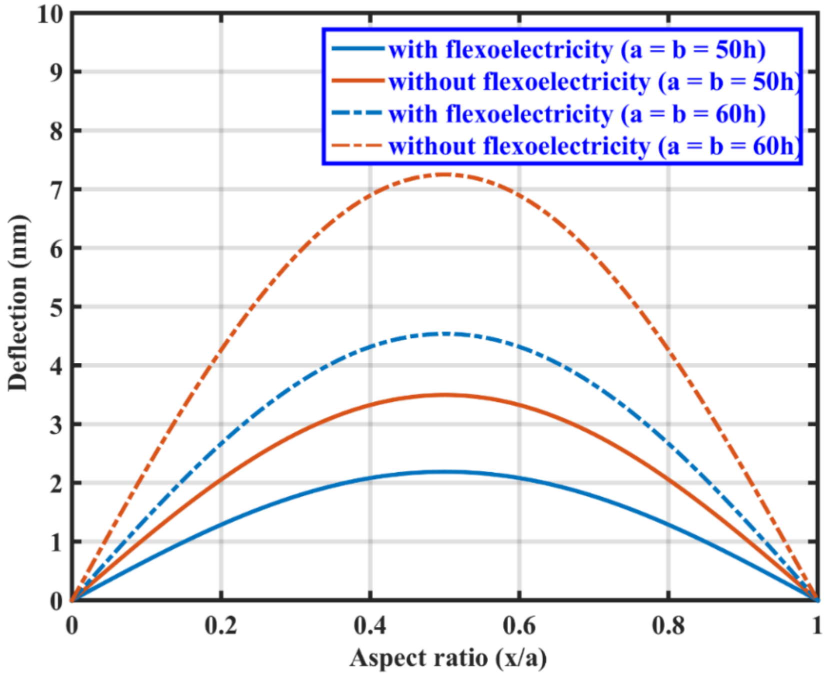

Figure 5.4: Effect of variation of plate aspect ratio (x/a) on the deflection of GRNC nanoplate under UDL.

In the previous sets of results, the static response of GRNC nanoplates subjected to the UDL is studied. However, the different types of loadings may influence the deflection behavior of nanoplates. Therefore, three different cases were considered for GRNC nanoplate under: (i) varying distributed load (VDL), (ii) point load and (iii) inline load. These cases represent the practical situation of different types of loadings applied to the thin plates. We considered the equivalent magnitude of loading in all situations. Table 5.1 illustrates the effect of three types of loading conditions on the deflection of GRNC nanoplates. As expected, the maximum deflection of the nanoplate occurs at its center irrespective of the type of loading in both the cases (with and without flexoelectricity). It is evident from this table that the consideration of flexoelectric effect results in the lowering the deflection of GRNC nanoplates compared to that of conventional plates. For example, the reduction in the static deflection of GRNC nanoplate having 4 nm thickness is found to be ~38.0% in all the loading cases. As expected, the maximum deflection of nanoplate occurs in case of the application of point load on it; the magnitude of maximum deflection of GRNC nanoplate observed in the following order: Point load > In-line load > UDL > VDL.

Table 5.1: Flexoelectric effect on the central deflection of GRNC plate under different loadings.

Sr. No.	Load $q\,(x,y)$	Figure	Deflection
1.	Varying distributed load $(x,y) = q_0 \frac{x}{a}$	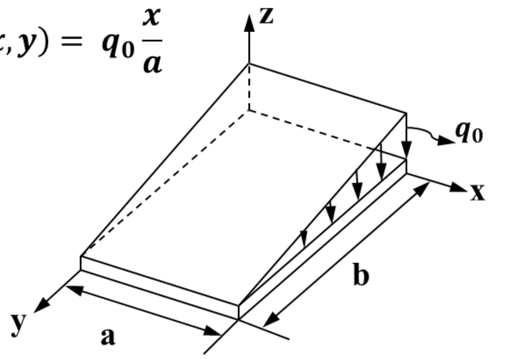	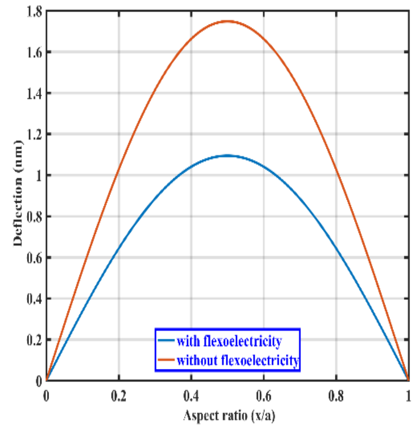
2.	Point load $q\,(x,y) = P\ at\ (x_0, y_0)$	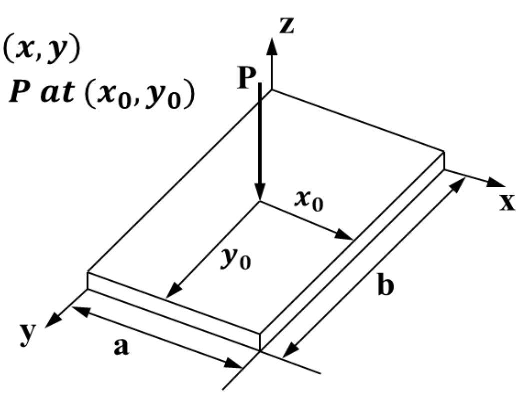	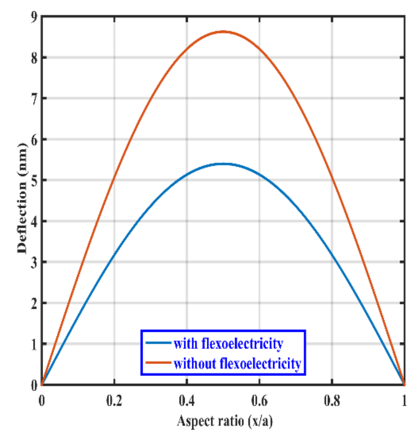
3.	Line load $q\,(x,y) = q_0$ $at\ x = x_0$	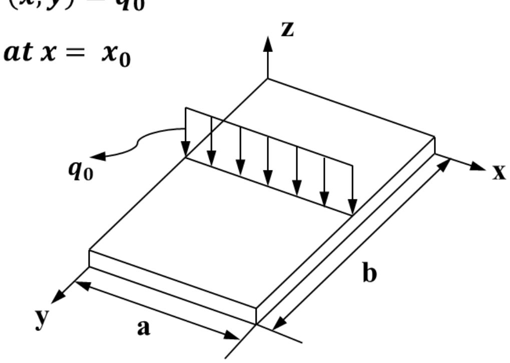	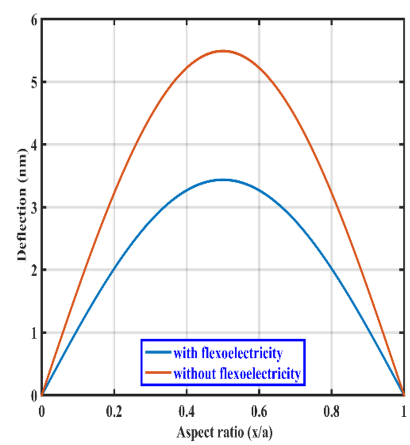

So far, the deflection characteristics of SS GRNC nanoplate are studied by considering its thickness as 4 nm. To explore the effect of thickness of GRNC nanoplate on its static behavior, once again the four discrete types of loading conditions are considered: UDL, VDL, inline load and point load. Table 5.2 summarizes the values of maximum deflections of GRNC nanoplates. The reductions in the static deflections of GRNC nanoplates, irrespective of the type of loading, are found to be ~71.0%, ~37.0%, ~21.0%, ~13.0% and ~9.0% corresponding to 2 nm, 4 nm, 6 nm, 8 nm and 10 nm thicknesses of nanoplate. It can be clearly seen that the influence of flexoelectricity on the maximum deflection of a nanoplate diminishes as its thickness increases and tends to approach the results of maximum deflection of the conventional GRNC nanoplate indicating that the flexoelectric effect is size dependent. It can be concluded from the above discussion that the effect of flexoelectricity is more prominent for thin plates and this finding agree well with the results obtained by other researchers (Yan and Jiang, 2012; Zhang and Jiang, 2014).

Table 5.2: Effect of flexoelectricity on the maximum deflection of GRNC nanoplate subjected to different types of loading conditions.

Thickness h (nm)		**Maximum Deflection (nm)**			
		UDL	**VDL**	**Point Load**	**In-line Load**
2	with flexoelectricity	0.5155	0.2578	1.2720	0.8098
	w/o flexoelectricity	1.7478	0.8739	4.3125	2.7454
4	with flexoelectricity	2.1881	1.0940	5.3989	3.4370
	w/o flexoelectricity	3.4956	1.7478	8.6250	5.4908
6	with flexoelectricity	4.1431	2.0715	10.2226	6.5079
	w/o flexoelectricity	5.2434	2.6217	12.9375	8.2362
8	with flexoelectricity	6.0825	3.0412	15.0079	9.5544
	w/o flexoelectricity	6.9911	3.4956	17.2499	10.9816
10	with flexoelectricity	7.9763	3.9882	19.6808	12.5292
	w/o flexoelectricity	8.7389	4.3695	21.5624	13.7271

Figure 5.5 shows the effect of variation of plate aspect ratio (a/h) on the maximum deflection of GRNC nanoplates for different flexoelectric coefficients. We kept thickness

of GRNC nanoplate constant to study the effect of its aspect ratio. It can be observed from Fig. 5.5 (c) that the flexoelectric effect is more prominent when the values of aspect ratio of plate and flexoelectric coefficient are 40 and 10^{-9} C/m, respectively. When the value of flexoelectric coefficient is 10^{-10} C/m then both the cases provide almost same results (Fig. 5.5d). On the other hand, the flexoelectric effect on the deflection behavior of nanoplates is negligible when the values of flexoelectric coefficients are 10^{-7} C/m and 10^{-8} C/m (Figs. 5.5a and b). It can also be observed that the flexoelectricity plays an important role when the in-plane dimensions of the plates are on the order of nm. However, flexoelectricity does not much influence the static behavior of nanoplate when its aspect ratio is less than 30 demonstrating the strong size-dependent behavior. We considered the value of flexoelectric coefficient as 10^{-9} C/m to study the effect of flexoelectricity on the dynamic response of GRNC nanoplates.

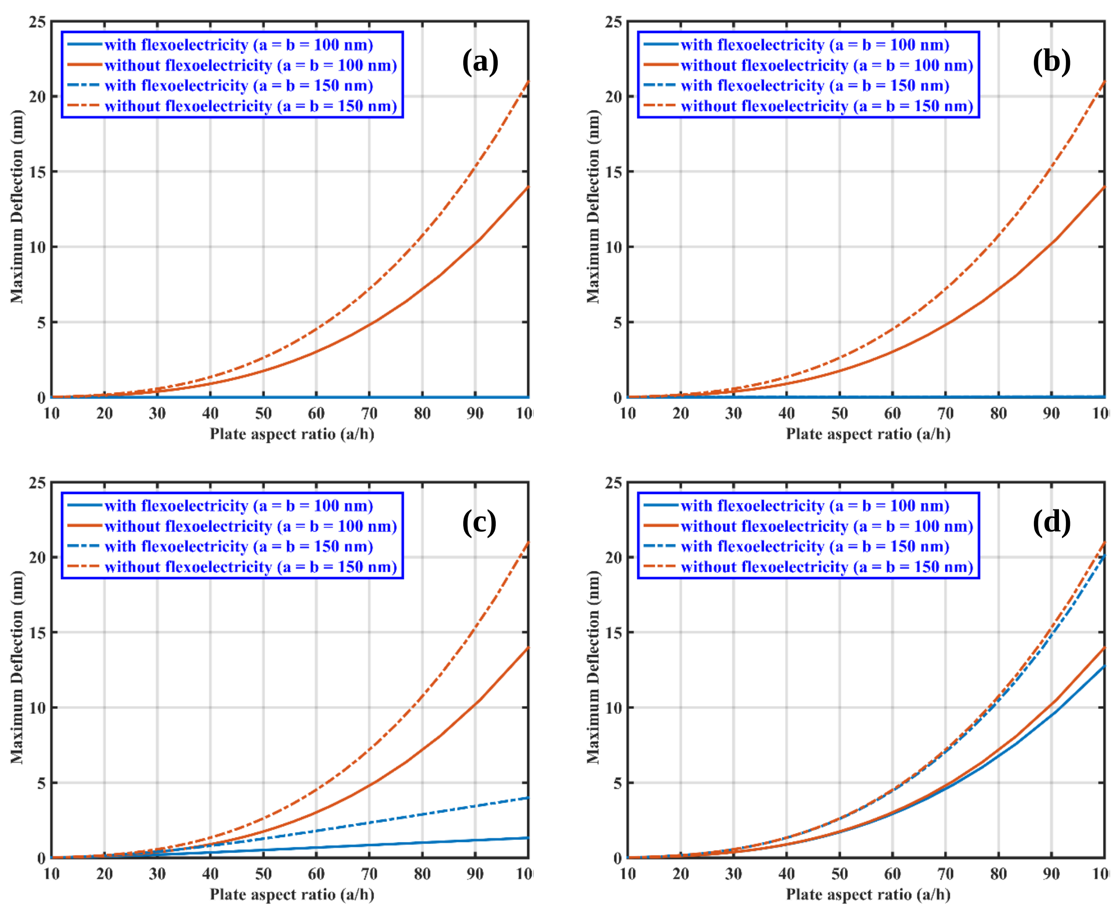

Figure 5.5: Effect of variation of plate aspect ratio (a/h) on the maximum deflection of GRNC nanoplate, with fixed in-plane dimensions, considering different flexoelectric coefficients: (a) 10^{-7} C/m, (b) 10^{-8} C/m, (c) 10^{-9} C/m and (d) 10^{-10} C/m.

5.3.2 Dynamic Response of GRNC Plates

In this sub-section, the investigations are carried out to study the effect of flexoelectricity on the dynamic response of GRNC nanoplates for mode (1,1). Figures 5.6 illustrates the effect of flexoelectricity on the resonant frequency of mode (1,1) of GRNC nanoplates against the plate aspect ratio. We kept the in-plane dimensions of plates constant (a = b = 100 and 150 nm) and varied their thickness. It can be observed that the resonant frequency is higher for the flexoelectric nanoplate over that of the conventional plate when the plate thickness is less than 3 nm. The flexoelectricity does not much influence the resonant frequencies of nanoplates having larger thickness (> 4 nm) and this is due to the fact that the effect of size-dependent flexoelectricity diminishes as the thickness of nanoplate increases. This figure also reveals that the resonant frequency largely depends on the in-plane dimensions of nanoplate; resonant frequency of the nanoplate diminishes as its in-plane dimensions increase.

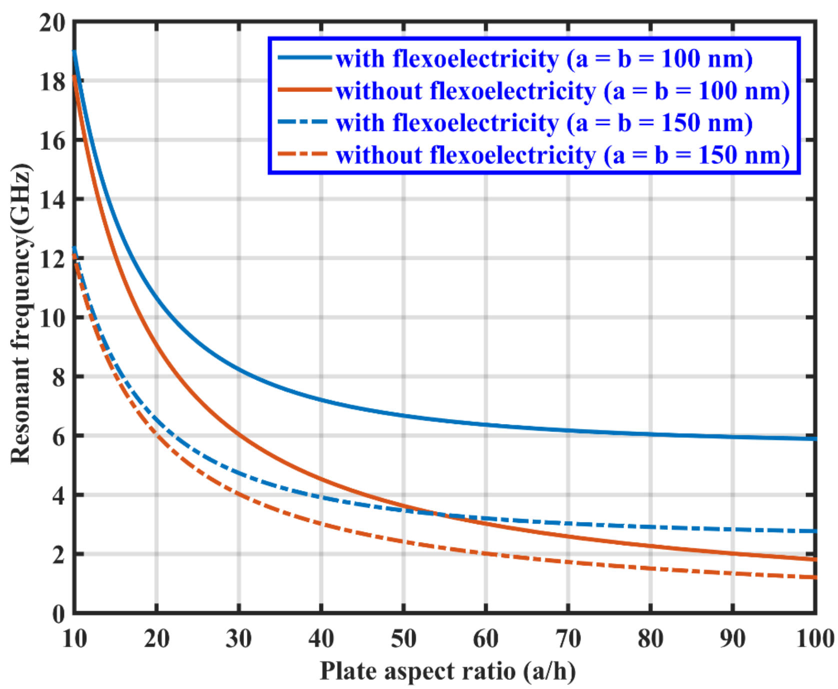

Figure 5.6: Effect of variation of plate thickness ($h = a/x$) on the resonant frequency of GRNC nanoplate.

So far, the effect of flexoelectricity on the resonant frequencies of GRNC nanoplate is studied by varying its thickness from 1 to 15 (Fig. 5.6). Here, the parametric results of resonant frequencies of GRNC nanoplates are presented to investigate the effect of flexoelectricity considering the plate thicknesses as 1 nm and 2 nm. Figure 5.7 demonstrates the effect of flexoelectricity on the resonant frequency of GRNC nanoplate with mode (1,1). It can be observed that the resonant frequency decreases as the aspect ratio of plate increases. The effect of flexoelectricity is noteworthy in case of thin plate. For instance, resonant frequencies of GRNC nanoplate with flexoelectricity are enhanced by ~225% for the plate aspect ratios of 10 to 30 when the plate thickness is 1 nm. On the contrary, when the aspect ratio is sufficiently large, the difference between the resonant frequencies is very small, therefore, the flexoelectric effect can be neglected. The results shown in Figs. 5.6 and 5.7 are significant which indicate that the flexoelectricity plays an important role in the dynamics of thin plates and needs to be accounted properly. It is observed from Figs. 5.2–5.7 that as the thickness of nanostructure increases the flexoelectric effect starts diminishing, and this finding agree well with the results obtained by other researchers (Su et al., 2019; Shi and Wang, 2019).

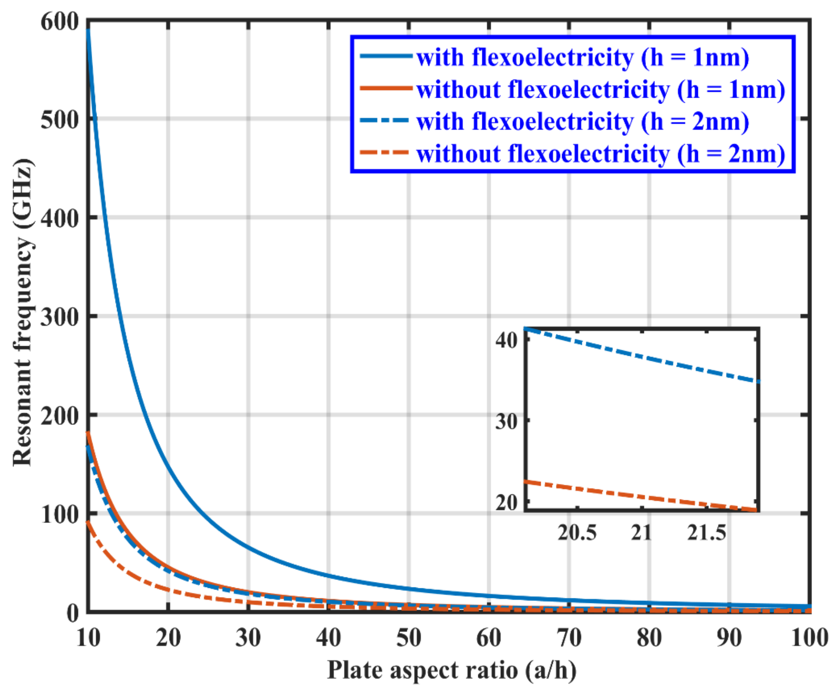

Figure 5.7: Effect of variation of plate aspect ratio (a = hx) on the resonant frequency of GRNC nanoplate.

5.4 Conclusions

This Chapter deals with the study of static and dynamic behaviors of novel GRNC nanoplates with the flexoelectric effect. The exact analytical solutions for flexoelectric

GRNC nanoplate based on Kirchhoff's plate theory, Navier's solution and extended linear theory of piezoelectricity were obtained. Based on this, the static and dynamic behaviors of simply-supported GRNC nanoplates under different types of loadings such as uniformly distributed, point, in-line and varying distributed loads were investigated to study the role of flexoelectricity. These loading cases represent the practical situation of different types of loadings applied to the thin nanostructured plates. It is found that the bending stiffness of nanoplates having less thickness increases significantly due to the incorporation of flexoelectric effect and such effect cannot be neglected for studying the static response of thin structures. Also, the effect of different flexoelectric coefficients on the maximum deflections of nanoplate is investigated. The dynamic response of GRNC nanoplates is enhanced due to the flexoelectric effect as the plate thickness reduces. Resonant frequencies of GRNC nanoplates are significantly enhanced for the smaller plate thickness. Our results indicate that the flexoelectricity plays an important role on the static and dynamic behaviors of thin plates and needs to be accounted properly while modelling 2-D nanostructures.

Apart from nanobeam and nanoplate, nanowires have found NEMS applications. Therefore, the electromechanical behavior such as electric potential and deflection of GRNC cantilevered nanowires, considering the flexoelectric and piezoelectric effects, are studied in the next Chapter.

Chapter 6

Electromechanical Behavior of Flexoelectric GRNC Wires

In this Chapter, the electromechanical behavior of a novel GRNC wire with flexoelectric effect is investigated by deriving the analytical model using the concept of strain gradient and FE model. The electromechanical responses such as the distribution of electric potential and deflection of cylindrical GRNC cantilevered nanowire are studied. Effects of different parameters such as different diameter, length and flexoelectric coefficients are taken into consideration for studying the electromechanical behavior of GRNC nanowire.

6.1 Introduction

The literature review presented in chapter 1 indicates that the piezoelectric contribution in nanowire-based nanogenerators was studied by several researchers. However, the electromechanical behavior of GRNC nanowire considering the flexoelectric effect is yet to be studied, that offer various opportunities for developing next-generation NEMS. Hence, further investigation is needed. Specifically, this Chapter is concerned with the development of analytical and FE models for the GRNC cantilevered nanowire, considering the flexoelectric effect, to study the distribution of electric potential in it. The electromechanical responses such as distribution of electric potential and deflection of GRNC cantilevered nanowire are investigated. The electromechanical behavior of GRNC cantilevered nanowire was studied to achieve the desired response via a number of ways such as by varying diameter and length of nanowires as well as flexoelectric coefficients.

6.2 Electromechanical Response of GRNC Wires

This Section presents the derivation of a continuum model to investigate the electromechanical response of GRNC wires, considering both the piezoelectric and flexoelectric effects.

6.2.1 Piezoelectric and Flexoelectric Effects

In this sub-section, the concept of piezoelectric and flexoelectric effects in case of deformed GRNC nanowire is presented. Figure 6.1 demonstrates the configuration of GRNC nanowire as a nanogenerator. This mechanism is based on the deflection of piezoelectric nanowire through point load resulting in the distribution of electric potential in it.

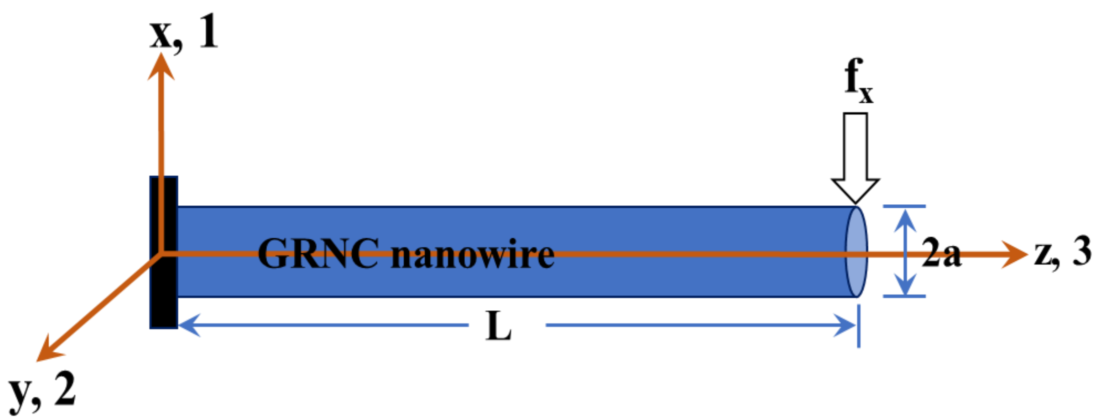

Figure 6.1: GRNC nanowire subjected to the applied transverse force (f_x).

The principal material coordinate and problem coordinate systems are represented by x-y-z and 1-2-3, respectively, and they are exactly coincide with each other. The aim of this Chapter is to obtain a relationship between the applied transverse force (f_x) in x-direction and distribution of the electric dipoles in GRNC nanowire using both piezoelectric as well as flexoelectric effects. The free end of a GRNC nanowire is subjected to the transverse force (f_x) that simulates the actual applied load or deflection.

According to the direct piezoelectric effect, the mechanical elastic strain induces the piezoelectric polarization in the piezoelectric material, which can be expressed as follows:

$$P_i = e_{ijk}\varepsilon_{jk}, \tag{6.2a}$$

where P_i, ε_{jk} and e_{ijk} represent the polarization vector, second-order strain tensor and third-order linear piezoelectric tensor, respectively. Contrast to Eq. (6.2a), the polarization induced due to the flexoelectric effect by small infinitesimal deformation follows the relation in-terms of strain gradients as follows:

$$P_i = e_{ijk}\varepsilon_{jk} + \mu_{ijkl}\frac{\partial \varepsilon_{jk}}{\partial x_l}, \tag{6.2b}$$

in which μ_{ijkl} is the fourth-order flexoelectric tensor. Using a relationship of the flexoelectric tensors, Shu et al. (2011) presented the symmetry of these coefficients in the crystalline medium as follows:

$$\begin{gathered}\mu_{1111} = \mu_{2222} = \mu_{3333} = \mu_{11} \\ \mu_{1133} = \mu_{2233} = \mu_{1122} = \mu_{2121} = \mu_{3232} = \mu_{3131} = \mu_{111} \\ \mu_{1221} = \mu_{1331} = \mu_{2112} = \mu_{2332} = \mu_{3223} = \mu_{3113} = \mu_{14}\ .\end{gathered} \tag{6.3a}$$

For isotropic medium, the relationship between direct flexoelectric coefficients (Eq. 6.3a) can be obtained as follows (Shu et al., 2011):

$$\mu_{14} = \frac{1}{2}(\mu_{11} - \mu_{111}). \tag{6.3b}$$

After some manipulation, for the simplification purpose, the above flexoelectric coefficients can be written as:

$$\mu_{3\times18} = \begin{pmatrix} \mu_{11} & 0 & 0 & \mu_{14} & 0 & 0 & \mu_{14} & 0 & 0 & 0 & \mu_{111} & 0 & 0 & 0 & \mu_{111} & 0 & 0 & 0 \\ 0 & \mu_{14} & 0 & 0 & \mu_{11} & 0 & 0 & \mu_{14} & 0 & \mu_{111} & 0 & 0 & 0 & 0 & 0 & 0 & 0 & \mu_{111} \\ 0 & 0 & \mu_{14} & 0 & 0 & \mu_{14} & 0 & 0 & \mu_{11} & 0 & 0 & 0 & \mu_{111} & 0 & 0 & 0 & \mu_{111} & 0 \end{pmatrix} \tag{6.4}$$

Furthermore, in case of isotropic materials, there is a relationship between the flexoelectric coefficients μ_{11}, μ_{111} and μ_{14}, and these independent coefficients can be reduced to two. The polarization charges in nanowire generated due to the piezoelectric and flexoelectric effects are bound charges instead of free charges. So, in absence of free charges, the Gauss's law yields to

$$\nabla . D = \rho_s = 0. \tag{6.5}$$

Here, for the cylindrical nanowire, the surface charge density (ρ_s) is 0, and D denotes a component of the electric displacement that can be obtained as follows:

$$D = -\in \nabla\emptyset + P. \tag{6.6}$$

where $\emptyset$ and $\in$ represent the corresponding electric potential and relative permittivity of GRNC.

6.2.2 Continuum Model of GRNC Wires

The continuum mechanics based analytical model was developed by considering GRNC as a continuum medium. We consider the GRNC nanowire having a cylindrical shape with constant cross-sectional area of length L and diameter $2a$. The flexoelectric coefficients of GRNC can be obtained from Eqs. (6.3b) and (6.4). The relationship between the stresses and strains in nanowire can be expressed as follows:

$$\begin{pmatrix} \varepsilon_{xx} \\ \varepsilon_{yy} \\ \varepsilon_{zz} \\ 2\varepsilon_{yz} \\ 2\varepsilon_{zx} \\ 2\varepsilon_{xy} \end{pmatrix} = \frac{1}{E} \begin{pmatrix} 1 & -\vartheta & -\vartheta & 0 & 0 & 0 \\ -\vartheta & 1 & -\vartheta & 0 & 0 & 0 \\ -\vartheta & -\vartheta & 1 & 0 & 0 & 0 \\ 0 & 0 & 0 & 2(1+\vartheta) & 0 & 0 \\ 0 & 0 & 0 & 0 & 2(1+\vartheta) & 0 \\ 0 & 0 & 0 & 0 & 0 & 2(1+\vartheta) \end{pmatrix} \times \begin{pmatrix} \sigma_{xx} \\ \sigma_{yy} \\ \sigma_{zz} \\ \tau_{yz} \\ \tau_{zx} \\ \tau_{xy} \end{pmatrix}, \tag{6.7}$$

in which E and ϑ represent Young's modulus and Poisson's ratio.

We assumed that the free end of GRNC nanowire is purely subjected to the transverse force (f_x) and no torque is induced in it. Hence, according to Saint-Venant's pure bending theory, the stress generated in nanowire can be expressed as follows (Green and Zerna, 2012):

$$\begin{pmatrix} \sigma_{xx} \\ \sigma_{yy} \\ \sigma_{zz} \\ \tau_{yz} \\ \tau_{zx} \\ \tau_{xy} \end{pmatrix} = \begin{pmatrix} 0 \\ 0 \\ -\frac{f_x}{I}x(L-z) \\ \frac{f_x(3+2\vartheta)}{8I(1+\vartheta)}\left(a^2 - x^2 - \frac{1-2\vartheta}{3+2\vartheta}y^2\right) \\ -\frac{f_x(1+2\vartheta)}{4I(1+\vartheta)}yx \\ 0 \end{pmatrix}, \tag{6.8}$$

where $I = (\pi/4)a^4$ is the moment of inertia of nanowire. By making use of Eqs. (6.7) and (6.8), the strain fields in the nanowire can be obtained as:

$$\begin{pmatrix} \varepsilon_{xx} \\ \varepsilon_{yy} \\ \varepsilon_{zz} \\ 2\varepsilon_{yz} \\ 2\varepsilon_{zx} \\ 2\varepsilon_{xy} \end{pmatrix} = \frac{f_x}{EI} \begin{pmatrix} \vartheta(L-z)x \\ \vartheta(L-z)x \\ -(L-z)x \\ \dfrac{(3+2\vartheta)\left(a^2 - x^2 - \dfrac{1-2\vartheta}{3+2\vartheta}y^2\right)}{4} \\ -\dfrac{(1+2\vartheta)}{2}yx \\ 0 \end{pmatrix}, \tag{6.9}$$

in which non-zero strain gradient components are

$$\varepsilon_{xx,y} = \varepsilon_{yy,y} = \tfrac{\vartheta f_x}{EI}(L-z), \quad \varepsilon_{xx,z} = \varepsilon_{yy,z} = -\tfrac{\vartheta f_x}{EI}x,$$

$$\varepsilon_{zz,y} = -\tfrac{f_x}{EI}(L-z), \;\; \varepsilon_{zz,z} = \tfrac{xf_x}{EI},$$

$$\varepsilon_{yz,x} = -\tfrac{f_x}{2EI}(1-2\vartheta)y, \; \varepsilon_{yz,y} = -\tfrac{f_x}{2EI}(3+2\vartheta)x,$$

$$\varepsilon_{zx,x} = -\tfrac{f_x}{2EI}(1+2\vartheta)x, \; \varepsilon_{zx,y} = -\tfrac{f_x}{2EI}(1+2\vartheta)y. \tag{6.10}$$

Hence, the material can be known as piezoelectric and flexoelectric when it provides polarization (electric response) due to the non-zero strain and strain gradient, respectively, and it can be seen from Eqs. (6.2a) and (6.2b).

By solving the simultaneous Eqs. (6.2), (6.3), (6.4), (6.9) and (6.10), we have

$$P = \frac{f_x}{EI} \begin{pmatrix} -\left(\dfrac{1}{2} + \vartheta\right) e_{15}xy \\ \dfrac{(3+2\vartheta)}{4} e_{15}\left(a^2 - x^2 - \dfrac{1-2\vartheta}{3+2\vartheta}y^2\right) + F(L-z) \\ (2\vartheta e_{31} - e_{33})x(L-z) + x[\mu_{11} - 2\mu_{111}(1+\vartheta) - 2\mu_{14}\vartheta] \end{pmatrix}, \tag{6.11}$$

where $F = \mu_{11}\vartheta + \mu_{14}\vartheta - \mu_{14}$.

In case of piezoelectric effect, the polarization effect in the nanowire is generated due to bound charges instead of free charges. From Eq. 6.5, we can obtain the surface charge density of nanowire as $\rho_s = 0$ (in case of flexoelectric effect, the polarization is produced only due to surface charge density). On both the end surfaces of nanowire, the surface charge density can be neglected because nanowire does not carry a substantial inherent electric field inside in it because of its large aspect ratio. Hence, the electric charge density due to only piezoelectric effect (without flexoelectricity) in the GRNC nanowire can be introduced as:

$$\rho_v = -\nabla.P = \frac{f_x[2(1+\vartheta)e_{15} + 2\vartheta e_{31} - e_{33}]x}{EI} = Ax\,, \tag{6.12}$$

where $A = \frac{f_x[2(1+\vartheta)e_{15}+2\vartheta e_{31}-e_{33}]}{EI}$.

By combining Poisson's Eqs. (6.5) and (6.6), the relationship between the electric charge density (ρ_v) and electric potential ($\emptyset$) can be obtained as follows:

$$\nabla^2\emptyset = -\frac{\rho_v}{\epsilon}. \tag{6.13}$$

Subsequently, Poisson's Eqs. (6.5) and (6.6) formulated in the form of cylindrical coordinates as follows:

$$\frac{1}{r}\frac{\partial}{\partial r}\left(r\frac{\partial\emptyset}{\partial r}\right) + \frac{1}{r^2}\frac{\partial^2\emptyset}{\partial\theta^2} + \frac{\partial^2\emptyset}{\partial z^2} = -\frac{\rho_v}{\epsilon} = -\frac{Ar}{\epsilon}\sin\theta. \tag{6.14a}$$

Initially, Eq. (6.14a) is solved by combining of general solution ($\emptyset^{\#}$) of homogeneous differential equation and particular solution ($\emptyset^{*}$) of non-homogeneous differential equation, which can be chosen to be independent of z-coordinate as right side of this Eq. is independent of z. In this, the following boundary condition can be considered in Eq. (6.14a) to get general and particular solutions.

$$\emptyset|_{r=0} \neq \infty \text{ and } \emptyset|_{r=\infty} = 0. \tag{6.14b}$$

As the piezoelectric charge presents only in GRNC nanowire, the distribution of electric potential should satisfy the following conditions:

$$r > a, \quad A = 0, \tag{6.14c}$$

$$r \leq a, \quad A \neq 0. \tag{6.14d}$$

To solve the general solution of homogeneous differential equation, we can ignore the terms on right-hand side of Eq. (6.14a) considering $\emptyset^{\#} = R(r,\theta)Z(z)$. Thus, Eq. (6.14a) can be re-written as:

$$\frac{1}{Rr}\frac{\partial}{\partial r}\left(r\frac{\partial R}{\partial r}\right) + \frac{1}{Rr^2}\frac{\partial^2 R}{\partial\theta^2} + \frac{1}{Z}\frac{d^2 Z}{dz^2} = 0. \tag{6.15}$$

From Eqs. (6.5) and (6.12), it can be noted that the surface charge density is independent of z. Hence, the electric potential $\emptyset = \emptyset(x, y) = \emptyset(r, \theta)$(in cylindrical coordinate) is also independent of z.

In Eq. (6.15), the first two terms are functions of r and θ, while the third term is a function of z. Hence, to solve Eq. (6.15), functions R and Z must fulfill the condition expressed by below relations:

$$\frac{1}{Rr}\frac{\partial}{\partial r}\left(r\frac{\partial R}{\partial r}\right) + \frac{1}{Rr^2}\frac{\partial^2 R}{\partial \theta^2} = q^2, \tag{6.16a}$$

$$\frac{1}{Z}\frac{d^2 Z}{dz^2} = -q^2, \tag{6.16b}$$

where q is a constant. To obtain an exact solution, the constant q must be equal to 0. Hence,

$$Z(z) = A_1 z + A_2, \tag{6.17}$$

in which A_1 and A_2 are integration constants/unknown coefficients and we can determine value A_1 and A_2 for function Z(z). By using the procedure of series expansion of R with suitable functions, Eq. (6.16a) can be solved and the function $R(r, \theta)$ can be expressed as:

$$R(r, \theta) = R_0(r) + \sum_{n=1}^{\infty}[R_{n1}(r)\cos(n\theta) + R_{n2}(r)\sin(n\theta)]. \tag{6.18}$$

Consequently, by determining $R_0(r)$, $R_{n1}(r)$ and $R_{n2}(r)$, the expression of $R(r, \theta)$ can be obtained. Substituting Eq. (6.18) into Eq. (6.16a), the corresponding equations can be obtained as:

$$\frac{1}{r}\frac{\partial}{\partial r}\left(r\frac{\partial R_0}{\partial r}\right) = 0, \tag{6.19a}$$

$$\frac{1}{r}\frac{\partial}{\partial r}\left(r\frac{\partial R_{n1}}{\partial r}\right) - \frac{n^2 R_{n1}}{r^2} = 0 \qquad n = 1, 2, 3 \ldots \tag{6.19b}$$

$$\frac{1}{r}\frac{\partial}{\partial r}\left(r\frac{\partial R_{n2}}{\partial r}\right) - \frac{n^2 R_{n2}}{r^2} = 0 \qquad n = 1, 2, 3 \ldots \tag{6.19c}$$

Using Eq. (6.19a), we can obtain

$$R_0(r) = B_1 \ln(r) + B_2. \tag{6.20}$$

In Eqs. (6.19b) and (6.19c), the terms $R_{n1}(r)$ and $R_{n2}(r)$ can be obtained as follows:

$$R_{n1}(r) = g_{n1}r^{n} + h_{n1}r^{-n}, \qquad n = 1, 2, 3 \ldots \tag{6.21a}$$

$$R_{n2}(r) = g_{n2}r^{n} + h_{n2}r^{-n}, \qquad n = 1, 2, 3 \ldots \tag{6.21b}$$

where B_1, B_2, g_{n1}, h_{n1}, g_{n2} and h_{n2} are unknown coefficients. Subsequently, the solution of Eq. (6.18) can be re-expressed as:

$$R(r,\theta) = R_0(r) + \sum_{n=1}^{\infty} R_{n1}(r)J + \sum_{n=2}^{\infty} R_{n2}(r)K$$

$$= B_1 \ln(r) + B_2 + \sum_{n=1}^{\infty}(g_{n1}r^{n} + h_{n1}r^{-n})J + \sum_{n=1}^{\infty}(g_{n2}r^{n} + h_{n2}r^{-n})K, \tag{6.22}$$

with $J = \cos(n\theta)$ and $K = \sin(n\theta)$.

Hence, the general solution $\emptyset^{\#}$ of Eq. (6.14a) can be expressed as:

$$\emptyset^{\#} = R(r,\theta)Z(z),$$

$$\emptyset^{\#} =$$

$$\left\{B_1 \ln(r) + B_2 + \sum_{n=1}^{\infty}(g_{n1}r^{n} + h_{n1}r^{-n})J + \sum_{n=1}^{\infty}(g_{n2}r^{n} + h_{n2}r^{-n})K\right\}(A_1 z + A_2). \tag{6.23}$$

The solution of following second-order non-homogeneous differential Eq. (6.24) is equal to the particular solution ($\emptyset^{*}$) of Eq. (6.14a) and it can be formulated as:

$$\frac{1}{r}\frac{\partial}{\partial r}\left(r\frac{\partial \emptyset^{*}}{\partial r}\right) + \frac{1}{r^2}\frac{\partial^2 \emptyset^{*}}{\partial \theta^2} = -\frac{Ar}{\epsilon}\sin\theta. \tag{6.24}$$

By using the approach of series expansion of $\emptyset^{*}$ with suitable functions, Eq. (6.24) can also be determined as follows:

$$\emptyset^{*}(r,\theta) = \emptyset_0(r) + \sum_{m=1}^{\infty} \emptyset_{n1}(r)J + \emptyset_{n2}(r)K. \tag{6.25}$$

Then, by calculating $\emptyset_0(r), \emptyset_{n1}(r)$ and $\emptyset_{n2}(r)$, the expression of $\emptyset^{*}$can be derived. One can obtain the series of following Eqs. (6.26a – 6.26d) by substituting Eq. (6.25) into Eq. (6.24) as follows:

$$\frac{1}{r}\frac{\partial}{\partial r}\left(r\frac{\partial \emptyset_0}{\partial r}\right) = 0, \tag{6.26a}$$

$$\frac{1}{r}\frac{\partial}{\partial r}\left(r\frac{\partial \emptyset_{12}}{\partial r}\right) - \frac{1}{r^2}\emptyset_{12} = -\frac{Ar}{\epsilon}, \tag{6.26b}$$

$$\frac{1}{r}\frac{\partial}{\partial r}\left(r\frac{\partial \emptyset_{n1}}{\partial r}\right)-\frac{n^2\emptyset_{n1}}{r^2}=0, \qquad n = 1,2,3\ldots \tag{6.26c}$$

$$\frac{1}{r}\frac{\partial}{\partial r}\left(r\frac{\partial \emptyset_{n2}}{\partial r}\right)-\frac{n^2\emptyset_{n2}}{r^2}=0. \qquad n = 1,2,3\ldots \tag{6.26d}$$

The solutions of Eqs. (6.26a – 6.26d) can obtained using the following relations:

$$\emptyset_0(r) = C_1\ln(r) + C_2, \tag{6.27a}$$

$$\emptyset_{12}(r) = C_3 r + \frac{C_4}{r} - \frac{Ar^3}{8\in}, \tag{6.27b}$$

$$\emptyset_{n1}(r) = C_{n1}r^n + d_{n1}r^{-n}\,, \qquad n = 1,2,3\ldots \tag{6.27c}$$

$$\emptyset_{n2}(r) = C_{n2}r^n + d_{n2}r^{-n}\,, \qquad n = 2,3,4\ldots \tag{6.27d}$$

in which C_1, C_2, C_3, C_4, c_{n1}, d_{n1}, c_{n2} and d_{n2} are unknown coefficients. Hence, a particular solution $\emptyset^*$can be formulated as follows:

$$\emptyset^* = \emptyset_0(r) + \emptyset_{12}(r)\sin(\theta) + \sum_{m=1}^{\infty}\emptyset_{n1}(r)J + \sum_{n=2}^{\infty}\emptyset_{n2}(r)K$$

$$= C_1\ln(r) + C_2 + \left(C_3 r + \frac{C_4}{r} - \frac{Ar^3}{8\in}\right)\sin(\theta) + \sum_{n=1}^{\infty}(c_{n1}r^n + d_{n1}r^{-n}\,)J$$

$$+\sum_{n=2}^{\infty}(c_{n2}r^n + d_{n2}r^{-n})K. \tag{6.28}$$

Now, the solution of Eq. (6.14) can be formulated as:

$$\emptyset = \emptyset^{\#} + \emptyset^*,$$

$$\emptyset = \left[B_1\ln(r) + B_2 + \sum_{n=1}^{\infty}(g_{n1}r^n + h_{n1}r^{-n})J + \sum_{n=1}^{\infty}(g_{n2}r^n + h_{n2}r^{-n})K\right]z + C_1\ln(r)$$

$$+C_2 + \left(C_3 r + \frac{C_4}{r} - \frac{Ar^3}{8\in}\right)\sin(\theta) + \sum_{n=1}^{\infty}(c_{n1}r^n + d_{n1}r^{-n}\,)J$$

$$+\sum_{n=2}^{\infty}(c_{n2}r^n + d_{n2}r^{-n})K. \tag{6.29a}$$

One can obtain a piecewise function divided by $r = a$ using the boundary conditions $\emptyset|_{r=0} \neq \infty$ and $\emptyset|_{r=\infty} = 0$, when $r > a$, $A = 0$ as follows:

$$\emptyset = \begin{cases} \left[B_2 + \sum_{n=1}^{\infty}(g_{n1}r^n)J + \sum_{n=1}^{\infty}(g_{n2}r^n)J\right]z + C_2 + \left(C_3 r - \dfrac{Ar^3}{8\,\epsilon}\right)\sin\theta \\ \qquad + \sum_{n=1}^{\infty}(C_{n1}r^n)J + \sum_{n=1}^{\infty}(C_{n2}r^n)K, \quad r \le a \\ \left[\sum_{n=1}^{\infty}(h_{n1}r^{-n})J + \sum_{n=1}^{\infty}(h_{n2}r^{-n})K\right]z + \left(\dfrac{C_4}{r}\right)\sin\theta \\ \qquad + \sum_{n=1}^{\infty}(d_{n1}r^{-n})J + \sum_{n=2}^{\infty}(d_{n2}r^{-n})K, \quad r > a \end{cases} \quad . \qquad (6.29b)$$

Making use of continuity conditions of the electric field ($\emptyset$) and charge at the surface ($r = a$) of GRNC nanowire and for obtaining all the unknown coefficients, the free space can be written as follows:

$$\emptyset|_{r=a^-} = \emptyset|_{r=a^+},$$

$$(D_i m_i)|_{r=a^-} - (D_i m_i)|_{r=a^+} = \rho_s = 0\,, \qquad (6.30)$$

where m indicates the exterior normal unit vector $(\cos\theta\,, \sin\theta\,, 0)$.

The following two equations can be obtained by substituting Eq. (6.29) into the Eq. (6.30):

$$\left[B_2 + \sum_{n=1}^{\infty}(g_{n1}a^n)J + \sum_{n=1}^{\infty}(g_{n2}a^n)K\right]z + C_2 + \left(C_3 a - \frac{Aa^3}{8\,\epsilon}\right)\sin\theta + \sum_{n=1}^{\infty}(c_{n1}a^n)J$$
$$+ \sum_{n=2}^{\infty}(c_{n2}a^n)K$$
$$= \left[\sum_{n=1}^{\infty}(h_{n1}a^{-n})J + \sum_{n=1}^{\infty}(h_{n2}a^{-n})K\right]z + \left(\frac{C_4}{a}\right)\sin\theta + \sum_{n=1}^{\infty}(d_{n1}a^{-n})J$$
$$+ \sum_{n=2}^{\infty}(d_{n2}a^{-n})K, \qquad (6.31a)$$

and

$$-\in\left\{\left[\sum_{n=1}^{\infty}(ng_{n1}a^{n-1})J+\sum_{n=1}^{\infty}(ng_{n2}a^{n-1})K\right]z+\left(C_3-\frac{3Aa^2}{8\in}\right)\sin\theta+\sum_{n=1}^{\infty}(nc_{n1}a^{n-1})J\right.$$

$$\left.+\sum_{n=2}^{\infty}(nc_{n2}a^{n-1})K\right\}+F(L-z)\sin\theta$$

$$=-\in_0\left\{\left[\sum_{n=1}^{\infty}(-nh_{n1}a^{-n-1})J+\sum_{n=1}^{\infty}(-nh_{n2}a^{-n-1})K\right]z-\left(\frac{C_4}{a^2}\right)\sin\theta\right.$$

$$\left.+\sum_{n=1}^{\infty}(-nd_{n1}a^{-n-1})J+\sum_{n=2}^{\infty}(-nd_{n2}a^{-n-1})K\right\}. \tag{6.31b}$$

The following system of equations can be obtained by comparing the coefficients of J and K appeared in Eqs. (6.31a) and (6.31b):

$$g_{n1}a^nz+c_{n1}a^n=h_{n1}a^{-n}z+d_{n1}a^{-n}-\in(ng_{n1}a^{n-1}z+nc_{n1}a^{n-1})$$
$$=-\in_0(-nh_{n1}a^{-n-1}z-nd_{n1}a^{-n-1}),\quad n=1,2,3,4\dots \tag{6.32a}$$

$$g_{n2}a^nz+c_{n2}a^n=h_{n2}a^{-n}z+d_{n2}a^{-n}-\in(ng_{n2}a^{n-1}z+nc_{n2}a^{n-1})$$
$$=\in_0(nh_{n2}a^{-n-1}z+nd_{n2}a^{-n-1}),\qquad n=2,3,4,5\dots \tag{6.32b}$$

$$g_{12}az+C_3a-\frac{Aa^3}{8\in}=h_{12}a^{-1}z+C_4a^{-1}-\in\left(g_{12}z+C_3-\frac{3Aa^2}{8\in}\right)+\frac{Ff_x}{EI}(L-z)$$
$$=\in_0(h_{12}a^{-2}z+C_4a^{-2}), \tag{6.32c}$$

$$B_2z+C_2=0, \tag{6.32d}$$

where B_2, $C_{1\text{-}4}$, C_{n1}, d_{n1}, C_{n2}, d_{n2}, g_{n1}, h_{n1}, g_{n2} and h_{n2} are unknown coefficients.

Then, by comparing the respective coefficients of z and constant terms in Eq. (6.32a – 6.32d), the expressions of coefficients in Eq. (6.29) can be determined as follows:

$$g_{n1}=c_{n1}=h_{n1}=d_{n1}=0,\qquad n=1,2,3\dots$$
$$g_{n2}=c_{n2}=h_{n2}=d_{n2}=0,\qquad n=2,3,4\dots$$
$$B_2=g_{21}=h_{21}=g_{22}=h_{22}=C_2=0,$$
$$C_3=\frac{Aa^2(3\in+\in_0)}{8\in(\in+\in_0)}+\frac{Ff_xL}{EI(\in+\in_0)},C_4=\frac{Aa^4}{4(\in+\in_0)}+\frac{Ff_xLa^2}{EI(\in+\in_0)},$$

$$g_{12} = -\frac{Ff_x}{EI(\in + \in_0)}, h_{12} = -\frac{Ff_x a^2}{EI(\in + \in_0)}. \tag{6.33}$$

Finally, the solution for the distribution of electric potential about the GRNC nanowire can be obtained as follows:

$$\emptyset = \begin{cases} \frac{f_x}{EI}\left[\frac{2(1+\vartheta)e_{15} + 2\vartheta e_{31} - e_{33}}{8 \in}\left(\frac{3 \in + \in_0}{\in + \in_0} a^2 r - r^3\right) + \frac{\vartheta\mu_{11} + \mu_{14}\vartheta - \mu_{14}}{\in + \in_0}(L - z)r\right]\sin\theta, \\ r \le a \\ \frac{f_x}{EI(\in + \in_0)r}\left[\frac{2(1+\vartheta)e_{15} + 2\vartheta e_{31} - e_{33}}{4}(a^4) + (\vartheta\mu_{11} + \mu_{14}\vartheta - \mu_{14})(a^2)(L - z)\right]\sin\theta. \\ r > a \end{cases} \tag{6.34}$$

If the flexoelectric effect is not considered ($\mu_{11} = \mu_{14} \to 0$), then Eq. (6.34) reduces to

$$\emptyset = \begin{cases} \frac{f_x}{EI}\left[\frac{2(1+\vartheta)e_{15} + 2\vartheta e_{31} - e_{33}}{8 \in}\left(\frac{3 \in + \in_0}{\in + \in_0} a^2 r - r^3\right)\right]\sin\theta, \\ r \le a \\ \frac{f_x}{EI(\in + \in_0)r}\left[\frac{2(1+\vartheta)e_{15} + 2\vartheta e_{31} - e_{33}}{4}(a^4)\right]\sin\theta. \\ r > a \end{cases} \tag{6.35}$$

These estimates are in coherence with the results obtained by Shao et al. (2010). From above Eq. (6.35), the maximum potential is generated at the surface (r = a) of nanowire on the tension ($\theta = -90^0$) and compression ($\theta = +90^0$) sides which can be written as:

$$\emptyset_{ten,com}^{max} = \mp \frac{f_x}{\pi E(\in + \in_0)}\left[\frac{2(1+\vartheta)e_{15} + 2\vartheta e_{31} - e_{33}}{a}\right]. \tag{6.36}$$

According to the theory of strength of materials, as the GRNC nanowire is subjected to only transverse mechanical force (f_x) and then the maximum deflection can be obtained as follows (z = L):

$$\delta_{max} = \frac{f_x L^3}{3EI}. \tag{6.37}$$

From Eqs. (6.36) and (6.37), the maximum piezoelectric potential obtained in terms of maximum deflection is given by ($\mu_{11} = \mu_{14} \rightarrow 0$):

$$\emptyset_{\mathrm{ten,com}}^{\mathrm{max}} = \mp \frac{3}{4(\epsilon + \epsilon_0)} \left[\frac{(2(1+\vartheta)e_{15} + 2\vartheta e_{31} - e_{33})a^3}{L^3} \delta_{\mathrm{max}} \right]. \quad (6.38)$$

6.2.3 FE Modelling of GRNC Wires

In this sub-section, 3-D FE models were developed to validate the predictions obtained from the continuum model derived in the previous Section. In the FE analysis, the material and geometrical properties of GRNC nanowire are used same as that used in the analytical model. A commercially available software **(ANSYS-APDL)** was used for the FE analysis. The 3D multi-field 20 noded coupled-field brick elements “solid 226” with displacement and electric voltage DOF were used for FE modelling of GRNC nanowire. For piezoelectric analysis, four DOF labels can be represented as U_X, U_Y, U_Z, VOLT at each node. Figure 6.2a shows the discretization of GRNC nanowire with “Hexahedral-Quad” elements. A hexahedron refers to a topological cube, with 6 quadrilateral faces, 8 vertices, and 12 edges. It is also called a hex or a brick. The accuracy of solutions in hexahedral meshes is the highest. Figure 6.2 illustrates the loading condition, distribution of piezoelectric potential and deformation of FE model of GRNC nanowire having 50 nm diameter which is subjected to only mechanical transverse force. In FE simulations, meshing of continuum GRNC nanowire was performed by using “Hexahedral-Quad” sweep type element which results into 26923 and 5969 number of nodes and elements, respectively. The obtained FE results are discussed in Section 6.3.

6.2.3.1 Effects of Surface and Body Charge Densities

To predict the piezoelectric potential, the surface and body charge densities can be used as boundary conditions in the FE model. Contrast to the response of piezoelectricity, due to the surface charge, electric polarization is generated considering only flexoelectric effect and body charge becomes very negligible. On both the end surfaces of nanowire, the surface charge density can be neglected because nanowire does not carry a substantial inherent electric field inside in it because of its large aspect ratio.

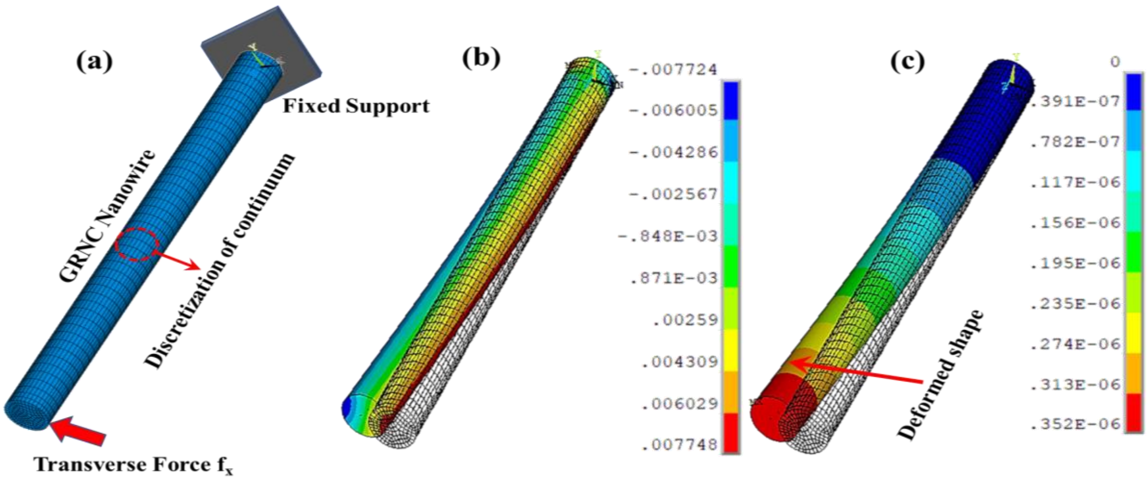

Figure 6.2: GRNC nanowire: (a) loading condition with transverse force (f_x), (b) distribution of maximum and minimum electric potentials and (c) deformation.

6.3 Results and Discussions

In this Section, the results obtained from the continuum and numerical models for studying the electromechanical behavior of GRNC wires, considering both piezoelectric and flexoelectric effects, are presented and discussed. The electromechanical responses such as the distribution of electric potential and deflection of cylindrical GRNC cantilevered nanowire were investigated. The effective properties of GRNC determined by means of micromechanics and FE models were used for GRNC wires. Considering the volume fraction of graphene as 5%, the effective properties of GRNC were determined, as summarized in Table 6.1.

Table 6.1: Effective properties of GRNC ($v_g = 0.05$).

Properties	**Analytical Model**	**FE Model**
E (GPa)	53.24	53.29
$\boldsymbol{\vartheta}$	0.39	0.39
$\mathbf{e_{31}}$ **(C/m²)**	-1.052×10^{-4}	-1.058×10^{-4}
$\mathbf{e_{33}}$ **(C/m²)**	0.0168	0.0167
$\mathbf{e_{15}}$ **(C/m²)**	-4.473×10^{-5}	-4.515×10^{-5}
$\boldsymbol{\in_{33}}$ **(F/m)**	3.412×10^{-11}	3.415×10^{-11}

In this, we assumed the flexoelectric coefficient $\mu_{11} \approx \mu_{14} \approx 10^{-9}\ \mathrm{C/m}$. A GRNC nanowire of diameter $(2a)$ 50 nm and length 600 nm was considered. From Eq. (6.34), it can be noted that the electric potential is directly proportional to the transverse force on the nanowire. The free end of GRNC wire was subjected to the transverse force $f_x = 80\mathrm{nN}$ for further analysis. Figure 6.3 illustrates the distribution of electric potential at different radii in the transverse cross-section of GRNC nanowire at $z = l/2$ (=300 nm) with and without considering flexoelectricity. It may be observed that there is substantial increase in the distribution of electric potential when the flexoelectric effect is considered ($\mu_{11} = \mu_{14} = 1$ nC/m). It can be observed from Fig. 6.3 that the electric potential in the tensile part of nanowire is positive while it is negative in the compressive part, and they are antisymmetric about the x-axis. The electric potential of GRNC nanowire is improved significantly when the flexoelectric effect is considered for the 50 nm diameter with the application of 80 nN force over that of a conventional nanowire (i.e., without flexoelectricity). From Figs. 6.2 and 6.3, it is clearly seen that the maximum and minimum numerical values of electrical potential present at the extreme surface along the length of nanowire have the opposite signs. All values are separated by a reference line of zero-valued electric potential in the mid of nanowire. According to our formulation, the first case $(r \leq a)$ of Eq. (6.34), the function of electric potential is directly proportional to the square of radius (a^2) of nanowire but in the second case $[(r > a)$ and $(r < -a)]$ it is proportional to the fourth power of radius (a^4) of nanowire. Therefore, the maximum value of electric potential is obtained when $r = a$ in both the cases and it decreases when $r < -a$ or $r > a$ while it increases when $r < a$. It is obviously seen from Eq. (6.38) that the maximum electric potential is directly proportional to the maximum deflection and inversely proportional to the aspect ratio of nanowire. The respective values of electric potentials determined by using the analytical and FE models are 7.45 mV and 7.72 mV for 50 nm diameter. From Fig. 6.3(b), it can be observed that the analytical and FE models show better agreement for distribution of electric potential considering only piezoelectric effect. Figure 6.4 demonstates the 3D representation of distribution and contours of electric potential in the transverse cross-section of GRNC nanowire at $z = l/2$ (=300 nm) with and without considering flexoelectricity. It can be seen that the distribution of electric potential of GRNC nanowire considering the flexoelectric effect (Fig. 6.4a) shows the better enhancement compared to the distribution of electric potential without considering the flexoelectric effect (Fig. 6.4b). The colorbars in Fig. 6.4 represent clear increment in the value of electric potential. Contours under the mesh plot show the variation of electric potential along the length of nanowire plotted in x–y plane. Similar to Fig. 6.3 it is obviously seen that the maximum and minimum values of electrical potential occur at the extreme surfaces of nanowire. It is clearly observed from Figs. (6.2b) and (6.4b) that the colorbars show the good agreement between the analytical and FE predictions for the distribution of electric potential. Figure 6.5 shows the variation of electric potential at different transverse cross-sections of GRNC nanowire along its length (z) considering the flexoelectricity. This figure illustrates the distribution of electric dipoles inside the GRNC nanowire with cantilever boundary condition and body charge. As expected, it can be observed that the electric potential decreases as the length (z) of nanowire increases and at $z = l$, it reaches to a minimum value. This is attributed to the fact that the stresses (tensile and compressive) are maximum at the fixed end of beam (z = 0) and their values start decreasing as the point of interest along its length moves towards the free end (z = l). This results in the larger strain gradients at the fixed end of beam which eventually shows the higher electric potential. The distribution of electric potential reveals the behavior like a "parallel plate capacitor" (Fig. 6.2). Because of the relatively small diameter compared to the length of nanowire, the charges on both ends of nanowire shows an insignificant effect on the electric field.

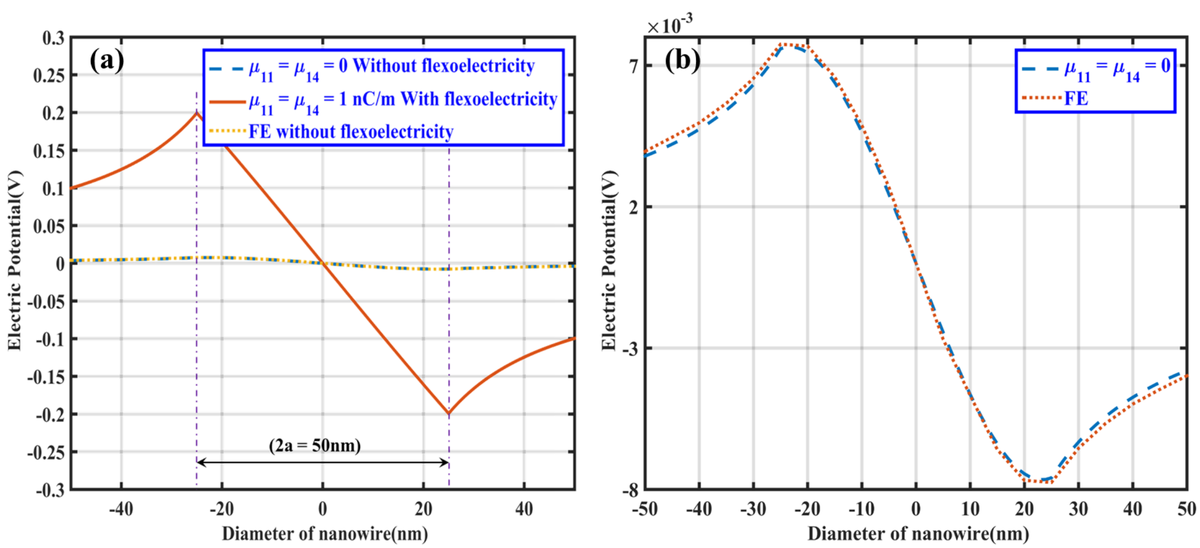

Figure 6.3: Variation of electric potential in the transverse cross-section of GRNC nanowire at $z = l/2$ (=300 nm) (a) with and without considering flexoelectricity, and (b) considering only piezoelectricity using analytical and FE model.

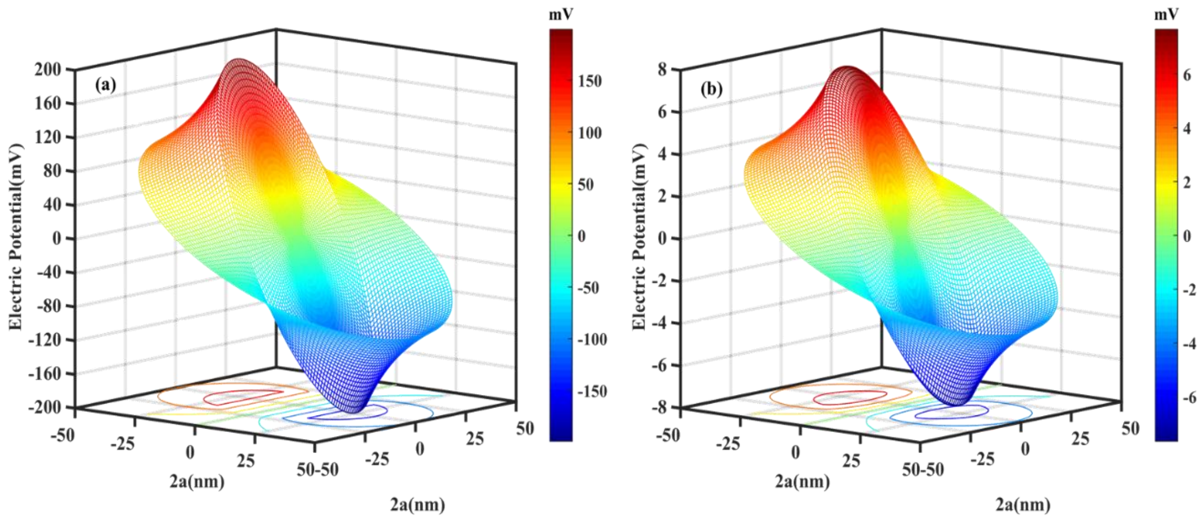

Figure 6.4: The 3D representation of distribution and contours of electric potential in the transverse cross-section of GRNC nanowire at $z = l/2$ (=300 nm) (a) with and (b) without considering flexoelectricity.

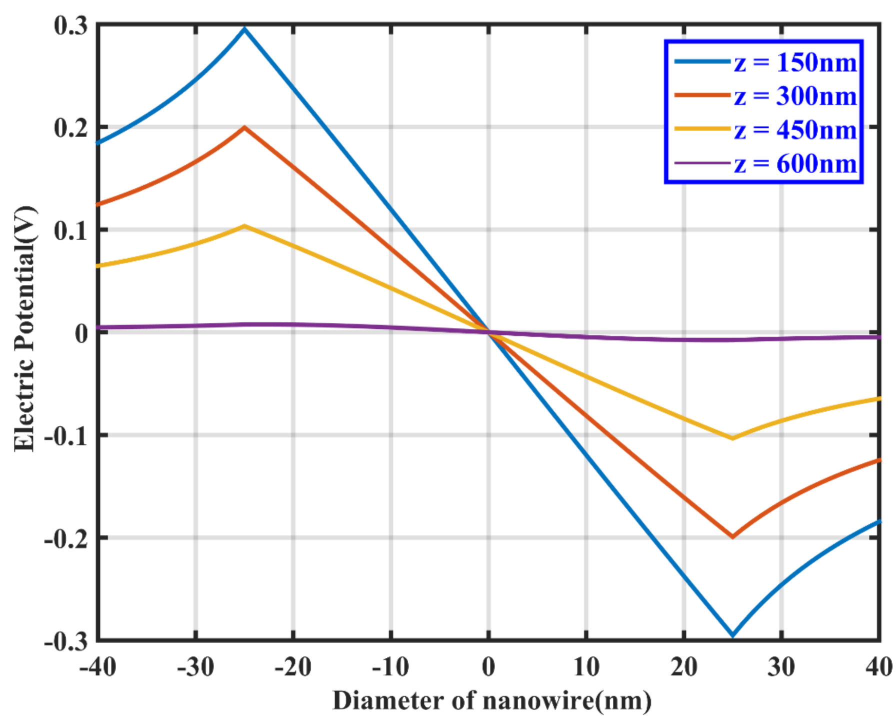

Figure 6.5: Variation of electric potential at different transverse cross-sections of GRNC nanowire along its length considering the flexoelectricity.

Next, we considered different values of flexoelectric coefficients. For the first set, we considered the same magnitude of flexoelectric coefficients: $\mu_{11} = \mu_{14} =$

$1\,\mathrm{nC/m}$; $\mu_{11} = \mu_{14} = -1\,\mathrm{nC/m}$; $\mu_{11} = \mu_{14} = 0\ \mathrm{nC/m}$. For the other set, we considered the different values: $\mu_{11} = 0.75\ \mathrm{nC/m}$ and $\mu_{14} = 1.25\ \mathrm{nC/m}$; $\mu_{11} = 0.5\ \mathrm{nC/m}$ and $\mu_{14} = 2.0\ \mathrm{nC/m}$; and $\mu_{11} = 2.0\ \mathrm{nC/m}$ and $\mu_{14} = 0.5\ \mathrm{nC/m}$. Figure 6.6 depicts the variation of electric potential in the transverse cross-section of GRNC nanowire at $z = l/2$ (=300 nm) considering different values of flexoelectric constants. It can be noticed that the incorporation flexoelectric effect significantly influences the distribution of electric potential of GRNC nanowire compared to that of the conventional nanowire ($\mu_{11} = \mu_{14} = 0\ \mathrm{nC/m}$). This is attributed to the fact that the term $\left\{\frac{\vartheta\mu_{11}+\mu_{14}\vartheta-\mu_{14}}{\epsilon+\epsilon_0}\right\}$ in Eq. (6.34) influences the distribution of electric potential of GRNC nanowire in which μ_{11} and μ_{14} are the longitudinal and shear flexoelectric coefficients, respectively. It can be observed that the shear flexoelectric coefficient largely influences the response compared to that of the longitudinal flexoelectric coefficient but usually the latter is larger than that of the former in magnitude.

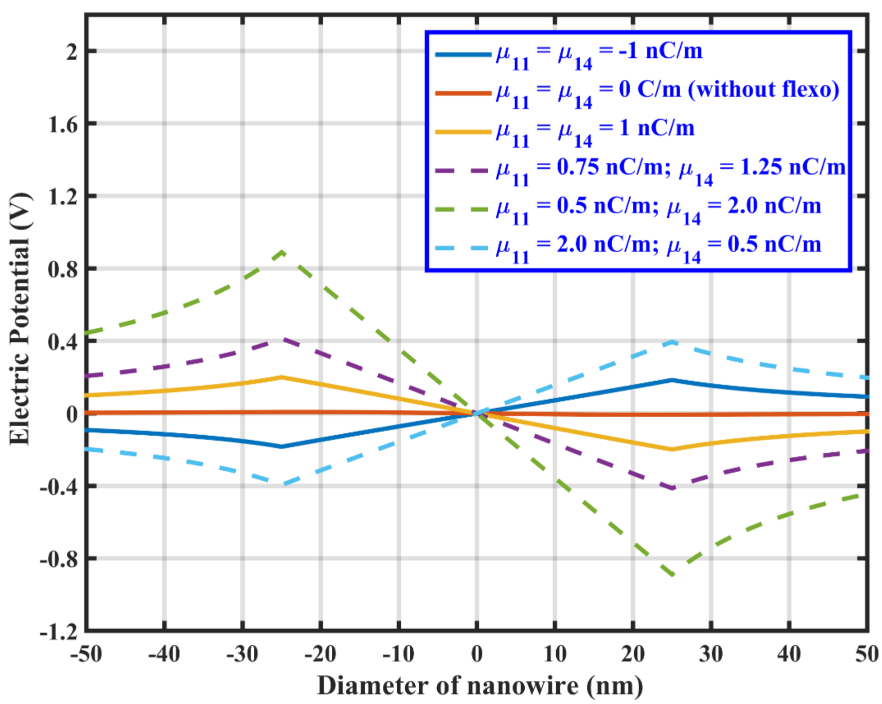

Figure 6.6: Variation of electric potential in the transverse cross-section of GRNC nanowire at $z = l/2$ (=300 nm) considering different values of flexoelectric constants.

Figure 6.7 illustrates the variation of electric potential against the diameter of GRNC nanowire in its transverse cross-section at $z = l/2$ (=300 nm) considering flexoelectricity. Five discrete values of diameters of GRNC nanowires were considered: 30 nm, 40 nm, 50 nm, 60 nm and 70 nm. As expected it can be observed that on decreasing the diameter the voltage increases because the flexoelectric effect is a size-dependent phenomenon. Hence, it is obvious that the flexoelectric effect cannot be neglected for studying the electromechanical behavior of thin structures. The relative difference of electric voltage $\{(V_f - V_0)/V_0\}$ is the ratio of difference of electric voltages of GRNC nanowire with and without considering the flexoelectric effect $\{(V_f - V_0)\}$ and without considering the flexoelectric effect $\{V_0\}$. Figure 6.8 demonstrates the variation of electric voltage $\{(V_f - V)/V_0\}$ against the radius of GRNC nanowire in its transverse cross-section at $z = l/2$ (=300 nm). It can be noticed from Figs. 6.7 and 6.8 that the flexoelectric effect is more dominant for smaller diameter of nanowires indicating that the flexoelectric effect becomes negligible when the diameter of nanowire increases. Thus, the current results obviously reveal that the flexoelectric effect should be considered in case of bending or stretching of smaller diameter nanowires.

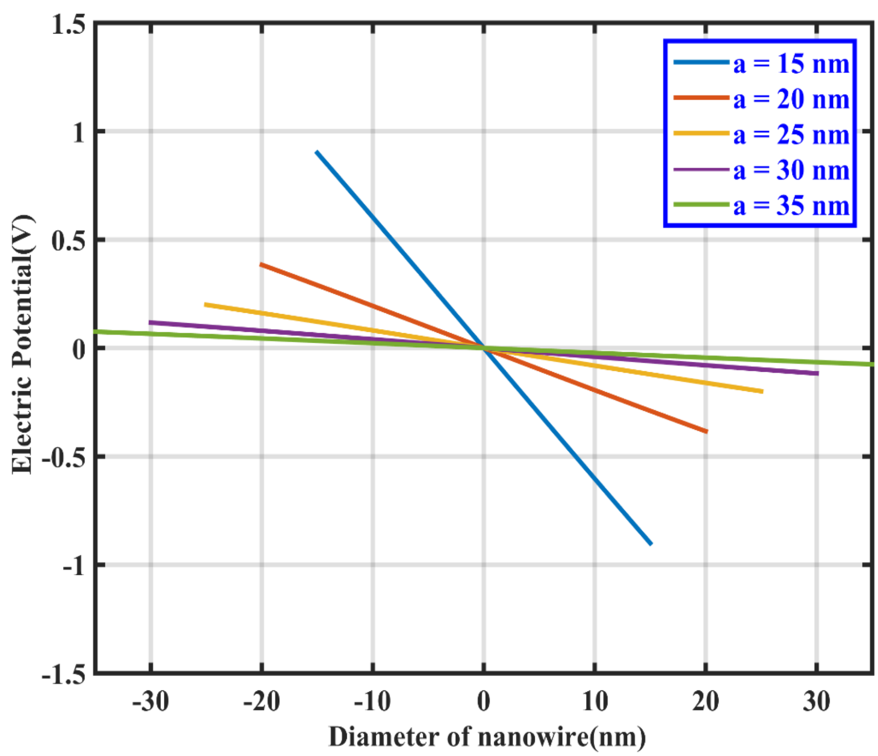

Figure 6.7: Variation of electric potential against the diameter of GRNC nanowire in its transverse cross-section at $z = l/2$ (=300 nm) considering flexoelectricity.

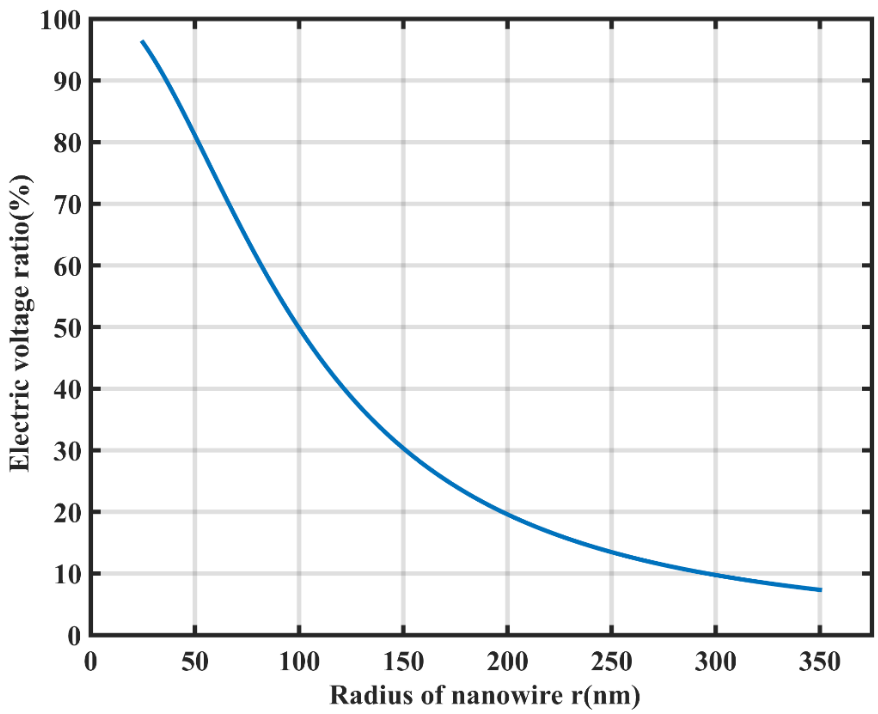

Figure 6.8: Variation of electric voltage $\{(V_f - V)/V_0\}$ against the radius of GRNC nanowire in its transverse cross-section at $z = l/2$ (=300 nm).

The variation of deflection of end point of GRNC nanowire (at $z = l$ (=600 nm)) against the transverse force imposed on its top surface is shown in Fig. 6.9. It is noticed that the value of deflection $\{\delta_{max}\}$ increases linearly with the applied transverse force. According to the simple theory of elasticity, when the piezoelectric GRNC nanowire subjected to the transverse mechanical load considering only body charge, then the solution behaves as per the elastic homogeneous solution for deflection (see Eq. 6.37). From Eq. (6.37), it can be noted that the maximum deflection of nanowire is directly proportional to the applied transverse force and cube of length of nanowire. The respective values of maximum deflection of nanowire determined using the analytical and FE models are 352.6 nm and 352.00 nm, and this comparison validates our analytical model. Results illustrated in Figs. 6.2–6.9 clearly reveal that the electric potential distribution of GRNC nanowire is significantly influenced by the incorporation of flexoelectric effect and one can tailor the electromechanical response of nanowires and thin nanostructures by varying their geometrical parameters such as radius, length and volume fraction of nano-reinforcements. Obtained results produce a fundamental basis and suggest new parameters for investigation of the electromechanical response of nanowires which find interesting NEMS applications such as field effect transistors (FETs), nanopiezotronics, piezoelectric nanogenerators, gated diode, resonators, etc.

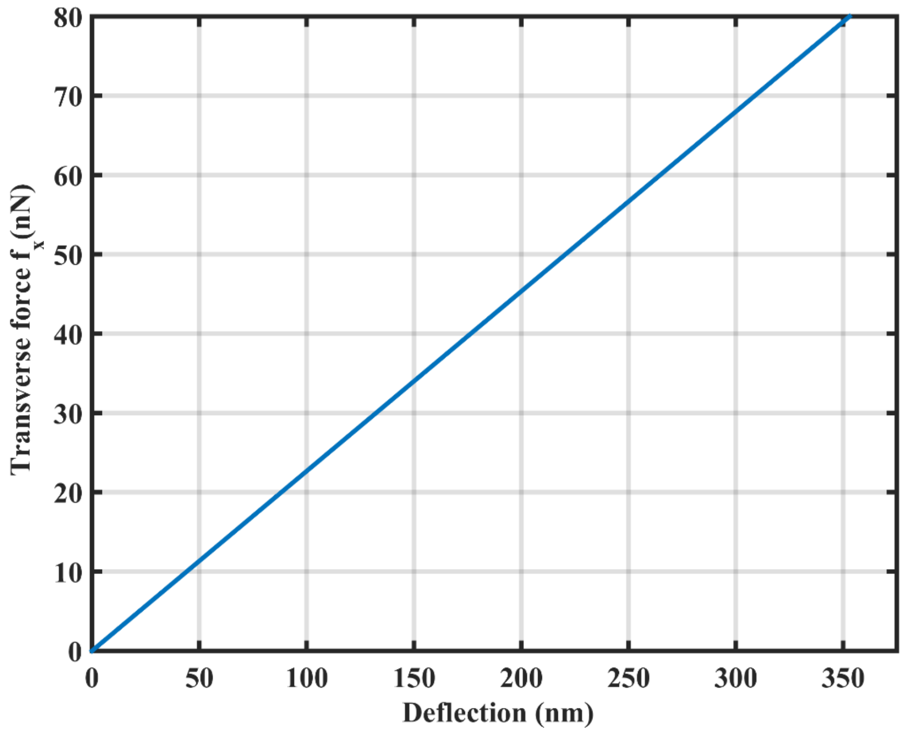

Figure 6.9: Variation of deflection of end point of GRNC nanowire (at z = l (=600 nm)) against the transverse force imposed on its top surface.

6.4 Conclusions

The electromechanical response of a novel GRNC nanowire was studied in this Chapter. An analytical model was developed for studying the distribution of electric potential in GRNC nanowire accounting the flexoelectric effect. The 3D FE models were also developed to validate the analytical predictions. The piezoelectric potential in the GRNC nanowire depends on the transverse force but it is not a function of the force acting along its axial direction. Electric potential distribution in the tensile and compressive sections of a nanowire is antisymmetric along its cross-section, which makes nanowire a "parallel plate capacitor" for the application of nanopiezotronics devices. The shear flexoelectric coefficient (μ_{14}) largely influences the response of GRNC nanowire compared to that of longitudinal flexoelectric coefficient (μ_{11}). It is concluded that the flexoelectric effect is more dominant for smaller diameter of GRNC nanowires and it cannot be ignored in case of bending or stretching of smaller diameter of nanowires as well as composite nanostructures. It is also revealed that to improve the transfer efficiency from mechanical to electrical energy, one can use the flexoelectric concept for thin nanostructures under strain gradients.

Creating NEMS structure by laminating a novel GRNC layer to the conventional fluid flowing thin shell to harvest the energy generated by its mechanical vibrations is an interesting research problem which is not studied yet. Therefore, the electromechanical behavior of laminated shell considering the flexoelectric effect is studied in the next Chapter by developing analytical and 3-D FE models.

Chapter 7

Electromechanical Behavior of Shell Laminated with GRNC layer

In this Chapter, an analytical model is developed for the elastic shell laminated with GRNC layer based on Kirchhoff–Love theory considering both piezoelectric and flexoelectric effects to investigate the electric potential distributions in it. Moreover, FE models are developed to validate the analytical results. Effect of different parameters such as various modes, GRNC layer thickness and shell radius are taken into consideration for investigating the electromechanical behavior of laminated shells.

7.1 Introduction

The review of literature presented on graphene-based composite shells indicate that graphene is the most interesting 2D material, vastly studied in recent years. The cylindrical shells are generally used to carry fluid in transport and industrial applications. Due to the flow of fluid, the mechanical kinetic energy gets generated in the fluid-flowing shell due to the structural vibrations and it can be converted to electrical energy via the use of distributed piezoelectric/flexoelectric patches attached to it. However, the study of electromechanical response of conventional thin shell laminated with GRNC layer is not carried out yet, which may find NEMS applications. Specifically, this Chapter deals with the development of an analytical model based on the theory of Kirchhoff–Love for the simply-supported elastic shell attached with GRNC layer (hereinafter the "laminated shell") to study its electromechanical response. Moreover, FE models were developed to validate the analytical results.

7.2 Continuum Model of Laminated Shell

This Section presents the development of a continuum model to investigate the electromechanical response of laminated shell, considering both the piezoelectric and flexoelectric effects.

7.2.1 Flexoelectric Effect on Electric Potential Distribution

In this sub-section, the ability of sensing and signal generation properties of laminated shell at different modes is presented. Considering the assumptions of theory of Kirchhoff–Love for a thin-walled shell, the strain developed in such a laminated shell can be divided into four components: axial and circumferential bending strains as well as and axial and circumferential membrane strains.

- **Assumptions of Kirchhoff-Love theory:**
  - The thickness of the shell is small as compared to other dimensions.
  - Straight lines normal to the mid-surface (i.e., transverse normals) before deformation remain straight after deformation.
  - The strains are infinitesimal so that all nonlinear terms are neglected.
  - The transverse normals rotate such that they remain normal to the middle surface after deformation.

The first assumption allows us to ignore the higher power terms of h/R in the mathematical formulation of shell. The second assumption (also same as plate theory assumption) allows us to neglect of transverse shear strain.

In case of semi-static or dynamic deformation, the influence of four strain components depends on the vibration modes and location. In this study, it is assumed that there is a perfect bonding exists between the elastic shell and a GRNC layer i.e., no slippage occurs between them. The GRNC layer is divided into several parts (patches) considering each patch covering the elastic shell, as illustrated in Fig. 7.1. The dimensions of patches are measured from x_1 to x_2 in the axial (x) direction and Φ_1 to Φ_2 in the circumferential (Φ) direction. Such GRNC composite patches are made by assuming the piezoelectric graphene sheet as a continuum medium reinforced into the polyimide (PI) matrix. These patches are assumed as continuous and elastic. Parameters h, R and L denote the thickness, radius and length of base shell, respectively; b denotes the width of composite patch; and h_f denotes the thickness of patch. It is assumed that $h_f <<< h$, therefore, the mass and stiffness of composite patch can be ignored. The internal strains produced in the GRNC layer are considered to be same as that of strains produced on the outer surface of base shell.

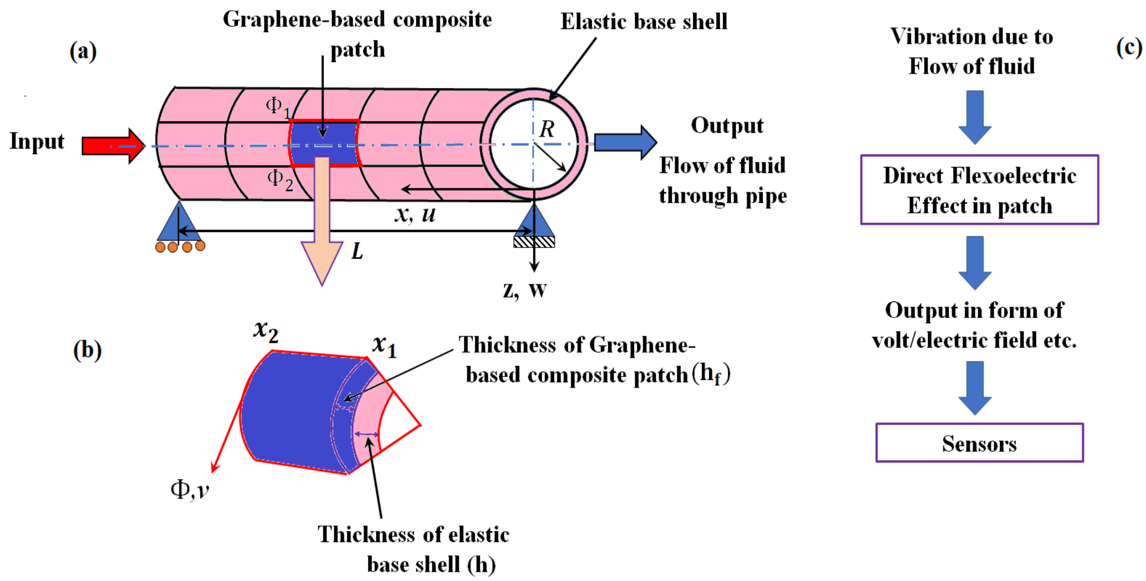

Figure 7.1: (a) Laminated shell subjected to simply supported boundary conditions (conventional elastic shell laminated with a GRNC layer/patches), (b) expanded view of patch from laminated shell, and (c) flowchart representing direct flexoelectric effect.

The direct flexoelectric effect was considered to study the modal analysis of laminated shell. The fundamental relation for the electric flux density (electric displacement) considering the direct flexoelectric effect can be written as follows:

$$D_i = e_{ijk}\,\varepsilon_{jk} + \mu_{ijkl}\,\nabla_l \varepsilon_{jk} + \epsilon_{ij}\,E_j\,, \tag{7.1}$$

in which ∇ used for gradient. Here, the patches are assumed to be attached with electrodes in the transverse direction, and the electric flux density and field in the x and Φ directions are considered as zero, and can be written as:

$$\{D_i\} = [D_x\ \ D_y\ \ D_z]^T = [0\ \ 0\ \ D_z]^T\,, \tag{7.2a}$$

$$\{E_j\} = [E_x\ \ E_y\ \ E_z]^T = [0\ \ 0\ \ E_z]^T\,. \tag{7.2b}$$

The permittivity constant matrix can be written as:

$$[\epsilon_{ij}] = \begin{bmatrix} \epsilon_{11} & 0 & 0 \\ 0 & \epsilon_{22} & 0 \\ 0 & 0 & \epsilon_{33} \end{bmatrix} = \begin{bmatrix} 0 & 0 & 0 \\ 0 & 0 & 0 \\ 0 & 0 & \epsilon_{33} \end{bmatrix}. \tag{7.3}$$

For the cylindrical shells, the gradient operator in Eq. (7.1) can be expressed as:

$$(\nabla) = \begin{bmatrix} \frac{\partial}{\partial x} & 0 & 0 & 0 & \frac{\partial}{\partial z} & \frac{1}{R}\frac{\partial}{\partial \Phi} \\ 0 & \frac{1}{R}\frac{\partial}{\partial \Phi} & 0 & \frac{\partial}{\partial z} & 0 & \frac{\partial}{\partial x} \\ 0 & 0 & \frac{\partial}{\partial z} & \frac{1}{R}\frac{\partial}{\partial \Phi} & \frac{\partial}{\partial x} & 0 \end{bmatrix}. \tag{7.4}$$

In case of a centrosymmetric crystal, which is subjected to non-homogeneous deformation, the polarization is induced due to the strain gradient; therefore, the flexoelectric effect can be examined independently. Hence, for a cubic crystal, the nonzero flexoelectric coefficients are μ_{1111}, μ_{1122} and μ_{1212}, or in the simplified matrix notation, one can write the respective terms μ_{11}, μ_{12} and μ_{44} in the following matrix form (Ma and Cross, 2001; Shu et al., 2011):

$$[\mu_{ij}] = \begin{bmatrix} \mu_{11} & \mu_{12} & \mu_{12} & 0 & 0 & 0 \\ \mu_{12} & \mu_{11} & \mu_{12} & 0 & 0 & 0 \\ \mu_{12} & \mu_{12} & \mu_{11} & 0 & 0 & 0 \\ 0 & 0 & 0 & \mu_{44} & 0 & 0 \\ 0 & 0 & 0 & 0 & \mu_{44} & 0 \\ 0 & 0 & 0 & 0 & 0 & \mu_{44} \end{bmatrix}. \tag{7.5}$$

According to the assumptions of theory of Kirchhoff–Love for thin shell, the transverse strains are neglected. Thus, the strain vector can be written as follows:

$$\begin{aligned} \{\varepsilon_{ij}\} &= [\varepsilon_{xx} \quad \varepsilon_{\Phi\Phi} \quad \varepsilon_{zz} \quad \varepsilon_{\Phi z} \quad \varepsilon_{xz} \quad \varepsilon_{x\Phi}]^T, \\ &= [\varepsilon_{xx} \quad \varepsilon_{\Phi\Phi} \quad 0 \quad 0 \quad 0 \quad 0]^T. \end{aligned} \tag{7.6}$$

Using Eqs. (7.1) to (7.6), the expression for transverse electric flux density (D_z) of the flexoelectric layer laminated to the elastic shell can be written as:

$$D_z = \mu_{12}\left(\frac{\partial \varepsilon_{xx}}{\partial z} + \frac{\partial \varepsilon_{\Phi\Phi}}{\partial z}\right) + \epsilon_{33}\, E_z. \tag{7.7}$$

The mechanical strains (ε_{ij}) include the bending and membrane strain components and can be written as:

$$\varepsilon_{ij} = \varepsilon_{ij}^0 + z k_{ij}, \tag{7.8}$$

in which ε_{ij}^{0} denote the membrane strains and terms zk_{ij} denote the bending strains. In case of flexoelectric effect, the membrane strain is very negligible, therefore, it is neglected. Using Eq. (7.8) into Eq. (7.7), the transverse electric flux density (D_z) can be obtained as follows:

$$D_z = \mu_{12}(k_{xx} + k_{\Phi\Phi}) + \epsilon_{33}\, E_z. \tag{7.9}$$

The components of bending strains of the laminated shell corresponding to the displacements can be expressed as:

$$k_{xx} = -\frac{\partial^2 w}{\partial x^2}, \tag{7.10}$$

$$k_{\Phi\Phi} = \frac{1}{R^2}\left(\frac{\partial v}{\partial \Phi} - \frac{\partial^2 w}{\partial \Phi^2}\right), \tag{7.11}$$

in which v and w are the displacements in the respective Φ and z–directions.

By substituting Eqs. (7.10) and (7.11) into Eq. (7.9), the following relation for the electric flux density can be obtained:

$$D_z = \mu_{12}\left[-\frac{\partial^2 w}{\partial x^2} + \frac{1}{R^2}\left(\frac{\partial v}{\partial \Phi} - \frac{\partial^2 w}{\partial \Phi^2}\right)\right] + \epsilon_{33}\, E_z\,. \tag{7.12}$$

In case of open-circuit condition, the electric flux density is zero ($D_z \rightarrow 0$); hence, the corresponding electric field can be obtained as:

$$E_z = -\frac{\mu_{12}}{\epsilon_{33}}\left[-\frac{\partial^2 w}{\partial x^2} + \frac{1}{R^2}\left(\frac{\partial v}{\partial \Phi} - \frac{\partial^2 w}{\partial \Phi^2}\right)\right]. \tag{7.13a}$$

Based on Maxwell's relation ($\emptyset = -E_z h_f$), the relation for electric potential (voltage) in the GRNC layer considering the flexoelectricity can be expressed as:

$$\emptyset = \frac{\mu_{12}\, h_f}{\epsilon_{33}}\left[-\frac{\partial^2 w}{\partial x^2} + \frac{1}{R^2}\left(\frac{\partial v}{\partial \Phi} - \frac{\partial^2 w}{\partial \Phi^2}\right)\right]. \tag{7.13b}$$

Hence, an arithmetic average of all voltage signals in the GRNC layer provides the total electric potential generated in it and can be obtained by integrating Eq. (7.13b) (Rao and Tzou, 2011):

$$\emptyset^{\text{flexo}} = \frac{1}{A_e}\int_{x_1}^{x_2}\int_{\Phi_1}^{\Phi_2} \emptyset\, A_x A_\Phi\, dx\, d\Phi\,, \tag{7.14a}$$

where A_e denotes the effective electrode area of the GRNC patch on the base shell and can be expressed as (Rao and Tzou, 2011):

$$A_e = \int_{x_1}^{x_2} \int_{\Phi_1}^{\Phi_2} A_x A_\Phi dxd\Phi. \qquad (7.14b)$$

A_x and A_Φ are the respective Lame parameters in the axial and circumferential directions; due to the small deformation of shell, these parameters can be taken as $A_x = 1$ and $A_\Phi = R$ and hence, the effective electrode area can be re-expressed as (Tzou et al. 2013):

$$A_e = \int_{x_1}^{x_2} \int_{\Phi_1}^{\Phi_2} Rdxd\Phi\,. \qquad (7.14c)$$

From Eqs. (7.13b and 7.14a), electric potential induced by strain gradient is given by,

$$\emptyset^{flexo} = \frac{h_f}{A_e} \int_{x_1}^{x_2} \int_{\Phi_1}^{\Phi_2} \frac{R\mu_{12}}{\epsilon_{33}} \left[-\frac{\partial^2 w}{\partial x^2} + \frac{1}{R^2} \left(\frac{\partial v}{\partial \Phi} - \frac{\partial^2 w}{\partial \Phi^2} \right) \right] dxd\Phi\,. \qquad (7.15)$$

7.2.2 Modal Analysis of Laminated Shell

We considered the simply supported laminated shell to investigate its modal analysis considering piezoelectric as well as flexoelectric effects. Figure 1 illustrates a schematic of simply supported laminated shell. The co-ordinate system (x, Φ, z) of laminated shell in which x is taken in the axial direction wherein Φ and z are taken in circumferential and radial directions of shell. u_x , v_Φ and w_z are the respective displacements in axial, circumferential and transverse directions, respectively. Therefore, in case of simply supported laminated shell, following boundary conditions at $x = 0$ and $x = L$ must be satisfied.

$$u = w = 0;\ N_x = M_x = 0, \qquad \text{at } x = 0, L \qquad (7.16a)$$

in which N_x and M_x denote the axial normal force and bending moment in shell when it deforms, respectively.

By considering the natural modal behaviors of laminated shell, the expression (7.15) for the signals can be expanded further to the modal signals. It is also assumed that all points on the cylinder oscillate harmonically at natural frequency. Using the modal expansion technique, the displacements (u_i) can be obtained as (Soedel, 2004):

$$u_i(x, \Phi, t) = \sum_{m=1}^{\infty}\sum_{n=1}^{\infty} \eta_{mn}(t) U_{imn}(x, \Phi), \quad i = x, \Phi, z \tag{7.16b}$$

in which $\eta_{mn}(t)$ and $U_{imn}(x, \Phi)$ indicate the temporal part – an amplitude factor i.e., modal participation factor and mode shape function, respectively. $\eta_{mn}(t)$ is a function of time. For free modal oscillation, all external mechanical and electric excitations are assumed to be zero and hence, modal participation factor is assumed harmonic $\eta_{mn}(t) = e^{jw_{mn}t}$ (Tzou and Zhang, 2016) where ω_{mn} is the (m, n)th natural frequency and $j = \sqrt{-1}$. Therefore, η_{mn} is assumed to be constant ($\eta_{mn} = 1$) for further analysis (Tzou, 1991; Rao and Tzou, 2011).

From Eq. (7.15), it can be observed that the electric potential is induced due to the axial and circumferential bending. Note that the displacement components of simply supported cylindrical shell with length (L) are directly proportional to the products of trigonometric functions of sine and cosine. In case of simply-supported laminated shell, the axial, circumferential and transverse mode shape functions can be obtained as:

$$\begin{aligned}
U_{xmn}(x, \Phi) &= A_{mn} \cos\left(\frac{m\pi x}{L}\right) \cos n(\Phi - \Phi_0), \\
V_{\Phi mn}(x, \Phi) &= B_{mn} \sin\left(\frac{m\pi x}{L}\right) \sin n(\Phi - \Phi_0), \\
W_{zmn}(x, \Phi) &= C_{mn} \sin\left(\frac{m\pi x}{L}\right) \cos n(\Phi - \Phi_0),
\end{aligned} \tag{7.16c}$$

where m and n denote the axial and circumferential mode numbers; A_{mn}, B_{mn} and C_{mn} denote the amplitude of shape functions.

The influence of rotary inertia can be ignored by considering transverse shear strain zero from the assumption of Kirchhoff-love theory. A_{mn}, B_{mn} and C_{mn} can be determined by solving Love's governing equations in Soedel (2004) without considering Lorentz forcing functions. For every m, n combination, we thus have three frequencies. The lowest is related with the mode where the transverse component dominates, while the other two are usually higher by an order of magnitude and are related with the mode where the displacements in the tangent plane dominate. For every m, n combination, we have taken the three combination of A_{mn}, B_{mn} and C_{mn}. By solving A_{mn}, B_{mn} in terms of C_{mn}, one can obtain:

$$\frac{A_{imn}}{C_{imn}} = -\frac{k_{13}(\rho h\omega_{imn}^2 - k_{22}) - k_{12}k_{23}}{(\rho h\omega_{imn}^2 - k_{11})(\rho h\omega_{imn}^2 - k_{22}) - k_{12}^2}, \text{and} \tag{7.16d}$$

$$\frac{B_{imn}}{C_{imn}} = -\frac{k_{23}(\rho h\omega_{imn}^2 - k_{11}) - k_{21}k_{13}}{(\rho h\omega_{imn}^2 - k_{11})(\rho h\omega_{imn}^2 - k_{22}) - k_{12}^2}, \quad i = 1, 2, 3. \tag{7.16e}$$

in which ρ is density, and k_{11}, k_{12}, k_{13}, k_{21}, k_{22} and k_{23} can be found in Ref. Soedel (2004) which are not presented here for brevity. Readers are referred to Soedel (2004) for more detailed explanation. Thus, the natural modes that are related with respective frequencies at each m, n combination and corresponding modal shapes of shell can be represented as:

$$\begin{Bmatrix} U_x \\ V_\Phi \\ W_z \end{Bmatrix}_{mn} = C_{mn} \begin{Bmatrix} \frac{A_{mn}}{C_{mn}} \cos\left(\frac{m\pi x}{L}\right) \cos n(\Phi - \Phi_0) \\ \frac{B_{mn}}{C_{mn}} \sin\left(\frac{m\pi x}{L}\right) \sin n(\Phi - \Phi_0) \\ \sin\left(\frac{m\pi x}{L}\right) \cos n(\Phi - \Phi_0) \end{Bmatrix}. \tag{7.16f}$$

For simplicity, the modal amplitude of transverse modes (C_{mn}) is normalized to unity (Tzou, 2019) ($\text{i.e.}, C_{mn} = 1$) as it is arbitrary constants (Soedel, 2004). In this, it is also assumed that there is no initial phase angle of mode shape ($\Phi_0 = 0$), and by solving above equations for respective modes we can get values of A_{mn} and B_{mn}. In case of flexoelectric effect, the axial displacement becomes very negligible as compared to transverse and circumferential displacements. Therefore, A_{mn} is not considered in calculation and B_{mn} is calculated corresponding to m and n. The major advantage of flexoelectric layer over that of piezoelectric layer is that the former is not influenced by the in-plane strains of base shell. In addition to this, piezoelectric effect is caused due to bending and membrane vibration while flexoelectric effect is caused only due to bending vibration.

By substituting Eq. (7.16f) into Eq. (7.15), one can obtain the following modal expression for flexoelectric potential distribution:

$$\left(\emptyset_{mn}^{flexo}\right)_{Total} = \frac{R\mu_{12}\, h_f}{A_e \in_{33}} \int_{x_1}^{x_2} \int_{\Phi_1}^{\Phi_2} \left[-\frac{\partial^2 W_{zmn}}{\partial x^2} + \frac{1}{R^2}\left(\frac{\partial V_{\Phi mn}}{\partial \Phi} - \frac{\partial^2 W_{zmn}}{\partial \Phi^2}\right)\right] dx d\Phi\,. \tag{7.17}$$

This electric potential totally depends on the axial $\left(\emptyset_{mn}^{flexo}\right)_{x,bend}$ and circumferential $\left(\emptyset_{mn}^{flexo}\right)_{\Phi,bend}$ bending components. These bending components can be obtained as:

$$\left(\emptyset_{mn}^{flexo}\right)_{x,bend} = \frac{\mu_{12}\ R\ h_f}{\epsilon_{33}\ A_e} \times \int_{x_1}^{x_2} \int_{\Phi_1}^{\Phi_2} \left[-\frac{\partial^2 W_{zmn}}{\partial x^2}\right] dxd\Phi\ , \tag{7.18a}$$

$$= -\frac{h_f \mu_{12}\ R\ m\pi}{A_e\ \epsilon_{33}\ nL} \cos\left(\frac{m\pi x}{L}\right)\Big|_{x_1}^{x_2} \sin(n\Phi)\big|_{\Phi_1}^{\Phi_2}, \tag{7.18b}$$

$$\left(\emptyset_{mn}^{flexo}\right)_{\Phi,bend} = \frac{\mu_{12}\ R\ h_f}{\epsilon_{33}\ A_e} \int_{x_1}^{x_2} \int_{\Phi_1}^{\Phi_2} \left[\frac{1}{R^2}\left(\frac{\partial V_{\Phi mn}}{\partial \Phi} - \frac{\partial^2 W_{zmn}}{\partial \Phi^2}\right)\right] dxd\Phi\ , \tag{7.19a}$$

$$= -\frac{h_f\ \mu_{12}}{A_e\ \epsilon_{33}} \frac{L(B_{mn} + n)}{Rm\pi} \cos\left(\frac{m\pi x}{L}\right)\Big|_{x_1}^{x_2} \sin(n\Phi)\big|_{\Phi_1}^{\Phi_2}. \tag{7.19b}$$

7.2.3 Piezoelectric Effect on Electric Potential Distribution

Steps involved in the formulation of continuum model for the distribution of electric potential accounting the piezoelectric effect ($e_{31} \neq 0; \mu_{12} \to 0$) are same as that of continuum model presented in previous Section for flexoelectric effect with a few changes. Therefore, a detailed procedure for the same is not presented here for the sake of brevity. The electric potential ($\emptyset^{piezo}$) generated in the piezoelectric GRNC layer laminated to the elastic shell can be obtained as:

$$\emptyset^{piezo} = \frac{h_f}{A_e} \int_{\Phi} \int_{x} e_{31} \left[\frac{\partial U_{xmn}}{\partial x} - \left(\frac{h_f + h}{2}\right) \frac{\partial^2 W_{zmn}}{\partial x^2}\right] +$$

$$e_{31} \left[\frac{1}{R}\left(\frac{\partial V_{\Phi mn}}{\partial \Phi} + W_{zmn}\right) + \left(\frac{h_f + h}{2}\right)\left(\frac{1}{R^2}\frac{\partial V_{\Phi mn}}{\partial \Phi} - \frac{1}{R^2}\frac{\partial^2 W_{zmn}}{\partial \Phi^2}\right)\right] Rdxd\Phi\ . \tag{7.20}$$

Note that the axial and circumferential displacements of shell are small and generally much lesser as compared to the transverse displacement (Li et al., 2010, 2011; Tzou, 2019). However, we accounted the same determining the total electric potential which includes the axial, transverse and circumferential components. Thus, using the mode shape function from Eq. (7.16f) into Eq. (7.20), the total electric potential considering the piezoelectric effect $\left(\emptyset_{total}^{Piezo}\right)$ can be written as:

$$\emptyset_{\text{total}}^{\text{Piezo}} =$$

$$= \frac{-h_f\, e_{31}}{A_e\, \epsilon_{33}} \left(\frac{L}{nm\pi} + \frac{R(h_f + h)m\pi}{2nL} + \frac{L(h_f + h)}{2m\pi} \frac{n}{R} \right) \cos\left(\frac{m\pi x}{L}\right)\Big|_{x_1}^{x_2} \sin(n\Phi)\Big|_{\Phi_1}^{\Phi_2} . (7.21)$$

In such a way, we can determine the electric potential distributions with $(\mu_{12} \neq 0)$ and without $(\mu_{12} \rightarrow 0)$ considering the flexoelectric effect using continuum modelling.

7.2.4 FE Modelling of Laminated Shell

In this sub-section, 3D FE models were developed to validate the analytical predictions. It is important to mention that the continuum models are based on some assumptions, and numerical or experimental investigations may be carried out to verify these assumptions because both the analyses do not require any such approximations. Therefore, in the current study, FE models were developed to validate the assumptions used for continuum modelling of laminated shell using the COMSOL multiphysics version 5.3 software package. Using COMSOL, FE method is used for modelling and simulation of MEMS composite module which combines both solid mechanics and electrostatics problems, but one cannot study the effect of flexoelectricity as it is generally absent in it. Hence, this FE model is not suitable for studying the effect of flexoelectricity because of complexity of the additional terms of the strain gradients and flexoelectric coefficients. Hence, this can be characterized as an electrostatic problem without considering flexoelectricity. In the FE analysis, the material and geometrical properties of shell and GRNC layer are used same as that of continuum model. The couplings present in the laminated shell can be categorized based on the stress $(e = C/m^2)$ or strain charge $(d = C/N)$, and we have chosen the stress charge form. Figure 7.2 demonstrates the flow diagram of steps followed in COMSOL multiphysics modelling. FE modelling is divided into three stages: pre-processor, solver and post-processor. In pre-processor stage, the modelling was done by selecting suitable geometry with specific multiphysics model such as “piezoelectric and eigen-frequency”. The material properties, initial boundary and loading conditions were also assigned in the pre-processing stage. After the imposition of loading and initial boundary conditions, discretization (meshing) of a continuum was done followed by optimization. Subsequently, the set of algebraic equations were solved, which provided the nodal solutions of continuum laminated shell model. Once the solutions of problems are obtained, the post-processor allowed us to study the FE results such as electric potential, modes, displacement, etc. The meshing of laminated shell was done using “free tetrahedral” type of elements which resulted into number of vertex elements (24), edge elements (1360), boundary elements (36804) and number of elements (69877). Figure 7.3 illustrates the minimum and maximum values of electric potentials generated in the piezoelectric GRNC shell as well as deformed and undeformed shapes of laminated shells.

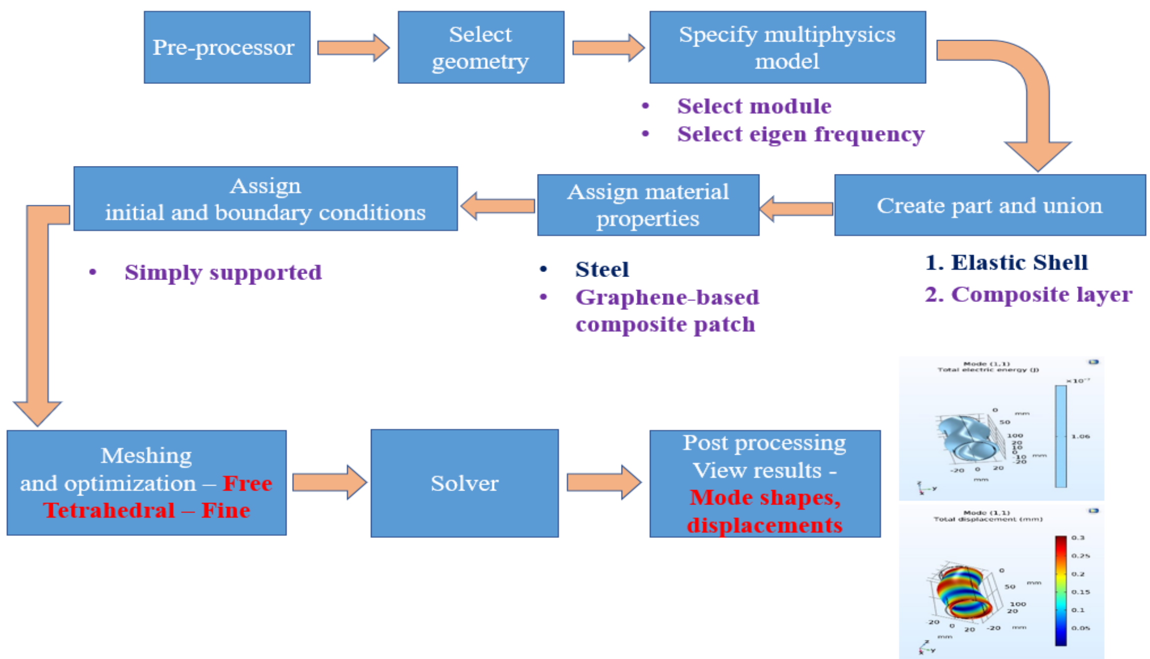

Figure 7.2: Flowchart of FE modelling.

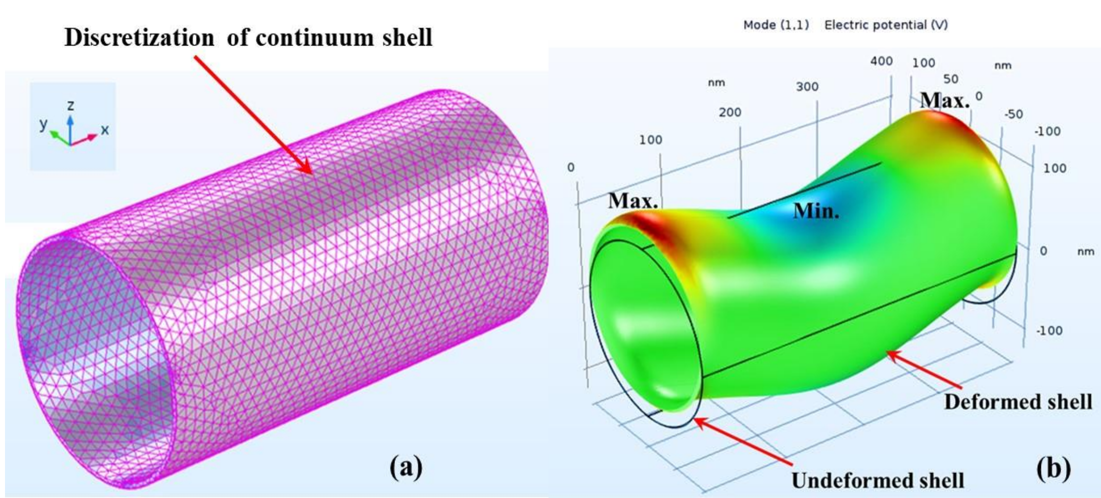

Figure 7.3: (a) Meshing of laminated shell and (b) distribution of electric potential in GRNC layer.

7.3 Results and Discussions

In this Section, the distribution of electric potentials of piezoelectric or flexoelectric GRNC layer laminated to the cylindrical shell at different modes such as (1,1), (1,2), (2,1) and (2,2) are studied. Subsequently, the parametric analysis is carried out. The main objective of parametric analysis is to obtain the design parameters that can be used for practical applications and experimental studies. The elastic shell is considered to be made of mild steel and the GRNC layer is laminated on it. The material and geometrical properties of the laminated shell are summarized in Tables 7.1 and 7.2, respectively.

Table 7.1: Material properties of laminated shell.

Properties	**Elastic shell (Steel)**	**GRNC layer/patch**
Ref.	(Landesmann et al., 2016)	(Shingare and Kundalwal, 2019)
Density ($\rho = \mathrm{Kg/m^3}$)	7800	2200
Young's modulus (E = GPa)	210	494.01
Poisson's ratio (ϑ)	0.3	0.3
Electric permittivity ($\in_{33}$= F/m)	-	7.2×10^{-11}
Flexoelectric coefficient ($\mu_{12} = \mathrm{C/m}$)	-	1×10^{-09}
Piezoelectric stress const. ($e_{31} = e_{32} = \mathrm{C/m^2}$)	-	-2.1×10^{-3}

Table 7.2: Geometrical properties of elastic shell and GRNC patch.

Parameters	**Geometry**
Length (L)	400 nm
Radius (R)	100 nm
Shell thickness (h)	4 nm
Axial (**x**) and circumferential (Φ) dimensions of patch	2 nm and 5^0
Patch thickness ($\mathbf{h_f}$)	0.9 nm

Note that the GRNC layer is made of distributed patches attached to the elastic shell. Each GRNC patch offers "nanoscale" distributions of electric potential and its contributions for various modes of the overall GRNC layer attached to the steel shell. Such layer is made up of the array of 200 × 72 patches uniformly distributed on overall cylindrical shell.

7.3.1 Piezoelectric Effect on Electric Potential Distributions

In this, the effect of piezoelectricity on the distribution of electric potentials in the laminated shell at different modes is presented. Modes are characteristics of any structural system and are a function of its mass, stiffness and boundary conditions. Each mode can be characterized by using mode shape, modal frequency and damping known as "modal parameters". For presenting the results for demonstrating the effect of piezoelectricity, we showed the distribution of total electric potentials which combines both the axial and circumferential bending potentials. Figures 7.4–7.7 illustrate that the distribution of total electric potentials due to the piezoelectric effect for the modes (1,1), (1,2), (2,1) and (2,2). Modes are numbered according to the number of half and full waves (crest and trough) in the vibration of laminated shell. In these figures, subplots (a) and (b) represent the results predicted by the analytical and 3D FE models, respectively.

From Figs. 7.4 and 7.5 it can be observed that the distribution of electric potentials at mode (1,1) is less as compared to at mode (1,2). Same is true for another set of modes (2,1) and (2,2). This is attributed to the fact that mode (1,1) is a fundamental mode of vibration which is the lowest natural frequency of the system. Normally, only the first few modes are vital from the practical application point of view, therefore, the results for the higher modes are not presented here. It is clearly seen from equation of electric potential that the total electric potential due to the piezoelectric effect strongly depends on the mode numbers m and n. It also depends on other parameters which are discussed in detail in next 7.3.3. From Figs. 7.4–7.7 it can be noticed that the electric potential increases as the mode number increases and one can clearly observe the different electric potentials at different mode shapes with different frequencies. The comparison and error data for different modes and lengths of shell are summarized in Table 7.3 and Table 7.4, respectively. It can be observed that the electric potential of laminated shell increases as mode number increases and it decreases as length of shell increases. It is due to the fact that the electric potential is directly proportional to mode numbers (m, n) and thickness of patch while it is inversely proportional to radius and length of shell. The relative error between the results of continuum and numerical modelling is increasing with the increment in mode numbers and length of shell. It is attributed to the fact that the FE analysis do not require any assumptions which were considered in continuum modelling. The comparison of predictions of both analytical and numerical (FE) models are found to be in good agreement and the error is less than 4%, therefore, the analytical model was used to determine the subsequent results.

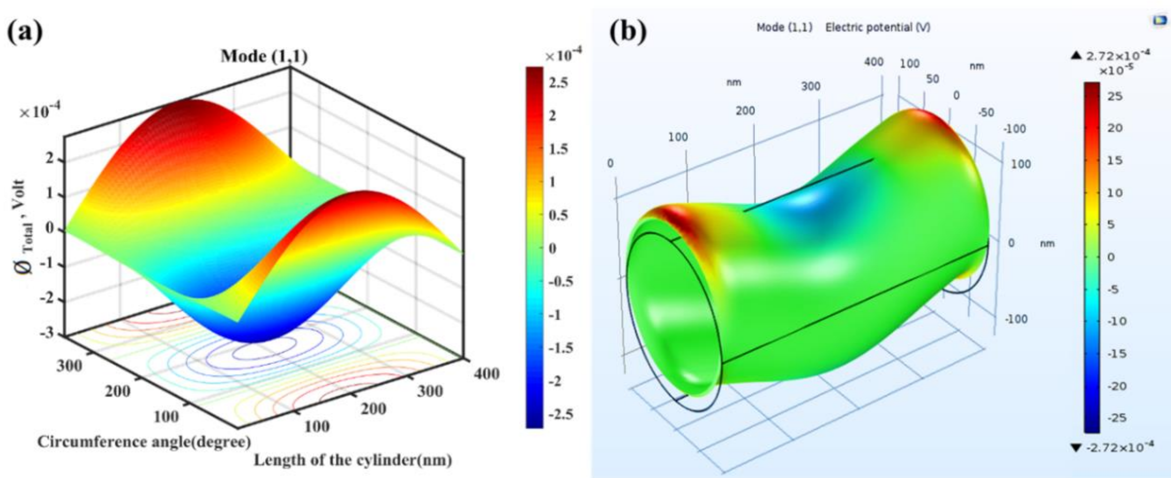

Figure 7.4: Effect of piezoelectricity on the distributions of total electric potential in the laminated shell for mode (1, 1).

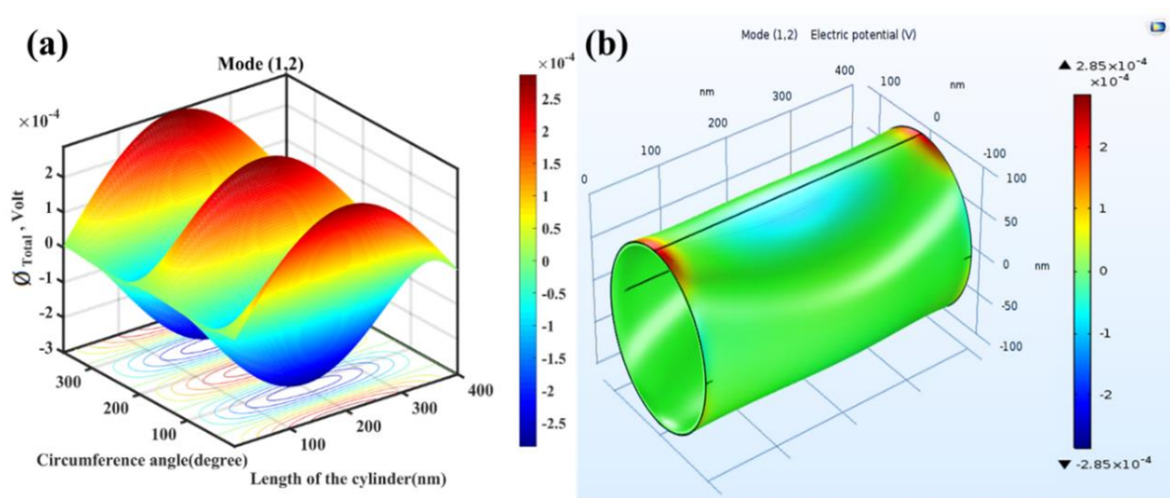

Figure 7.5: Effect of piezoelectricity on the distributions of total electric potential in the laminated shell for mode (1, 2).

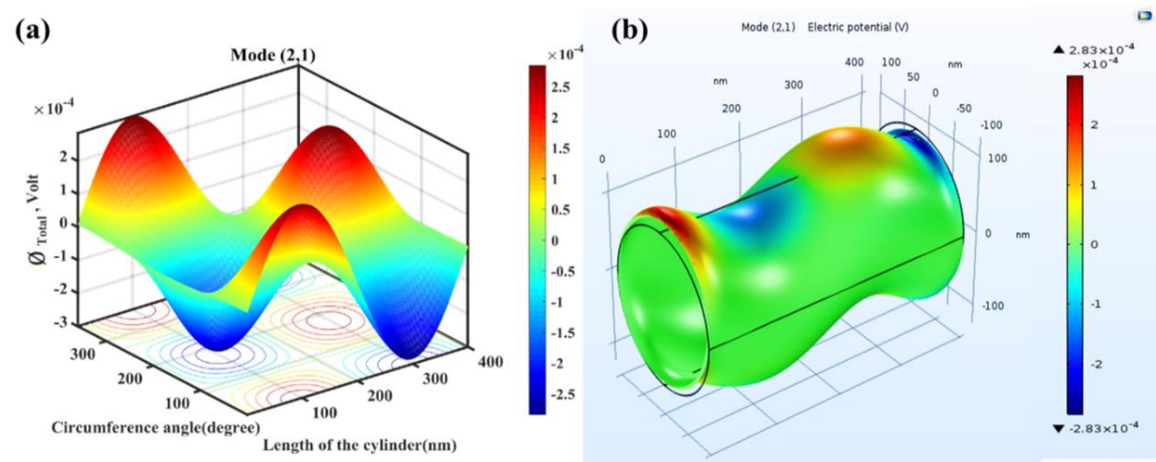

Figure 7.6: Effect of piezoelectricity on the distributions of total electric potential in the laminated shell for mode (2, 1).

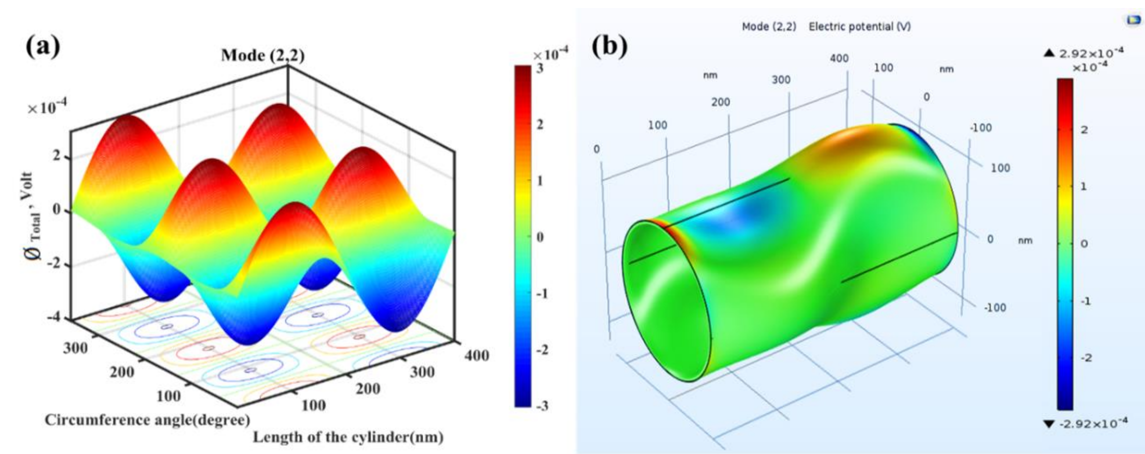

Figure 7.7: Effect of piezoelectricity on the distributions of total electric potential in the laminated shell for mode (2, 2).

Table 7.3: The comparison of predictions by the continuum and numerical models.

Modes	$(\emptyset_{\text{Total}}^{\text{piezo}})$ **Continuum Model (Volt)**	$(\emptyset_{\text{Total}}^{\text{piezo}})$ **Numerical Model (FE) (Volt)**	**Error (%) =** $\frac{\text{Analytical value} - \text{Numerical value}}{\text{Analytical value}}$
(1,1)	2.73×10^{-4}	2.72×10^{-4}	0.367
(1,2)	2.86×10^{-4}	2.85×10^{-4}	0.351
(2,1)	2.85×10^{-4}	2.83×10^{-4}	0.706
(2,2)	3.03×10^{-4}	2.92×10^{-4}	3.767

Table 7.4: The comparison of predictions by the continuum and numerical models for different length of shell in case of mode (1,1).

Length (nm)	$\left(\emptyset_{\text{Total}}^{\text{piezo}}\right)$ **Continuum Model** (V)	$\left(\emptyset_{\text{Total}}^{\text{piezo}}\right)$ **Numerical Model (FE)** (V)	**Error (%) =** $\frac{\textbf{Analytical value}-\textbf{Numerical valu}}{\textbf{Analytical value}}$
200	2.81×10^{-4}	2.805×10^{-4}	**0.177**
300	2.76×10^{-4}	2.751×10^{-4}	**0.326**
400	2.73×10^{-4}	2.720×10^{-4}	**0.367**
500	2.70×10^{-4}	2.677×10^{-4}	**0.851**
600	2.68×10^{-4}	2.65×10^{-4}	**1.11**

7.3.2 Flexoelectric Effect on Electric Potential Distribution

In this sub-section, the effect of flexoelectricity $(e_{31}, \mu_{12} \neq 0)$ on the distribution of electric potentials in the laminated shell at different modes is presented. The terms $\left(\emptyset^{f}\right)_{x,\text{bend}}$, $\left(\emptyset^{f}\right)_{\Phi,\text{bend}}$ and $\left(\emptyset^{f}\right)_{\Phi,\text{total}}$ denote the electric potentials under the axial, circumferential and total bending effects, respectively, at different modes. For presenting the results, the distribution of total electric potentials combining both the axial and circumferential bending potentials is shown. In case of modes (1,1), (1,2), (2,1) and (2,2), the magnitudes of axial electric potentials are much greater than the circumferential electric potentials as demonstrated in Figs. 7.8–7.11 and Table 7.5. Table 7.5 demonstrates the results for maximum electric potentials for the axial and circumferential bending components and their corresponding ratios considering the flexoelectric effect. It is attributed to the fact that cylindrical shell is softer or flexible in the circumferential direction as compared to the axial direction. The results demonstrate that the electric potential due to the incorporation of flexoelectricity mainly dominated by the axial bending component. The optimum positions of the flexoelectric GRNC patches or sensors are indicated by the peaks in signal plots.

From these results, it can be concluded that the flexoelectric GRNC patches should be attached to the shell along its axial direction as the larger strain gradients occur due to the axial bending than the circumferential bending. It can be observed from Figs. 7.4–7.11 that the incorporation of flexoelectric effect significantly improves the results compared to the piezoelectricity. For example, from Figs. 7.4 and 7.8 it is obvious that the maximum value of total electric potential due to the incorporation flexoelectric effect enhanced by ~340% as compared to the piezoelectric case for mode (1,1) results. Results also reveal that the electric potential due to the piezoelectric effect are sensitive to the bending and membrane vibrations while in case of flexoelectric effect, results are sensitive to the bending vibrations only.

Table 7.5: The maximum axial and circumferential electric potentials and their corresponding ratios considering the flexoelectric effect.

Modes	$\left(\emptyset_{\mathbf{mn}}^{\mathbf{flexo}}\right)_{\mathbf{x,bend}}$ (V)	$\left(\emptyset_{\mathbf{mn}}^{\mathbf{flexo}}\right)_{\mathbf{\Phi,bend}}$(V)	$\left(\emptyset_{\mathbf{mn}}^{\mathbf{flexo}}\right)_{\mathbf{x,bend}} / \left(\emptyset_{\mathbf{mn}}^{\mathbf{flexo}}\right)_{\mathbf{\Phi,bend}}$
(1,1)	0.817×10^{-3}	2.592×10^{-5}	31.52
(1,2)	0.816×10^{-3}	2.315×10^{-4}	3.52
(2,1)	3.311×10^{-3}	2.593×10^{-5}	127.68
(2,2)	3.312×10^{-3}	2.315×10^{-4}	143.06

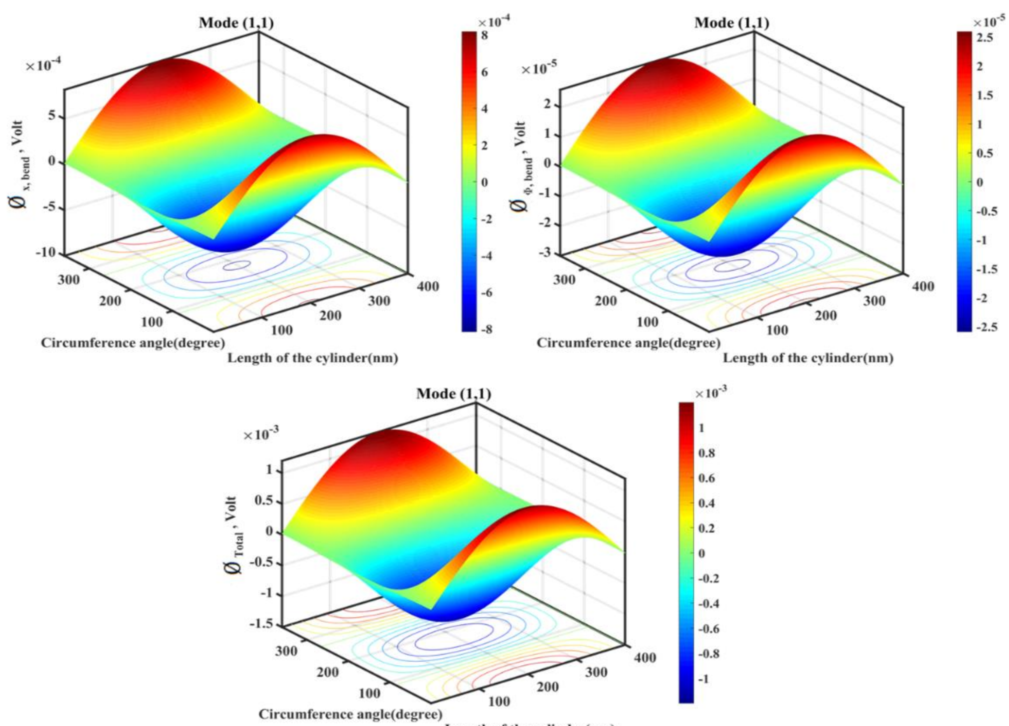

Figure 7.8: Effect of flexoelectricity on the distributions of total electric potential in the laminated shell for mode (1,1).

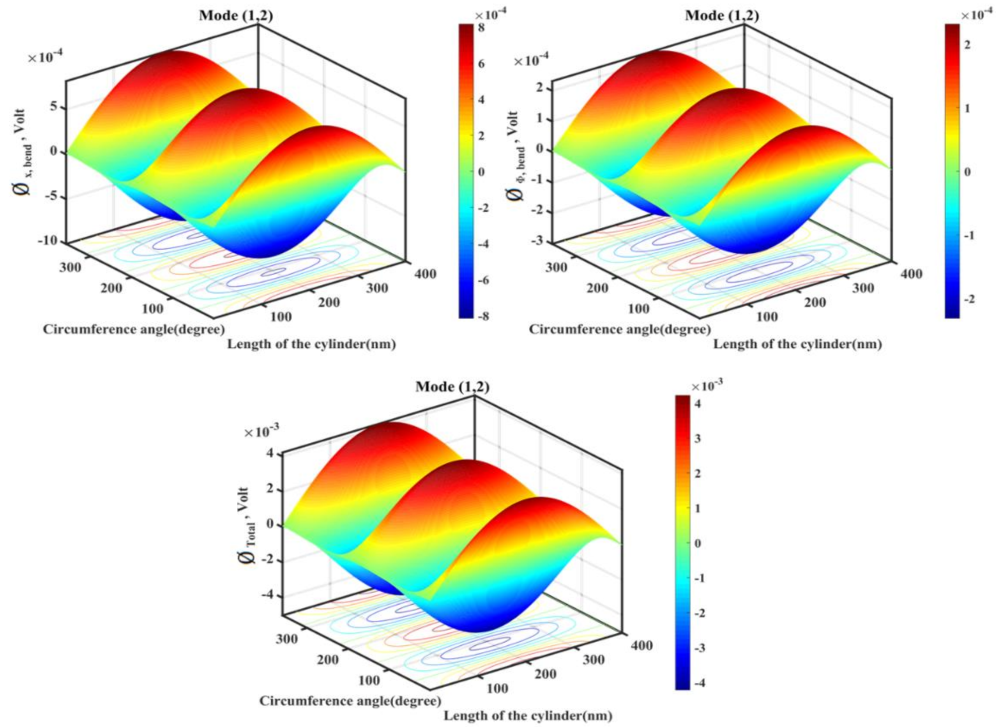

Figure 7.9: Effect of flexoelectricity on the distributions of total electric potential in the laminated shell for mode (1,2).

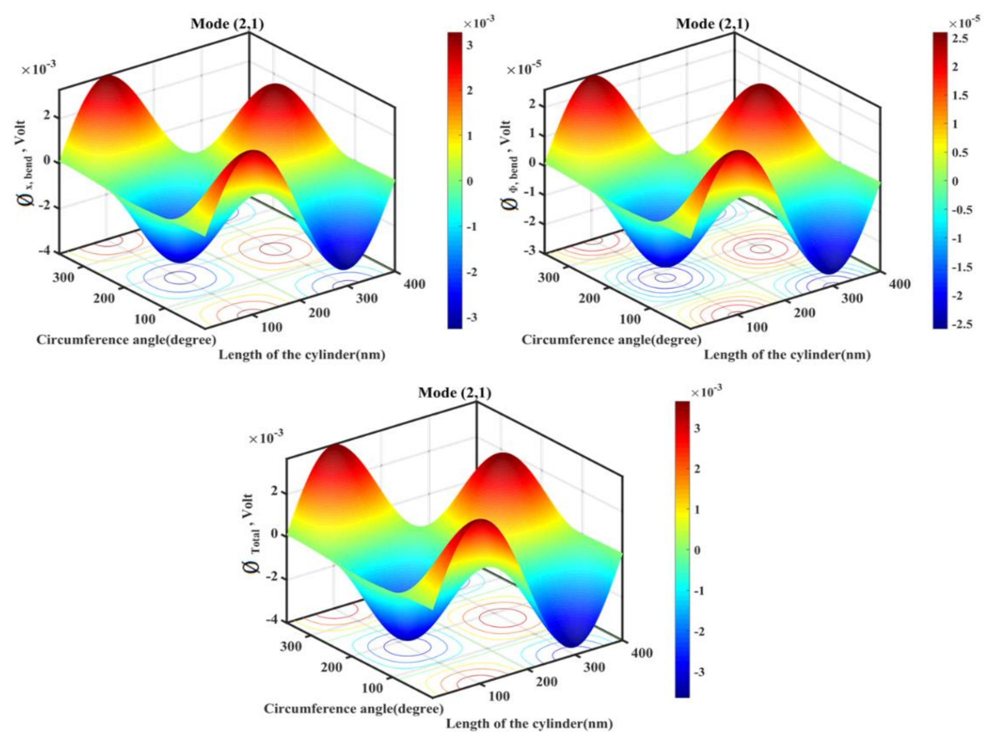

Figure 7.10: Effect of flexoelectricity on the distributions of total electric potential in the laminated shell for mode (2,1).

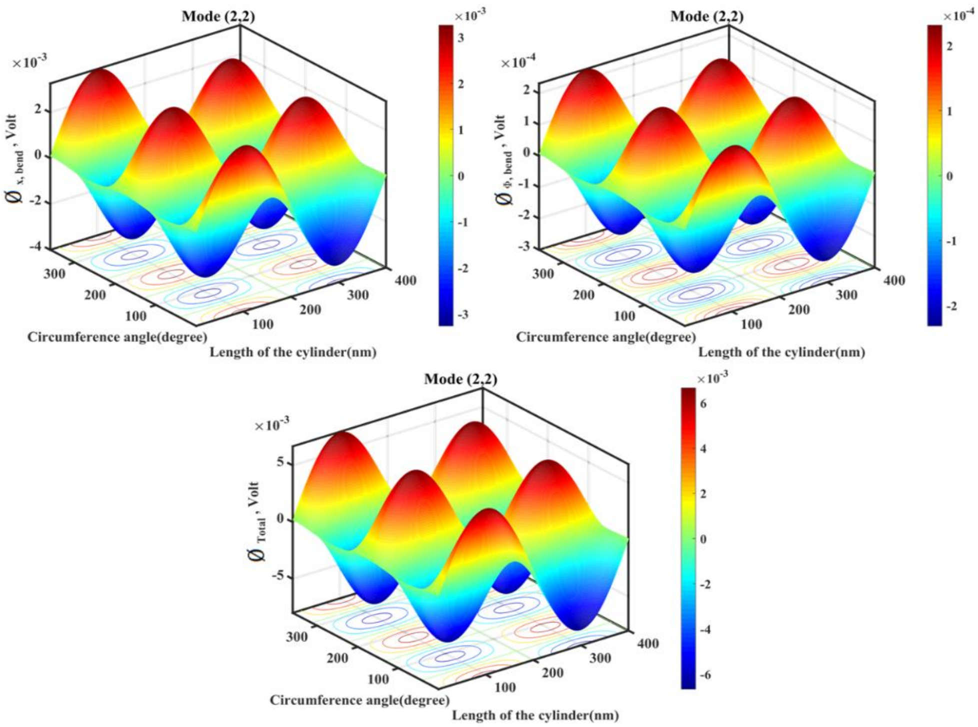

Figure 7.11: Effect of flexoelectricity on the distributions of total electric potential in the laminated shell for mode (2,2).

7.3.3 Parametric Analysis

The generations of electric potentials in the laminated shell depend on various parameters such as mode numbers, patch thickness (h_f), radius of shell (R) and shell thickness (h). Therefore, parametric analysis is carried out in this sub-section.

7.3.3.1 Mode Numbers

Figure 7.12 demonstrates the variation of maximum values of electric potentials for axial, circumferential and total bending cases, accounting the flexoelectric effect at each mode (1–6, 1–6). From this figure, it is observed that (i) the axial bending electric potential increases as the value of m increases but it does not vary with n, and (ii) the circumferential electric potential increases as the value of n increases but it does not vary with m. Therefore, the combined results showing the total electric potentials with respect to the mode numbers (m and n) show increment as the mode number increases. It can be concluded that if the axial mode number is greater than the circumferential mode number ($m \geq n$) then the contribution of axial component is more to the total electric potential and the converse is true in case of $m < n$.

7.3.3.2 Patch Thickness

Figure 7.13 shows the variation of maximum total electric potentials against the thickness of GRNC patch with and without considering the flexoelectric effect. The case without the flexoelectric effect can be considered as a conventional case accounting only the piezoelectric effect. This figure reveals that the electric potentials increase as the thickness of patch increases in both the cases but the incorporation of flexoelectric effect shows significant enhancement. For instance, the value of total electric potential increased by ~300% over that of conventional case with 15 nm patch thickness when the flexoelectric effect is considered. In case of flexoelectric effect, it can be observed from Eq. (7.18) that the total electric potential is directly proportional to the patch thickness. Also, from Eq. (7.19) it can be seen that the axial as well as circumferential bending components depend on the thickness of patch and, hence, the total electric potential depends on the thickness of patch.

7.3.3.3 Radius of Shell

Figure 7.14 illustrates the variation of maximum total electric potentials with respect to the radius of shell with and without considering the flexoelectric effect. This figure reveals that the electric potentials steeply decrease as the radius of shell increases in both the cases but the incorporation of flexoelectric effect shows significant enhancement. The decreasing trend of total electric potentials is attributed to the reduced strain gradient of the shell as its radius increases. The shell with smaller radius provides larger electric potentials when the flexoelectric effect is considered. Note that the flexoelectricity is a size-dependent phenomenon and the large strain gradients present at the nanoscale level lead to the strong electromechanical coupling. The maximum value of total electric potential of shell with radius 50 nm increased by 315% over that of conventional case when the flexoelectric effect is considered.

7.3.3.4 Shell Thickness

Figure 7.15 illustrates the variation of maximum total electric potential with respect to the shell thickness with and without considering the flexoelectric effect for mode (1,1). It can be noticed that the shell thickness does not influence the electric potential when the flexoelectric effect is considered because it is primarily generated due to the strain gradient induced by bending and is not associated with the membrane strains. In case of flexoelectric effect, it is clearly seen that the electric potential remains unaffected as the shell thickness increases because the strain gradient is not dependent on the shell thickness.

It is important to note that the value of electric potential due to flexoelectric effect is not increasing but it is greater as compared to the piezoelectric effect. In case of piezoelectric effect, the electric potential increases slightly as the shell thickness increases. The maximum value of total electric potential of shell with shell thickness 40 nm increased by 244% over that of conventional case when the flexoelectric effect is considered.

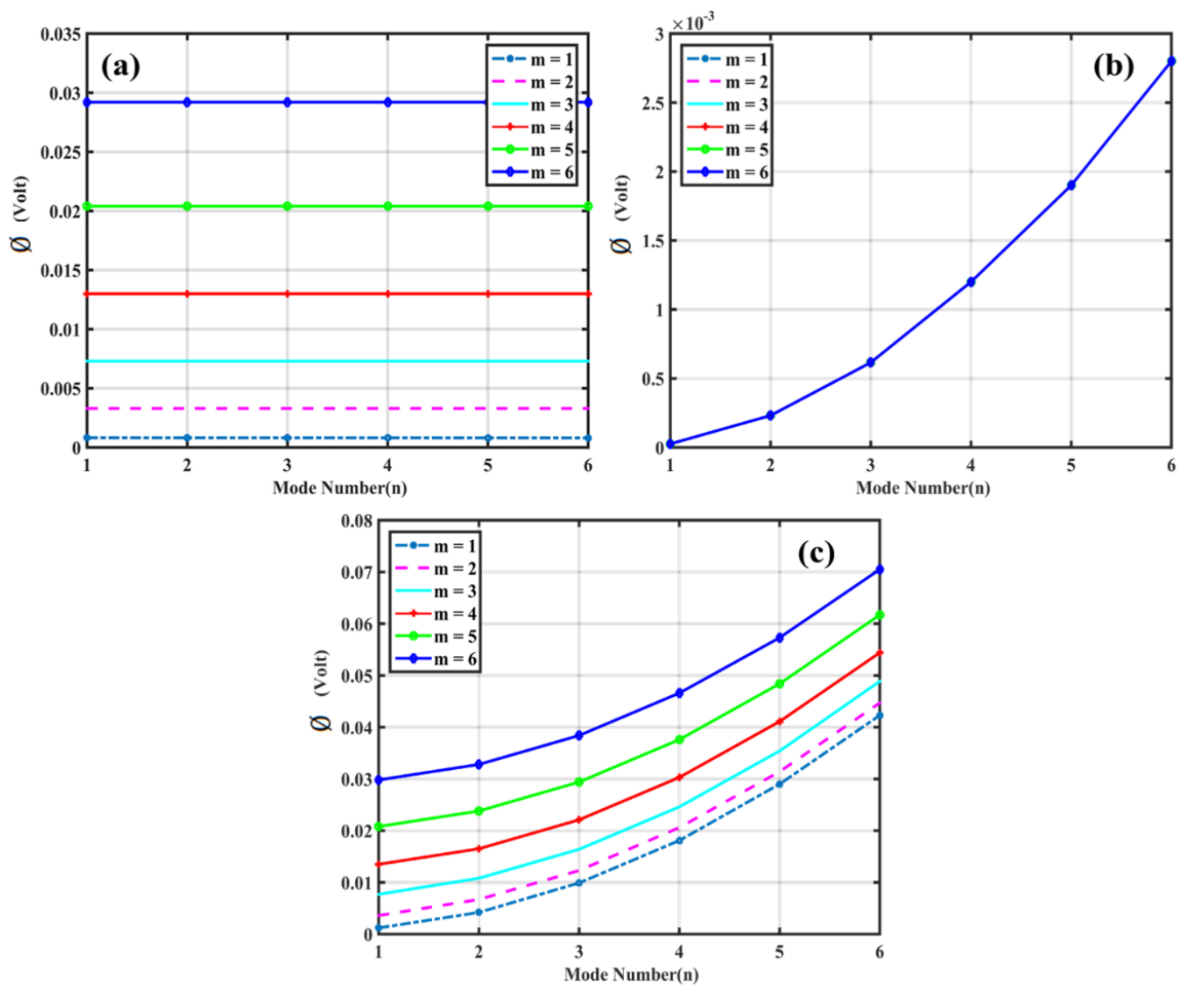

Figure 7.12: The maximum values of electric potentials at each mode considering the flexoelectric effect: (a) axial, (b) circumferential and (c) total bending effects.

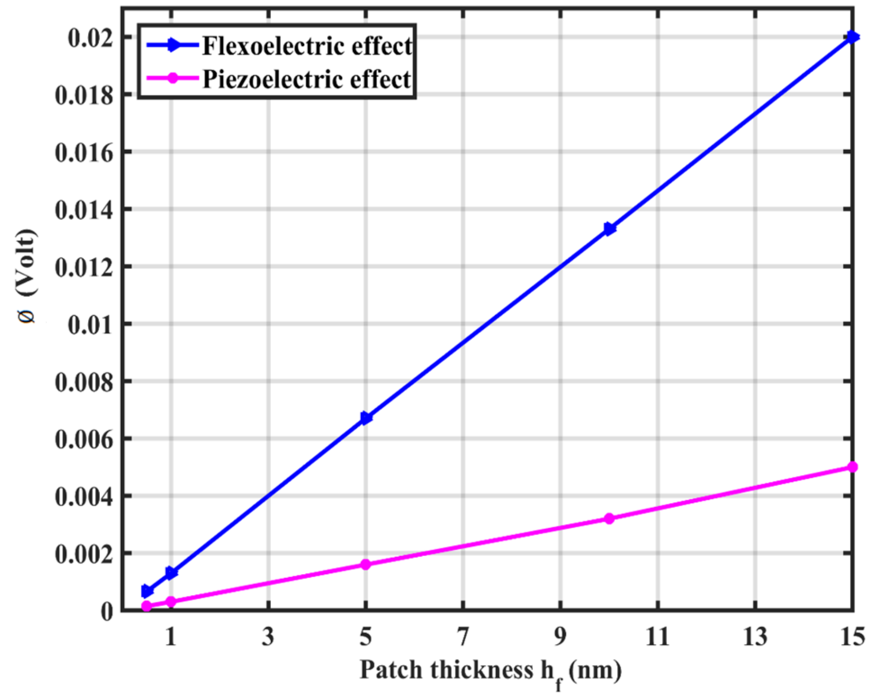

Figure 7.13: Variation of maximum total electric potentials with respect to GRNC patch thickness for mode (1,1).

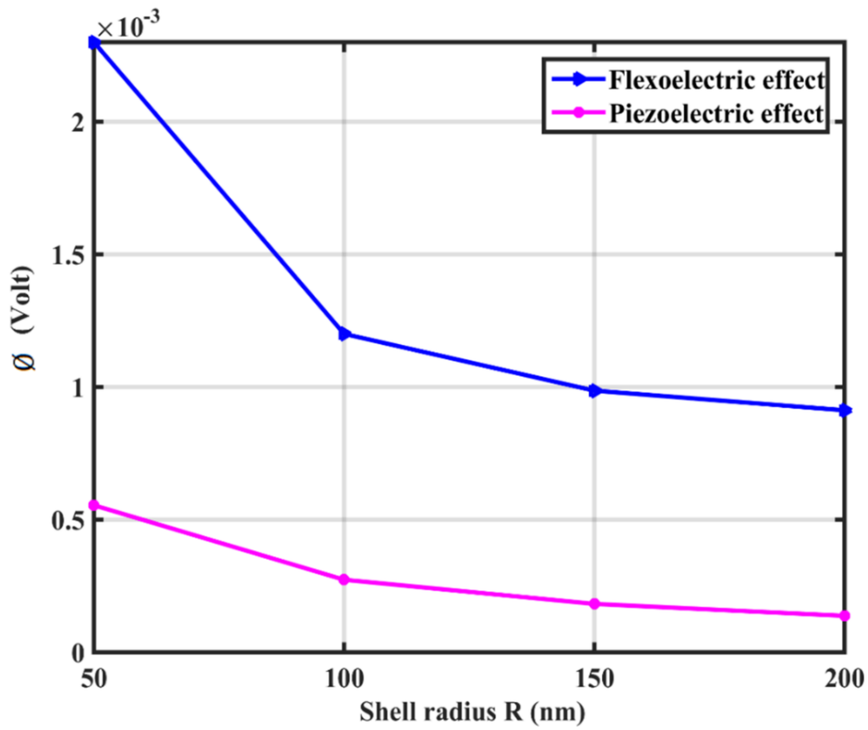

Figure 7.14: Variation of maximum total electric potentials with respect to the radius of shell for mode (1,1).

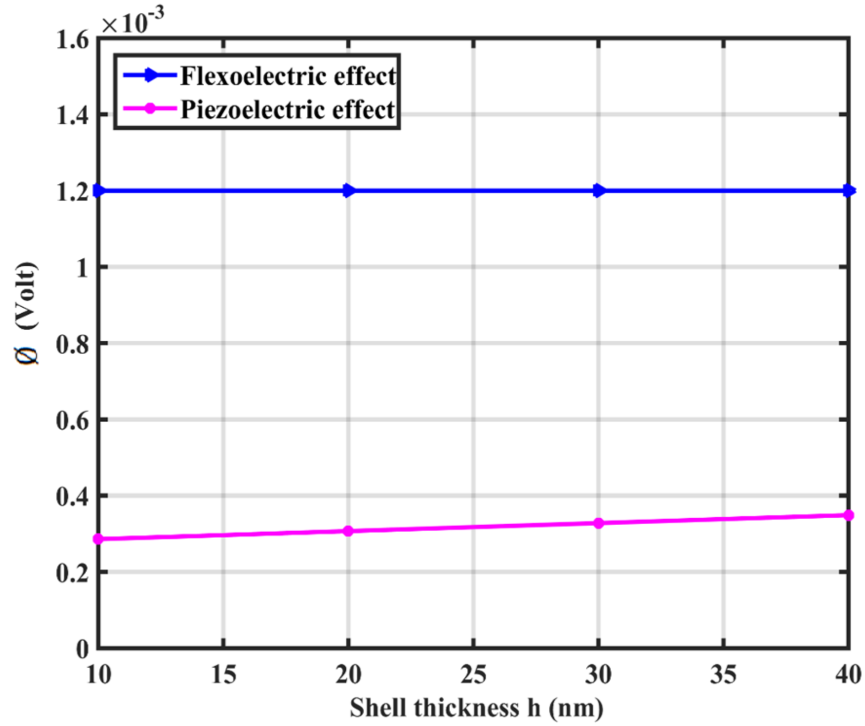

Fig. 7.15. Variation of maximum total electric potentials with respect to the shell thickness for mode (1,1).

7.4 Conclusions

The electromechanical response of thin elastic shell laminated with GRNC layer, accounting piezoelectric and flexoelectric effects, was studied. An analytical model was developed for the laminated shell based on Kirchhoff–Love theory to investigate the electric potential distributions in it due to the mechanical vibrations. The analytical predictions are found to be in good agreement with the FE results. The parametric study also carried out to study the effect of variation of mode numbers, patch thickness, shell thickness and shell radius on the values of electric potentials generated in the laminated shell. The current results reveal that the electromechanical behavior of laminated shell is significantly improved due to the incorporation of flexoelectric effect. If the axial mode number is greater than the circumferential mode number ($m \geq n$) then the contribution of axial component is more to the total electric potential and the converse is true in case of $m < n$. The maximum value of total electric potential due to the incorporation of flexoelectric effect enhanced by ~340 % as compared to the piezoelectricity case for mode (1,1). The electric potentials increase significantly as the thickness of flexoelectric composite patch increases. For instance, the value of total electric potential of laminated shell considering the flexoelectricity increased by ~300% over that of conventional case with 15 nm patch thickness. The electric potentials of laminated shell steeply decrease as the radius of shell increases but the incorporation of flexoelectric effect provides better estimates. The maximum value of total electric potential of shell with radius 50 nm increased by 315% over that of conventional case when the flexoelectric effect is considered. The electric potentials of laminated shell are found to be higher and constant as its thickness increases due to the incorporation of flexoelectric effect compared to piezoelectric effect. The maximum value of total electric potential of laminated shell with thickness 40 nm increased by ~244% over that of conventional case when the flexoelectric effect is considered.

The next Chapter summarizes the significant outcomes and conclusions from this Thesis along with the identified directions for future research work. The scope for further research on graphene-based composite and its structures are also suggested.

Chapter 8

Conclusions and Future Scope

In this Chapter, major conclusions drawn from the current research work are highlighted. Moreover, scope for further research on GRNC and its structures are suggested.

8.1 Major Conclusions

Owing to its unique multifunctional and scale-dependent physical properties, graphene is emerged as promising reinforcement to enhance the overall response of its nanotailored composite materials. Most recently, the piezoelectricity phenomenon in graphene sheets was found through interplay between different non-centrosymmetric pores, curvature and flexoelectricity concept. This has added new multifunctionality to existing graphene. Piezoelectric NEMS-based structures such as beams, plates, wires and shells have found enormous applications in areas of sensors, actuators, nanogenerators and distributors. Surprisingly, the application of piezoelectric graphene for modelling of graphene-based structures was not explored in the literature and this provided the motivation for this Thesis. The piezoelectric, flexoelectric and surface effects play a significant role on the static/dynamic behavior of nanostructures. Therefore, a comprehensive analytical and numerical modelling was carried out herein to (i) determine the effective properties of GRNC and (ii) study the electromechanical behavior of GRNC beam, plate, wire and shell accounting the piezoelectric, flexoelectric and surface effects.

The following main conclusions are drawn from the work carried out in this Thesis:

- First, the elastic properties of pristine and defective graphene sheets were determined using MD simulations and the obtained results are found in good agreement with the existing experimental and numerical results. Second, the effective elastic, piezoelectric and dielectric properties of GRNC were determined by the analytical and numerical micromechanics models, and their predictions are found to be in good agreement for the lower values of graphene volume fraction. Thus, for predicting the effective properties of advanced nanocomposite one may adopt analytical micromechanical approaches as they require much less computational time than the FE models.

- The effective axial elastic, piezoelectric and dielectric properties of GRNC are exceptionally larger than those of the transverse and shear effective properties. If the loading is applied along the 3-axis of GRNC then the effective constants C_{33}^{eff}, C_{13}^{eff}, e_{33}^{eff}, e_{31}^{eff} and $\in_{33}^{eff}$ show higher and reliable results predicted by MOM, SOM and FE models. If the loading is applied in the transverse direction of GRNC then the results obtained for C_{11}^{eff}, C_{12}^{eff}, C_{44}^{eff} and C_{66}^{eff} show the discrepancies. This is attributed to the fact that the transverse properties of composites are matrix dependent.
- An analytical beam model was derived using the extended linear piezoelectricity and Euler beam theories incorporating the flexoelectricity effect. The FE models were developed to validate the analytical predictions. The flexoelectricity has significant effect on the electromechanical response of GRNC beam. It is revealed that the electromechanical response GRNC cantilever beam is improved with the increase in graphene volume fraction and it can be tuned via applying different electric potentials.
- The closed form solutions were obtained for GRNC nanobeams based on the size-dependent Euler-Bernoulli and linear piezoelectricity theories accounting the flexoelectric and surface effects. Furthermore, the FE models were developed based on Galerkin's weighted residual method for validating the analytical results of response of GRNC beams with different boundary conditions. The respective static deflections of GRNC cantilever, simply-supported and clamped-clamped nanobeams are reduced by (i) ~19% irrespective of boundary condition when only the flexoelectric effect was considered and (ii) ~86%, ~68% and ~52% when the combined flexoelectric-surface effects were considered compared to that of corresponding cases of conventional beams. Due to the incorporation of flexoelectric effect, it is found that the electromechanical coupling coefficient of nanobeams

having thickness less than 20 nm increases substantially, and such effect should be accounted for studying the static behavior of thin nanostructures.

- The exact solutions for flexoelectric GRNC nanoplate based on Kirchhoff's plate theory, Navier's solution and extended linear theory of piezoelectricity were obtained. Based on this, the static and dynamic behaviors of simply supported GRNC nanoplates under different types of loadings were investigated to study the role of flexoelectricity. It is found that the bending stiffness of nanoplates having thickness less than 5 nm increases significantly due to the incorporation of flexoelectricity effect and such effect cannot be neglected for predicting static response of thin structures. Similarly, the dynamics response of GRNC nanoplates is enhanced due to the flexoelectric effect as the plate thickness reduces. Resonant frequencies of GRNC nanoplates are enhanced by ~225% for the plate aspect ratios of 10 to 30 when the plate thickness is 1 nm.
- An analytical model was developed for studying the distribution of electric potential in GRNC nanowire accounting the flexoelectric effect. The electromechanical responses such as electric potential and deflection of GRNC nanowire were investigated, and the FE models were also developed to validate the analytical predictions. The piezoelectric potential in the GRNC nanowire depends on the transverse force but it is not a function of the force acting along its axial direction. Electric potential distribution in the tensile and compressive sections of a nanowire is antisymmetric along its cross-section, which makes it a "parallel plate capacitor" for the application of nanopiezotronics devices. The shear flexoelectric coefficient largely influences the response of GRNC nanowire compared to that of longitudinal flexoelectric coefficient. The flexoelectric effect is more dominant for smaller diameter of GRNC nanowires and it cannot be ignored in case of bending or stretching of smaller diameter nanowires as well as composite nanostructures.
- The electromechanical response of thin elastic shell laminated with GRNC layer, accounting piezoelectric and flexoelectric effects, was studied. An analytical model was developed for the laminated shell based on Kirchhoff–Love theory to investigate the electric potential distributions in it due to the mechanical vibrations. The analytical predictions are found to be in good agreement with the FE results. The results reveal that the electromechanical behavior of laminated shell is significantly

improved due to the incorporation of flexoelectric effect. If the axial mode number is greater than the circumferential mode number ($m \geq n$) then the contribution of axial component is more to the total electric potential and the converse is true in case of $m < n$. The maximum value of total electric potential due to the incorporation of flexoelectric effect enhanced by ~340 % as compared to the piezoelectric layer case for mode (1,1). The electric potentials increase significantly as the thickness of flexoelectric composite patch increases. For instance, the value of total electric potential of laminated shell considering the flexoelectricity increased by ~300% over that of conventional case with 15 nm patch thickness. The electric potentials of laminated shell steeply decrease as the radius of shell increases but the incorporation of flexoelectric effect provides better estimates. The maximum value of total electric potential of shell with radius 50 nm increased by 315% over that of conventional case when the flexoelectric effect is considered.

The current results are significant, which reveal that the flexoelectric phenomenon in graphene induced due to the strain gradient can be exploited to form next generation NEMS for various applications. The overall conclusion is that the flexoelectric effect is found to be more dominant for thin structures and it cannot be ignored while modeling 1D, 2D and 3D composite nanostructures.

8.2 Scope for Future Research

The current fundamental study sheds a light on the possibility of developing high-performance and light-weight graphene-based NEMS such as nanosensors, nanogenerators and nanoresonators using non-piezoelectric graphene as compared with the existing heavy, brittle and toxic piezoelectric materials. Thus, the present research may be followed for further experimental investigation to examine the multifunctional characteristics of a novel GRNC and its structures. Some of the further research works that may be undertaken in line with the present work are as follows:

- An experimental characterization of novel GRNC is a natural extension of this work. Moreover, experimental characterization of GRNC structures to explore their practical NEMS applications needs to be done.

- As the assumptions of uniform/constant electric field considered in micromechanical model makes the study highly restricted and thus, the non-uniformity of the field may be considered as the future scope of this study.
- Micromechanics models developed herein cannot provide the estimates for thermal and thermoelastic properties of GRNC, therefore, the predictions of its such properties using different models may be considered as future research work.
- Both flexoelectric and surface effects exist simultaneously for a dielectric piezoelectric nanomaterial. In this research work, both effects were considered only in case of GRNC nanobeams and hence, further investigation is necessary for all other types of structural elements.
- For layered piezoelectric GRNC structures, in addition to flexoelectric and surface effects, the consideration of interfacial effect between the graphene-matrix interface may also be an interesting scope for future work.

References

Abdollahi, A., Peco, C., Millan, D., Arroyo, M. and Arias, I. (2014), Computational evaluation of the flexoelectric effect in dielectric solids, *Journal of Applied Physics*, 116(9), p.093502. (DOI: 10.1063/1.4893974)

Allen, M.P. and Tildesley, D.J. (1987), Computer Simulation of Liquids (Clarendon Press, Oxford).

Alian, A.R., Kundalwal, S.I. and Meguid, S.A. (2015a), Interfacial and mechanical properties of epoxy nanocomposites using different multiscale modeling schemes, *Composite Structures*, 131, pp.545–555.

Alian, A.R., Kundalwal, S.I. and Meguid, S.A. (2015b), Multiscale modeling of carbon nanotube epoxy composites, *Polymer*, 70, pp.149–160.

Alian, A.R., Meguid, S.A. and Kundalwal, S.I. (2017), Unraveling the influence of grain boundaries on the mechanical properties of polycrystalline carbon nanotubes, *Carbon*, 125, pp.180–188. (DOI: 10.1016/j.carbon.2017.09.056)

Anton, S.R. and Sodano, H.A. (2007), A review of power harvesting using piezoelectric materials (2003–2006), *Smart materials and Structures*, 16(3), p.R1. (DOI: 10.1088/0964-1726/16/3/R01)

Bahamon, D.A., Qi, Z., Park, H.S., Pereira, V.M. and Campbell, D.K. (2015), Conductance signatures of electron confinement induced by strained nanobubbles in graphene, *Nanoscale*, 7(37), pp.15300–15309. (DOI: 10.1039/c5nr03393d)

Balandin, A.A., Ghosh, S., Bao, W., Calizo, I., Teweldebrhan, D., Miao, F. and Lau, C.N. (2008), Superior Thermal Conductivity of Single-Layer Graphene. *Nano Letter*, 8, pp. 902–907. (DOI: 10.1021/nl0731872)

Beeby, S.P., Tudor, M.J. and White, N.M. (2006), Energy harvesting vibration sources for microsystems applications, *Measurement Science and Technology*, 17(12), p.R175. (DOI: 10.1088/0957-0233/17/12/R01)

Benveniste, Y. and Dvorak, G.J. (1992), Uniform fields and universal relations in piezoelectric composites, *Journal of the Mechanics and Physics of Solids*, 40(6), pp.1295–1312. (DOI: 10.1016/0022-5096(92)90016-u)

Berger, H., Kari, S., Gabbert, U., Rodríguez-Ramos, R., Bravo-Castillero, J. and Guinovart-Díaz, R. (2005), A comprehensive numerical homogenisation technique for calculating effective coefficients of uniaxial piezoelectric fibre composites, *Materials Science and Engineering A*, 412(1-2), pp.53–60.

Bernholc, J., Nakhmanson, S.M., Nardelli, M.B. and Meunier, V. (2004), Understanding and enhancing polarization in complex materials, *Computing in Science and Engineering*, 6(6), pp.12–21.

Bhavanasi, V., Kumar, V., Parida, K., Wang, J. and Lee, P.S. (2016), Enhanced piezoelectric energy harvesting performance of flexible PVDF-TRFE bilayer films with graphene oxide, *ACS Applied Materials and Interfaces*, 8(1), pp.521–529. (DOI: 10.1021/acsami.5b09502)

Bouyge, F., Jasiuk, I. and Ostoja-Starzewski, M., (2001), A micromechanically based couple–stress model of an elastic two-phase composite, *International Journal of Solids and Structures*, 38(10-13), pp.1721-1735.

Bouyge, F., Jasiuk, I., Boccara, S. and Ostoja-Starzewski, M., (2002), A micromechanically based couple-stress model of an elastic orthotropic two-phase composite, *European Journal of Mechanics-A/Solids*, 21(3), pp.465-481.

Chandra, Y., Chowdhury, R., Scarpa, F., Adhikari, S., Sienz, J., Arnold, C., Murmu, T., Bould, D. (2012), Vibration frequency of graphene based composites: a multiscale approach, *Materials Science and Engineering: B*, 177, pp.303–310. (DOI: 10.1016/j.mseb.2011.12.024)

Chandratre, S. and Sharma, P. (2012), Coaxing graphene to be piezoelectric, *Applied Physics Letters*, 100(2), p.023114. (DOI: 10.1063/1.3676084)

Chatzigeorgiou, G., Javili, A. and Meraghni, F., (2019), Micromechanical method for effective piezoelectric properties and electromechanical fields in multi-coated long fiber composites. *International Journal of Solids and Structures*, 159, pp.21-39.

Chen, D., Yang, J. and Kitipornchai, S. (2017), Nonlinear vibration and postbuckling of functionally graded graphene reinforced porous nanocomposite beams, *Composites Science and Technology*, 142, pp.235–245. (DOI: 10.1016/j.compscitech.2017.02.008)

Chen, F., Gupta, N., Behera, R.K. and Rohatgi, P.K. (2018), Graphene-Reinforced Aluminum Matrix Composites: A Review of Synthesis Methods and Properties, *JOM*, 70(6), pp.837–845.

Chen, W. (2011), Surface effect on Bleustein-Gulyaev wave in a piezoelectric half-space, *Theoretical and Applied Mechanics Letters*, 1(4), p.041001. (DOI: 10.1063/2.1104101)

Chen, Z., Yang, F. and Meguid, S.A., (2014), Multi-level modeling of woven glass/epoxy composite for multilayer printed circuit board applications, *International Journal of Solids and Structures*, *51*(21-22), pp.3679-3688.

Chu, B. and Salem, D.R. (2012), Flexoelectricity in several thermoplastic and thermosetting polymers, *Applied Physics Letters*, 101(10), p.103905. (DOI: 10.1063/1.4750064)

Conley, H., Lavrik, N.V., Prasai, D. and Bolotin, K.I. (2011), Graphene bimetallic-like cantilevers: Probing graphene/substrate interactions, *Nano Letters*, 11(11), pp.4748–4752.

Cui, Y., Kundalwal, S.I. and Kumar, S. (2016), Gas barrier performance of graphene/polymer nanocomposites, *Carbon*, pp.313–333. (DOI: 10.1016/j.carbon.2015.11.018)

Da Cunha Rodrigues, G., Zelenovskiy, P., Romanyuk, K., Luchkin, S., Kopelevich, Y., Kholkin, A. (2015), Strong piezoelectricity in single-layer graphene deposited on SiO2 grating substrates, *Nature Communications,* 6, p.7572.

Merthe, D.J. and Kresin, V.V., (2016), Transparency of graphene and other direct-gap two-dimensional materials. *Physical Review B*, 94 (20), p.205439.

Dasari, B.L., Morshed, M., Nouri, J.M., Brabazon, D. and Naher, S. (2018), Mechanical properties of graphene oxide reinforced aluminium matrix composites, *Composites Part B: Engineering*, 145, pp.136–144. (DOI: 10.1016/j.compositesb.2018.03.022)

Davis, C.L. and Lesieutre, G.A. (1995), A modal strain energy approach to the prediction of resistively shunted piezoceramic damping, *Journal of Sound and Vibration*, 184(1), pp.129–139. (DOI: 10.1006/jsvi.1995.0308)

Dewapriya, M.A.N., Rajapakse, R.K.N.D., Nigam, N. (2015), Influence of hydrogen functionalization on the fracture strength of graphene and the interfacial properties of graphene-polymer nanocomposite, *Carbon*, 93, pp.830–842.

Du, X., Skachko, I., Barker, A. and Andrei, E.Y. (2008), Approaching ballistic transport in suspended graphene, *Nature Nanotechnology*, 3(8), pp.491–495. (DOI: 10.1038/nnano.2008.199)

Esteva, M. and Spanos, P. (2009), Effective elastic properties of nanotube reinforced composites with slightly weakened interfaces, *Journal of Mechanics of Materials and Structures*, 4(5), pp.887–900. (DOI: 10.2140/jomms.2009.4.887)

Feng, C., Kitipornchai, S. and Yang, J. (2017), Nonlinear bending of polymer nanocomposite beams reinforced with non-uniformly distributed graphene platelets (GPLs), *Composites Part B: Engineering*, 110, pp.132–140. (DOI: 10.1016/j.compositesb.2016.11.024)

Firooz, S., Chatzigeorgiou, G., Meraghni, F. and Javili, A., (2019), Homogenization accounting for size effects in particulate composites due to general interfaces. *Mechanics of Materials*, *139,* p.103204.

Gamboa, D., Priolo, M.A., Ham, A. and Grunlan, J.C. (2010), Note: Influence of rinsing and drying routines on growth of multilayer thin films using automated deposition system, *Review of Scientific Instruments*, 81(3), p.036103. (DOI: 10.1063/1.3310088)

Gangwar, R.K., Dhumale, V.A., Kumar, A., Alegaonkar, P., Sharma, R.B. and Datar, S.S., (2012), Gold-graphene nanocomposite based ultrasensitive electrochemical glucose sensor, *IEEE In 2012 1st International Symposium on Physics and Technology of Sensors,* pp.282-285.

Gao, X.L. and Li, K. (2005), A shear-lag model for carbon nanotube-reinforced polymer composites, *International Journal of Solids and Structures*, 42(5–6), pp.1649–1667. (DOI: 10.1016/j.ijsolstr.2004.08.020)

Gao, Y., and Wang, Z.L. (2007), Electrostatic potential in a bent piezoelectric nanowire. The fundamental theory of nanogenerator and nanopiezotronics, *Nano letters*, 7(8), pp. 2499–2505.

García-Macías, E., Rodríguez-Tembleque, L. and Sáez, A. (2018), Bending and free vibration analysis of functionally graded graphene vs. carbon nanotube reinforced composite plates, *Composite Structures*, 186, pp.123–138. (DOI: 10.1016/j.compstruct.2017.11.076)

Gharbi, M., Sun, Z.H., Sharma, P., White, K., and El-Borgi, S. (2011), Flexoelectric properties of ferroelectrics and the nanoindentation size-effect. *International Journal of Solids and Structures*, 48(2), pp.249–256.

Gong, L., Young, R.J., Kinloch, I.A., Riaz, I., Jalil, R. and Novoselov, K.S. (2012), Optimizing the reinforcement of polymer-based nanocomposites by graphene, *ACS Nano*, 6(3), pp.2086–2095. (DOI: 10.1021/nn203917d)

Gupta, S.S. and Batra, R.C. (2010), Elastic properties and frequencies of free vibrations of single-layer graphene sheets, *Journal of Computational and Theoretical Nanoscience*, 7(10), pp.2151–2164. (DOI: 10.1166/jctn.2010.1598)

Gurtin, M.E. and Murdoch, A.I. (1975), A continuum theory of elastic material surfaces. *Archive for rational mechanics and analysis*, 57(4), pp.291–323. (DOI: 10.1007/bf00261375)

Gradinar, D.A., Mucha-Kruczyński, M., Schomerus, H. and Fal'ko, V.I. (2013), Transport signatures of pseudomagnetic landau levels in strained graphene ribbons, *Physical Review Letters*, 110(26) p.266801. (DOI: 10.1103/PhysRevLett.110.266801)

Green, A.E. and Zerna, W. (2012), Theoretical Elasticity, New York, Dover Publications.

Habibi, M., Mohammadgholiha, M. and Safarpour, H. (2019), Wave propagation characteristics of the electrically GNP-reinforced nanocomposite cylindrical shell, *Journal of the Brazilian Society of Mechanical Sciences and Engineering*, Springer Berlin Heidelberg, 41(5), p.221. (DOI: 10.1007/s40430-019-1715-x)

Hashin, Z. (1983), Analysis of composite materials – a survey, *Journal of Applied Mechanics*, 50, pp.481–505.

Hadjesfandiari, A.R. (2013), Size-dependent piezoelectricity, *International Journal of Solids and Structures*, 50(18), pp.2781–2791. (DOI: 10.1016/j.ijsolstr.2013.04.020)

He, J. (2015), Surface stress on the effective Young's modulus and Poisson's ratio of isotropic nanowires under tensile load, *AIP Advances*, 5(11), p.117206. (DOI: 10.1063/1.4935439)

He, J. and Lilley, C.M. (2008), Surface effect on the elastic behavior of static bending nanowires, *Nano Letters*, 8(7), pp.1798–1802. (DOI: 10.1021/nl0733233)

Hill, R. (1963), Elastic properties of reinforced solids: some theoretical principles, *Journal of the Mechanics and Physics of Solids*, 11, pp.357–372.

Hill, R. (1964), Theory of mechanical properties of fibre-strengthened materials: II. Inelastic behaviour, *Journal of the Mechanics and Physics of Solids*, 12(4), pp.213–218.

Hosseini-Hashemia, S., Sepahi-Boroujenia, A., Sepahi-Boroujeni, S. (2018), Analytical and molecular dynamics studies on the impact loading of single-layered graphene sheet by fullerene, *Applied Surface Science*, 437, pp.366–374. (DOI: 10.1016/j.apsusc.2017.12.141)

Hu, K.M., Zhang, W.M., Zhong, Z.Y., Peng, Z.K. and Meng, G. (2014), Effect of surface layer thickness on buckling and vibration of nonlocal nanowires, *Physics Letters, Section A: General, Atomic and Solid State Physics*, 378(7–8), pp.650–654. (DOI: 10.1016/j.physleta.2014.01.005)

Hu, S. and Shen, S, (2009). Electric field gradient theory with surface effect for nano-dielectrics. *Computers, Materials & Continua* (CMC), 13(1), p.63.

Huang, G.Y. and Yu, S.W. (2006), Effect of surface piezoelectricity on the electromechanical behaviour of a piezoelectric ring, *Physica Status Solidi (B) Basic Research*, 243(4), pp.22–24. (DOI: 10.1002/pssb.200541521)

Huang, Y., Wu, J., Hwang, K.C. (2006), Thickness of graphene and single-wall carbon nanotubes, *Physical Review B*, 74, p.245413. (DOI: 10.1103/physrevb.74.245413)

Hwang, S.H., Park, H. W., Park, Y. and Bin. (2013), Piezoresistive behavior and multi-directional strain sensing ability of carbon nanotube-graphene nanoplatelet hybrid sheets, *Smart Materials and Structures*, 22(1), p.015013.

Ibn-Mohammed, T., Koh, S.C.L., Reaney, I.M., Sinclair, D.C., Mustapha, K.B., Acquaye, A. and Wang, D. (2017), Are lead-free piezoelectrics more environmentally friendly?, *MRS Communications*, 7(1), pp.1-7.

Jensen, F. (2017), Introduction to computational chemistry, Third Edition, John Wiley & sons, p.660.

Ji, X., Xu, Y., Zhang, W., Cui, L. and Liu, J. (2016), Review of functionalization, structure and properties of graphene/polymer composite fibers, *Composites Part A: Applied Science and Manufacturing*, 87, pp.29–45. (DOI: 10.1016/j.compositesa.2016.04.011)

Jiang, B., Liu, C., Zhang, C., Liang, R. and Wang, B. (2009), Maximum nanotube volume fraction and its effect on overall elastic properties of nanotube-reinforced composites, *Composites Part B: Engineering*, 40(3), pp.212–217. (DOI: 10.1016/j.compositesb.2008.11.003)

Jiang, X., Huang, W. and Zhang, S. (2013), Flexoelectric nano-generator: Materials, structures and devices, *Nano Energy*, pp.1079–1092. (DOI: 10.1016/j.nanoen.2013.09.001)

Jing, N., Xue, Q., Ling, C., Shan, M., Zhang, T., Zhou, X. and Jiao, Z. (2012), Effect of defects on Young's modulus of graphene sheets: a molecular dynamics simulation, *RSC Advances*, 2(24), p.9124.

Kandpal, M., Palaparthy, V., Tiwary, N., Rao, V.R. (2017), Low cost, large area, flexible graphene nanocomposite films for energy harvesting applications, *IEEE Transactions on Nanotechnology*, 16(2), pp.259–264. (DOI: 10.1109/tnano.2017.2659383)

Karimi, M., Shahidi, A.R. and Ziaei-Rad, S. (2017), Surface layer and nonlocal parameter effects on the in-phase and out-of-phase natural frequencies of a double-layer piezoelectric nanoplate under thermo-electro-mechanical loadings, *Microsystem Technologies*, 23(10), pp.4903–4915. (DOI: 10.1007/s00542-017-3395-8)

Karimiasl, M., Ebrahimi, F. and Mahesh, V. (2020), On nonlinear vibration of sandwiched polymer- CNT/GPL-fiber nanocomposite nanoshells, *Thin-Walled Structures*, 146, p. 106431. (DOI: 10.1016/j.tws.2019.106431)

Khan, U., Young, K., O'Neill, A. and Coleman, J.N. (2012), High strength composite fibres from polyester filled with nanotubes and graphene, *Journal of Materials Chemistry*, 22(25), pp.12907–12914. (DOI: 10.1039/c2jm31946b)

Kiani, Y. and Mirzaei, M. (2018), Enhancement of non-linear thermal stability of temperature dependent laminated beams with graphene reinforcements, *Composite Structures*, 186, pp.114–122. (DOI: 10.1016/j.compstruct.2017.11.086)

Kim, J.S., Wang, K.W. and Smith, E.C. (2005), High-authority piezoelectric actuation system synthesis through mechanical resonance and electrical tailoring, *Journal of intelligent material systems and structures*, 16(1), pp.21–31. (DOI: 10.1177/1045389X05046686)

Kogan, S.M. (1964), Piezoelectric effect during inhomogeneous deformation and acoustic scattering of carriers in crystals, *Soviet Physics-Solid State*, 5(10), pp.2069–2070.

Kumar, A. and Chakraborty, D. (2009), Effective properties of thermo-electro-mechanically coupled piezoelectric fiber reinforced composites, *Materials and Design*, 30, pp.1216–1222.

Kundalwal, S.I. and Meguid, S.A. (2017), Multiscale modeling of regularly staggered carbon fibers embedded in nano-reinforced composites, *European Journal of Mechanics, A/Solids*, 64, pp.69–84.

Kundalwal, S.I., Meguid, S.A. and Weng, G.J. (2017), Strain gradient polarization in graphene, *Carbon*, 117, pp.462–472. (DOI: 10.1016/j.carbon.2017.03.013)

Kundalwal, S.I. and Ray, M.C. (2011), Micromechanical analysis of fuzzy fiber reinforced composites, *International Journal of Mechanics and Materials in Design*, 7(2), pp.149–166.

Kundalwal, S.I. and Ray, M.C. (2013), Effect of carbon nanotube waviness on the elastic properties of the fuzzy fiber reinforced composites, *Journal of Applied Mechanics*, 80(2), p.021010. (DOI: 10.1115/1.4007722)

Kundalwal, S.I., Shingare, K.B. and Rathi, A. (2019). Effect of flexoelectricity on the electromechanical response of graphene nanocomposite beam, *International Journal of Mechanics and Materials in Design*, 15(3), pp. 447–470. (DOI: 10.1007/s10999-018-9417-6)

Kvashnin, A.G., Sorokin, P.B., Yakobson, B.I. (2015), Flexoelectricity in carbon nanostructures: Nanotubes, fullerenes, and nanocones, *Journal of Physical Chemistry Letters*, 6(14), pp.2740–2744.

Landesmann, A., Camotim, D. and Garcia, R. (2016), On the strength and DSM design of cold-formed steel web/flange-stiffened lipped channel columns buckling and failing in distortional modes, *Thin-Walled Structures*, 105, pp.248–265. (DOI: 10.1016/j.tws.2016.03.023)

Lee, C., Wei, X., Kysar, J.W. and Hone, J. (2008), Measurement of the elastic properties and intrinsic strength of monolayer graphene, *Science*, 321(5887), pp.385–388. (DOI: 10.1126/science.1157996)

Li, H., Hu, K. and Tzou, H.S., (2018). Distributed flexoelectric modal signals on circular cylindrical shells. *Proceedings of the Institution of Mechanical Engineers, Part C: Journal of Mechanical Engineering Science*, 232(6), pp.952-961.

Li, Z., Zou, H. and Liu, P. (2015), Morphology and properties of porous polyimide films prepared through thermally induced phase separation, *RSC Advances. Royal Society of Chemistry*, 5(47), pp.37837–37842. (DOI: 10.1039/c5ra01514f)

Li, A., Zhou, S., Zhou, S. and Wang, B. (2014), Size-dependent analysis of a three-layer microbeam including electromechanical coupling, *Composite Structures*, 116(1), pp.120–127. (DOI: 10.1016/j.compstruct.2014.05.009)

Li, J. and Narita, Y. (2014), The effect of aspect ratios and edge conditions on the optimal damping design of thin soft core sandwich plates and beams, *Journal of Vibration and Control*, *20*(2), pp.266-279.

Li, P., You, Z., Cui, T. (2012), Graphene cantilever beams for nano switches, *Applied Physics Letters*, 101(9), p.093111.

Li, X., Chuang, K. and Tzou, H. (2010), Energy harvesting using a circular cylindrical shell laminated with a segmented piezoelectric layer, Proceedings of the 2010 Symposium on Piezoelectricity, *Acoustic Waves and Device Applications*, SPAWDA10, pp.139–144. (DOI: 10.1109/spawda.2010.5744290)

Li, X., Chuang, K.C., Li, H. and Tzou, H.S. (2011), Modal energy transduction of a cylindrical shell laminated with a segmented piezoelectric layer, *ASME 2011 International Mechanical Engineering Congress and Exposition*, American Society of Mechanical Engineers Digital Collection, pp.855–862. (DOI: 10.1115/imece2011-63037)

Liu, C., Ke, L.L., Wang, Y.S., Yang, J. and Kitipornchai, S. (2013), Thermo-electro-mechanical vibration of piezoelectric nanoplates based on the nonlocal theory, *Composite Structures*, 106, pp.167–174. (DOI: 10.1016/j.compstruct.2013.05.031)

Liu, C. and Rajapakse, R.K.N.D. (2010), Continuum models incorporating surface energy for static and dynamic response of nanoscale beams, *IEEE Transactions on Nanotechnology*, 9(4), pp.422–431. (DOI: 10.1109/tnano.2009.2034142)

Liu, C. and Rajapakse, R.K.N.D. (2013), A size-dependent continuum model for nanoscale circular plates, *IEEE Transactions on Nanotechnology*, 12(1), pp.13–20. (DOI: 10.1109/tnano.2012.2224880)

Liu, D., Kitipornchai, S., Chen, W. and Yang, J. (2018), Three-dimensional buckling and free vibration analyses of initially stressed functionally graded graphene reinforced composite cylindrical shell, *Composite Structures*, 189, pp.560–569. (DOI: 10.1016/j.compstruct.2018.01.106)

Liu, C., Rajapakse, R.K.N.D. and Phani, A.S. (2011), Finite element modeling of beams with surface energy effects, *Journal of Applied Mechanics*, 78(3), p.031014. (DOI: 10.1115/1.4003363)

Liu, J., Yan, H., Reece, M.J. and Jiang, K. (2012), Toughening of zirconia/alumina composites by the addition of graphene platelets, *Journal of the European Ceramic Society* 32, pp.4185–4193. (DOI: 10.1016/j.jeurceramsoc.2012.07.007)

Liu, Y., Wang, X. and Li, Y. (2020), Distributed piezoelectric actuator layout-design for active vibration control of thin-walled smart structures, *Thin-Walled Structures*, 147, p. 106530. (DOI: 10.1016/j.tws.2019.106530)

Ma, W. and Cross, L.E. (2001), Observation of the flexoelectric effect in relaxor Pb(Mg1/3Nb2/3)O3ceramics, *Applied Physics Letters*, 78(19), pp.2920–2921. (DOI: 10.1063/1.1356444)

Ma, W. and Cross, L.E. (2003), Strain-gradient-induced electric polarization in lead zirconate titanate ceramics, *Applied Physics Letters*, 82(19), pp.3293–3295. (DOI: 10.1063/1.1570517)

Majdoub, M.S., Sharma, P. and Cagin, T. (2008), Enhanced size-dependent piezoelectricity and elasticity in nanostructures due to the flexoelectric effect, *Physical Review B - Condensed Matter and Materials Physics*, 77(12), pp.1–9. (DOI: 10.1103/PhysRevB.77.125424)

Maranganti, R., Sharma, N.D. and Sharma, P. (2006), Electromechanical coupling in nonpiezoelectric materials due to nanoscale nonlocal size effects: Green's function solutions and embedded inclusions, *Physical Review B*, 74(1), p.014110. (DOI: 10.1103/physrevb.74.014110)

Mashkevich, V.S. and Tolpygo, K.B. (1957), Electrical, optical and elastic properties of diamond type crystals, *Soviet Physics JETP*, 5(3), pp.435–439.

Masson, B. (2009), Emergence of the alumina matrix composite in total hip arthroplasty, *International Orthopaedics* 33, pp.359–363. (DOI: 10.1007/s00264-007-0484-9)

Miller, R.E. and Shenoy, V.B. (2000), Size-dependent elastic properties of nanosized structural elements, *Nanotechnology*, 11(3), pp.139–147. (DOI: 10.1088/0957-4484/11/3/301)

Mindlin, R.D. (1968), Polarization gradient in elastic dielectrics, *International Journal of Solids and Structures*, 4(6), pp.637–642. (DOI: 10.1016/0020-7683(68)90079-6)

Mohan, V.B., Lau, K.T., Hui, D. and Bhattacharyya, D. (2018), Graphene-based materials and their composites: A review on production, applications and product limitations, *Composites Part B: Engineering*, 142, pp.200–220. (DOI: 10.1016/j.compositesb.2018.01.013)

Momeni, K., Odegard, G.M. and Yassar, R.S. (2010), Nanocomposite electrical generator based on piezoelectric zinc oxide nanowires, *Journal of Applied Physics*, 108(11), p.114303. (DOI: 10.1063/1.3517095)

Moreno, M.E., Tita, V. and Marques, F.D. (2009), September. Finite element analysis applied to evaluation of effective material coefficients for piezoelectric fiber composites, *Brazilian Symposium on Aerospace Eng. & Applications*.

Morozovska, A.N., Eliseev, E.A., Tagantsev, A.K., Bravina, S.L., Chen, L.Q., Kalinin, S.V. (2011), Thermodynamics of electromechanically coupled mixed ionic-electronic conductors: Deformation potential, Vegard strains, and flexoelectric effect, *Physical Review B - Condensed Matter and Materials Physics*, 83(19), p.195313.

Muñoz-Hernández, A., Diaz, G., Calderón-Muñoz, W.R., Leal-Quiros, E. (2017), Thermal-electric modeling of graphite: Analysis of charge carrier densities and Joule heating of intrinsic graphite rods, *Journal of Applied Physics*, 122(24), p.245107. (DOI: 10.1063/1.4997632)

Nguyen, T.D., Mao, S., Yeh, Y.W., Purohit, P.K. and McAlpine, M.C. (2013), Nanoscale flexoelectricity, *Advanced Materials*, 25(7), pp.946–974. (DOI: 10.1002/adma.201203852)

Nimje, S.V. and Panigrahi, S.K., (2014), Numerical simulation for stress and failure of functionally graded adhesively bonded tee joint of laminated FRP composite plates, *International Journal of Adhesion and Adhesives*, 48, pp.139-149.

Novoselov, K.S., Geim, A.K., Morozov, S.V., Jiang, D., Zhang, Y., Dubonos, S.V., Grigorieva, I.V. and Firsov, A.A. (2004), Electric field effect in atomically thin carbon films, *Science*, 306 (5696), pp.666–669. (DOI: 10.1126/science.1102896)

Odegard, G.M. (2004), Constitutive modeling of piezoelectric polymer composites Constitutive modeling of piezoelectric polymer composites Constitutive modeling of piezoelectric polymer composites, *Acta Materialia*, 52(18), pp.5315–5330.

Odegard, G.M., Clancy, T.C. and Gates, T.S. (2005), Modeling of the mechanical properties of nanoparticle/polymer composites, *Polymer*, 46(2), pp.553–562. (DOI: 10.1016/J.ploymer.2004.11.022)

Panigrahi, S.K., (2009), Damage analyses of adhesively bonded single lap joints due to delaminated FRP composite adherends, *Applied Composite Materials*, 16(4), pp.211-223.

Papageorgiou, D.G., Kinloch, I.A. and Young, R.J. (2017), Mechanical properties of graphene and graphene-based nanocomposites, *Progress in Materials Science*, 90, pp. 75–127. (DOI: 10.1016/j.pmatsci.2017.07.004)

Papageorgiou, D.G., Li, Z., Liu, M., Kinloch, I.A. and Young, R.J. (2020), Mechanisms of mechanical reinforcement by graphene and carbon nanotubes in polymer nanocomposites, *Nanoscale*, 12, pp.2228–2267. (DOI: 10.1039/c9nr06952f)

Parashar, A., Mertiny, P. (2012), Representative volume element to estimate buckling behavior of graphene / polymer nanocomposite, *Nanoscale research letter*, 7(1), p.515. (DOI: 10.1186/1556-276X-7-515)

Park, Y.J., Park, C.H., Shin Park, J., Kong, K., Chang, H., Im, S. (2010), Multiscale computations for carbon nanotubes based on a hybrid QM/QC (quantum mechanical and quasi continuum) approach, *Journal of the Mechanics and Physics of Solids*, 58(2), pp.86–102.

Pei, Q.X., Zhang, Y.W. and Shenoy, V.B. (2010), A molecular dynamics study of the mechanical properties of hydrogen functionalized graphene, *Carbon*, 48, pp.898–904. (DOI: 10.1016/j.carbon.2009.11.014)

Pettermann, H.E. and Suresh, S. (2000), A comprehensive unit cell model: A study of coupled effects in piezoelectric 1-3 composites, *International Journal of Solids and Structures*, 37(39), pp.5447–5464. (DOI: 10.1016/S0020-7683(99)00224-3)

Plimpton, S. (1995), Fast parallel algorithms for short-range molecular dynamics, *Journal of Computational Physics*, 117(1), pp.1–19.

Politano, A., Chiarello, G. (2013), Probing the Young's modulus and Poisson's ratio in graphene/metal interfaces and graphite: a comparative study, *Nano Research*, 8(6), pp. 1847–1856. (DOI: 10.1007/s12274-014-0691-9)

Popat, K.C. and Desai, T.A. (2013), Alumina. Biomaterials Science: An Introduction to Materials, Third Edition, pp.162–166. (DOI: 10.1016/B978-0-08-087780-8.00018-8)

Pradhan, S.C. and Murmu, T. (2009), Small-scale effect on vibration analysis of single-walled carbon nanotubes embedded in an elastic medium using nonlocal elasticity theory, *Journal of Applied Physics*, 105, p.124306. (DOI: 10.1063/1.3151703)

Prolongo, S.G., Jiménez-Suárez, A., Moriche, R. and Ureña, A. (2014), Graphene nanoplatelets thickness and lateral size influence on the morphology and behavior of epoxy composites, *European Polymer Journal,* 53, pp.292–301. (DOI: 10.1016/j.eurpolymj.2014.01.019)

Prolongo, S.G., Jiménez-Suárez, A., Moriche, R. and Ureña, A. (2018), Influence of thickness and lateral size of graphene nanoplatelets on water uptake in epoxy/graphene nanocomposites, *Applied Science*, 8 (9), p.1550. (DOI: org/10.3390/app8091550)

Rafiee, M.A., Rafiee, J., Yu, Z.Z. and Koratkar, N. (2009), Buckling resistant graphene nanocomposites, *Applied Physics Letters*, 95(22), p.223103. (DOI: 10.1063/1.3269637).

Rao, Z. and Tzou, H.S. (2011), Diagonal flexoelectric sensor on cylindrical shell substructure, *Symposium on Piezoelectricity, Acoustic Waves and Device Applications* (SPAWDA), pp. 502-505. IEEE.

Ray, M.C. (2006), Micromechanics of piezoelectric composites with improved effective piezoelectric constant, *International Journal of Mechanics and Materials in Design*, 3(4), pp.361–371. (DOI: 10.1007/s10999-007-9046-y)

Ray, M.C. and Pradhan, A.K. (2006), The performance of vertically reinforced 1-3 piezoelectric composites in active damping of smart structures, *Smart Materials and Structures*, 15(2), pp.631–641.

Reddy, J.N. (2003), Mechanics of laminated composite plates and shells: theory and analysis, Second Edition, p.858. (DOI: 10.1038/sj.leu.2403242)

Roberts, M.W., Clemons, C.B., Wilber, J.P., Young, G.W., Buldum, A., Quinn, D.D. (2010), Continuum plate theory and atomistic modeling to find the flexural rigidity of a graphene sheet interacting with a substrate, *Journal of Nanotechnology*, pp.1–8.

Ru, C.Q. (2009), Thermoelastic dissipation of nanowire resonators with surface stress, *Physica E: Low-Dimensional Systems and Nanostructures*, 41(7), pp.1243–1248. (DOI: 10.1016/j.physe.2009.02.008)

Rupa, N.S. and Ray, M.C. (2017), Analysis of flexoelectric response in nanobeams using nonlocal theory of elasticity, *International Journal of Mechanics and Materials in Design*, 13(3), pp. 453–467.

Saber, N., Araby, S., Meng, Q., Hsu, H.Y., Yan, C., Azari, S., Lee, S.H., Xu, Y., Ma, J. and Yu, S. (2014), Superior piezoelectric composite films: Taking advantage of carbon nanomaterials, *Nanotechnology*, 25(4), p.045501.

Sadeghzadeh, S. (2016), Benchmarking the penetration-resistance efficiency of multilayer graphene sheets due to spacing the graphene layers, *Applied Physics A*, 122(7), pp.1–12. (DOI: 10.1007/s00339-016-0186-5)

Sahmani, S., Bahrami, M. and Aghdam, M.M. (2016), Surface stress effects on the nonlinear postbuckling characteristics of geometrically imperfect cylindrical nanoshells subjected to axial compression, *International Journal of Engineering Science*, 99, pp.92–106. (DOI: 10.1016/j.ijengsci.2015.10.010)

Sapsathiarn, Y. and Rajapakse, R.K.N.D. (2017), Static and dynamic analyses of nanoscale rectangular plates incorporating surface energy, *Acta Mechanica*, 228(8), pp.2849–2863. (DOI: 10.1007/s00707-015-1521-1)

Smith, W.A. and Auld, B.A. (1991), Modeling 1–3 composite piezoelectrics: thickness-mode oscillations, *IEEE Transactions on Ultrasonics, Ferroelectrics, and Frequency Control*, 38(1), pp.40–47. (DOI: 10.1109/58.67833)

Shao, Z.Z., Wen, L.Y., Wu, D.M., Wang, X.F., Zhang, X.A. and Chang, S.L. (2010), A continuum model of piezoelectric potential generated in a bent ZnO nanorod, *Journal of Physics D: Applied Physics*, 43(24), p.245403. (DOI: 10.1088/0022-3727/43/24/245403)

Sharma, N.D., Maranganti, R. and Sharma, P. (2007), On the possibility of piezoelectric nanocomposites without using piezoelectric materials, *Journal of the Mechanics and Physics of Solids*, 55(11), pp.2328–2350. (DOI: 10.1016/j.jmps.2007.03.016)

Shen, H.S., Xiang, Y. and Lin, F. (2017), Thermal buckling and postbuckling of functionally graded graphene- reinforced composite laminated plates resting on elastic foundations, *Thin-Walled Structures*, 118, pp.229–237. (DOI: 10.1016/j.tws.2017.05.006)

Shen, H.S., Xiang, Y., Lin, F. and Hui, D. (2017), Buckling and postbuckling of functionally graded graphene-reinforced composite laminated plates in thermal environments, *Composites Part B: Engineering*, 119, pp.67–78. (DOI: 10.1016/j.compositesb.2017.03.020)

Shen, S. and Hu, S. (2010), A theory of flexoelectricity with surface effect for elastic dielectrics, *Journal of the Mechanics and Physics of Solids*, 58(5), pp.665–677. (DOI: 10.1016/j.jmps.2010.03.001)

Shi, Y. and Wang, Y. (2019), Size-dependent and multi-field coupling behavior of layered multiferroic nanocomposites, *Materials*, 12(2), p.260. (DOI: 10.3390/ma12020260)

Shingare, K.B., Gupta, M. and Kundalwal, S.I. (2020), Evaluation of effective properties for smart graphene reinforced nanocomposite materials, *Materials Today: Proceedings*, 23, pp.523–527. (DOI: 10.1016/j.matpr.2019.05.399)

Shingare, K.B. and Kundalwal, S.I. (2019), Static and dynamic response of graphene nanocomposite plates with flexoelectric effect, *Mechanics of Materials*, 134, pp.69–84. (DOI: 10.1016/j.mechmat.2019.04.006)

Shingare, K.B. and Kundalwal, S.I. (2020), Flexoelectric and surface effects on the electromechanical behavior of graphene-based nanobeams, *Applied Mathematical Modelling*, 81, pp.70–91. (DOI: 10.1016/j.apm.2019.12.021)

Shu, L., Wei, X., Pang, T., Yao, X. and Wang, C. (2011), Symmetry of flexoelectric coefficients in crystalline medium, *Journal of Applied Physics*, 110(10), p.104106. (DOI: 10.1063/1.3662196)

Soedel, W. (2004), Vibrations of shells and plates, Third ed., CRC Press, pp.1683–1683. (DOI: 10.1121/1.1873932)

Song, M., Kitipornchai, S. and Yang, J. (2017), Free and forced vibrations of functionally graded polymer composite plates reinforced with graphene nanoplatelets, 159, pp.579–588 *Composite Structures*. (DOI: 10.1016/j.compstruct.2016.09.070)

Song, Y.S. and Youn, J.R. (2006), Modeling of effective elastic properties for polymer based carbon nanotube composites, *Polymer*, 47(5), pp.1741–1748. (DOI: 10.1016/j.polymer.2006.01.013)

Spanos, K.N., Georgantzinos, S.K. and Anifantis, N.K. (2015), Mechanical properties of graphene nanocomposites : A multiscale finite element prediction, *Composite Structures*, 132, pp.536–544. (DOI: 10.1016/j.compstruct.2015.05.078)

Sreenivasulu, B., Ramji, B.R. and Nagaral, M. (2018), A review on graphene reinforced polymer matrix composites, *Materials Today: Proceedings*, 5(1), pp.2419–2428. (DOI: 10.1016/j.matpr.2017.11.021)

Stuart, S.J., Tutein, A.B., and Harrison, J.A. (2000), A reactive potential for hydrocarbons with intermolecular interactions, *The Journal of Chemical Physics*, 112(14), p.6472.

Su, Y., Li, J.J. and Weng, G.J. (2018), Theory of thermal conductivity of graphene-polymer nanocomposites with interfacial Kapitza resistance and graphene-graphene contact resistance, *Carbon*, 137, pp.222–233.

Su, Y.X., Zhou, Z.D. and Yang, F.P. (2019), Electromechanical analysis of bilayer piezoelectric sensors due to flexoelectricity and strain gradient elasticity, *AIP Advances*, 9(1), p.015207. (DOI: 10.1063/1.5081072)

Sun, J., Gao, L., Jin, X. (2005), Reinforcement of alumina matrix with multi-walled carbon nanotubes, *Ceramics International*, 31, pp.893–896. (DOI: 10.1016/j.ceramint.2004.10.002)

Sundar, U., Cook-Chennault, K.A., Banerjee, S., Refour, E. (2016), Dielectric and piezoelectric properties of percolative three-phase piezoelectric polymer composites. *Journal of Vacuum Science & Technology B, Nanotechnology and Microelectronics: Materials, Processing, Measurement, and Phenomena*, 34(4), p.41232.

Tian, W., Li, S., Wang, B., Chen, X., Liu, J. and Yu, M. (2016), Graphene-reinforced aluminum matrix composites prepared by spark plasma sintering, *International Journal of Minerals, Metallurgy, and Materials*, 23(6), pp.723–729.

Trindade, M.A. and Benjeddou, A. (2009), Effective electromechanical coupling coefficients of piezoelectric adaptive structures: Critical evaluation and optimization, *Mechanics of Advanced Materials and Structures*, 16(3), pp.210–223. (DOI: 10.1080/15376490902746863)

Tzeng, P., Stevens, B., Devlaming, I., Grunlan, J.C. (2015), Polymer-graphene oxide quadlayer thin-film assemblies with improved gas barrier, *Langmuir* 31 (21), pp.5919–5927. (DOI: 10.1021/acs.langmuir.5b00717)

Tzou, H.S., Rao, Z. and Hu, S.D. (2013), August. Diagonal Flexoelectric Sensors and Sensitivity Analysis on Cylindrical Shells, In International Design Engineering Technical Conferences and Computers and Information in Engineering Conference (Vol. 55997, p. V008T13A078). American Society of Mechanical Engineers.

Tzou, H.S. and Zhang, X.F. (2016), A flexoelectric double-curvature nonlinear shell energy harvester. Journal of Vibration and Acoustics, 138(3), p. 031006.

Tzou, H. S. (1991), Distributed modal identification and vibration control of continua: theory and applications, *Journal of Dynamic Systems, Measurement, and Control*, pp. 494-499.

Tzou, H.S. (2019), Tubular shell energy harvester, In piezoelectric shells springer, Dordrecht. pp.385–407.

Verma, D., Gupta, S.S. and Batra, R.C. (2014), Vibration mode localization in single- and multi-layered graphene nanoribbons, *Computational Materials Science*, 95, pp.41–52. (DOI: 10.1016/j.commatsci.2014.07.005)

Wang J., Li, J.J., Weng, G.J. and Su, Y. (2020), The effects of temperature and alignment state of nanofillers on the thermal conductivity of both metal and nonmetal based graphene nanocomposites, *Acta Materialia*, 185, pp.461–473.

Wang, J., Li, Z., Fan, G., Pan, H., Chen, Z. and Zhang, D. (2012), Reinforcement with graphene nanosheets in aluminum matrix composites, *Scripta Materialia*, 66(8), pp.594–597.

Wang, K., Wang, Y., Fan, Z., Yan, J. and Wei, T. (2011), Preparation of graphene nanosheet/alumina composites by spark plasma sintering, *Materials Research Bulletin* 46, pp.315–318. (DOI: 10.1016/j.materresbull.2010.11.005)

Wang, K.F. and Wang, B.L. (2016), An analytical model for nanoscale unimorph piezoelectric energy harvesters with flexoelectric effect, *Composite Structures*, 153, pp.253–261. (DOI: 10.1016/j.compstruct.2016.05.104)

Wang, M., Xu, Y.G., Qiao, P. and Li, Z.M. (2019), A two-dimensional elasticity model for bending and free vibration analysis of laminated graphene-reinforced composite beams, *Composite Structures*, 211, pp.364–375. (DOI: 10.1016/j.compstruct.2018.12.033)

Wang, Y., Feng, C., Zhao, Z., Lu, F. and Yang, J. (2018), Torsional buckling of graphene platelets (GPLs) reinforced functionally graded cylindrical shell with cutout, *Composite Structures*, 197, pp.72–79. (DOI: 10.1016/j.compstruct.2018.05.056)

Wang, Y., Feng, C., Zhao, Z. and Yang, J. (2018), Eigenvalue buckling of functionally graded cylindrical shells reinforced with graphene platelets (GPL), *Composite Structures*, 202, pp.38–46. (DOI: 10.1016/j.compstruct.2017.10.005)

Wang, Z.L. (2007), The new field of nanopiezotronics Semiconducting and piezoelectric nanowires and nanobelts have exciting, *Materials Today*, 10(5), pp.20–28. (DOI: 10.1016/S1369-7021(07)70076-7)

Wang, Z.L. and Song, J. (2006), Piezoelectric nanogenerators based on zinc oxide nanowire arrays, *Science*, 312(5771), pp.242–246.

Wozniak, J., Kurtycz, P., Broniszewski, K., Kostecki, M., Morgiel, J. and Olszyna, A. (2015), Properties of alumina matrix composites reinforced with nickel-coated graphene, *Materials Today: Proceedings,* 2, pp.376–382. (DOI: 10.1016/j.matpr.2015.04.036)

Wu, H., Yang, J. and Kitipornchai, S. (2017), Dynamic instability of functionally graded multilayer graphene nanocomposite beams in thermal environment, *Composite Structures*, 162, pp.244–254. (DOI: 10.1016/j.compstruct.2016.12.001)

Xu, R., Lu, Y., Jiang, C., Chen, J., Mao, P., Gao, G., Zhang, L. and Wu, S. (2014), Facile fabrication of three-dimensional graphene foam/poly (dimethylsiloxane) composites and their potential application as strain sensor, *ACS applied materials & interfaces,* 6(16), pp.13455–13460. (DOI:10.1021/am502208g)

Yan, Z. and Jiang, L.Y. (2011), Surface effects on the electromechanical coupling and bending behaviours of piezoelectric nanowires, *Journal of Physics D: Applied Physics*, 44(7), p.075404. (DOI: 10.1088/0022-3727/44/7/075404)

Yan, Z. and Jiang, L.Y. (2012), Vibration and buckling analysis of a piezoelectric nanoplate considering surface effects and in-plane constraints, *Proceedings of the Royal Society A: Mathematical, Physical and Engineering Sciences*, 468(2147), pp.3458–3475. (DOI: 10.1098/rspa.2012.0214)

Yan, Z., and Jiang, L.Y. (2013), Flexoelectric effect on the electroelastic responses of bending piezoelectric nanobeams, *Journal of Applied Physics*, 113(19), p.194102.

Yan, Z. and Jiang, L.Y. (2015), Effect of flexoelectricity on the electroelastic fields of a hollow piezoelectric nanocylinder, *Smart Materials and Structures*, 24(6), p.065003.

Yang, F. and Meguid, S.A., (2013), Efficient multi-level modeling technique for determining effective board drop reliability of PCB assembly, *Microelectronics Reliability*, *53*(7), pp.975-984.

Yang, L., Phua, S.L., Toh, C.L., Zhang, L., Ling, H., Chang, M., Zhou, D., Dong, Y. and Lu, X. (2013), Polydopamine-coated graphene as multifunctional nanofillers in polyurethane, *RSC Advances*, 3(18), pp.6377–6385. (DOI: 10.1039/c3ra23307c)

Yang, W., Liang, X. and Shen, S. (2015), Electromechanical responses of piezoelectric nanoplates with flexoelectricity, *Acta Mechanica*, 226(9), pp.3097–3110. (DOI: 10.1007/s00707-015-1373-8)

Yang, Y.H., Bolling, L., Priolo, M.A. and Grunlan, J.C. (2013), Super gas barrier and selectivity of graphene oxide-polymer multilayer thin films, *Advanced Materials* 25 (4), pp.503–508. (DOI:10.1002/adma.201202951)

Yildirim, O.A. and Ozturk, T. (2018), Graphene-semiconductor composites as visible light-induced photocatalyst, *IntechOpen*. (DOI: 10.5772/intechopen.70709).

Ying, C. and Zhifei, S. (2005), Exact solutions of functionally gradient piezothermoelastic cantilevers and parameter identification, *Journal of Intelligent Material Systems and Structures*, 16(6), pp.531–539. (DOI: 10.1177/1045389X05053208)

Yolshina, L.A., Muradymov, R.V., Korsun, I.V., Yakovlev, G.A. and Smirnov, S.V. (2016). Novel aluminum-graphene and aluminum-graphite metallic composite materials: Synthesis and properties. *Journal of alloys and compounds*, 663, pp.449–459.

Young, R.J., Kinloch, I.A., Gong, L. and Novoselov, K.S. (2012), The mechanics of graphene nanocomposites: A review, *Composites Science and Technology*, 72(12), pp. 1459–1476. (DOI: 10.1016/j.compscitech.2012.05.005)

Zelisko, M., Hanlumyuang, Y., Yang, S., Liu, Y., Lei, C., Li, J., Ajayan, P.M. and Sharma, P. (2014), Anomalous piezoelectricity in two-dimensional graphene nitride nanosheets, *Nature Communications*, 5(1), pp.1–7. (DOI: 10.1038/ncomms5284)

Zhang, C., Chen, W. and Zhang, C. (2012), On propagation of anti-plane shear waves in piezoelectric plates with surface effect, Physics Letters, Section A: General, *Atomic and Solid State Physics*, 376(45), pp.3281–3286. (DOI: 10.1016/j.physleta.2012.09.027)

Zhang, C., Zhu, J., Chen, W. and Zhang, C. (2014), Two-dimensional theory of piezoelectric shells considering surface effect, *European Journal of Mechanics, A/Solids*, 43, pp.109–117. (DOI: 10.1016/j.euromechsol.2013.09.007)

Zhang, S., Xu, M., Liang, X. and Shen, S. (2015), Shear flexoelectric coefficient μin polyvinylidene fluoride, *Journal of Applied Physics*, 117(20), p.204102. (DOI: 10.1063/1.4921444)

Zhang, Y.B., Tan, Y.W., Stormer, H.L., Kim, P. (2005), Experimental observation of the quantum Hall effect and Berry's phase in graphene, *Nature*, 438(7065), pp.201–204. (DOI: 10.1038/nature04235)

Zhang, Z. and Jiang, L. (2014), Size effects on electromechanical coupling fields of a bending piezoelectric nanoplate due to surface effects and flexoelectricity, *Journal of Applied Physics*, 116(13), p.134308. (DOI: 10.1063/1.4897367)

Zhang, Z., Li, Y., Wu, H., Zhang, H., Wu, H., Jiang, S. and Chai, G. (2018), Mechanical analysis of functionally graded graphene oxide-reinforced composite beams based on the first-order shear deformation theory, *Mechanics of Advanced Materials and Structures*, 27(1), pp.3-11. (DOI: 10.1080/15376494.2018.1444216)

Zhao, M., Qian, C., Lee, S.W.R., Tong, P., Suemasu, H. (2012), Electro-elastic analysis of piezoelectric laminated plates, *Journal of Advanced Composite Materials*, 16, pp.63–81. (DOI: 10.1163/156855107779755273)

Zhao, X., Zhang, Q., Chen, D. and Lu, P. (2010), Enhanced mechanical properties of graphene-based poly (vinyl alcohol) composites, *Macromolecules*, 43(5), pp.2357–2363. (DOI: 10.1021/ma902862u)

Zhao, Z., Feng, C., Wang, Y., Yang, J. (2017), Bending and vibration analysis of functionally graded trapezoidal nanocomposite plates reinforced with graphene nanoplatelets (GPLs), *Composite Structures*, 180, pp.799–808. (DOI: 10.1016/j.compstruct.2017.08.044)

Zhao, S., Zhao, Z., Yang, Z., Ke, L., Kitipornchai, S. and Yang, J., (2020), Functionally graded graphene reinforced composite structures: A review. *Engineering Structures*, 210, p.110339.

Zhou, H., Pei, Y., Hong, J., Fang, D., (2016), Analytical method to determine flexoelectric coupling coefficient at nanoscale, *Applied Physics Letter*, 108, p.101908. (DOI: 10.1063/1.4943660)

Zhu, J., Lim, J., Lee, C., Joh, H., Kim, H.C., Park, B., You, N. and Lee, S. (2014), Multifunctional polyimide/graphene oxide composites via in situ polymerization, *Journal of Applied Polymer Science*, p.40177, pp. 1–7. (DOI: 10.1002/app.40177)

Zubko, P., Catalan, G. and Tagantsev, A.K. (2013), Flexoelectric effect in solids, *Annual Review of Materials Research*, 43(1), pp.387–421. (DOI: 10.1146/annurev-matsci-071312-121634)

List of Publications from the Thesis

The following papers are published/ under review from the research work carried out in this Thesis:

A1. Refereed Journal Publications:

1. S. I. Kundalwal, **K. B. Shingare** and A. Rathi, "Effect of flexoelectricity on the electromechanical response of graphene nanocomposite beam", *International Journal of Mechanics and Materials in Design*, vol. 15, pp. 447–470, 2019.
2. **K. B. Shingare** and S. I. Kundalwal, "Static and dynamic response of graphene nanocomposite plates with flexoelectric effect", *Mechanics of Materials*, vol. 134, pp. 69–84, 2019.
3. **K. B. Shingare** and S. I. Kundalwal, "Flexoelectric and surface effects on the electromechanical behavior of graphene-based beams", *Applied Mathematical Modelling*, vol. 81, pp. 70–91, 2020.
4. S. I. Kundalwal, **K. B. Shingare** and M. Gupta, "Flexoelectric effect on electric potential in piezoelectric cylindrical graphene-based composite nanowire: Analytical and numerical modelling", *European Journal of Mechanics – A/Solids*, vol. 84, p. 104050, 2020.
5. S. I. Kundalwal and **K. B. Shingare**, "Electromechanical response of thin shell laminated with flexoelectric composite layer", *Thin-Walled Structures*, vol. 157, p. 107138, 2020.

A2. Refereed Conference Proceedings:

1. **K. B. Shingare**, M. Gupta and S. I. Kundalwal, "Evaluation of effective properties for smart graphene reinforced nanocomposite materials", *Materials Today Proceedings*, vol. 23, pp. 523–527, 2020.
2. **K. B. Shingare**, and S. I. Kundalwal, "Effect of piezoelectricity on the electromechanical response of graphene nanocomposite", *2nd International Conference on Nano Science and Engineering Applications ICONSEA-2018*, Hyderabad, India, October 4-6, 2018.

3. **K. B. Shingare**, M. Gupta and S. I. Kundalwal, “Effect of size-dependent properties on static and dynamic behavior of the graphene nanocomposite plate: Analytical approach”, *International Conference on Precision, Meso, Micro and Nano Engineering (COPEN 2019)*, IIT Indore. (Under review)
4. **K. B. Shingare**, M. Gupta and S.I. Kundalwal, “Piezoelectric Effect on a Circular Cylindrical Shell integrated with non-piezoelectric graphene-based composite layer”, *IEEE 20th International Conference on Nanotechnology (IEEE-NANO)*, July 29-31, 2020, Hotel Bonaventure, Montreal, Canada.

A3. Book Chapter:

1. S. I. Kundalwal, **K. B. Shingare**, and P. P. Maware, “Carbon Fiber Reinforced Nanocomposites: A Multiscale Modeling of Regularly Staggered Carbon Fibers”, Fiber-Reinforced Nanocomposites: Fundamentals and Applications, *Micro and Nano Technologies*, Elsevier, pp. 101–127, 2020.

Curriculum Vitae

Name	**Mr. Kishor Balasaheb Shingare** **PhD Research Scholar**	
Post-secondary Education and Degrees:	SVERI's College of Engineering Pandharpur, Maharashtra (India) 2009–2013 **B.E.** (Mechanical) AISSMS College of Engineering Pune, Maharashtra (India) 2013–2015 **M.E.** (Design Engineering) Indian Institute of Technology Indore Madhya Pradesh (India) 2017–2020 **Ph.D.** (Mechanical Design Engineering)	
Honour and Awards:	CSIR SRF 2019–2021	
Experience:	Assistant Professor JSPM College of Engineering, Pune. 2016–2017	
Related work Experience:	Teaching Assistant Indian Institute of Technology Indore 2017–2020	
Title of Thesis:	**Modelling of Flexoelectric Graphene-Based Structures: Beam, Plate, Wire and Shell**	
Thesis Supervisor:	Dr. Shailesh I Kundalwal	

Technical skills	**Designing software:** AutoCAD, Creo Parametric **Design Analysis:** ANSYS, COMSOL Multiphysics, FEAST **Mathematical Analysis:** Matlab **Documentation tools:** MS office, Origin.
Personal Details:	**Date of Birth:** 09/11/1991 **Sex:** Male **Marital Status:** Married **Nationality:** Indian **Permanent Address:** Sr. No. 26/2, Bombale Hanuman Chowk, Osmanabad - 413501, Maharashtra, India. **Present Address:** Applied and Theoretical Mechanics (ATOM) lab, IIT Indore, Simrol - 453532, Madhya Pradesh, India. **Languages Known:** Marathi, Hindi, English : kishorshingare911@gmail.com; phd1701203008@iiti.ac.in +91-9028555435; 8600440655 https://in.linkedin.com https://scholar.google.co.in